



# Etude numérique d'hélices cycloïdales : Analyse des écoulements tourbillonnaires instationnaires et optimisation

Lei Shi

## ► To cite this version:

Lei Shi. Etude numérique d'hélices cycloïdales : Analyse des écoulements tourbillonnaires instationnaires et optimisation. Génie des procédés. HESAM Université, 2021. Français. NNT : 2021HESAE059 . tel-03683567

**HAL Id: tel-03683567**

<https://pastel.hal.science/tel-03683567>

Submitted on 31 May 2022

**HAL** is a multi-disciplinary open access archive for the deposit and dissemination of scientific research documents, whether they are published or not. The documents may come from teaching and research institutions in France or abroad, or from public or private research centers.

L'archive ouverte pluridisciplinaire **HAL**, est destinée au dépôt et à la diffusion de documents scientifiques de niveau recherche, publiés ou non, émanant des établissements d'enseignement et de recherche français ou étrangers, des laboratoires publics ou privés.

**ÉCOLE DOCTORALE SCIENCES DES MÉTIERS DE L'INGÉNIUR**  
**[Laboratoire de Mécanique des Fluides de Lille – Campus de Lille]**

# THÈSE

présentée par : **Lei SHI**

soutenue le : **16 Décembre 2021**

pour obtenir le grade de : **Docteur d'HESAM Université**

préparée à : **École Nationale Supérieure d'Arts et Métiers**

Spécialité : **Génie énergétique**

## **Etude numérique d'hélices cycloïdales : Analyse des écoulements tourbillonnaires instationnaires et optimisation**

THÈSE dirigée par :

**M. COUTIER-DELGOSHA Olivier**

et dirigée par :

**Mme. BAYEUL-LAINÉ Annie-Claude**

**Jury**

<b>M. Jacques-André ASTOLFI</b> , Professeur, Ecole Navale	Président
<b>M. Antoine DUCOIN</b> , Maître de Conférences HDR, Ecole Centrale de Nantes	Rapporteur
<b>M. Jean-Luc ESTIVALEZ</b> , Professeur, Institut de Mécanique des Fluides de Toulouse	Rapporteur
<b>Mme. Céline GABILLET</b> , Maître de Conférences, Ecole Navale	Examinateuse
<b>M. Moble BENEDICT</b> , Professeur, Texas A&M University	Examinateur
<b>M. Pierre-Luc DELAFIN</b> , Maître de Conférences, Institut National Polytechnique de Grenoble	Examinateur
<b>Mme. Annie-Claude BAYEUL-LAINÉ</b> , Maître de Conférences HDR, Arts et Métiers Sciences et Technologies	Examinateuse
<b>M. Olivier COUTIER-DELGOSHA</b> , Professeur, Arts et Métiers Sciences et Technologies	Examinateur
<b>M. Frédéric HAUVILLE</b> , Maître de Conférences, Ecole Navale	Invité

T  
H  
È  
S  
E



## Acknowledgements

Firstly, I would like to show my gratitude to my supervisors, Prof Olivier Coutier-Delgosha and Annie-Claude Bayeul-Lainé, for providing me an opportunity to study in Arts et Métiers, ENSAM. Their constructive suggestions and comments indeed improve the work in the thesis significantly.

I would also like to thank my committee members including Prof. Antoine Ducoin (Ecole Centrale de Nantes), Prof. Jean-Luc Estivalez (Institut de Mécanique des Fluides de Toulouse), Prof. Jacques-André Astolif (Ecole Navale), Prof. Céline Gabillet (Ecole Navale) Prof. Moble Benedict (Texas A&M University), Prof. Pierre-Luc Delafin (Institut National Polytechnique de Grenoble) and Prof. Frédéric Heauville (Ecole Navale) for reviewing the work in my thesis and providing some suggestions and comments.

Sincere thanks are given to Prof. Jacques André Astolfi, Patrick Dupond and Sophie Simonet for being my academic follow-up committee. They really provide me some good ideas and suggestions to improve my work continuously.

I am grateful to all the colleagues in ENSAM for the help in my work and life, especially to Mr. Pierre Guiol, Mr. Alberto Baretter, Dr. Guangjian Zhang, Dr. Xinlei Zhang, Dr. Yuxing Bai, Mr. Kunpeng Long, Mrs. Naly Ratolojanahary, Mr. Hui Wang, Mr. Shuo Liu, Mr. Meng Fan, Mr. Zhidian Yang and Mrs. Xintong Chen.

I also show my appreciation to the ARC in Virginia Tech, for providing the powerful computational platform. The special thanks are given to a friend from VT, Khanh Nguyen, for giving me some guidelines how to use the super-computer.

Finally and most importantly, I would like to show my love to my parents, my wife and child, for the companion and support in my PhD life.

# List of contents

<b>List of figures.....</b>	<b>III</b>
<b>List of tables.....</b>	<b>IX</b>
<b>1 INTRODUCTION AND LITERATURE REVIEW .....</b>	<b>1</b>
1.1 BACKGROUND OF PRESENT WORK.....	1
1.2 MECHANISMS OF TRANSITION AND DYNAMIC STALL .....	2
1.3 TRANSITION AND DYNAMIC STALL ON AIRFOILS/HYDROFOILS .....	3
1.4 STATE-OF-THE-ART INVESTIGATIONS OF VARIABLE-PITCH TURBINES AND PROPELLERS.....	6
1.5 PARAMETRICAL STUDY AND OPTIMIZATION OF VARIABLE-PITCH TURBINES AND PROPELLERS .....	8
1.6 OBJECTIVE OF PRESENT WORK.....	10
<b>2 CALIBRATION AND VALIDATION OF THE SST <math>\gamma - \widetilde{Re}_{\theta t}</math> MODEL</b>	<b>11</b>
2.1 TRANSITIONAL FLOWS AROUND A NACA0018 AIRFOIL .....	11
2.1.1 Introduction.....	11
2.1.2 SST $\gamma - \widetilde{Re}_{\theta t}$ transition model.....	11
2.1.3 Flow configuration, meshing and numerical setup .....	12
2.1.4 Effect of mesh distribution .....	14
2.1.5 Effect of inlet turbulence condition .....	15
2.1.6 Effect of correlations and parameter .....	18
2.1.7 Effect of turbulence model .....	21
2.1.8 Effect of angle-of-attack.....	23
2.1.9 Effect of Reynolds number .....	29
2.1.10 Conclusions .....	31
2.2 APPLICATION OF THE SST $\gamma - \widetilde{Re}_{\theta t}$ MODEL TO A CYCLOIDAL ROTOR.....	33
2.2.1 Introduction.....	33
2.2.2 Geometry parameters, meshing and numerical setup .....	33
2.2.3 Analysis of unsteady vortical flows.....	40
2.2.4 Main features of laminar-turbulence transition.....	63
2.2.5 Conclusions .....	68

<b>3</b>	<b>PARAMETRICAL STUDY AND OPTIMIZATION OF A CYCLOIDAL ROTOR.....</b>	<b>70</b>
3.1	INFLUENCE OF THE PITCHING KINEMATIC .....	70
3.1.1	Introduction.....	70
3.1.2	Symmetrical/asymmetrical pitching kinematics.....	70
3.1.3	Conclusions.....	87
3.2	INFLUENCE OF THE CHORD-TO-RADIUS RATIO.....	89
3.2.1	Introduction.....	89
3.2.2	Effect of $c/R$ .....	89
3.2.3	Effect of $Re$ .....	98
3.2.4	Effect of $\lambda$ .....	106
3.2.5	Conclusions.....	114
3.3	INFLUENCE OF THE PITCH-PIVOT-POINT .....	115
3.3.1	Introduction.....	115
3.3.2	Effect of $x/c$ .....	115
3.3.3	Effect of $Re$ .....	126
3.3.4	Effect of $\lambda$ .....	133
3.3.5	Conclusions.....	142
3.4	INFLUENCE OF THE BLADE PROFILE .....	143
3.4.1	Introduction.....	143
3.4.2	Symmetrical/asymmetrical profiles.....	143
3.4.3	Effect of $Re$ .....	155
3.4.4	Effect of $\lambda$ .....	161
3.4.5	Conclusions.....	168
<b>4</b>	<b>OVERALL SUMMARY AND PERSPECTIVES .....</b>	<b>169</b>
4.1	CALIBRATION AND VALIDATION OF THE SST $\gamma - \widetilde{Re}_{\theta t}$ MODEL.....	169
4.2	PARAMETRICAL STUDY AND OPTIMIZATION OF A CYCLOIDAL ROTOR.....	170
4.3	PERSPECTIVES .....	171
<b>REFERENCES.....</b>	<b>173</b>	
<b>FRENCH EXTENDED SUMMARY.....</b>	<b>179</b>	

## List of figures

<b>Fig.1.1</b> Sketch of (a) pitching motion, (b) heaving motion and (c) flapping motion [1]. .....	1
<b>Fig.1.2</b> Application of cycloidal propeller. (a) Large-size ship; (b) Unmanned aircraft.....	1
<b>Fig.1.3</b> Sketch of blade motion. (a) Blade angle definition; (b) Coordinate system.....	2
<b>Fig.1.4</b> Sketch of transition and dynamic stall. (a) Mechanism of LSB generation; (b) Typical vortices of dynamic stall.....	3
<b>Fig.1.5</b> Principle diagrams of different VATs. (a) Cycloidal controllabe-pitch VAT; (b) Variable-pitch VAT .	7
<b>Fig.2.1</b> Computation configuration and mesh generation. (a) Global mesh; (b) Unstructured mesh; (c) Structured mesh.....	13
<b>Fig.2.2</b> Distributions of mean pressure coefficient and velocity profiles near the boundary layer. (a) Pressure coefficients; Velocity profiles at (b) $x/c=0.06$ ; (c) $x/c=0.21$ ; (d) $x/c=0.34$ . ....	15
<b>Fig.2.3</b> Distributions of mean pressure and skin friction coefficients at different inflow conditions. (a) Pressure coefficients for various free-stream turbulence levels; (b) Skin friction coefficients for various free-stream turbulence levels; (c) Pressure coefficients for various eddy viscosity ratios; (d) Skin friction coefficients for various eddy viscosity ratios.....	16
<b>Fig.2.4</b> Distributions of intermittency for various free-stream turbulence levels. (a) $Tu=0.1\%$ ; (b) $Tu=0.2\%$ ; (c) $Tu=0.3\%$ ; (d) $Tu=0.5\%$ . ....	17
<b>Fig.2.5</b> Distributions of mean pressure and skin friction coefficients for various correlations. (a) Pressure coefficients; (b) Skin friction coefficients. ....	19
<b>Fig.2.6</b> Distributions of mean pressure and skin friction coefficients for various values of $S1$ . (a) Pressure coefficients; (b) Skin friction coefficients. ....	20
<b>Fig.2.7</b> Mean velocity profiles near the boundary layer. (a) $x/c=0.06$ ; (c) $x/c=0.17$ ; (d) $x/c=0.21$ .....	21
<b>Fig.2.8</b> Distributions of mean pressure coefficients and velocity profiles. (a) Pressure coefficients; Velocity profiles at (b) $x/c=0.06$ ; (c) $x/c=0.17$ ; (d) $x/c=0.21$ ; (e) $x/c=0.28$ ; (f) $x/c=0.34$ .....	22
<b>Fig.2.9</b> Distributions of turbulent kinetic energy for various turbulence models. (a) SST $k-\omega$ ; (b) RSM; (c) SST TM. ....	23
<b>Fig.2.10</b> Distributions of mean pressure and velocity profiles at $0^\circ$ . (a) Pressure coefficient; Velocity profile at (b) $x/c=0.43$ ; (c) $x/c=0.51$ ; (d) $x/c=0.60$ ; (e) $x/c=0.73$ ; (f) $x/c=0.87$ .....	25
<b>Fig.2.11</b> Distributions of mean pressure and velocity profiles at $5^\circ$ . (a) Pressure coefficient; Velocity profile at (b) $x/c=0.20$ ; (c) $x/c=0.24$ ; (d) $x/c=0.32$ ; (e) $x/c=0.40$ ; (f) $x/c=0.52$ .....	26
<b>Fig.2.12</b> Distributions of mean pressure and velocity profiles at $15^\circ$ . (a) Pressure coefficient; Velocity profile at (b) $x/c=0.04$ ; (c) $x/c=0.10$ ; (d) $x/c=0.15$ ; (e) $x/c=0.19$ ; (f) $x/c=0.24$ .....	27
<b>Fig.2.13</b> Turbulent kinetic energy contours at different incidences. (a) $0^\circ$ ; (b) $5^\circ$ ; (c) $15^\circ$ .....	29
<b>Fig.2.14</b> Distributions of mean pressure and skin friction coefficients at different $Re$ . (a) and (b) Pressure coefficients; (c) and (d) Skin friction coefficients.....	30
<b>Fig.2.15</b> Distributions of turbulent kinetic energy at different $Re$ . (a) $2.5 \times 10^4$ ; (b) $5.0 \times 10^4$ ; (c) $2.0 \times 10^5$ ; (d) $4.0 \times 10^5$ . ....	31
<b>Fig.2.16</b> Computational configuration and mesh distributions. (a) Mesh in computational domain; (b) Mesh in three rotating parts; (c) Mesh near the blade surface. ....	35
<b>Fig.2.17</b> Instantaneous performance of one blade in a revolution. (a) Vertical force coefficient; (b) Propulsive force coefficient.....	36
<b>Fig.2.18</b> Spanwise vorticity contours at $\psi=140^\circ$ . (a) Case 1; (b) Case 2; (c) Case 3; (d) Case 4. ....	36
<b>Fig.2.19</b> Velocity profiles at $\psi=140^\circ$ . (a) $y/c=0.4$ ; (b) $y/c=0.5$ ; (c) $y/c=0.6$ ; (d) $y/c=0.8$ . ....	37
<b>Fig.2.20</b> Instantaneous performance of one blade in a revolution. (a) Vertical force coefficient; (b) Propulsive force coefficient.....	38
<b>Fig.2.21</b> Instantaneous performance of one blade in a revolution. (a) Vertical force coefficient; (b) Propulsive force coefficient.....	38
<b>Fig.2.22</b> Instantaneous performance of one blade in a revolution. (a) Vertical force coefficient; (b) Propulsive force coefficient.....	39

<b>Fig.2.23</b> Instantaneous performance of one blade in last 5 cycles. (a) Vertical force coefficient; (b) Propulsive force coefficient.....	39
<b>Fig.2.24</b> Instantaneous vertical force, propulsive force and power coefficients of one blade in a revolution at two $\lambda$ . (a), (b) and (c) at $\lambda=0.52$ ; (d), (e) and (f) at $\lambda=0.73$ .....	41
<b>Fig.2.25</b> Sketch of main forces acting on one blade at different $\psi$ . (a) $\psi=32^\circ$ ; (b) $\psi=90^\circ$ ; (c) $\psi=144^\circ$ ; (d) $\psi=270^\circ$ .....	43
<b>Fig.2.26</b> Velocity contours. (a) Experiment; (b) SST $k-\omega$ ; (c) SST TM.....	44
<b>Fig.2.27</b> vorticity contours. (a) Experiment; (b) SST $k-\omega$ ; (c) SST TM.....	45
<b>Fig.2.28</b> Pressure distributions. (a) Pressure of blade A; (b) Pressure of blade B.....	45
<b>Fig.2.29</b> Relative velocity of blade B. (a) SST $k-\omega$ ; (b) SST TM.....	46
<b>Fig.2.30</b> Velocity contours. (a) Experiment; (b) SST $k-\omega$ ; (c) SST TM.....	47
<b>Fig.2.31</b> Vorticity contours. (a) Experiment; (b) SST $k-\omega$ ; (c) SST TM.....	48
<b>Fig.2.32</b> Pressure distributions. (a) Pressure of blade A; (b) Pressure of blade B.....	48
<b>Fig.2.33</b> Relative velocity of two blades and velocity profiles. (a) and (c) SST $k-\omega$ ; (b) and (d) SST TM; (e) Velocity profile of blade B at $x/c=0.05$ on lower surface; (f) Velocity profile of blade B at $x/c=0.1$ on lower surface.....	49
<b>Fig.2.34</b> Velocity contours. (a) Experiment; (b) SST $k-\omega$ ; (c) SST TM.....	50
<b>Fig.2.35</b> Vorticity contours. (a) Experiment; (b) SST $k-\omega$ ; (c) SST TM.....	51
<b>Fig.2.36</b> Pressure distributions. (a) Pressure of blade A; (b) Pressure of blade B.....	51
<b>Fig.2.37</b> Relative velocity of two blades. (a) and (c) SST $k-\omega$ ; (b) and (d) SST TM.....	52
<b>Fig.2.38</b> Velocity contours. (a) Experiment; (b) SST $k-\omega$ ; (c) SST TM.....	53
<b>Fig.2.39</b> Vorticity contours. (a) Experiment; (b) SST $k-\omega$ ; (c) SST TM.....	54
<b>Fig.2.40</b> Pressure distributions. (a) Pressure of blade A; (b) Pressure of blade B.....	54
<b>Fig.2.41</b> Relative velocity of blade B and velocity profiles. (a) SST $k-\omega$ ; (b) SST TM; (c) Velocity profile of blade B at $x/c=0.05$ on pressure side; (d) Velocity profile of blade B at $x/c=0.15$ on pressure side.....	55
<b>Fig.2.42</b> Velocity contours. (a) Experiment; (b) SST $k-\omega$ ; (c) SST TM.....	56
<b>Fig.2.43</b> Vorticity contours. (a) Experiment; (b) SST $k-\omega$ ; (c) SST TM.....	57
<b>Fig.2.44</b> Pressure distributions. (a) Pressure of blade A; (b) Pressure of blade B.....	57
<b>Fig.2.45</b> Relative velocity of two blades. (a) and (c) SST $k-\omega$ ; (b) and (d) SST TM.....	58
<b>Fig.2.46</b> Velocity contours. (a) Experiment; (b) SST $k-\omega$ ; (c) SST TM.....	59
<b>Fig.2.47</b> Vorticity contours. (a) Experiment; (b) SST $k-\omega$ ; (c) SST TM.....	60
<b>Fig.2.48</b> Pressure distributions. (a) Pressure of blade A; (b) Pressure of blade B.....	60
<b>Fig.2.49</b> Relative velocity of two blades. (a) and (c) SST $k-\omega$ ; (b) and (d) SST TM.....	61
<b>Fig.2.50</b> Instantaneous performance of the rotating system. (a) and (b) Lift and propulsive force coefficients at $\lambda=0.52$ ; (c) and (d) Lift and propulsive force coefficients at $\lambda=0.73$ .....	62
<b>Fig.2.51</b> Pressure and relative velocity. (a) Pressure of blade A; (b) Pressure of blade B; (c) and (e) SST $k-\omega$ ; (d) and (f) SST TM.....	63
<b>Fig.2.52</b> Distributions of turbulence kinetic energy. (a) SST $k-\omega$ at $\psi=50^\circ$ ; (b) SST TM at $\psi=50^\circ$ ; (c) SST $k-\omega$ at $\psi=60^\circ$ ; (d) SST TM at $\psi=60^\circ$ ; (e) SST $k-\omega$ at $\psi=70^\circ$ ; (f) SST TM at $\psi=70^\circ$ ; (g) SST $k-\omega$ at $\psi=80^\circ$ ; (h) SST TM at $\psi=80^\circ$ .....	65
<b>Fig.2.53</b> Distributions of skin friction coefficients at different $\psi$ . (a) $\psi=50^\circ$ ; (b) $\psi=60^\circ$ ; (c) $\psi=70^\circ$ ; (d) $\psi=80^\circ$ .....	66
<b>Fig.2.54</b> Distributions of turbulence kinetic energy. (a) SST $k-\omega$ at $\psi=60^\circ$ ; (b) SST TM at $\psi=60^\circ$ ; (c) SST $k-\omega$ at $\psi=70^\circ$ ; (d) SST TM at $\psi=70^\circ$ ; (e) SST $k-\omega$ at $\psi=80^\circ$ ; (f) SST TM at $\psi=80^\circ$ ; (g) SST $k-\omega$ at $\psi=90^\circ$ ; (h) SST TM at $\psi=90^\circ$ .....	67
<b>Fig.2.55</b> Distributions of skin friction coefficients at different $\psi$ . (a) $\psi=60^\circ$ ; (b) $\psi=70^\circ$ ; (c) $\psi=80^\circ$ ; (d) $\psi=90^\circ$ .....	68
<b>Fig.3.1</b> Performance curves at different $\lambda$ . (a) Lift coefficient; (b) Propulsive force coefficient; (c) Power coefficient; (d) Efficiency.....	71
<b>Fig.3.2</b> Performance curves at different $\lambda$ for various pitching kinematics. (a) Lift coefficient; (b) Propulsive force coefficient; (c) Power coefficient; (d) Efficiency; (e) Variation of incidence.....	72

<b>Fig.3.3</b> Flow structures for different pitching kinematics. (a) $\theta=15^\circ\sin(\psi+\pi/2)$ ; (b) $\theta=35^\circ\sin(\psi+\pi/2)$ ; (c) $\theta=55^\circ\sin(\psi+\pi/2)$ ; (d) $\theta=5^\circ+35^\circ\sin(\psi+\pi/2)$ ; (e) $\theta=-5^\circ+35^\circ\sin(\psi+\pi/2)$ ; (f) $\theta=15^\circ+35^\circ\sin(\psi+\pi/2)$ ; (g) $\theta=15^\circ+35^\circ\sin(\psi+\pi/2)$ .....	74
<b>Fig.3.4</b> Performance curves for various pitching kinematics in a revolution. (a) Lift coefficient of the rotating system; (b) Propulsive force coefficient of the rotating system; (c) Vertical force coefficient of single blade; (d) Propulsive force coefficient of single blade.....	75
<b>Fig.3.5</b> Pressure distributions for various pitching kinematics at $\psi=35^\circ$ . (a) Sketch of force; (b) Pressure distribution of blade A; (c) Pressure distribution of blade B.....	77
<b>Fig.3.6</b> Flow structures of blade A for various pitching kinematics at $\psi=35^\circ$ . (a) $0^\circ-35^\circ$ ; (b) $0^\circ-55^\circ$ ; (c) $5^\circ-35^\circ$ ; (d) $10^\circ-35^\circ$ ; (e) $-5^\circ-35^\circ$ .....	78
<b>Fig.3.7</b> Flow structures of blade B for various pitching kinematics at $\psi=35^\circ$ . (a) $0^\circ-35^\circ$ ; (b) $0^\circ-55^\circ$ ; (c) $5^\circ-35^\circ$ ; (d) $10^\circ-35^\circ$ ; (e) $-5^\circ-35^\circ$ .....	79
<b>Fig.3.8</b> Pressure distributions for various pitching kinematics at $\psi=123^\circ$ . (a) Sketch of force; (b) Pressure distribution of blade A; (c) Pressure distribution of blade B.....	80
<b>Fig.3.9</b> Flow structures of blade A for various pitching kinematics at $\psi=123^\circ$ . (a) $0^\circ-35^\circ$ ; (b) $0^\circ-55^\circ$ ; (c) $5^\circ-35^\circ$ ; (d) $10^\circ-35^\circ$ ; (e) $-5^\circ-35^\circ$ .....	81
<b>Fig.3.10</b> Flow structures of blade B for various pitching kinematics at $\psi=123^\circ$ . (a) $0^\circ-35^\circ$ ; (b) $0^\circ-55^\circ$ ; (c) $5^\circ-35^\circ$ ; (d) $10^\circ-35^\circ$ ; (e) $-5^\circ-35^\circ$ .....	82
<b>Fig.3.11</b> Pressure distributions for various pitching kinematics at $\psi=160^\circ$ . (a) Sketch of force; (b) Pressure distribution of blade A; (c) Pressure distribution of blade B.....	83
<b>Fig.3.12</b> Flow structures of blade A for various pitching kinematics at $\psi=160^\circ$ . (a) $0^\circ-35^\circ$ ; (b) $0^\circ-55^\circ$ ; (c) $5^\circ-35^\circ$ ; (d) $10^\circ-35^\circ$ ; (e) $-5^\circ-35^\circ$ .....	84
<b>Fig.3.13</b> Flow structures of blade B for various pitching kinematics at $\psi=160^\circ$ . (a) $0^\circ-35^\circ$ ; (b) $0^\circ-55^\circ$ ; (c) $5^\circ-35^\circ$ ; (d) $10^\circ-35^\circ$ ; (e) $-5^\circ-35^\circ$ .....	85
<b>Fig.3.14</b> Pressure distributions of two blades for symmetrical pitching with amplitude of $55^\circ$ at different $\psi$ . (a) Blade A; (b) Blade B;.....	86
<b>Fig.3.15</b> Flow structures of two blades for symmetrical pitching with amplitude of $55^\circ$ at different $\psi$ . (a) and (d) $\psi=15^\circ$ ; (b) and (e) $\psi=75^\circ$ ; (c) and (f) $\psi=147^\circ$ .....	87
<b>Fig.3.16</b> Performance curves at $\lambda=0.52$ and $Re=2.46\times10^4$ . (a) Lift coefficient; (b) Propulsive force coefficient; (c) Power coefficient; (d) Efficiency.....	90
<b>Fig.3.17</b> Performance curves for various $c/R$ in a revolution. (a) Lift coefficient of the rotating system; (b) Propulsive force coefficient of the rotating system; (c) Vertical force coefficient of single blade; (d) Propulsive force coefficient of single blade.....	91
<b>Fig.3.18</b> Global flow structures for various $c/R$ at $\psi=45^\circ$ . (a) $c/R=0.375$ ; (b) $c/R=0.45$ ; (c) $c/R=0.60$ .....	92
<b>Fig.3.19</b> Near-wall flow structures for various $c/R$ at $\psi=45^\circ$ . (a) Pressure distribution of blade A; (b) Pressure distribution of blade B; (c) and (f) $c/R=0.375$ ; (d) and (g) $c/R=0.45$ ; (e) and (h) $c/R=0.60$ .....	93
<b>Fig.3.20</b> Global flow structures for various $c/R$ at $\psi=142^\circ$ . (a) $c/R=0.375$ ; (b) $c/R=0.45$ ; (c) $c/R=0.60$ .....	94
<b>Fig.3.21</b> Near-wall flow structures for various $c/R$ at $\psi=142^\circ$ . (a) Pressure distribution of blade A; (b) Pressure distribution of blade B; (c) and (f) $c/R=0.375$ ; (d) and (g) $c/R=0.45$ ; (e) and (h) $c/R=0.60$ .....	95
<b>Fig.3.22</b> Global flow structures for various $c/R$ . (a) $c/R=0.375$ at $\psi=180^\circ$ ; (b) $c/R=0.45$ at $\psi=180^\circ$ ; (c) $c/R=0.60$ at $\psi=160^\circ$ .....	96
<b>Fig.3.23</b> Flow structures for various $c/R$ . (a) Pressure distribution of blade A; (b) Pressure distribution of blade B; (c) and (f) $c/R=0.375$ at $\psi=180^\circ$ ; (b) and (e) $c/R=0.45$ at $\psi=180^\circ$ ; (c) and (h) $c/R=0.60$ at $\psi=160^\circ$ .....	97
<b>Fig.3.24</b> Performance curves at different $Re$ . (a) Lift coefficient; (b) Propulsive force coefficient; (c) Power coefficient; (d) Efficiency.....	98
<b>Fig.3.25</b> Performance curves at different $Re$ in a revolution. (a) Lift coefficient of the rotating system; (b) Propulsive force coefficient of the rotating system; (c) Vertical force coefficient of single blade; (d) Propulsive force coefficient of single blade.....	99
<b>Fig.3.26</b> Global flow structures for various $Re$ at $\psi=110^\circ$ . (a) $Re=1.47\times10^4$ ; (b) $Re=3.44\times10^4$ ; (c) $Re=5.41\times10^4$ .....	100

<b>Fig.3.27</b> Flow structures for various $Re$ at $\psi=110^\circ$ . (a) Pressure distribution of blade A; (b) Pressure distribution of blade B; (c) and (f) $Re=1.47 \times 10^4$ ; (d) and (g) $Re=3.44 \times 10^4$ ; (e) and (h) $Re=5.41 \times 10^4$ .....	101
<b>Fig.3.28</b> Global flow structures for various $Re$ at $\psi=35^\circ$ . (a) $Re=1.47 \times 10^4$ ; (b) $Re=3.44 \times 10^4$ ; (c) $Re=5.41 \times 10^4$ .....	102
<b>Fig.3.29</b> Flow structures for various $Re$ at $\psi=35^\circ$ . (a) Pressure distribution of blade A; (b) Pressure distribution of blade B; (c) and (f) $Re=1.47 \times 10^4$ ; (d) and (g) $Re=3.44 \times 10^4$ ; (e) and (h) $Re=5.41 \times 10^4$ .....	103
<b>Fig.3.30</b> Global flow structures for various $Re$ at $\psi=180^\circ$ . (a) $Re=1.47 \times 10^4$ ; (b) $Re=3.44 \times 10^4$ ; (c) $Re=5.41 \times 10^4$ .....	104
<b>Fig.3.31</b> Flow structures for various $Re$ at $\psi=180^\circ$ . (a) Pressure distribution of blade A; (b) Pressure distribution of blade B; (c) and (f) $Re=1.47 \times 10^4$ ; (d) and (g) $Re=3.44 \times 10^4$ ; (e) and (h) $Re=5.41 \times 10^4$ .....	105
<b>Fig.3.32</b> Performance curves at different $\lambda$ . (a) Lift coefficient; (b) Propulsive force coefficient; (c) Power coefficient; (d) Efficiency.....	106
<b>Fig.3.33</b> Performance curves at different $\lambda$ in a revolution. (a) Lift coefficient of the rotating system; (b) Propulsive force coefficient of the rotating system; (c) Vertical force coefficient of single blade; (d) Propulsive force coefficient of single blade. ....	107
<b>Fig.3.34</b> Global flow structures for various $\lambda$ at $\psi=45^\circ$ . (a) $\lambda=0.35$ ; (b) $\lambda=0.45$ ; (c) $\lambda=0.63$ .....	108
<b>Fig.3.35</b> Flow structures for various $\lambda$ at $\psi=45^\circ$ . (a) Pressure distribution of blade A; (b) Pressure distribution of blade B; (c) and (f) $\lambda=0.35$ ; (d) and (g) $\lambda=0.45$ ; (e) and (h) $\lambda=0.63$ .....	109
<b>Fig.3.36</b> Global flow structures for various $\lambda$ at $\psi=135^\circ$ . (a) $\lambda=0.35$ ; (b) $\lambda=0.45$ ; (c) $\lambda=0.63$ .....	110
<b>Fig.3.37</b> Flow structures for various $\lambda$ at $\psi=135^\circ$ . (a) Pressure distribution of blade A; (b) Pressure distribution of blade B; (c) and (f) $\lambda=0.35$ ; (d) and (g) $\lambda=0.45$ ; (e) and (h) $\lambda=0.63$ .....	111
<b>Fig.3.38</b> Global flow structures for various $\lambda$ at $\psi=12^\circ$ . (a) $\lambda=0.35$ ; (b) $\lambda=0.45$ ; (c) $\lambda=0.63$ .....	112
<b>Fig.3.39</b> Flow structures for various $\lambda$ at $\psi=12^\circ$ . (a) Pressure distribution of blade A; (b) Pressure distribution of blade B; (c) and (f) $\lambda=0.35$ ; (d) and (g) $\lambda=0.45$ ; (e) and (h) $\lambda=0.63$ .....	113
<b>Fig.3.40</b> Global performance of the cycloidal propeller. (a) Lift coefficient; (b) Propulsive force coefficient; (c) Power coefficient; (d) Efficiency.....	116
<b>Fig.3.41</b> Performance curves in a revolution. (a) Lift coefficient of the rotating system; (b) Propulsive force coefficient of the rotating system; (c) Vertical force coefficient of single blade; (d) Propulsive force coefficient of single blade.....	117
<b>Fig.3.42</b> Flow structures for cases with different pitch-pivot-points. (a) $x/c=0.1$ ; (b) $x/c=0.2$ ; (c) $x/c=0.25$ ; (d) $x/c=0.3$ ; (e) $x/c=0.4$ ; (f) $x/c=0.5$ ; (g) $x/c=0.6$ .....	118
<b>Fig.3.43</b> Global flow structures at $\psi=95^\circ$ . (a) $x/c=0.25$ ; (b) $x/c=0.5$ .....	119
<b>Fig.3.44</b> Flow structures at $\psi=95^\circ$ . (a) Pressure distribution of blade A; (b) Pressure distribution of blade B; (c) and (e) $x/c=0.25$ ; (d) and (f) $x/c=0.5$ .....	120
<b>Fig.3.45</b> Global flow structures at $\psi=170^\circ$ . (a) $x/c=0.25$ ; (b) $x/c=0.5$ ; (c) $x/c=0.6$ .....	121
<b>Fig.3.46</b> Flow structures at $\psi=170^\circ$ . (a) Pressure distribution of blade A; (b) Pressure distribution of blade B; (c) and (f) $x/c=0.25$ ; (d) and (g) $x/c=0.5$ ; (e) and (h) $x/c=0.6$ .....	122
<b>Fig.3.47</b> Global flow structures at $\psi=47^\circ$ . (a) $x/c=0.25$ ; (b) $x/c=0.5$ .....	123
<b>Fig.3.48</b> Flow structures at $\psi=47^\circ$ . (a) Pressure distribution of blade A; (b) Pressure distribution of blade B; (c) and (e) $x/c=0.25$ ; (d) and (f) $x/c=0.5$ .....	124
<b>Fig.3.49</b> Global flow structures at $\psi=110^\circ$ . (a) $x/c=0.25$ ; (b) $x/c=0.5$ .....	125
<b>Fig.3.50</b> Flow structures at $\psi=47^\circ$ . (a) Pressure distribution of blade A; (b) Pressure distribution of blade B; (c) and (e) $x/c=0.25$ ; (d) and (f) $x/c=0.5$ .....	126
<b>Fig.3.51</b> Performance curves in a revolution. (a) Lift coefficient of the rotating system; (b) Propulsive force coefficient of the rotating system; (c) Vertical force coefficient of single blade; (d) Propulsive force coefficient of single blade.....	127
<b>Fig.3.52</b> Global flow structures at $\psi=105^\circ$ . (a) $Re=2.85 \times 10^4$ ; (b) $Re=7.11 \times 10^4$ .....	128
<b>Fig.3.53</b> Flow structures at $\psi=105^\circ$ . (a) Pressure distribution of blade A; (b) Pressure distribution of blade B; (c) and (e) $Re=2.85 \times 10^4$ ; (d) and (f) $Re=7.11 \times 10^4$ .....	129
<b>Fig.3.54</b> Global flow structures at $\psi=30^\circ$ . (a) $Re=2.85 \times 10^4$ ; (b) $Re=7.11 \times 10^4$ .....	130

<b>Fig.3.55</b> Flow structures at $\psi=30^\circ$ . (a) Pressure distribution of blade A; (b) Pressure distribution of blade B; (c) and (e) $Re=2.85\times10^4$ ; (d) and (f) $Re=7.11\times10^4$ .....	131
<b>Fig.3.56</b> Global flow structures at $\psi=170^\circ$ . (a) $Re=2.85\times10^4$ ; (b) $Re=7.11\times10^4$ .....	132
<b>Fig.3.57</b> Flow structures at $\psi=170^\circ$ . (a) Pressure distribution of blade A; (b) Pressure distribution of blade B; (c) and (e) $Re=2.85\times10^4$ ; (d) and (f) $Re=7.11\times10^4$ .....	133
<b>Fig.3.58</b> Global performance of the cycloidal propeller. (a) Lift coefficient; (b) Propulsive force coefficient; (c) Power coefficient; (d) Efficiency.....	134
<b>Fig.3.59</b> Performance curves. (a) Lift coefficient of the rotating system; (b) Propulsive force coefficient of the rotating system; (c) Vertical force coefficient of single blade; (d) Propulsive force coefficient of single blade.....	135
<b>Fig.3.60</b> Global flow structures at $\psi=46^\circ$ . (a) $\lambda=0.43$ ; (b) $\lambda=0.52$ ; (c) $\lambda=0.72$ .....	136
<b>Fig.3.61</b> Flow structures at $\psi=46^\circ$ . (a) Pressure distribution of blade A; (b) Pressure distribution of blade B; (c) and (f) $\lambda=0.43$ ; (d) and (g) $\lambda=0.52$ ; (e) and (h) $\lambda=0.72$ .....	137
<b>Fig.3.62</b> Global flow structures at $\psi=145^\circ$ . (a) $\lambda=0.43$ ; (b) $\lambda=0.52$ ; (c) $\lambda=0.72$ .....	138
<b>Fig.3.63</b> Flow structures at $\psi=145^\circ$ . (a) Pressure distribution of blade A; (b) Pressure distribution of blade B; (c) and (f) $\lambda=0.43$ ; (d) and (g) $\lambda=0.52$ ; (e) and (h) $\lambda=0.72$ .....	139
<b>Fig.3.64</b> Global flow structures at $\psi=160^\circ$ . (a) $\lambda=0.43$ ; (b) $\lambda=0.52$ ; (c) $\lambda=0.72$ .....	140
<b>Fig.3.65</b> Flow structures at $\psi=160^\circ$ . (a) Pressure distribution of blade A; (b) Pressure distribution of blade B; (c) and (f) $\lambda=0.43$ ; (d) and (g) $\lambda=0.52$ ; (e) and (h) $\lambda=0.72$ .....	141
<b>Fig.3.66</b> Global performance of cycloidal rotor. (a) Lift coefficient; (b) Propulsive force coefficient; (c) Power coefficient; (d) Efficiency.....	144
<b>Fig.3.67</b> Flow structures over symmetrical profiles at $\psi=0^\circ$ . (a) NACA0009; (b) NACA0012; (c) NACA0015; (d) NACA0018; (e) NACA0022.....	145
<b>Fig.3.68</b> Flow structures over asymmetrical profiles at $\psi=0^\circ$ . (a) NACA2415; (b) NACA4415; (c) NACA6415; (d) Inverse NACA2415; (e) Inverse NACA4415; (f) Inverse NACA6415.....	146
<b>Fig.3.69</b> Performance curves in a revolution. (a) Lift coefficient of cycloidal rotor; (b) Propulsive force coefficient of cycloidal rotor; (c) Vertical force coefficient of single blade; (d) Propulsive force coefficient of single blade.....	147
<b>Fig.3.70</b> Global flow structures at $\psi=46^\circ$ . (a) NACA0015; (b) NACA0022; (c) NACA6415; (d) NACA6415.....	148
<b>Fig.3.71</b> Flow structures at $\psi=46^\circ$ . (a) Pressure coefficient of blade A; (b) Pressure coefficient of blade B; (c) and (g) NACA0015; (d) and (h) NACA0022; (e) and (i) NACA6415; (f) and (j) Inverse NACA6415.....	149
<b>Fig.3.72</b> Global flow structures at $\psi=120^\circ$ . (a) NACA0015; (b) NACA0022; (c) NACA6415; (d) NACA6415.....	151
<b>Fig.3.73</b> Flow structures at $\psi=120^\circ$ . (a) Pressure coefficient of blade A; (b) Pressure coefficient of blade B; (c) and (g) NACA0015; (d) and (h) NACA0022; (e) and (i) NACA6415; (f) and (j) Inverse NACA6415.....	152
<b>Fig.3.74</b> Global flow structures at $\psi=180^\circ$ . (a) NACA0015; (b) NACA0022; (c) NACA6415; (d) NACA6415.....	153
<b>Fig.3.75</b> Flow structures at $\psi=120^\circ$ . (a) Pressure coefficient of blade A; (b) Pressure coefficient of blade B; (c) and (g) NACA0015; (d) and (h) NACA0022; (e) and (i) NACA6415; (f) and (j) Inverse NACA6415.....	154
<b>Fig.3.76</b> Performance in a revolution at two $Re$ . (a) Lift coefficient of cycloidal rotor; (b) Propulsive force coefficient of cycloidal rotor; (c) Vertical force coefficient of single blade; (d) Propulsive force coefficient of single blade.....	155
<b>Fig.3.77</b> Global flow structures at $\psi=140^\circ$ . (a) $Re=2.85\times10^4$ ; (b) $Re=7.11\times10^4$ .....	156
<b>Fig.3.78</b> Flow structures at $\psi=140^\circ$ . (a) Pressure coefficients of blade A; (b) Pressure coefficients of blade B; (c) and (e) $Re=2.85\times10^4$ ; (d) and (f) $Re=7.11\times10^4$ .....	157
<b>Fig.3.79</b> Global flow structures at $\psi=50^\circ$ . (a) $Re=2.85\times10^4$ ; (b) $Re=7.11\times10^4$ .....	158
<b>Fig.3.80</b> Flow structures at $\psi=50^\circ$ . (a) Pressure coefficients of blade A; (b) Pressure coefficients of blade B; (c) and (e) $Re=2.85\times10^4$ ; (d) and (f) $Re=7.11\times10^4$ .....	159
<b>Fig.3.81</b> Global flow structures at $\psi=180^\circ$ . (a) $Re=2.85\times10^4$ ; (b) $Re=7.11\times10^4$ .....	160

<b>Fig.3.82</b> Flow structures at $\psi=180^\circ$ . (a) Pressure coefficients of blade A; (b) Pressure coefficients of blade B; (c) and (e) $Re=2.85\times10^4$ ; (d) and (f) $Re=7.11\times10^4$ .....	160
<b>Fig.3.83</b> Global performance of cycloidal rotor. (a) Lift coefficient; (b) Propulsive force coefficient; (c) Power coefficient; (d) Efficiency.....	161
<b>Fig.3.84</b> Performance in a revolution at different $\lambda$ . (a) Lift coefficient of cycloidal rotor; (b) Propulsive force coefficient of cycloidal rotor; (c) Vertical force coefficient of single blade; (d) Propulsive force coefficient of single blade.....	162
<b>Fig.3.85</b> Global flow structures at $\psi=50^\circ$ . (a) $\lambda=0.72$ ; (b) $\lambda=0.43$ .....	163
<b>Fig.3.86</b> Flow structures at $\psi=50^\circ$ . (a) Pressure coefficients of blade A; (b) Pressure coefficients of blade B; (c) and (e) $\lambda=0.72$ ; (d) and (f) $\lambda=0.43$ .....	164
<b>Fig.3.87</b> Global flow structures at $\psi=145^\circ$ . (a) $\lambda=0.72$ ; (b) $\lambda=0.43$ .....	165
<b>Fig.3.88</b> Flow structures at $\psi=145^\circ$ . (a) Pressure coefficients of blade A; (b) Pressure coefficients of blade B; (c) and (e) $\lambda=0.72$ ; (d) and (f) $\lambda=0.43$ .....	166
<b>Fig.3.89</b> Global flow structures at $\psi=10^\circ$ . (a) $\lambda=0.72$ ; (b) $\lambda=0.43$ .....	167
<b>Fig.3.90</b> Flow structures at $\psi=10^\circ$ . (a) Pressure coefficients of blade A; (b) Pressure coefficients of blade B; (c) and (e) $\lambda=0.72$ ; (d) and (f) $\lambda=0.43$ .....	167

## List of tables

<b>Table 2.1</b> Information and performance prediction of five sets of meshes .....	14
<b>Table 2.2</b> Results with different time-steps.....	14
<b>Table 2.3</b> Separation, transition and reattachment locations at various incidences.....	28
<b>Table 2.4</b> Separation, transition and reattachment locations at different $Re$ .....	30
<b>Table 2.5</b> Main geometrical parameters of the cycloidal rotor.....	33
<b>Table 2.6</b> Mesh distributions of tested cases .....	35
<b>Table 2.7</b> Results of different turbulence models .....	40
<b>Table 2.8</b> Main production regions of forces and power.....	42

# 1 INTRODUCTION AND LITERATURE REVIEW

## 1.1 BACKGROUND OF PRESENT WORK

Oscillating foils with complex kinematics, are extensively employed in many engineering applications, such as vertical axis wind turbines (VAWT), the underwater propulsion systems, marine energy extraction equipment and micro air vehicles (MAV). As shown in figure 1.1, the motion mode of the oscillating foils can be mainly classified into three categories: plunging (or heaving), pitching and flapping (combination of heaving and pitching motions). The pitching motion is a relatively simple kinematic that the airfoils rotate around a pivot along the chord line in a limited range of incidence. In the process of oscillation, the foil incidence varies continuously, which changes the blade loading and the flow organizations on the surfaces significantly. At small incidence, the flow is attached on the foil surface and the laminar-turbulence transition is the main contributor to the modification of the variables near the wall. With the increase of the angle-of-attack, the flow starts to separate from the surface and generate shedding into the wakes, resulting in the onset of stall.

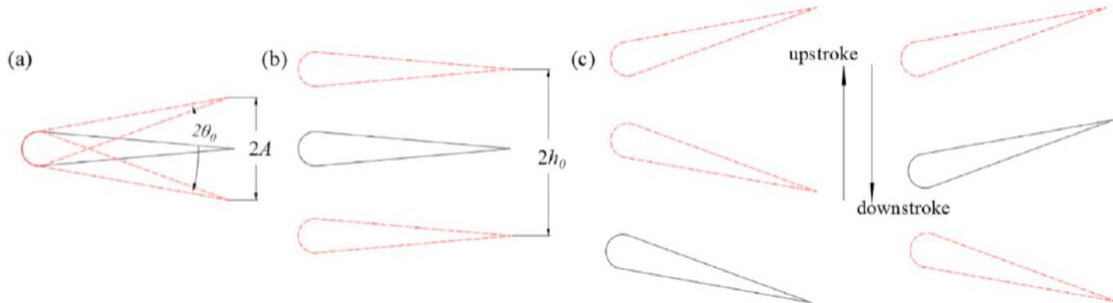


**Fig.1.1** Sketch of (a) pitching motion; (b) heaving motion and (c) flapping motion [1].

As a new-type propulsion system, the cycloidal rotor, which consists of several vertical blades, has been attracting much attention recently. Figure 1.2 presents the applications of cycloidal propeller to the large-scale ship and unmanned aircraft system. The main principle of the oscillation is that the blade not only rotates around the rotor center, but also has a pitching motion based on the pitch-pivot-point. This kind of propeller can produce a broad range of thrust and lateral forces by the variations of lift and drag of the blades.

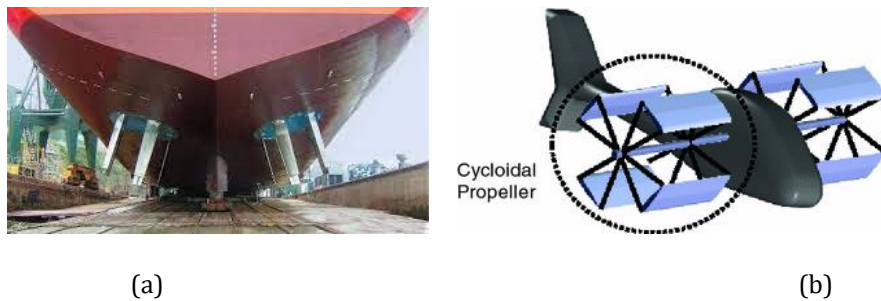


**Fig.1.2** Application of cycloidal propeller. (a) Large-size ship; (b) Unmanned aircraft.

When the absolute advance coefficient  $\lambda$ , given by  $\lambda = V_s / \omega R$  (where  $V_s$  is the mainstream velocity,  $\omega$  is the rotating speed and  $R$  is the rotating radius) is smaller than

1, the propeller is referred as the cycloidal propeller (low-pitch device), while in the other cases it is a trochoidal propeller (high-pitch device). Figure 1.3a shows the sketch of blade angle definition for a new designed trochoidal propeller with a sinusoidal pitching motion [2]. The sinusoidal pitch control functions for low-pitch and high-pitch devices are shown in equation 1.1 and 1.2 (where  $\beta$  is the relative pitch angle,  $\beta_{abs}$  is the absolute pitch angle,  $\alpha$  is the pitching amplitude,  $\Phi$  is the azimuthal angle and  $\Phi_p$  is the phase angle). The blade motion and definition of the coordinate system are displayed in figure 1.3b for a cycloidal rotor applied to the MAV [3]. The two-blade cycloidal rotor with a sinusoidal blade pitching can produce a propulsive force continuously in the forward flight, by changing the incidence, i.e. the angle between the blade chord line and tangential direction of the rotating trajectory. The blade relative angle  $\theta_A$  is a function of the azimuthal angle  $\psi$  and can be expressed with the sinusoidal function shown in equation 1.3 (where  $\theta_{amp}$  is the pitching amplitude and  $\phi$  is the phase angle).

$$\beta = -\alpha \sin(\Phi + \Phi_p) \quad \lambda < 1 \quad (1.1)$$

$$\beta_{abs} = -\alpha \sin(\Phi + \Phi_p) \quad \lambda > 1 \quad (1.2)$$

$$\theta_A = \theta_{amp} \sin(\psi + \phi) \quad (1.3)$$

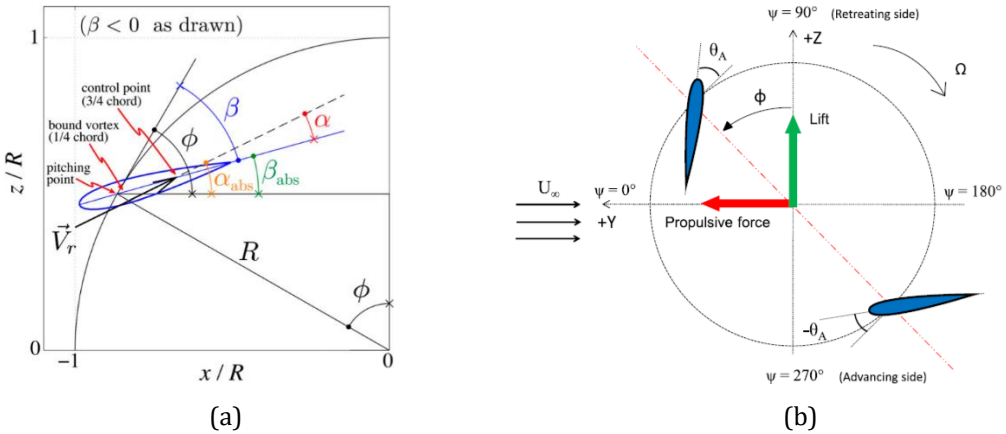


**Fig.1.3** Sketch of blade motion. (a) Blade angle definition; (b) Coordinate system.

## 1.2 MECHANISMS OF TRANSITION AND DYNAMIC STALL

The onset and extent of the laminar-turbulence transition are of major importance in many engineering devices, ranging from the single airfoil/hydrofoil to turbomachinery with complex configurations. Nowadays, there are two main types of transition that have been especially studied. The first one is the bypass transition widely existing in compressors and turbines with high free-stream turbulence level (typically about 5%~10%), in which Tollmien-Schlichting (TS) waves are completely bypassed and turbulent spots are directly produced within the boundary layer induced by the free-stream turbulence. The other transition mechanism is the separation-induced transition, where the laminar boundary layer on the blades separates, because of the adverse pressure gradient, and the transition develops within the separated shear layer. If the separated shear layer reattaches on the suction side, then a recirculation region named as laminar separation bubble (LSB) is created. Otherwise, if the separated shear layer does

not reattach, an open recirculation region including vortices with various sizes is formed. The mechanism of LSB generation is described in figure 1.4a [4].

Dynamic stall refers to the phenomenon involving a large amount of flow separations and reattachments that occur on an airfoil, or any other lifting surface, when it is subjected to a rapid unsteady motion such as pitching, plunging, flapping and vertical translating movements in the fluid flow with its maximum incidence being above the normal static stall angle [5]. The typical dynamic stall can be divided into four successive key stages during the upstroke and downstroke processes: the attached flow at low incidence, the development of leading-edge vortex (LEV), the shedding of LEV causing the full stall and the reattachment of the flows. Figure 1.4b shows the inception and development of LEV, trailing-edge vortex (TEV) and other vortices over the suction side of a pitching airfoil. When the airfoil has an oscillating motion, it is observed that the lift increases until the deep dynamic stall, which occurs when the maximal incidence exceeds the steady airfoil stall angle-of-attack. This can be ascribed to two mechanisms: (a) a delay in the boundary layer flow separation; (b) the generation of a closed separation bubble near the foil leading edge. Two reasons explain the delay in the boundary layer separation: (a) an increase in the effective camber that is predicted from the thin airfoil theory; (b) the acceleration of the boundary layer due to the Magnus effect produced by the leading-edge motion, as shown in the reference [6]. Carta [7] reported analytically that the adverse pressure gradient over the suction side of a pitching airfoil is weaker than in the case of a stationary airfoil, and is even further reduced as the pitching rate increases. Dynamic stall has a great impact on the performance of many energy conversion devices, such as horizontal axis wind turbine (HAWT) and VAWT. Moreover, in addition to these detrimental effects on the performance, dynamic stall is also a substantial source of structural vibration pertinent to the fatigue lift of the turbine [8].

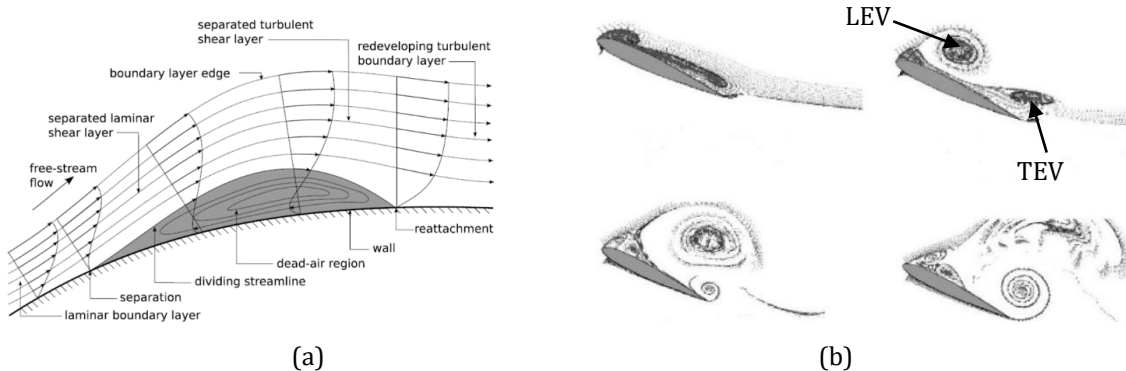


**Fig.1.4** Sketch of transition and dynamic stall. (a) Mechanism of LSB generation; (b) Typical vortices of dynamic stall.

### 1.3 TRANSITION AND DYNAMIC STALL ON AIRFOILS/HYDROFOILS

The investigations of the laminar-turbulence transition and the dynamic stall for the single airfoils/hydrofoils are widely performed using both experimental and numerical approaches. At relatively small incidence, the occurrence of transition based on the shear layer separation, transition and reattachment is the primary mechanism. Then, with the increase of the angle-of-attack, the LSB moves towards the leading edge gradually. Further increasing the incidence, near the stall condition, the LSB is almost located near the leading edge and an open recirculation region is generated after the flow separation point. Understanding the mechanisms of transition and dynamic stall is necessary to provide some guidelines to control these detrimental events.

Experimental measurement is a direct and effective way to obtain rich information about LSB and vortex shedding over the lifting surface. Particle-image velocimetry (PIV) and smoke-wire techniques are used to visualize and characterize the flow structures while the pressure taps mounted on the airfoil surface provide mean static pressure measurements. In addition, velocity profiles inside the boundary layer can be measured using hot-wire probes. More specifically, several experimental works have contributed to the study of the transition process in the last 20 years: Somers [9] performed some measurements of the lift and drag coefficients as well as the pressure distributions on a new designed airfoil, in order to design a high-lift and low-drag profile for wind-turbine applications, and the results show a good achievement. In addition, Yarusevych et al. [10] investigated the effect of the separated shear layer on the characteristics of the coherent structures for low-Reynolds-number flows, and two common flow regimes were identified: one is the separation bubble formation and the other is the boundary layer separation without reattachment. It is also observed that the fundamental frequency of the shear layer vortices presents a power law dependency on the Reynolds number for the two flow regimes, while the wake vortex shedding frequency is linearly correlated with the Reynolds number. Moreover, with the aid of time-resolved PIV and stereo scanning PIV set-up, Burgmann et al. [11] found that the temporal and spatial dynamics of the vortex roll-up is induced by the Kelvin-Helmholtz (K-H) instability. Recently, Boutilier and Yarusevych [12] combined the flow visualization, hot-wire measurement, surface pressure test and stability analysis to clarify the mechanism of the disturbance development in the shear layer by the predicted disturbance growth rate, disturbance wave number spectra and convection speed. Furthermore, Kirk and Yarusevych [13] gave a new insight into the development of the coherent structures in separation bubbles and their relations to the overall bubble dynamics and mean bubble topology. It is well-known that some parameters have a great impact on the transition process, which should be analyzed in detail in order to characterize the adverse consequences for such flows. Koca et al. [14] showed that the length of LSB would become longer as the incidence increases, which results in a lower frequency of the vortex shedding. Also, with the increase of the Reynolds number, the LSB becomes shorter and its location is much closer to the leading edge. When it comes to the influence of the inflow turbulence condition, Istvan et al. [15] and Istvan and Yarusevych [16] demonstrated that the bubble length is reduced as a result of the delayed separation and advanced reattachment when the inflow turbulence intensity increases. Simultaneously, it is also observed that a higher turbulence level can lead to the increase of the lift and delay the stall under pre-stall conditions. Concerning the surface-roughness effect on the separation bubble transition, Roberts and Yaras [17] observed that the increase of the roughness height, the spacing of the roughness elements and a roughness shape with negative skewness can promote the earlier transition inception, and the roughness height is the most influent parameter. Although the experimental measurements have already obtained some detailed information about the near-wall flow structures, it still has some significant uncertainties, because of the disturbance from the external elements. Yarusevych et al. [18] found that the conventional hot-wire probes can't capture the reverse flow in the separated region and also overestimates the velocities because of the additional heat losses. Therefore, Ducoin et al. [19] applied the Laser Doppler Velocimetry (LDV) system to get the mean velocity profiles around the hydrofoil at incidence of  $2^\circ$ , which is validated by the numerical simulations [20], even for the prediction of the negative streamwise velocity in the flow separation region.

In complement to these experimental works, Computational Fluid Dynamics (CFD), based mostly on Reynolds Averaged Navier-Stokes (RANS) methodology, but also on large eddy simulation (LES), can provide some more understanding of the transitional flows and dynamic stall characteristics for static or oscillating airfoils/hydrofoils. When an airfoil has an oscillation motion, the occurrence of the stall phenomenon is much delayed compared with a stationary case, due to the existence of the leading-edge vortex (LEV), which can maintain the high performance for a longer time. Visbal and Garmann [21] paid much attention to the generation and development of the dynamic stall vortex with the change of the incidence. Then, Guillaud et al. [22] found that the boundary layer separation and the shedding frequency of LEV are delayed at high incidence as the reduced frequency increases, which indicates that the lifetime of LEV on the suction side decreases significantly. Moreover, Benton and Visbal [23] investigated the dynamic stall process using the LES methodology for high Reynolds number flows, with special emphasis on the sensitivity to the Reynolds number.

The RANS-based turbulence models are always the first choice for most engineering flows due to the low requirements of computational resources and acceptable accuracy. However, it just resolves the fully turbulent flows and it should be modified when the transition effect is considered. As it was reported by Wauters and Degroote [4], there are mainly four RANS-based transition models, namely the shear stress transport (SST)  $k-\omega$  with low- $Re$  correction [24],  $k-k_1\omega$  [25], SST  $k-\omega \gamma - \widetilde{Re}_{\theta t}$  [26-28] and SST  $k-\omega \gamma$  [29]. The advantages and disadvantages of each model are discussed in the related references. The low Reynolds number turbulence models, which are often used to predict the engineering transition, are based on wall damping functions of the underlying turbulence models, to trigger the transition onset. A significant progress that has also been made by this kind of attractive concept. Schmidt and Patankar [30-31] firstly proposed a  $k-\epsilon$  low-Reynolds-number turbulence model to predict transition in external boundary layer flows subject to free-stream turbulence and then they modified this model by limiting the production term in the turbulence kinetic energy equation, using a simple stability criterion and the correlation with the free-stream turbulence level. Then, Biswas and Fukutama [32] made some modifications to the  $k-\epsilon$  low-Reynolds-number models by considering the wall limiter behavior, the free-stream turbulence level and the balance between production and destruction of turbulence. Furthermore, Tseng and Cheng [33] and Tseng and Hu [34] applied a modified  $k-\omega$  low-Reynolds-number model to clarify the mechanism of stall delay induced by the leading-edge vortex (LEV) at two stages, before and after the formation of LEV, and track the trajectory of the different vortex structures using Lagrangian coherent structures (LCS). However, the experience shows that this approach is not capable of capturing the influence of many factors, including the pressure gradients and flow separation, the Mach number, the turbulence length scale, the wall roughness and the streamline curvature.

Afterwards, the SST  $\gamma - \widetilde{Re}_{\theta t}$  transition model was developed by Menter et al. [26-27], and then it has been applied extensively to many engineering flows with transition effects [35-37]. In addition to the original two equations of the SST  $k-\omega$  turbulence model, two other equations, for the intermittency  $\gamma$  and the transition momentum thickness Reynolds number  $\widetilde{Re}_{\theta t}$ , are obtained by introducing the effective intermittency into the production and destruction terms in the turbulence kinetic energy equation. Several additional achievements have been obtained until now: Dong et al. [38] tested the effect of the Reynolds number on the flow structures inside the boundary layer and concluded that non-classical structures including the major vortex and small scales emerge as the Reynolds number increases from  $3\times 10^5$  to  $5\times 10^5$ . Wang and Xiao [39] used the SST  $\gamma$

model to predict the transition with the incidence increasing from  $0^\circ$  to  $18^\circ$ , the flow regime experiences different processes, i.e. flow transition, flow separation, and interaction between the LSB and the trailing edge separation bubble, which corresponds to the linear-lift stage, light-stall stage and deep-stall stage. For 3D transition flows, Bartl et al. [40] found that the prediction of the location and averaged length of LSB as well as the pressure distribution show a good agreement with the experiments under pre-stall conditions. Then, for oscillating airfoils, Ducoin et al. [41] investigated the effect of the pitching velocity on the boundary layer events and on the hydrodynamic loading, and the results show that the transition is delayed with the increase of the pitching velocity and can even be suppressed at the highest pitching velocity during the up-stroke stage. In the work of Karbasian and Kim [42], the importance of the special vortex lifetime, such as the primary LEV and TEV and secondary LEV, due to the interaction among different vortices is highlighted, as well as the delay between the maximal circulation of the main vortices and the corresponding peak of the lift coefficient. Recently, Zhang et al. [43] also checked the influence of the pitching rate on the hydrodynamic performance and the unsteady vortex structures. The results mainly show that the high pitching rate could result in a delay of the dynamic stall, while the low pitching rate shrinks the hysteresis loops and intensifies the force fluctuations. For the more complicated two-phase cavitating flows, Huang et al. [44] observed that the cavitation volume increases with the increase of the pitching rate, which in turn changes the cavity shedding frequency and consequently modifies the hydrodynamic loads. During the pitch-up motion, the general performance obtained by the RANS-based transition model is quite good because of the two-dimensional characteristics whereas there is a relatively large discrepancy as the airfoil undergoes the down-stroke process subject to the strong three-dimensional effect along the span [45]. Therefore, Wang et al. [5] and Singh and Páscoit [46] applied the SST  $\gamma - \widetilde{Re}_{\theta t}$  transition model coupled with detached eddy simulation (DES) and scale adaptive simulation (SAS), respectively, and could significantly improve the results during the down-stroke motion. However, in the transition model, some empirical coefficients and correlations need to be calibrated. For instance, Malan et al. [47] focused on the calibration of the SST  $\gamma - \widetilde{Re}_{\theta t}$  transition model in commercial CFD, with much attention on the correlation of  $F_{\text{length}}$  (controlling the transition region length) and critical momentum thickness Reynolds number  $Re_{\theta c}$  with  $\widetilde{Re}_{\theta t}$ . Moreover, the correlation of  $Re_{\theta c}$  with  $\widetilde{Re}_{\theta t}$  was modified by Wang et al. [48], and the results of the transition length and skin friction distribution are in good agreement with the experiments. In general, the transition model coupled with RANS-based turbulence models has the capability to predict the dynamics of the transition and the global performance, but it has to be used cautiously due to its sensitivity to many parameters.

## 1.4 STATE-OF-THE-ART INVESTIGATIONS OF VARIABLE-PITCH TURBINES AND PROPELLERS

There are many types of vertical axis turbines (VAT) applied to energy conversion devices. Based on the different techniques used to control the pitching kinematic, the vertical axis turbines can be generally divided into three types: cycloidal type controllable-pitch, spring-control pitch and passive variable-pitch turbines. The schemes of these different turbines are shown in figure 1.5 [49]. As a special type of propulsion system, the cycloidal controllable-pitch VAT produces a thrust force that is perpendicular to the rotation axis. Since the magnitude and direction of the thrust force vary continuously with the blade pitching angle, a high maneuverability of the propulsion

system can be achieved. For marine propulsion systems, such as the Voith Schneider Propeller (VSP), each blade of the cycloidal propeller can be controlled using a complex kinematic system, resulting in the presence of the eccentricity  $e=OP/R$  ( $R$  is the radius) between the rotor casing center and kinematic system center, where the correlation of the azimuthal angle  $\varphi$  with the pitch angle  $\Phi$  is given by

$$\Phi = -\alpha \tan^{-1} \left( \frac{e \sin \varphi}{1 + e \cos \varphi} \right) \quad (1.4)$$

where  $\alpha$  is the pitching amplitude.

Generally, when  $e$  is smaller than 1, the cycloidal propeller is known as a low-pitch propeller while it is regarded as a high-pitch propeller with  $e>1$ .

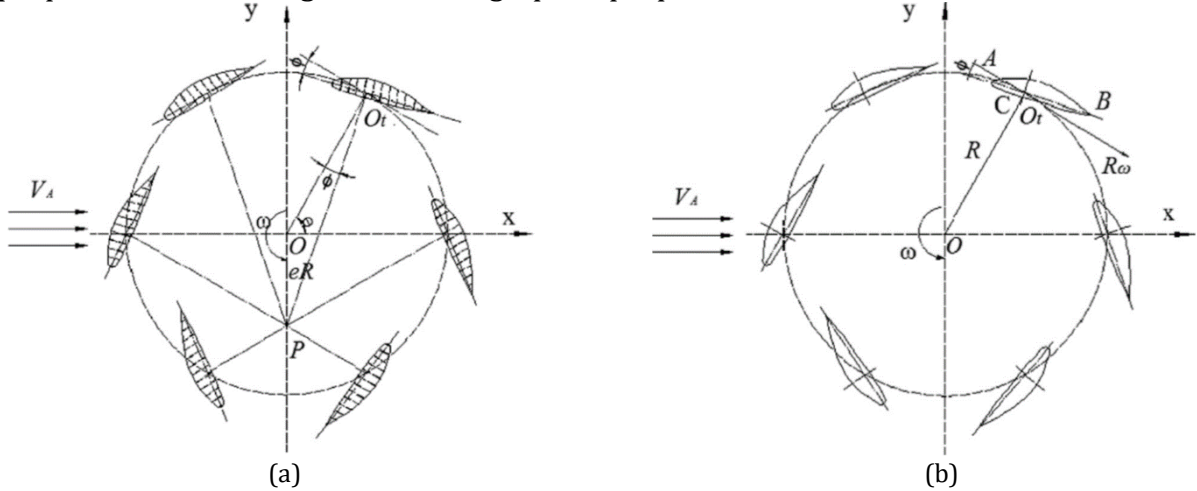


**Fig.1.5** Principle diagrams of different VATs. (a) Cycloidal controllable-pitch VAT; (b) Variable-pitch VAT.

The spring-control variable-pitch vertical axis turbine is a new type and its pitching mechanism is quite similar to the passive variable-pitch type. The turbines rotate around the center of the circularity and the blade is turning around the blade rotating center. However, for the passive variable-pitch turbines, the blade only swings in a limited range of the incidence and the variation of the blade pitch is controlled by the balance between the hydrodynamic moment and inertia moment continuously. The advantage of this turbine is the simple and reliable structure, as well as better capabilities of self-starting.

Although the variable-pitch propeller with sinusoidal pitching is less efficient than the cycloidal controllable-pitch propeller, the previous experimental data shows that the cycloidal controllable-pitch propeller has a quantity of noisy data and some poor results due to the high friction of the pitch control devices [2]. Simultaneously, the cycloidal motion can be replaced with the sinusoidal motion for the reason that it has a simpler mechanism, fewer parts, less frictional losses and a more rugged construction [50]. Nakonechny [51] conducted the experiments for the variable-pitch propeller with a modified sinusoidal motion, and showed that the efficiency is higher than the cycloidal controllable-pitch propeller with the same maximal pitch angle. In addition, the sinusoidal blade pitch motions were employed in many macro air vehicles successfully [52-53].

Compared with the fixed-blade VAT, the turbines with sinusoidal pitching can improve the overall performance. With an appropriate pitching amplitude, not only does the power efficiency increase, but also the fluctuations of the power, the rotation speed and the torque are reduced significantly [54]. Chen et al. [55] studied the effect of the pontoon-type channel on the hydrodynamic torques of the blade and the rotor, and they found that when the turbine is placed in a channel, the fluctuations of hydrodynamic

torques and rotational speed are significantly reduced, while the power output is more than 30% higher than the isolated turbine. With the sinusoidal pitching motion, Paillard et al. [56] used the SST  $\gamma - \widetilde{Re}_{\theta t}$  transition model to study the effect of the pitch angle on the torque coefficient and efficiency of the cross-flow tidal turbine, and the results show that the second harmonic pitch function, defined as  $\theta=2(\cos(2\omega t)-1)$ , can provide a large performance improvement. The choice of turbulence model is critical for the simulation accuracy in RANS computations. For example, the standard SST  $k-\omega$  over-predicts the maximal power coefficient when the turbines operate at low-Reynolds number conditions, which is attributed to the under-prediction of the flow separation after stall reported by McNaughton et al. [57]. Therefore, the low-Reynolds number version and some modifications are necessary to predict the correct laminar separation and reproduce the flow structures related to the dynamic stall. Moreover, the transition effect is vital in predicting the occurrence of the stall because of the existence of the laminar separation bubble which can lead to a large discrepancy of the power prediction [58]. Li et al. [59] observed that the lift coefficient is lower than in the experiments when the SST  $k-\omega$  model is employed to resolve the fully turbulent flows. Rezaeiha et al. [60] compared the power coefficient obtained by several turbulence models and found that the SST model variants (SST  $k-\omega$ , SST  $\gamma$  and SST  $\gamma - \widetilde{Re}_{\theta t}$ ) can provide a reasonable agreement with the experiments. The three-dimensionality also has a great impact on the power coefficient because the 2D flow does not account for the blade tip and strut effects. Therefore, Marsh et al. [61] suggest that the 3D domain with fully resolved boundary layer mesh should be used to predict the turbine power output. Additionally, the instantaneous properties of the performance and vortex evolution are quite different between 2D and 3D flows, though there is only a small error in time-averaged force. Hu et al. [62] found that the aerodynamic force fluctuation is reduced dramatically for 3D flows due to the weakened parallel blade vortex interactions induced by the dynamic stall vortices. The blade-vortex interaction is an issue that should be analyzed clearly for the reason that it can produce additional forces for the rotating system. Lind et al. [3] uncovered that the blade-vortex interactions are strongly associated with the peaks of the instantaneous forces, which shows their importance to the generation of lift and propulsive force of the cycloidal rotor. Besides, how to model the complex wake is questionable because of the complexity. Therefore, Tang et al. [63] combined the momentum theory, lifting-line method, free wake model and Leishman-Beddoes semi-empirical dynamic stall model, to model the unsteady wakes for the cycloidal propellers and the results present a fair agreement with the experiments, in terms of performance and instantaneous blade force variations. Generally, most previous works focus on the prediction of the global performance and unsteady vortex evolution of variable-pitch turbines and propellers, but how the internal flow structures influence the performance of the rotating system and the single blade is less understood at low Reynolds number, when the transition effect can't be neglected.

## 1.5 PARAMETRICAL STUDY AND OPTIMIZATION OF VARIABLE-PITCH TURBINES AND PROPELLERS

The final goal of studying the flow structures inside these working turbines or propellers is to optimize them by checking the effect of some single parameter independently, or by combining several factors using some optimization approaches. In complex rotating machines, there are many important parameters more or less affecting the propulsive force and efficiency of these devices. Therefore, a brief literature review is conducted hereafter.

The modification of the geometrical parameters is the primary choice for the optimization of the performance based on the internal flow structures. In the case of vertical axis wind turbines, many examples of optimization can be found in the literature. For example, Wang et al. [64] compared the power coefficients of symmetrical and asymmetrical profiles considering the influence of the thickness, maximal thickness position, camber and maximal camber position, and the results show the different tendency in power coefficient. Subramanian et al. [65] found that a thick airfoil performs better for low tip speed ratio  $\lambda$  (TSR) while the thin profile has a better performance for  $\lambda > 1.8$ . Baghdadi et al. [66] tested some rotor blades with deformed trailing edge and observed that the modified profile can improve the power output of the wind turbine. Using a fully automated optimization based on response surface approximation, Ismail and Vijayaraghavan [67] conducted some investigations on a NACA0015 airfoil with inward semi-circle dimple and Gurney flap on the lower surface and the results show that the aerodynamics of the wind turbine is greatly improved. Moreover, Tang et al. [68] established an aerodynamic-optimization-design method to have a new airfoil with maximal thickness and a small amount of positive camber, which can produce higher thrust and lower torque compared with the baseline geometry. Recently, Tirandaz and Rezaeiha [69] tested a series of symmetrical airfoils for the optimization of VAWT by changing the blade maximum thickness, the maximum thickness position and the leading-edge radius. The results show that these three parameters have a coupled impact on the turbine power and thrust coefficients, as well as the dynamic stall characteristics. Then, the solidity, defined as  $\sigma = Nc/r$  (where  $N$  is the blade number,  $c$  is the blade chord and  $r$  is the rotor radius), is also found to influence the aerodynamic performance. Eboibi et al. [70] performed experiments to investigate the power coefficient variation caused by the blade chord change and found that the higher solidity turbine attained better power coefficient because of the delayed dynamic stall. With special emphasis on the solidity and blade number, Rezaeiha et al. [71] demonstrated that regarding the output power uniformity and structural loads, a large number of blades yielding more uniform instantaneous loads and power is recommended, for the reason that it reduces the large-scale load fluctuations because of the smaller blade chord at a given solidity. Using the SST  $k-\omega$  turbulence model, Sagharichi et al. [72] observed that the variable-pitch VAWT at high solidity is interesting because it generates less vortex structures and more thrust.

The sinusoidal motion is the most common pitching kinematic for variable-pitch turbines and propellers. But the original sinusoidal motion is changed into an asymmetrical motion or different kinematics at different azimuthal angles, the overall performance can be improved. Chen et al. [73] adopted an asymmetry sinusoidal motion for azimuthal angles between  $0^\circ$  and  $180^\circ$ , and a fixed small pitching angle from  $180^\circ$  to  $360^\circ$ , which resulted in a power efficiency increase of 20%. When applied to micro-air-vehicles, the asymmetrical pitching kinematics, involving the mean incidence, pitching amplitude and phase angle, have great impact on the cycloidal rotor performance and wake-blade interactions, as reported by Benedict et al. [74]. When considering the dynamic virtual camber induced by the flow curvature, Walther et al. [75] found that the blade lift decreases in the upper half of the circular trajectory because of the negative camber while it increases in the lower half, thanks to the positive camber. Therefore, they introduced an asymmetrical pitching kinematic with a higher pitch in the upper half and a lower pitch in the bottom half. Besides, because of the flow curvature effect, the cycloidal rotor performance is strongly dependent on the chord-to-radius ratio and the blade pitching pivot location. Benedict et al. [76-77] pointed out that increasing the solidity by increasing the blade chord and moving the pivot location by about 25-35% from the

leading edge both result in a large improvement in power loading (thrust/power). They also observed that at low pitching amplitudes, the cycloidal rotor with short span has a higher power loading. For a self-pitch high-solidity vertical axis wind turbine, Xisto et al. [78] investigated the effect of different parameters on the aerodynamic efficiency and they found that the highest torque is obtained at a very low tip speed ratio with large blades. They also found that the optimum blade pitching axis location is between 35% and 50% of the chord. After considering nearly all parameters, Jarugumilli et al. [79] concluded that the 4-bladed cycloidal rotor using 1.3-inch NACA0015 blade section with an asymmetrical pitching of 45° at the top and 25° at the bottom and the pitching pivot of 25% chord achieves a higher power loading compared with the conventional one.

According to the work mentioned above, it seems that the main focus is on the optimization of global performance by increasing the efficiency and decreasing the power consumption, but the influence of the flow structures on the performance change under various operating conditions has not been extensively studied.

## 1.6 OBJECTIVE OF PRESENT WORK

The goal of my research work is to study the detailed flow structures inside a two-bladed cycloidal rotor with sinusoidal pitching using the RANS SST  $\gamma - \widetilde{Re}_{\theta t}$  transition model, with special emphasis on the flow-induced performance change of the rotating system and a single blade under various operating conditions. The work mainly composed of the two following parts:

(1) First of all, the SST  $\gamma - \widetilde{Re}_{\theta t}$  transition model is calibrated on an airfoil at different incidences, by checking the effects of the mesh arrangement in the streamwise and normal directions, the inflow turbulence conditions, the correlations and parameters in the transition model, and the turbulence model. The computations are compared to available experiments, in terms of the time-averaged pressure, near-wall velocity profiles and the separation, transition and reattachment locations. Then, the optimized transition model is applied directly to a two-bladed cycloidal rotor, to investigate the detailed internal flow structures and how they influence the performance of the rotating system and single blade. The results obtained by the transition model are compared to the existing experiments and some results obtained with other turbulence models.

(2) The second part is focused on the impact of four important parameters: the pitching kinematic (symmetrical/asymmetrical pitching), the chord-to-radius ratio, the pitching pivot location and the blade profile, for the purpose of optimizing the cycloidal propeller and explaining how the near-wall flows affect the performance. Attention is paid to the flow-induced performance variations at different Reynolds number and advance coefficient conditions.

## 2 CALIBRATION AND VALIDATION OF THE SST $\gamma - \widetilde{Re}_{\theta t}$ MODEL

### 2.1 TRANSITIONAL FLOWS AROUND A NACA0018 AIRFOIL

#### 2.1.1 Introduction

At moderate and low Reynolds number, the laminar-turbulence transition is a crucial phenomenon over any lifting surfaces, which has undesirable consequences related to the development of the LSB. In addition, the existing SST  $\gamma - \widetilde{Re}_{\theta t}$  transition model is extremely sensitive to many parameters, so it should be used carefully. In this chapter, the two-dimensional (2D) incompressible viscous flows around a NACA0018 airfoil are studied, and the effects of the mesh distribution, the inlet turbulence condition, and the correlations and parameter of the transition model are investigated. Afterwards, the results obtained with the transition model and other RANS turbulence models are compared. Finally, the influence of the incidence and Reynolds number are also considered.

#### 2.1.2 SST $\gamma - \widetilde{Re}_{\theta t}$ transition model

The SST  $k-\omega$  model is used as a baseline because it accounts for the transport of the turbulence shear stress and provides reasonably accurate predictions of the onset and the amount of flow separation under adverse pressure gradient [80]. It behaves like a hybrid model where the near-wall flows are resolved by the standard  $k-\omega$  model while the  $k-\varepsilon$  model is used to predict the flows in the free-stream region. The governing equations of the SST  $k-\omega$  model are given by:

$$\frac{\partial}{\partial t}(\rho k) + \frac{\partial}{\partial x_j}(\rho u_j k) = P_k - D_k + \frac{\partial}{\partial x_j}\left((\mu + \sigma_k \mu_t) \frac{\partial k}{\partial x_j}\right) \quad (2.1)$$

$$\frac{\partial}{\partial t}(\rho \omega) + \frac{\partial}{\partial x_j}(\rho u_j \omega) = \alpha \frac{P_k}{\nu_t} - D_\omega + C d_\omega + \frac{\partial}{\partial x_j}\left((\mu + \sigma_\omega \mu_t) \frac{\partial \omega}{\partial x_j}\right) \quad (2.2)$$

Where  $k$  is the turbulent kinetic energy,  $\rho$  is the density,  $u_i$  is the velocity component in the  $i$  direction,  $P_k$  and  $D_k$  are the production and destruction terms for  $k$ , respectively,  $\mu$  and  $\mu_t$  are the molecular and turbulent viscosities,  $\omega$  is the rate of dissipation of  $k$ ,  $D_\omega$  is the destruction term for  $\omega$  and  $C d_\omega$  is the cross-diffusion terms.

The eddy viscosity  $\mu_t$  used to close these two equations is calculated as follows:

$$\mu_t = \min\left[\frac{\rho k}{\omega}; \frac{a_1 \rho k}{S F_2}\right] \quad (2.3)$$

The detailed information regarding the empirical correlations and the values of the various parameters can be found in [81].

The transport equations of intermittency  $\gamma$  and transition momentum thickness Reynolds number  $\widetilde{Re}_{\theta t}$  are defined as follows:

$$\frac{\partial}{\partial t}(\rho\gamma) + \frac{\partial}{\partial x_j}(\rho u_j\gamma) = P_\gamma - E_\gamma + \frac{\partial}{\partial x_j}\left(\left(\mu + \frac{\mu_t}{\sigma_f}\right)\frac{\partial\gamma}{\partial x_j}\right) \quad (2.4)$$

$$\frac{\partial}{\partial t}(\rho\widetilde{Re}_{\theta t}) + \frac{\partial}{\partial x_j}(\rho u_j\widetilde{Re}_{\theta t}) = P_{\theta t} + \frac{\partial}{\partial x_j}\left(\sigma_{\theta t}(\mu + \mu_t)\frac{\partial\widetilde{Re}_{\theta t}}{\partial x_j}\right) \quad (2.5)$$

The production terms in the intermittency and transition momentum thickness Reynolds number equations, respectively, are written as follows:

$$P_{\gamma 1} = F_{length}c_{a1}\rho S[\gamma F_{onset}]^{0.5}(1-\gamma) \quad (2.6)$$

$$F_{onset1} = \frac{Re_v}{2.193Re_{\theta c}} \quad (2.7)$$

$$F_{onset2} = \min(\max(F_{onset1}, F_{onset1}^4), 2.0) \quad (2.8)$$

$$F_{onset3} = \max(1 - \left(\frac{R_T}{2.5}\right)^3, 0) \quad (2.9)$$

$$P_{\theta t} = c_{\theta t}\frac{\rho}{t}(Re_{\theta t} - \widetilde{Re}_{\theta t})(1 - F_{\theta t}) \quad (2.10)$$

Three important empirical correlations are needed:

$$F_{length} = f(\widetilde{Re}_{\theta t}); Re_{\theta c} = f(\widetilde{Re}_{\theta t}); Re_{\theta t} = f(Tu, \frac{dp}{ds}) \quad (2.11)$$

where  $F_{length}$  is used to control the length of the transition region,  $Re_{\theta c}$  can be thought as the location where turbulence begins to grow and  $Re_{\theta t}$  is the location where the velocity profile first starts to deviate from the pure laminar profile.  $Tu$  is the turbulence intensity and  $\frac{dp}{ds}$  is the streamwise pressure gradient. The detailed description of the other parameters can be found in [26-27].

Because of the introduction of the effective intermittency  $\gamma_{eff}$ , the production and diffusion terms of the  $k$ -equation in the original SST  $k-\omega$  turbulence model are modified according to the following formulation:

$$\frac{\partial}{\partial t}(\rho k) + \frac{\partial}{\partial x_j}(\rho u_j k) = \tilde{P}_k - \tilde{D}_k + \frac{\partial}{\partial x_j}\left((\mu + \sigma_k\mu_t)\frac{\partial k}{\partial x_j}\right) \quad (2.12)$$

$$\tilde{P}_k = \gamma_{eff}P_k; \tilde{D}_k = \min(\max(\gamma_{eff}, 0.1), 1.0)D_k \quad (2.13)$$

where  $P_k$  and  $D_k$  are the source terms in the turbulence kinetic energy equation.

According to the work reported by Menter et al. [26], this transition model has two advantages: the robustness due to the independence with momentum equations, and the ability to predict the influence of high free-stream turbulence level on buffeted laminar boundary layer.

### 2.1.3 Flow configuration, meshing and numerical setup

A two-dimensional NACA0018 airfoil with a chord length  $c=0.2m$  was used in the present study. The Reynolds number based on the chord length and inflow velocity is  $1\times 10^5$ . The pivot point is located at a distance of  $0.3c$  from the leading edge. As is shown

in figure 2.1a, the computational domain extends  $3c$  upstream from the leading edge and  $8c$  downstream from the trailing edge, which is sufficient because of the small amount of flow separation when the attack-of-angle is below  $15^\circ$ .

The experiments were conducted in a wind tunnel with a low inflow turbulence level of 0.2%, at University of Waterloo [12]. The mean static pressure measurements were obtained by 65 pressure taps attached on the foil surface along the center-span plan, and the uncertainty on these measurements is less than 2% of the free-stream dynamic pressure. Simultaneously, the mean velocity profiles near the boundary layer were measured with hot-wire probes, with an uncertainty less than 5% for  $U/U_0 > 0.2$  ( $U$  is the local velocity and  $U_0$  is the inflow velocity). Reference [12] gives more detailed information about the experimental setup and data materials.

Both structured and unstructured meshes were used in this work. The unstructured mesh consists of trimmed cell in the free-stream region and prism layers placed near the wall. The distributions of the unstructured and structured meshes at the incidence of  $10^\circ$  are displayed in figure 2.1b and 2.1c. Five sets of meshes were tested, to check the mesh influence on the numerical results. In Table 2.1, mesh 1 is a structured mesh with 300 nodes ( $N$ ) along the foil surface. Then, mesh 2, 3 and 4 are used to study the effect of mesh refinement in the streamwise direction by changing the target size  $t_f$  near the foil surface, and mesh 5 is employed to investigate the influence of the grid refinement near the wall by modifying the prism layer thickness  $t_p$  and the number of layers  $n_p$ . The growth rate for all unstructured meshes remains constant with a value of 1.2. The total number of the nodes ( $N$ ) and the resultant  $y^+$  ( $y^+ = u_\tau * y / v$ , where  $u_\tau$  is the friction velocity,  $y$  is the distance to the nearest wall and  $v$  is the kinematic viscosity), are listed in Table 2.1. Compared with mesh 3, the lift and drag coefficients obtained with mesh 1 are lower (the error is based on mesh 3). Therefore, additional comparisons will be reported in the following section. Then, it is observed that the predicted lift coefficient for mesh 2 is lower than the one obtained with mesh 3 and 4, which shows the importance of mesh refinement in the streamwise direction. The comparison between meshes 3 and 5 shows that the results are almost not affected by the mesh near the wall.

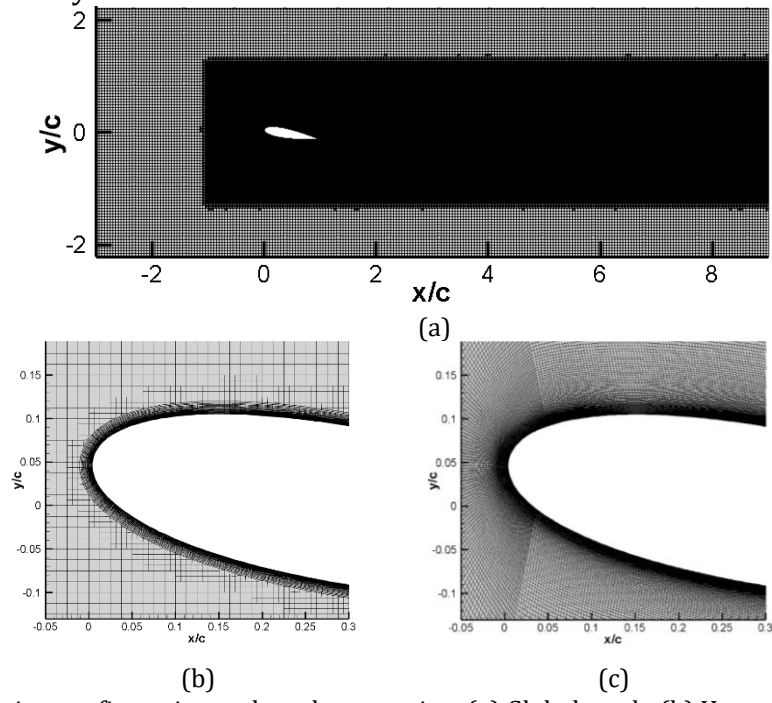


**Fig.2.1** Computation configuration and mesh generation. (a) Global mesh; (b) Unstructured mesh; (c) Structured mesh

**Table 2.1** Information and performance prediction of five sets of meshes.

Structured mesh	$N$	$y$ (m)			$C_L$	Error (%)	$C_D$	Error (%)	$N$	Maximal $y^+$
Mesh 1	300	$3 \times 10^{-6}$			0.783	3.81	0.0395	1.99	226,150	0.14
Unstructured meshes	$t_p$ (m)	$n_p$	$t_f$ (m)	$y$ (m)						
Mesh 2	$3 \times 10^{-3}$	50	$1 \times 10^{-3}$	$2.6 \times 10^{-6}$	0.776	4.67	0.0472	17.1	194,171	0.12
Mesh 3	$3 \times 10^{-3}$	50	$4 \times 10^{-4}$	$2.6 \times 10^{-6}$	0.814	--	0.0403	--	253,319	0.12
Mesh 4	$3 \times 10^{-3}$	50	$2 \times 10^{-4}$	$2.6 \times 10^{-6}$	0.811	0.369	0.0402	0.248	331,423	0.12
Mesh 5	$5 \times 10^{-3}$	70	$4 \times 10^{-4}$	$6.3 \times 10^{-7}$	0.812	0.246	0.0405	0.496	284,622	0.09

Incompressible 2D and unsteady flow calculations are performed using the STARCCM + code. For the boundary conditions, a constant velocity  $U_0$  is imposed in the inlet section while a constant pressure is assigned to the outlet section. The top and bottom walls are set as symmetry planes to eliminate the wall effect, and the foil surface is treated as a no-slip wall. When performing the implicit unsteady calculations, steady computations are used as initializations to get a faster convergence. The convergence target of the different resolved variables of the conservation equations is set to  $10^{-4}$ . Regarding the effect of the time step  $\Delta t$ , different values are tested at the incidence of  $10^\circ$  and the results are shown in Table 2.2. It is observed that there is not much difference in the performance prediction for different time-steps (error is based on the case  $\Delta t=1 \times 10^{-5}$ ). Therefore, a time-step of  $1 \times 10^{-5}$ s is finally employed for all the tested cases and the total time is set to 0.15s, which is enough due to the nearly unchanged history of lift and drag coefficients.

**Table 2.2** Results with different time-steps.

$\Delta t$ (s)	$C_L$	Error (%)	$C_D$	Error (%)
$5 \times 10^{-5}$	0.813	0.123	0.0402	0.248
$1 \times 10^{-5}$	0.814	--	0.0403	--
$8 \times 10^{-6}$	0.816	0.246	0.0402	0.248

#### 2.1.4 Effect of mesh distribution

In the study of the mesh influence, the lift and drag coefficients predicted with the structured mesh exhibit a little difference, compared with the unstructured mesh. Therefore, some additional variables, including the distributions of mean pressure coefficient  $C_p$  ( $C_p=p/(0.5*\rho*U_0^2)$ , where  $p$  is the pressure and  $\rho$  is the fluid density) and velocity profiles at three locations, are compared for different meshes at an incidence of  $10^\circ$ . It seems that the pressure coefficient distributions for different meshes are almost the same, except for mesh 2. But the pressure coefficient obtained with the structured mesh shows a small difference, compared with the unstructured mesh, in the laminar flow region before the transition, which is the main source of performance difference shown in Table 2.1. Then, the near-wall mean velocity profiles at three locations, representing the laminar boundary layer, transition region and fully turbulent boundary layer, are presented in figure 2.2b, 2.2c and 2.2d, respectively. It is observed that the boundary layer thickness becomes larger during the laminar-turbulence transition process. At  $x/c=0.06$ , there is no reverse flow very close to the wall, indicating that the flow separation does not

occur. However, near the transition region at  $x/c=0.21$ , a strong reverse flow characterized by a negative velocity magnitude is observed near the wall, induced by the existence of the LSB. The experiments can't detect the reverse flow because of the limitations of the conventional hot-wire measurement described by Yarusevych et al. [18]. Then, in the fully-turbulent boundary layer, the discrepancy between the numerical results and experiments becomes large. In general, mesh 2 exhibits the worst agreement with the experiments regarding the performance, the surface pressure and the near-wall velocity profiles, which shows the importance of the mesh refinement in the streamwise direction. Moreover, the unstructured mesh has the same ability to get a good result compared with the structured mesh, although there are some differences in performance prediction. Therefore, mesh 3 is adopted in the following calculations.

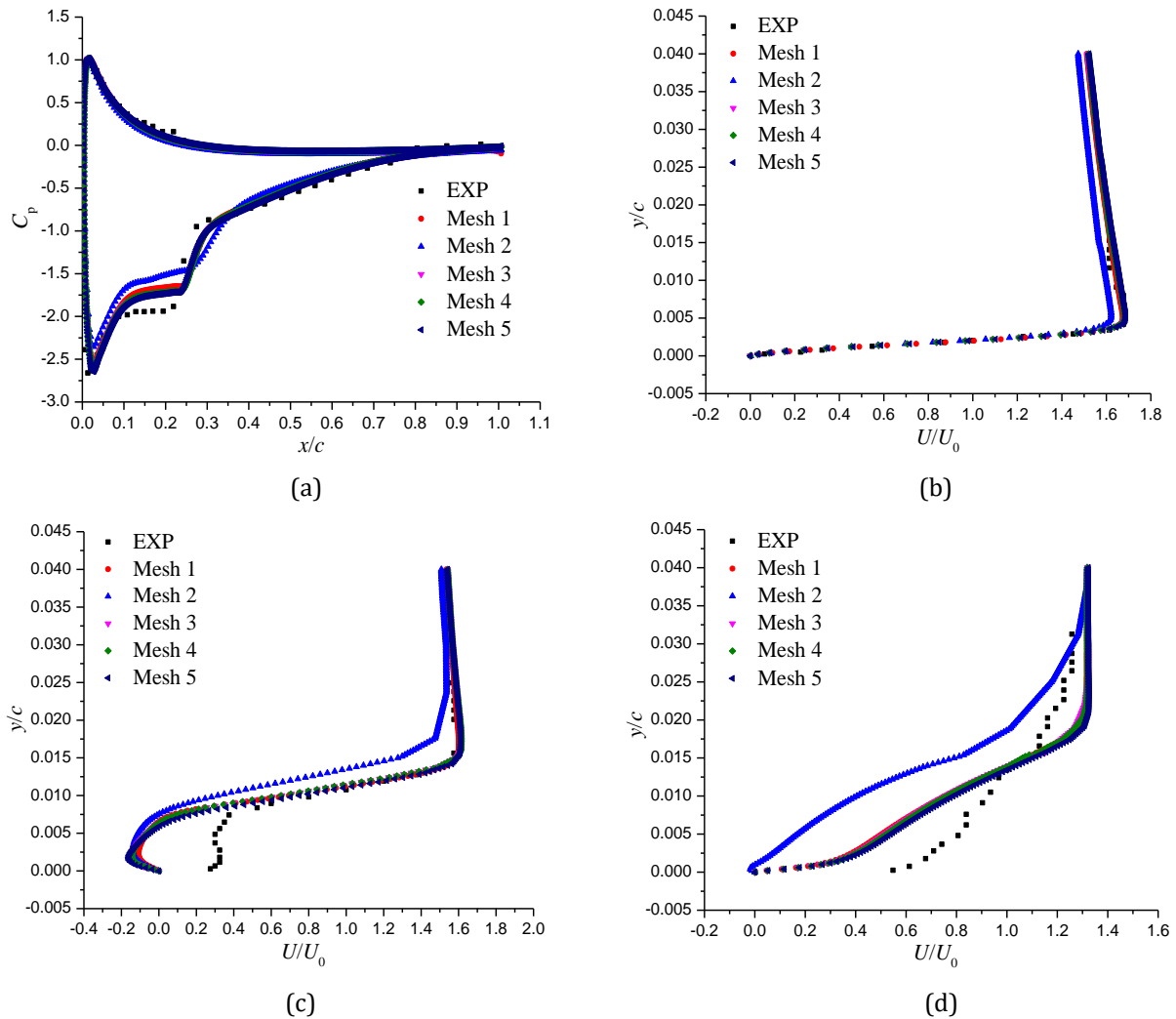


**Fig.2.2** Distributions of mean pressure coefficient and velocity profiles near the boundary layer. (a) Pressure coefficients; Velocity profiles at (b)  $x/c=0.06$ ; (c)  $x/c=0.21$ ; (d)  $x/c=0.34$ .

### 2.1.5 Effect of inlet turbulence condition

The inflow condition is critical to the locations of the separation, transition and reattachment points, so it should be chosen cautiously. Istvan et al. [15] and Istavan and Yarusevych [16] showed that an increase of the inflow turbulence intensity induces a motion of the mean separation downstream, while the mean transition and reattachment

points are shifted upstream and a wide range of frequencies, characteristics of some instabilities, are detected in the separated shear layer. If the free-stream turbulence level is very high, the flow-separation induced transition in the boundary layer is replaced with the bypass transition upstream from the airfoil. Breuer [81] employed the LES method to simulate the transition flows around SD7003 airfoil under different inflow conditions. They concluded that with the increase of the inflow turbulence level, the LSB first shrinks and finally completely vanishes, which causes a drastic increase of the lift-to-drag ratio. In this work, due to the relatively low inflow turbulence intensity in the wind tunnel, a small range of free-stream turbulence level  $Tu$  and eddy viscosity ratio  $\mu_t/\mu$  are evaluated. Fig.2.3 shows the distributions of pressure coefficient  $C_p$  and wall skin friction coefficient  $C_f$  ( $C_f = \tau_w / (0.5 * \rho * U_0^2)$ , where  $\tau_w$  is the wall shear stress) for various inflow conditions at incidence of  $10^\circ$ . It is observed that increasing both the turbulence intensity and the eddy viscosity ratio leads to a delayed separation and an early transition and reattachment, implying that the length of LSB decreases. However, it seems that the effect of the turbulence intensity is more obvious than the eddy viscosity ratio, and the reattachment point is more easily influenced by the free-stream turbulence level compared with the separation and transition locations. Both the distributions of pressure and skin friction coefficients can show the trend mentioned above.

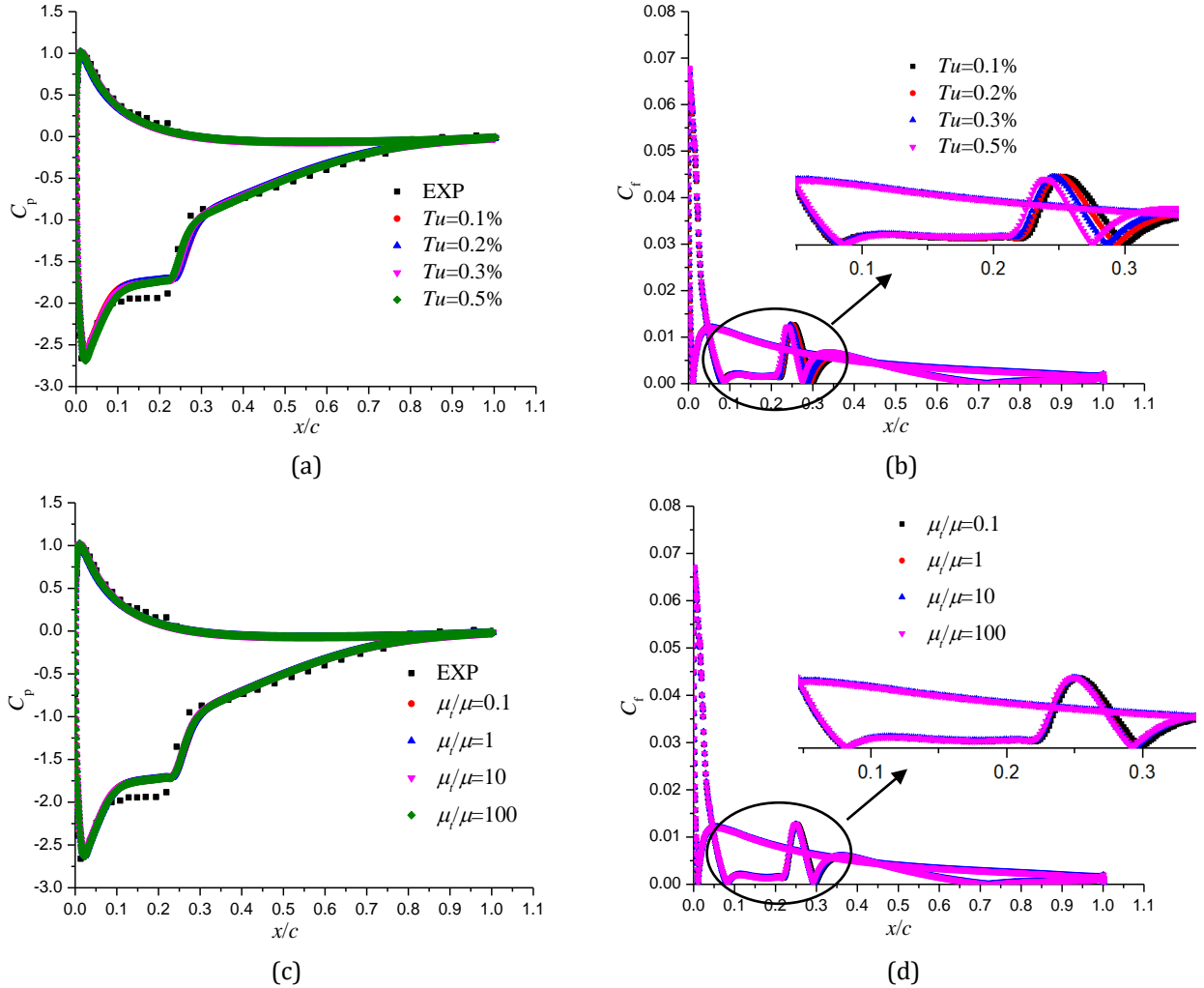


**Fig.2.3** Distributions of mean pressure and skin friction coefficients at different inflow conditions. (a) Pressure coefficients for various free-stream turbulence levels; (b) Skin friction coefficients for various free-stream turbulence levels; (c) Pressure coefficients for various eddy viscosity ratios; (d) Skin friction coefficients for various eddy viscosity ratios.

In order to better understand the physics of transition flows near the wall, the distribution of intermittency superimposed with the streamlines is shown in figure 2.4 for different freestream turbulence levels at the incidence of  $10^\circ$ . A value of intermittency equal to 1 means that the flow is fully turbulent, while a zero value means that it is laminar. In the region of free-stream flows, it is always turbulent while the occurrence of laminar-turbulence transition is obvious near the wall. When the free-stream turbulence level is relatively low, the LSB has a slender structure, and it becomes shorter with the increase of the turbulence intensity. Simultaneously, the height of LSB is also reduced under high turbulence level condition. Obviously, the reattachment point moves more upstream when the free-stream turbulence level is 0.5%. In a conclusion, increasing the free-stream turbulence level makes the gross size of LSB smaller, both in streamwise and normal directions. Furthermore, the reattachment point is more impacted by the free-stream turbulence level, and it moves upstream significantly with the increase of inlet turbulence intensity.

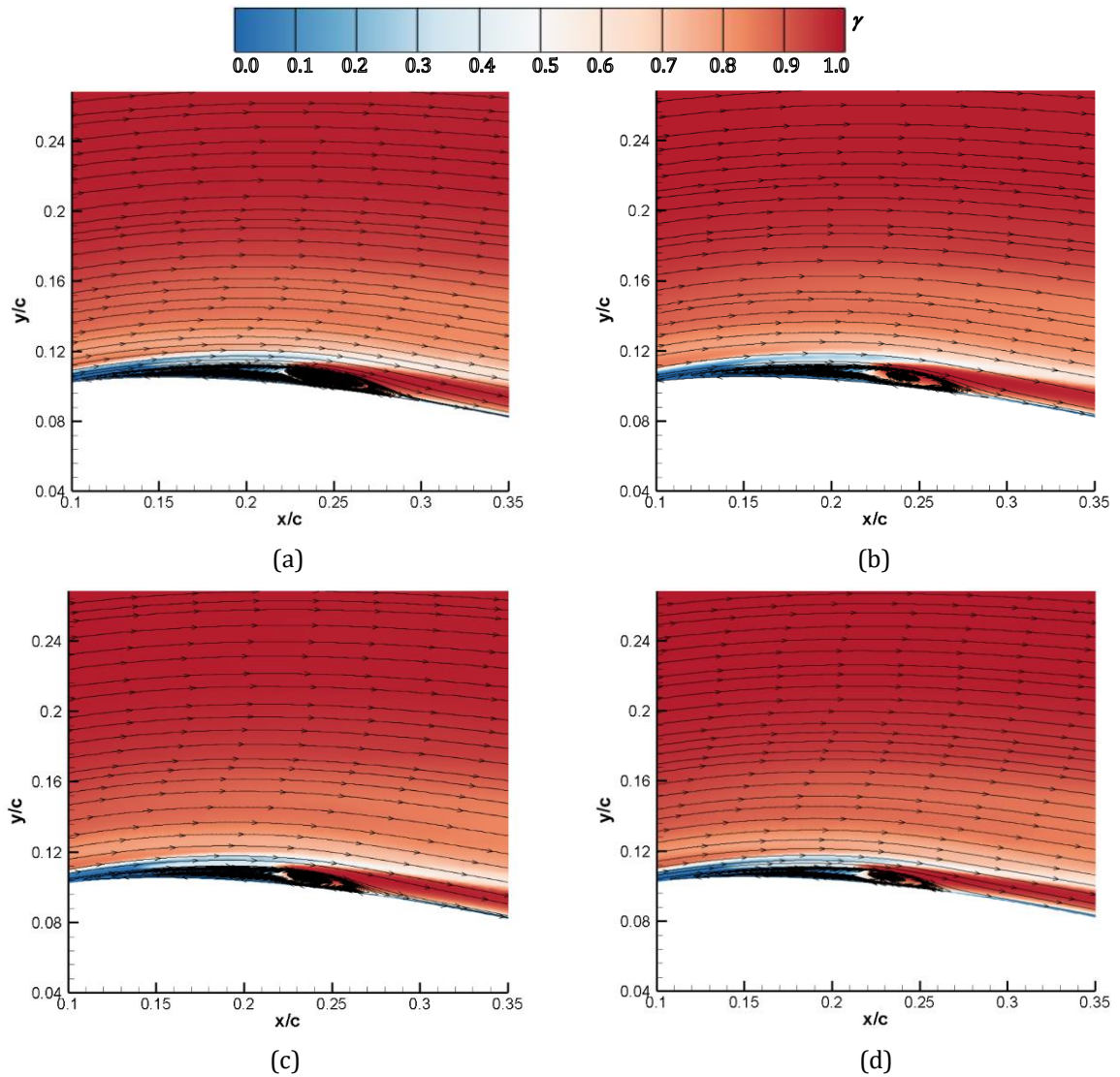


**Fig.2.4** Distributions of intermittency for various free-stream turbulence levels. (a)  $Tu=0.1\%$ ; (b)  $Tu=0.2\%$ ; (c)  $Tu=0.3\%$ ; (d)  $Tu=0.5\%$ .

### 2.1.6 Effect of correlations and parameter

Previous investigations show that there are three important correlations affecting the transition process, involving the  $F_{length}$ ,  $Re_{\theta c}$  and  $Re_{\theta t}$ .  $F_{length}$  and  $Re_{\theta c}$  have direct relationship with the transition momentum thickness Reynolds number  $\widetilde{Re}_{\theta t}$ , while  $Re_{\theta t}$  is closely associated with the inflow turbulence intensity and the adverse pressure gradient. Several combinations, presented by different formulations of these correlations, are evaluated in the present work. Firstly, the correlations of  $F_{length}$  and  $Re_{\theta c}$  are fixed according to the following formulations:

$$F_{length} = \min(300, \exp(7.618 - 0.01173\widetilde{Re}_{\theta t}) + 0.5) \quad (2.14)$$

$$Re_{\theta c} = \min(\widetilde{Re}_{\theta t}, 0.615\widetilde{Re}_{\theta t} + 61.5) \quad (2.15)$$

Three correlations of  $Re_{\theta t}$ , proposed by Abu-Ghannam and Shaw [82], Menter et al. [27] and Langtry [31], respectively, are given by

$$Re_{\theta t} = 163 + e^{(6.91-Tu)} \quad (2.16)$$

$$Re_{\theta t} = 803.73(Tu + 0.6067)^{-1.027} \quad (2.17)$$

$$Re_{\theta t} = \begin{cases} (1173.51 - 589.428Tu + 0.2196/Tu^2) & Tu \leq 1.3 \\ 331.5(Tu - 0.5658)^{-0.671} & Tu > 1.3 \end{cases} \quad (2.18)$$

The three correlations above, presented for zero pressure gradient, were originally presented in a form that includes the effect of a pressure gradient. There is some doubt that the pressure gradient effect is required in the correlation of  $Re_{\theta t}$ , since they arguably introduce a double-accounting of the pressure gradient effect [84]. Thus, three correlations of  $Re_{\theta t}$  considering the non-zero pressure gradient, are also tested by computing the Thwaites parameter  $\lambda_\theta$  and the acceleration parameter  $K$  in the case of Menter et al. [27], which are given by

$$Re_{\theta t} = 163 + e^{[F(\lambda_\theta)(1 - \frac{Tu}{6.91})]} \quad (2.19)$$

$$Re_{\theta t} = 803.73(Tu + 0.6067)^{-1.027}F(\lambda_\theta, K) \quad (2.20)$$

$$Re_{\theta t} = \begin{cases} (1173.51 - 589.428Tu + 0.2196/Tu^2)F(\lambda_\theta) & Tu \leq 1.3 \\ 331.5(Tu - 0.5658)^{-0.671}F(\lambda_\theta) & Tu > 1.3 \end{cases} \quad (2.21)$$

The detailed information about the functions can refer to the references [82], [27] and [83].

Then, the correlation of  $Re_{\theta t}$  in equation 2.18 which is default in STARCCM+ is used, combined with new correlations of  $F_{length}$  and  $Re_{\theta c}$  proposed by Suluksna et al. [84], which are expressed as follows:

$$F_{length} = \min(0.1 \exp(12 - 0.022\widetilde{Re}_{\theta t}) + 0.45; 300) \quad (2.22)$$

$$Re_{\theta c} = \min(\max[-(0.025\widetilde{Re}_{\theta t})^2 + 1.47\widetilde{Re}_{\theta t} - 120; 125]; \widetilde{Re}_{\theta t}) \quad (2.23)$$

The distributions of pressure and skin friction coefficients are displayed in figure 2.5 to clarify the correlation influence on the transition. At incidence of  $10^\circ$ , mesh 3 combined with a turbulence intensity of 0.2% and an eddy viscosity ratio equal to 10 is applied to the tested cases. According to the distributions of pressure and skin friction coefficients, it seems that the correlations with ZPG have a better prediction of pressure, especially in the region of transition. Simultaneously, the results obtained by the correlations with NZPG has almost no difference. Then, in figure 2.5b, based on the skin friction coefficient achieved by the correlations with NZPG, it is observed that the separation point moves downstream, while the transition and reattachment locations shift upstream, compared with that with ZPG. Actually, the influence of pressure effect parameter  $F(\lambda_\theta, K)$  can be neglected because it is largely canceled by the decay of the local turbulence intensity [84]. The use of the local turbulence intensity approximately equals to combine  $F(\lambda_\theta, K)$  with the ideal value of leading-edge turbulence intensity. Thus, the influence of pressure gradient is implicitly involved in the local turbulence intensity. By the way, the proposed correlations in reference [84] leads to a small delayed transition process, especially regarding the reattachment point. There is little difference among the three correlations of  $Re_{\theta t}$  with ZPG, due to the relatively low turbulence intensity. Based on the experiments, the correlations with ZPG proposed by Langtry [83] used to improve the results in low turbulence level, which is the default correlation of  $Re_{\theta t}$  in STARCCM + code, are favorable, in terms of the pressure distribution and transition region prediction.

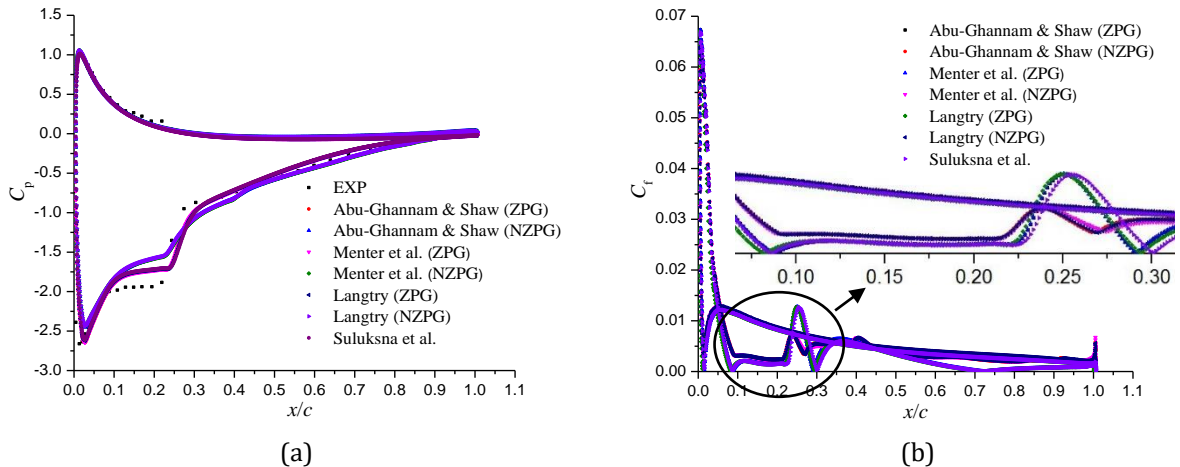


**Fig.2.5** Distributions of mean pressure and skin friction coefficients for various correlations. (a) Pressure coefficients; (b) Skin friction coefficients.

Because of the semi-empirical modelling, it exists a lot of parameters in the transition model, which have more or less effects on the transition process. After testing nearly all the constants in the equations of the transition model, a parameter  $S1$  used to control the size of LSB is assessed in the present work. It is embedded into the intermittency equation to correlate the transition model with the turbulence model, which is given by:

$$\gamma_{sep} = \min \left[ S1 \max \left( 0, \frac{Re_v}{3.235 Re_{\theta c}} - 1 \right) F_{reattach}, 2 \right] F_{\theta t} \quad (2.24)$$

where  $\gamma_{sep}$  is the parameter associated with effective intermittency  $\gamma_{eff}$ ,  $Re_v$  is the strain-rate Reynolds number,  $F_{reattach}$  and  $F_{\theta t}$  are the functions.

When the size of LSB is modified, the global performance and near-wall structures also vary considerably. The tested cases are at incidence of  $10^\circ$  with four values of  $S1$ . The distributions of pressure and skin friction coefficients are plotted in figure 2.6. As  $S1$  increases, the separation point moves downstream and both the transition and reattachment points shift upstream. However, it is observed that the reattachment point changes significantly, especially for  $S1=1$ . This trend indicates that the size of LSB decreases with the increase of the magnitude of  $S1$ . As a consequence, the global performance improves a lot. Then, in figure 2.7, the mean velocity profiles near the wall region at three locations are displayed to consider which value leads to the best agreement. Before the separation at  $x/c=0.06$ , there is only a difference in the free-stream velocity magnitude. However, in the separation region and near the transition location,  $S1 = 1$  overpredicts the thickness of the boundary layer while higher values of 4 and 8 underpredict the boundary layer thickness, which is related to the decrease of the LSB height when  $S1$  increases. Generally, the value  $S1=2$  has the best performance in predicting the size of LSB and the velocity profiles near the wall.

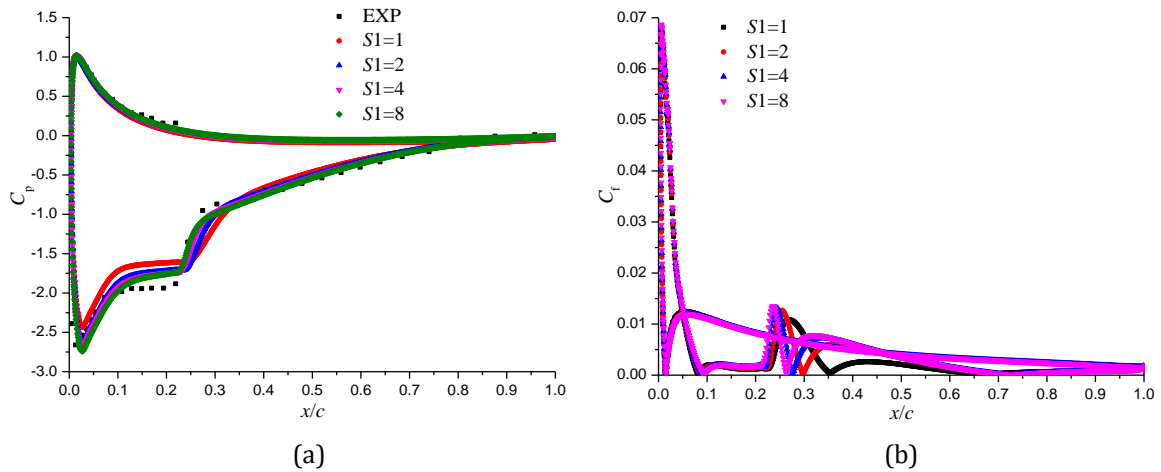


**Fig.2.6** Distributions of mean pressure and skin friction coefficients for various values of  $S1$ . (a) Pressure coefficients; (b) Skin friction coefficients.

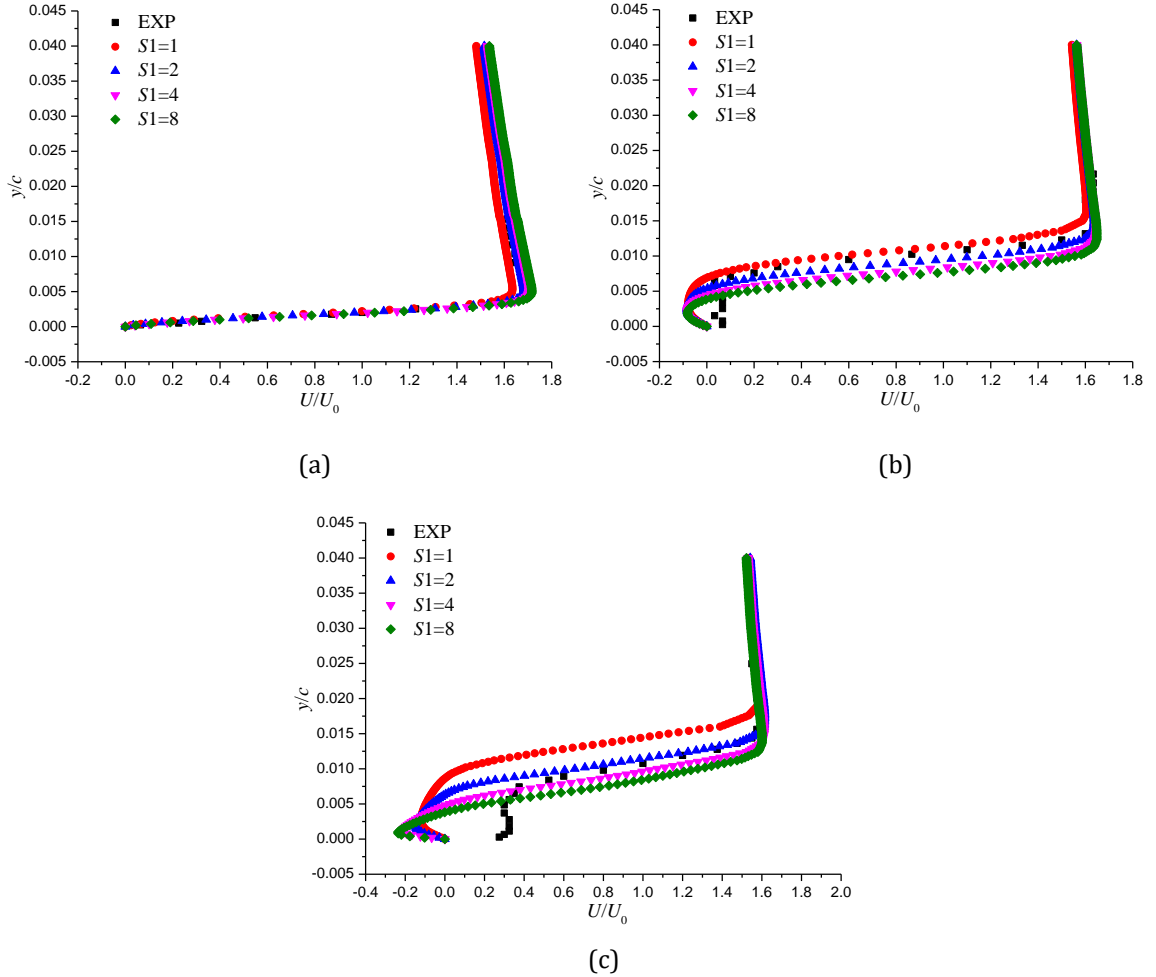


**Fig.2.7** Mean velocity profiles near the boundary layer. (a)  $x/c=0.06$ ; (c)  $x/c=0.17$ ; (d)  $x/c=0.21$ .

### 2.1.7 Effect of turbulence model

In order to quantify the discrepancy between the numerical simulations and the experiments, two other turbulence models, namely the SST  $k-\omega$  and the Reynolds stress model (RSM), are also evaluated in this work. The distributions of pressure and mean velocity profiles at five locations at incidence of  $10^\circ$  are presented in figure 2.8. Based on the comparison of the pressure coefficients, it is obvious that the original SST  $k-\omega$  turbulence model can't capture the transition process, since it is assuming that the flow is fully turbulent. The pressure obtained by RSM is much closer to the SST transition model. When it comes to the distributions of mean velocity profiles at different locations, it seems that the numerical results obtained with the SST TM are much better than what is simulated with the two other turbulence models. However, the boundary layer thickness obtained by the RSM is still better than the one predicted by the SST  $k-\omega$  model. Globally, the SST TM shows a clear superiority in predicting the laminar-turbulence transition process while the RSM has a better performance than the original SST  $k-\omega$  model.

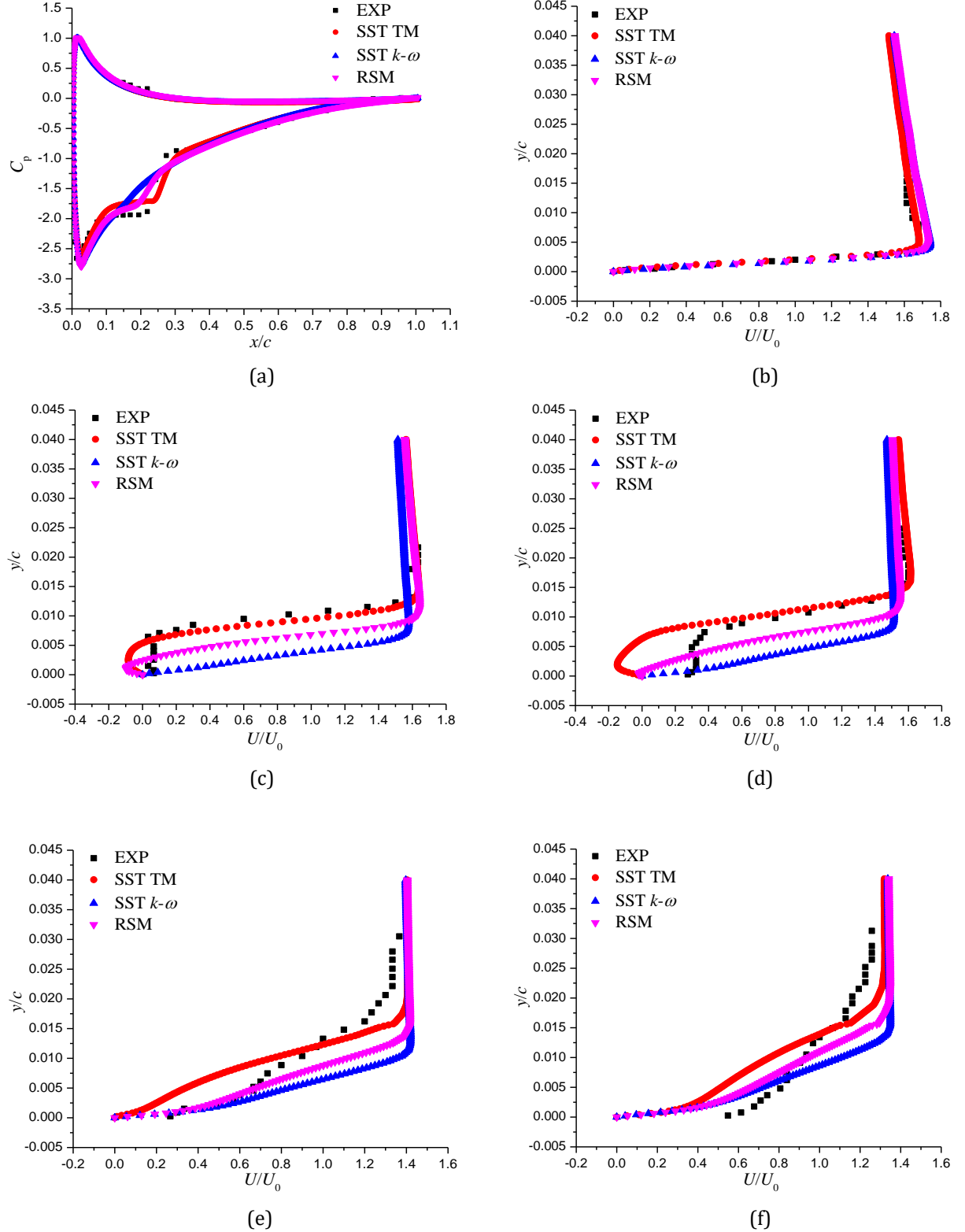


**Fig.2.8** Distributions of mean pressure coefficients and velocity profiles. (a) Pressure coefficients; Velocity profiles at (b)  $x/c=0.06$ ; (c)  $x/c=0.17$ ; (d)  $x/c=0.21$ ; (e)  $x/c=0.28$ ; (f)  $x/c=0.34$ .

In order to analyze the flow structures near the wall region, the distributions of turbulent kinetic energy are superimposed with the streamlines in figure 2.9 for the three turbulence models. The SST TM can resolve the high level of turbulent kinetic energy in the transition region, while the RSM does it partially. Conversely, the flow is quite smooth

near the wall region with the SST  $k-\omega$  turbulence model and the boundary layer is very thin due to the absence of LSB. Although the RSM can also capture the existence of transition induced by the separated shear layer, the LSB has a smaller size and the transition is located more upstream compared with SST TM, leading to the underpredicted boundary layer thickness shown in figure 2.8.

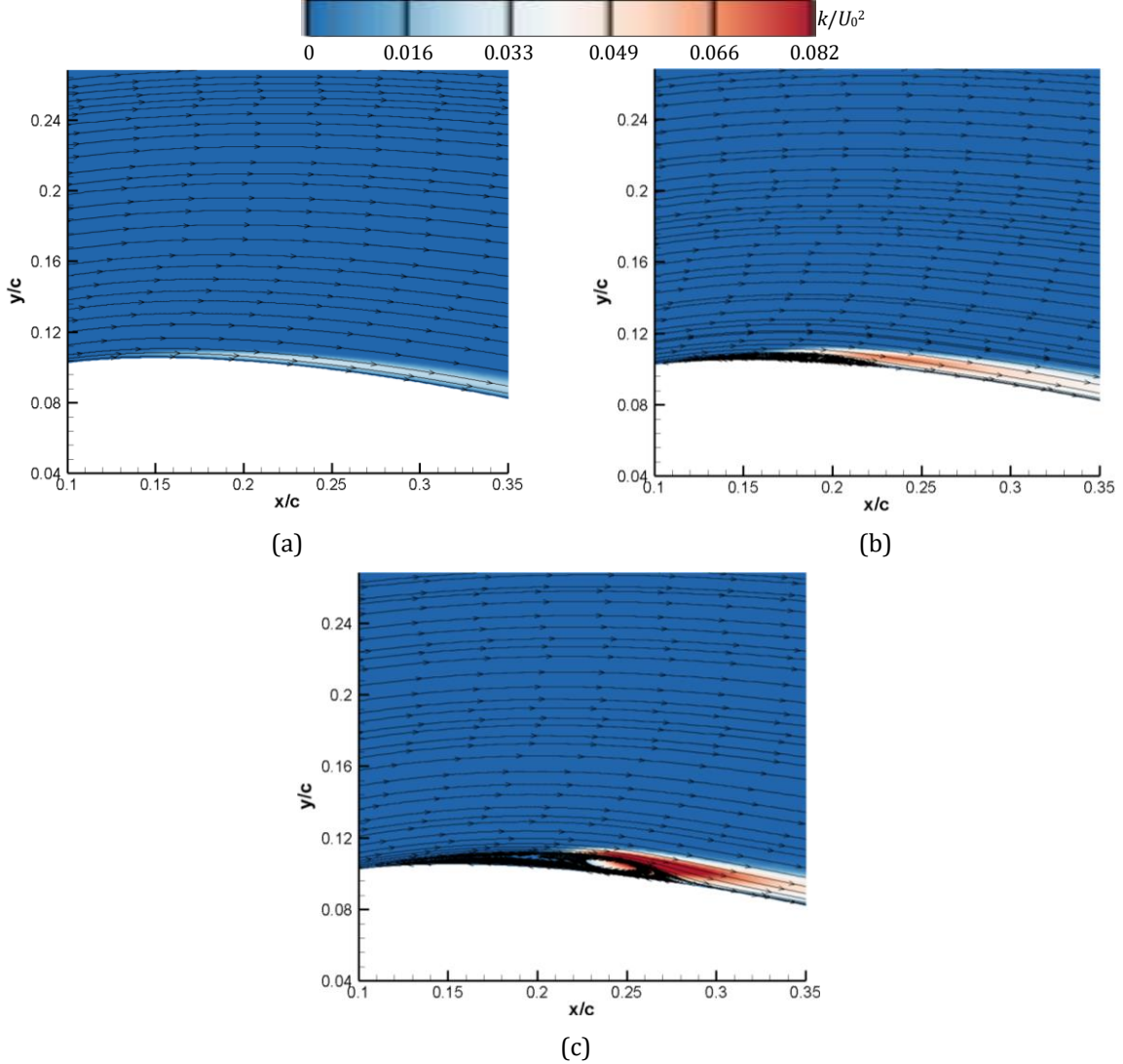
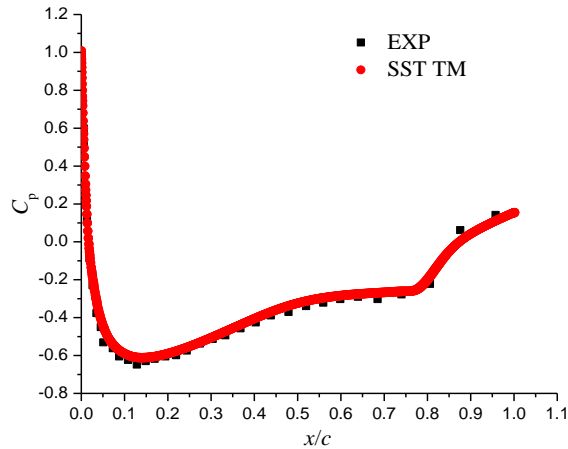


**Fig.2.9** Distributions of turbulent kinetic energy for various turbulence models. (a) SST  $k-\omega$ ; (b) RSM; (c) SST TM.

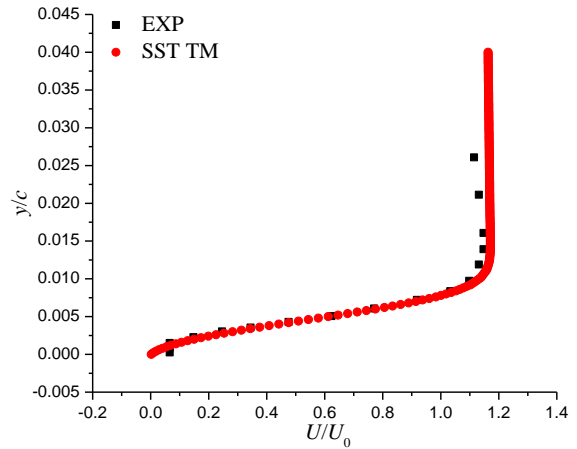
### 2.1.8 Effect of angle-of-attack

According to many previous investigations, the transition location also changes significantly with the incidence angle [14,20]. With the increase of the angle of attack, the transition location moves upstream along the airfoil surface, which changes the global performance. In the present work, three other incidences,  $0^\circ$ ,  $5^\circ$  and  $15^\circ$ , are also tested with the calibrated transition model mentioned above. The distributions of pressure and velocity profiles at five different locations are shown in figure 2.10, 2.11 and 2.12. At incidence of  $0^\circ$ , the flow is symmetrical on the upper and lower surfaces with a transition close to the trailing edge. Then, the transition moves significantly upstream on the upper surface at  $5^\circ$  and it is finally located near the leading edge at  $15^\circ$ . The velocity profiles agree

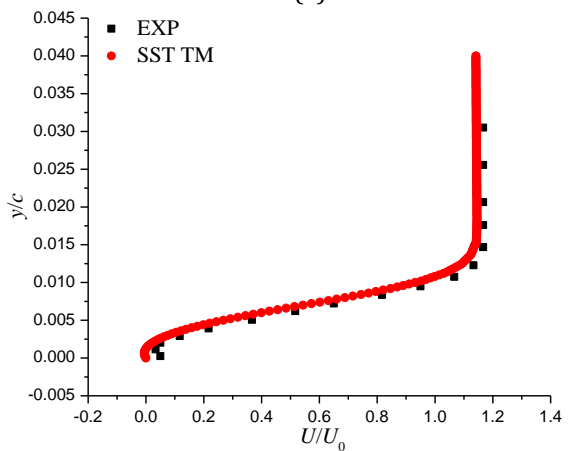
well with the experiments before the reattachment points at  $0^\circ$  and  $5^\circ$ . However, the discrepancy between the computation and the experiment increases after the reattachment locations, (see for example  $x/c=0.87$  at  $0^\circ$  and  $x/c=0.52$  at  $5^\circ$ ). This trend is also observed by Delafin et al. [20] and Langtry et al. [28], who mentioned the large discrepancies between the experiments and the simulations in near-wall flows after the reattachment. Langtry et al. [28] suggests that some adjustments to the separation-induced transition modification and to the diffusion coefficient  $\sigma_{\theta t}$  in the  $\widetilde{Re}_{\theta t}$  equation would be necessary, to better account for the effect of the flow history. Furthermore, as shown in figure 2.12, the distributions of pressure and near-wall velocity profiles show a relatively large error compared with the experiments, resulting from the difficulty to predict the narrow region between the separation and transition points, and the vortex shedding after the transition. Briefly, the SST TM can predict the mean pressure and velocity profiles before the reattachment points well and it fails in obtaining the accurate results in the fully turbulent boundary layer. Moreover, at relatively large incidence, the small length of transition near the leading edge, combined with the vortex shedding phenomenon after the transition make the simulation more challenging for RANS-based transition models.



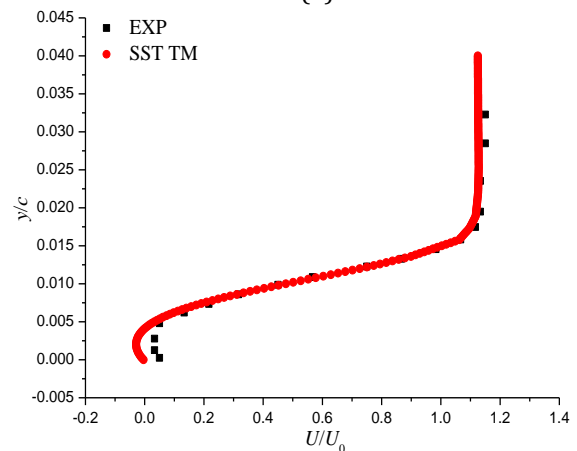
(a)



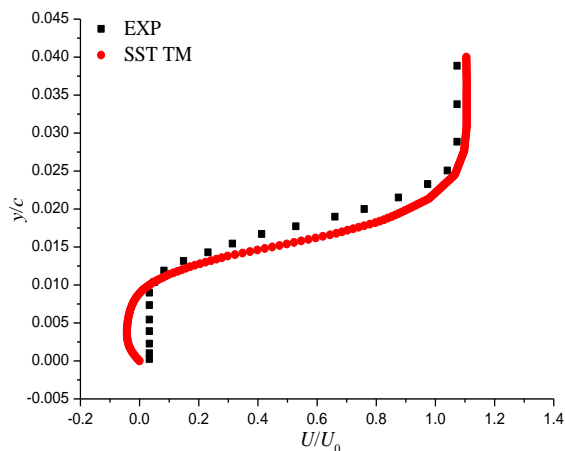
(b)



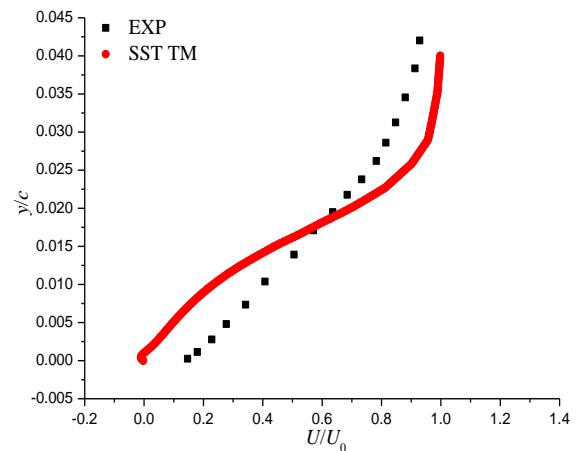
(c)



(d)

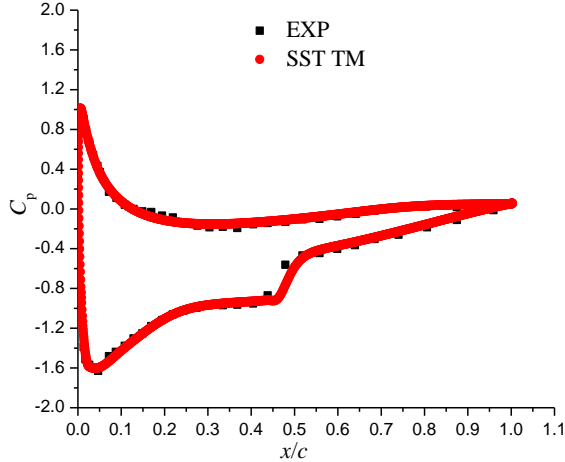


(e)

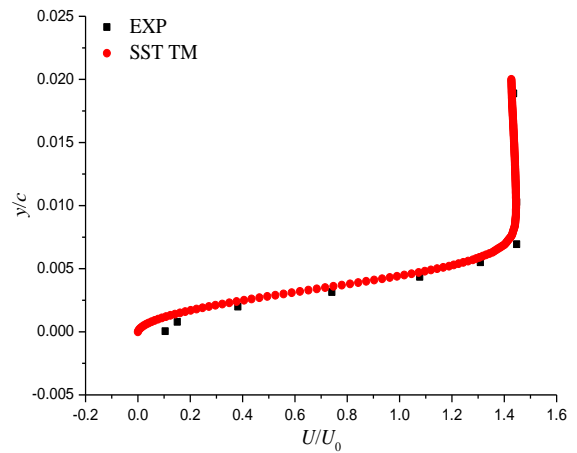


(f)

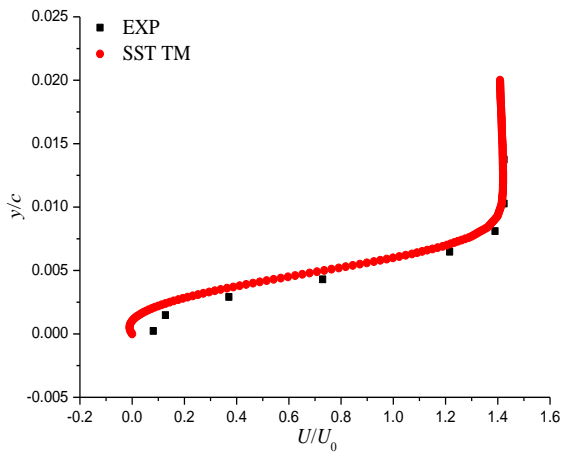
**Fig.2.10** Distributions of mean pressure and velocity profiles at  $0^\circ$ . (a) Pressure coefficient; Velocity profile at (b)  $x/c=0.43$ ; (c)  $x/c=0.51$ ; (d)  $x/c=0.60$ ; (e)  $x/c=0.73$ ; (f)  $x/c=0.87$ .



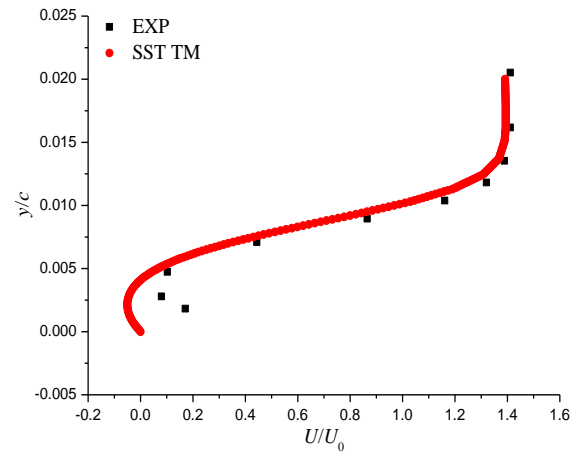
(a)



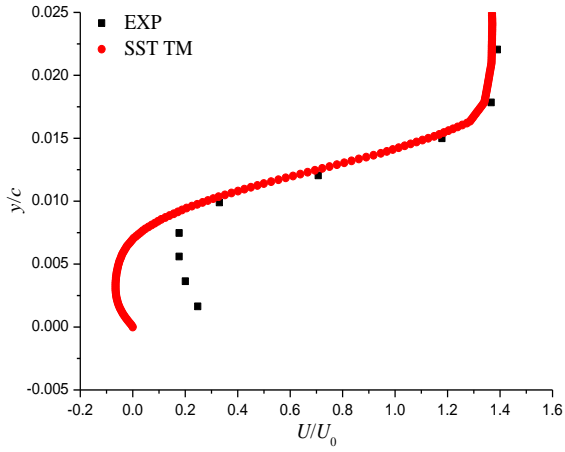
(b)



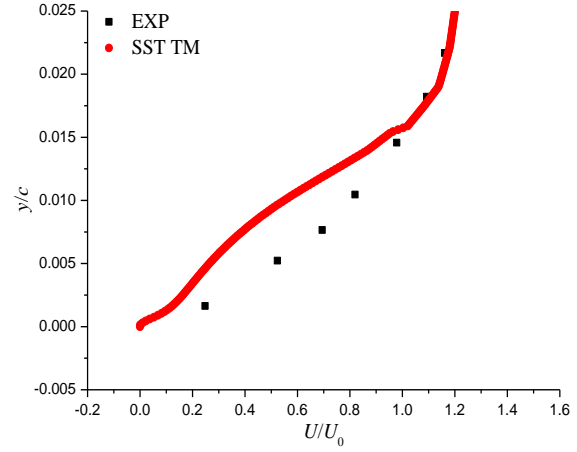
(c)



(d)

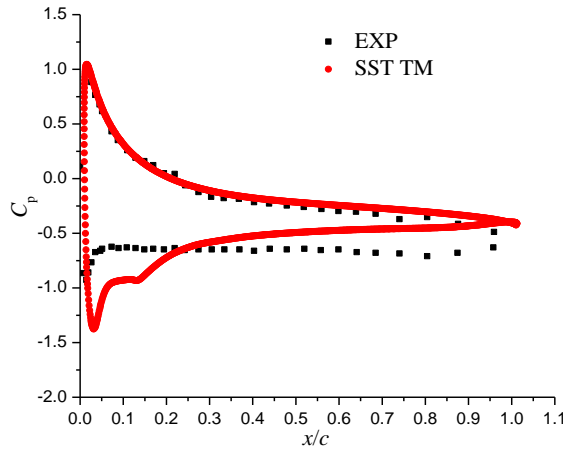


(e)

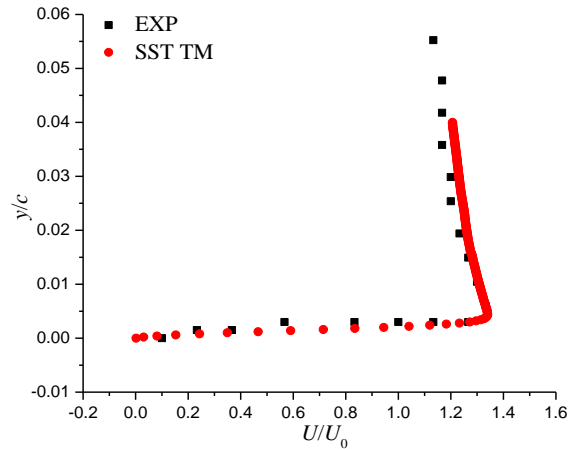


(f)

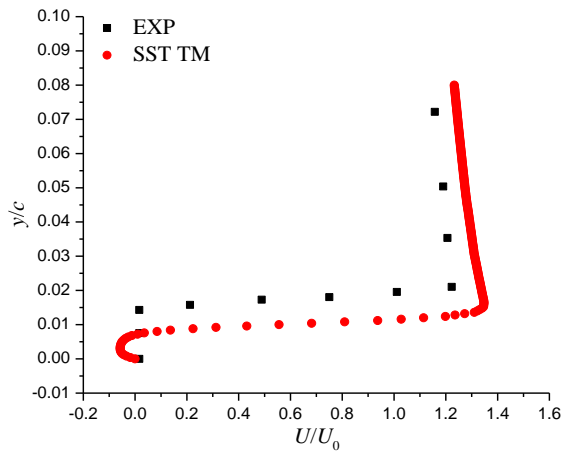
**Fig.2.11** Distributions of mean pressure and velocity profiles at  $5^\circ$ . (a) Pressure coefficient; Velocity profile at (b)  $x/c=0.20$ ; (c)  $x/c=0.24$ ; (d)  $x/c=0.32$ ; (e)  $x/c=0.40$ ; (f)  $x/c=0.52$ .



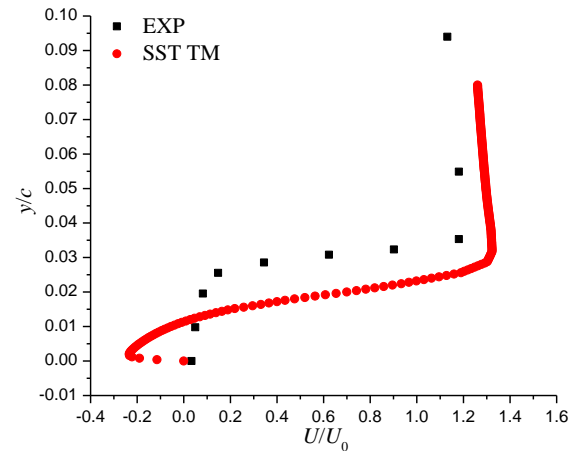
(a)



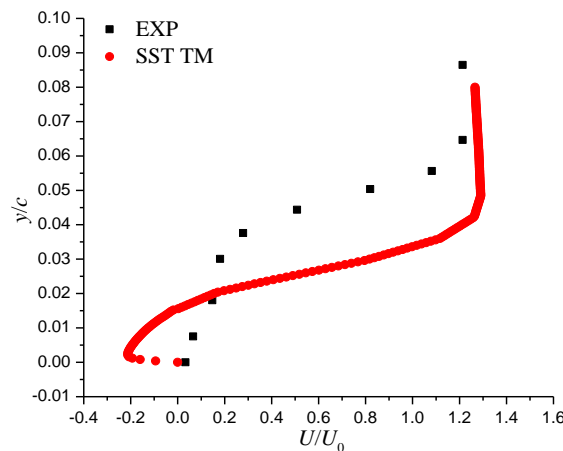
(b)



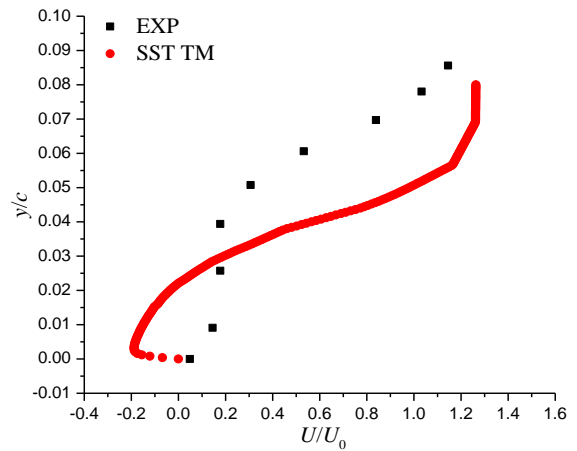
(c)



(d)



(e)



(f)

**Fig.2.12** Distributions of mean pressure and velocity profiles at  $15^\circ$ . (a) Pressure coefficient; Velocity profile at (b)  $x/c=0.04$ ; (c)  $x/c=0.10$ ; (d)  $x/c=0.15$ ; (e)  $x/c=0.19$ ; (f)  $x/c=0.24$ .

The predicted separation ( $X_s$ ), transition ( $X_t$ ) and reattachment ( $X_r$ ) points at various incidences are displayed in Table 2.3. The numerical results (NUM) are compared with the available experimental data. When the incidence is below  $10^\circ$ , the separation point is predicted slightly too early, while the transition and reattachment points are correctly located. At  $15^\circ$ , the transition is very close to the leading edge, which leads to larger uncertainties in the computational results, as shown by the velocity profiles in figure 2.12. However, the SST TM can still predict the separation point accurately.

The detailed flow structures near the wall region at four incidences are shown in figure 2.13, using the turbulent kinetic energy contours superimposed with the streamlines. As the incidence increases, the level of turbulent kinetic energy near the transition region becomes gradually higher. At  $0^\circ$ , the LSB is clearly visible both on the upper and lower surfaces. Then, it moves upstream with the increase of the incidence. At  $15^\circ$ , the LSB is not visible anymore near the leading edge, and the high level of TKE is obvious in the separated shear layer and the recirculation region.

**Table 2.3** Separation, transition and reattachment locations at various incidences

$\alpha$	$X_s$	$X_t$	$X_r$
$0^\circ$ (NUM)	0.48	0.76	0.90
$0^\circ$ (EXP)	0.50~0.54	0.77~0.84	0.84~0.92
$5^\circ$ (NUM)	0.22	0.44	0.52
$5^\circ$ (EXP)	0.23~0.26	0.42~0.46	0.50~0.52
$10^\circ$ (NUM)	0.08	0.22	0.29
$10^\circ$ (EXP)	0.08~0.10	0.21~0.23	0.26~0.29
$15^\circ$ (NUM)	0.04	0.135	--
$15^\circ$ (EXP)	0.04	0.180	--

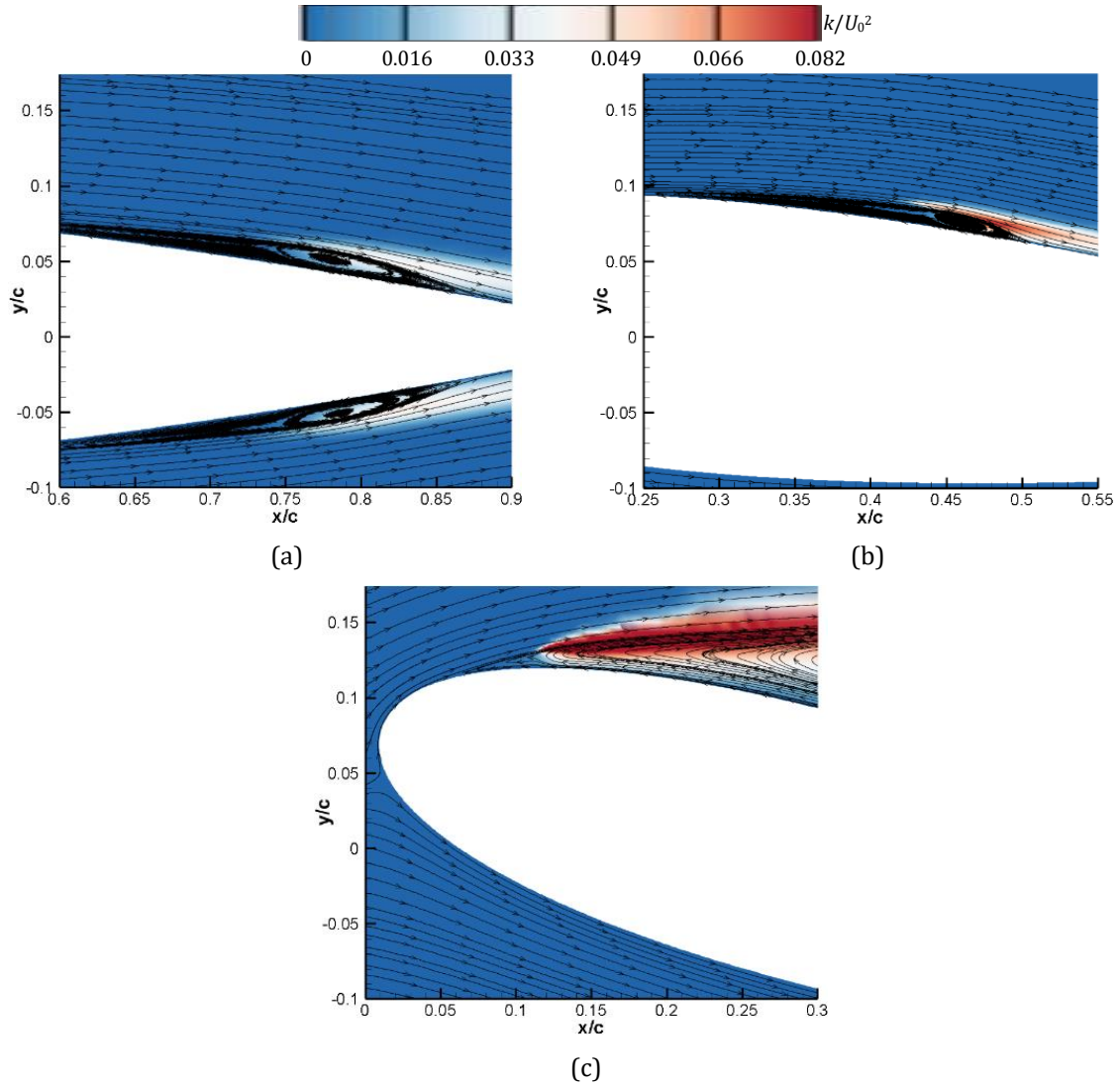


**Fig.2.13** Turbulent kinetic energy contours at different incidences. (a) 0°; (b) 5°; (c) 15°.

### 2.1.9 Effect of Reynolds number

Because it has a great impact on the transitional flows, the effect of Reynolds number is also considered in this work, at incidence of 10°. Calculations are performed at four different Reynolds numbers, namely  $2.5 \times 10^4$ ,  $5.0 \times 10^4$ ,  $2.0 \times 10^5$  and  $4.0 \times 10^5$ . With the increase of  $Re$ , the pressure difference between the upper and lower surface increases. Simultaneously, the wall shear stress also increases. At very low Reynolds number of  $2.5 \times 10^4$ , only the flow separation is observed. When the Reynold number increases up to  $5.0 \times 10^4$ , the separation and transition can be both detected, and the separation occurs a little bit earlier than for  $Re=2.5 \times 10^4$ . As the Reynolds number increases to the order of  $10^5$ , the complete transition process is shown clearly. Although the flow separation at  $Re=10^5$ ,  $2.0 \times 10^5$  and  $4.0 \times 10^5$  is almost the same, the transition and reattachment points move significantly upstream. At  $Re=4.0 \times 10^5$ , it is observed that the transition location is very close to the reattachment point, which is shown in figure 2.14b and 2.14d. In summary, when the Reynolds number is below  $5.0 \times 10^4$ , there is no reattachment point, and even no clear transition process is observed at  $2.5 \times 10^4$ . However, when  $Re$  becomes larger than  $1.0 \times 10^5$ , the transition and reattachment points move upstream, resulting in the reduction of LSB size. The detailed information about the separation, transition and reattachment

points for different Reynolds numbers is listed in Table 2.4.

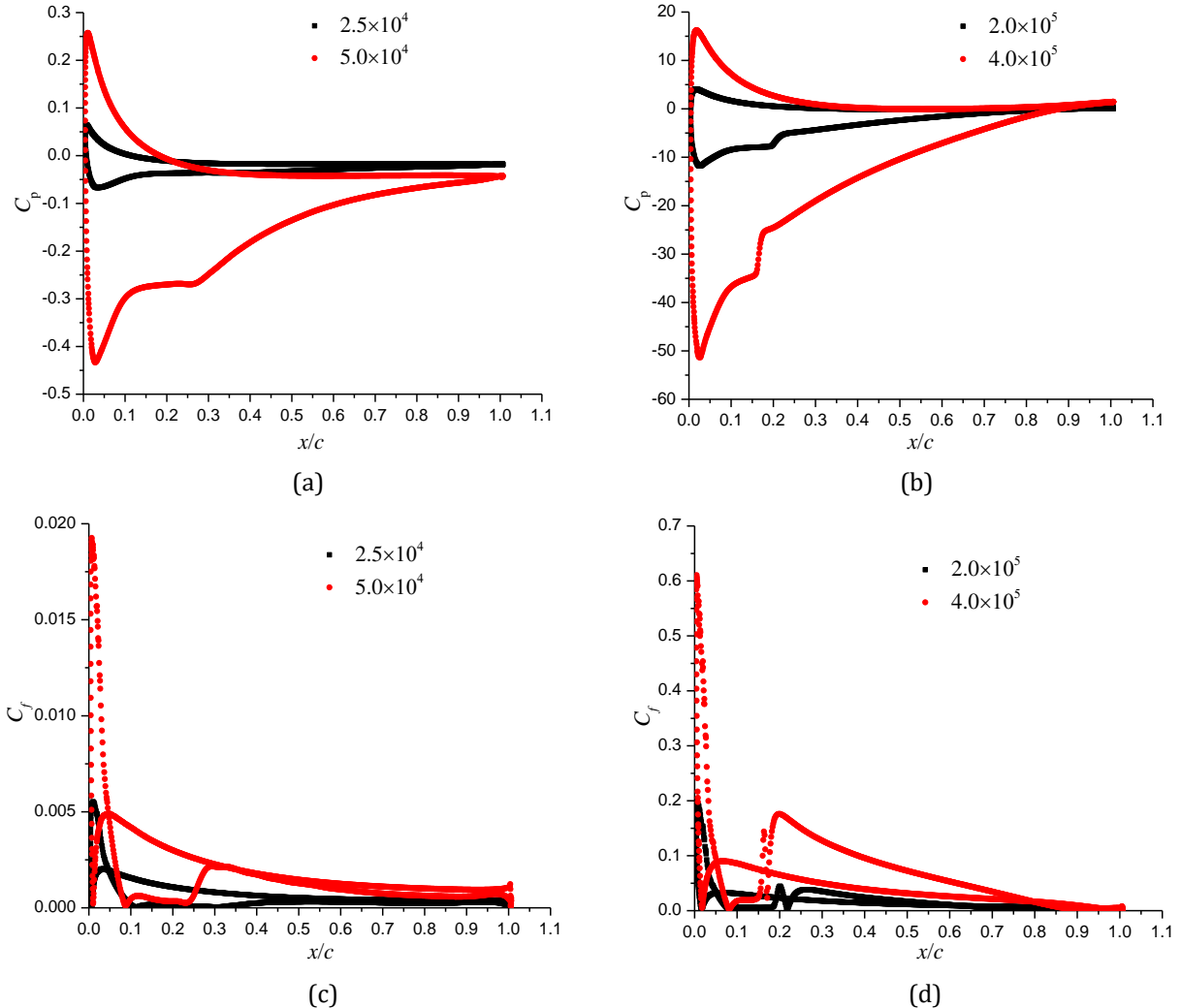


**Fig.2.14** Distributions of mean pressure and skin friction coefficients at different  $Re$ . (a) and (b) Pressure coefficients; (c) and (d) Skin friction coefficients.

**Table 2.4** Separation, transition and reattachment locations at different  $Re$

$Re$	$X_s$	$X_t$	$X_r$
$2.5 \times 10^4$	0.11	---	--
$5.0 \times 10^4$	0.09	0.23	--
$2.0 \times 10^5$	0.08	0.18	0.22
$4.0 \times 10^5$	0.08	0.14	0.17

In order to analyze the flow physics at different  $Re$ , the turbulent kinetic energy contours and the streamlines are shown in figure 2.15. At  $2.5 \times 10^4$  and  $5.0 \times 10^4$ , because of the separated shear layer near the leading edge, a large vortex structure attached to the upper surface is observed, but the size is reduced at  $5.0 \times 10^4$ . This pattern, which is a classical signature of trailing edge stall on a thick, conventional foil at Reynolds number below  $5.0 \times 10^4$ , is also reported by Winslow et al. [85]. Furthermore, in figures 2.9c, 2.15c and 2.15d, the size of LSB is reduced gradually, both in length and height. The transition region becomes smaller with the increase of the Reynolds number, as the transition and

reattachment points move upstream, especially at  $4.0 \times 10^5$ .

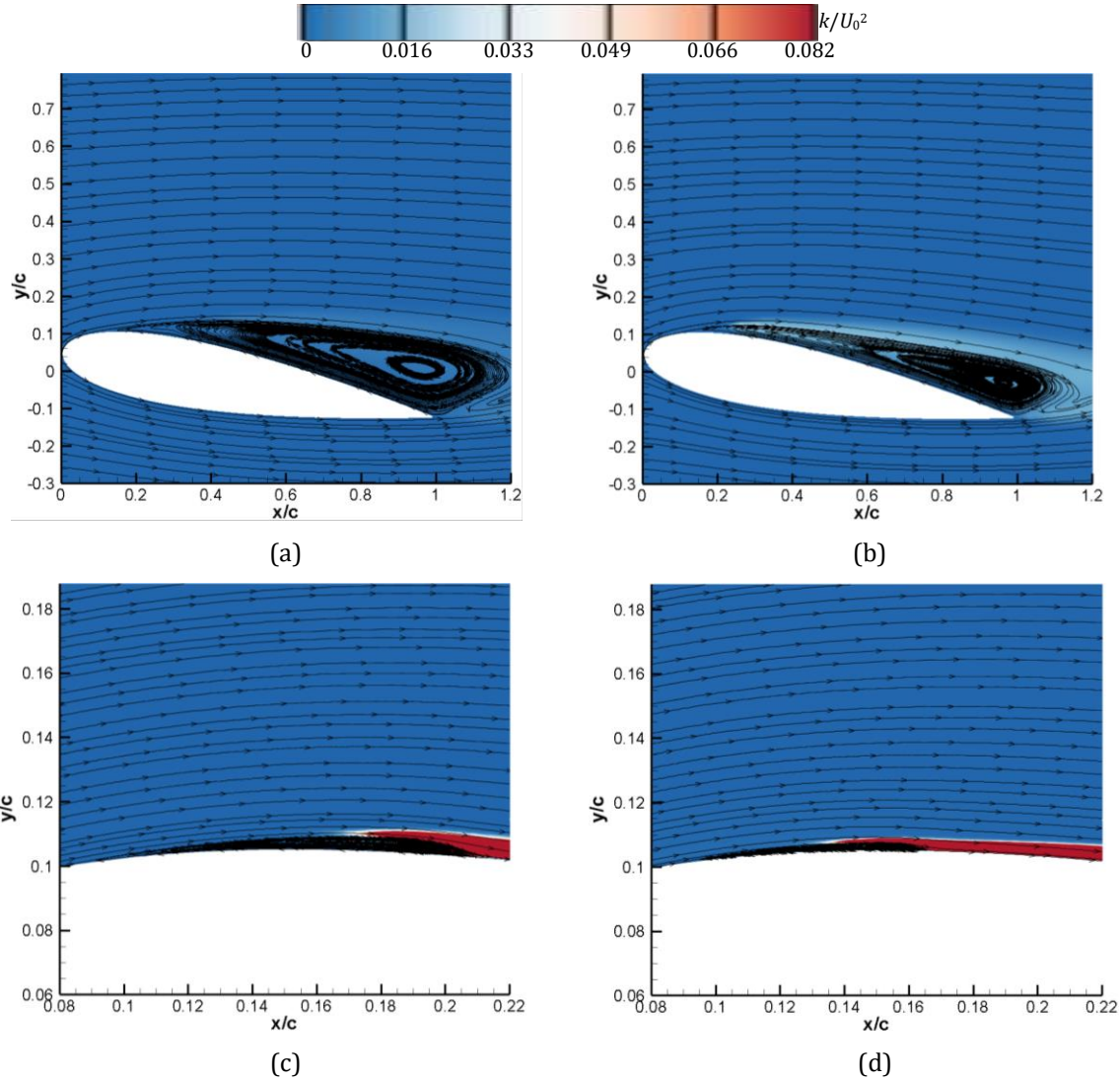


**Fig.2.15** Distributions of turbulent kinetic energy at different  $Re$ . (a)  $2.5 \times 10^4$ ; (b)  $5.0 \times 10^4$ ; (c)  $2.0 \times 10^5$ ; (d)  $4.0 \times 10^5$ .

### 2.1.10 Conclusions

In this section, the SST  $\gamma - \widetilde{Re}_{\theta t}$  transition model was firstly calibrated, in terms of the mesh resolution, inflow turbulence conditions, correlations and parameter in the transition model, and then it is applied to the transitional flows over a NACA0018 airfoil, to check the influence of the turbulence model, the angle of attack, and the Reynolds number. The main conclusions are listed below:

(1) Both the structured and unstructured meshes can capture the same transition location, but the little difference of predicted pressure in the laminar flow region is the main contributor to the performance difference. To get a better prediction of the transition, the mesh should be refined not only in the normal direction, but also in the streamwise direction.

(2) Increasing the inflow turbulence intensity makes the separation point move downstream, and the transition and reattachment locations shift upstream, which indicates that the length of LSB decreases. Compared with the separation and transition

points, the reattachment location is more easily affected by the inflow turbulent conditions. Simultaneously, the effect of the turbulence intensity on the transition is more evident than the eddy viscosity ratio.

(3) The results are influenced by the modification of the correlation  $Re_{\theta t}$  with NZPG, but this effect can be omitted due to the offset by the decay of inlet turbulence intensity. Besides, the separation, transition and reattachment points move downstream if the correlations of  $F_{length}$  and  $Re_{\theta c}$  are modified at the same time. Then, with the increase of the parameter  $S_1$  in the transition model, the length of LSB is reduced, because of the motion of the separation, transition and reattachment points.

(4) The SST  $\gamma - \widetilde{Re}_{\theta t}$  transition model demonstrates its superiority in predicting the boundary-layer transition, followed by the RSM model, which can also detect the existence of the LSB. Conversely, the SST  $k-\omega$  model only resolves the fully turbulent flow.

(5) By comparison of mean velocity profiles and transition locations, it is observed that the SST  $\gamma - \widetilde{Re}_{\theta t}$  transition model has a good performance before the reattachment when the incidence is below  $10^\circ$ . A large discrepancy is systematically obtained in the fully turbulent boundary layer. Furthermore, at  $15^\circ$ , because of both the short transition region and the vortex shedding after the transition, capturing these flow features becomes more challenging for the RANS-based transition model.

(6) When the Reynolds number increases, the length of the LSB shortens considerably and the transition point is very close to the reattachment at relatively high-Reynolds-number condition. Moreover, as the Reynolds number is below  $5.0 \times 10^4$ , there is a large-scale vortex attached to the foil surface and the transition becomes less obvious with the further reduction of Reynolds number.

## 2.2 APPLICATION OF THE SST $\gamma - \widetilde{Re}_{\theta t}$ MODEL TO A CYCLOIDAL ROTOR

### 2.2.1 Introduction

After the optimization on a single stationary airfoil, the modified SST  $\gamma - \widetilde{Re}_{\theta t}$  transition model is directly applied to a two-bladed cycloidal rotor, to show the unsteady vortical flows and transition event at two advance coefficients. Initially, the influence of the mesh arrangement, inlet turbulence condition, time-step and numerical convergence is evaluated. Then, the influence of the turbulence model is assessed. Afterwards, the numerical results are compared with the experimental measurements, including the velocity and vorticity fields. Finally, the transition predicted by the original SST  $k-\omega$  model and SST  $\gamma - \widetilde{Re}_{\theta t}$  transition model is compared.

### 2.2.2 Geometry parameters, meshing and numerical setup

The two-dimensional two-bladed cycloidal rotor is adopted in the present work and the main geometrical parameters are listed in table 2.5. It should be noted that the blade operates with a sinusoidal motion and the pitching amplitude  $\theta_{amp}$  is constant with a value of  $35^\circ$ . The initial position of azimuthal angle  $\psi$  is from negative X axis, while the phase angle changes from  $\psi=90^\circ$  in anticlockwise direction. When the blades move in clockwise direction, bringing about the continuous generation of propulsive force in negative X axis and lift in positive Y axis, which is shown in figure 1.3b. In this work, the flow structures are mainly investigated at  $\lambda=0.52$  and  $0.73$ . The corresponding Reynolds number defined in Table 2.5 [2] are  $3.56 \times 10^4$  and  $3.91 \times 10^4$  respectively.

**Table 2.5** Main geometrical parameters of the cycloidal rotor

Blade number ( $N_b$ )	2
Inlet velocity ( $U_0/(m/s)$ )	5, 7
Blade chord ( $c/m$ )	0.0495
Blade profile	NACA0015
Rotor radius ( $R/m$ )	0.076
Rotating speed ( $n/(r/min)$ )	1200
Pitching pivot location ( $\% \times c$ )	25
Blade pitching kinematics	$\theta_A = \theta_{amp} \sin(\psi + \Phi)$
Advance coefficient ( $\lambda$ )	$\lambda = U_0 / \omega R$
Reynolds number ( $Re$ )	$Re = \sqrt{U_0^2 + (\omega R)^2 c / \nu}$

The rectangular computational domain is shown in figure 2.16a, which has an extension of  $10c$  for the inlet section and  $30c$  for the outlet region, based on the rotating centre. The top-wall and bottom-wall have the same distance of  $10c$ . In figure 2.16b, the sliding mesh technique is employed to control the blade movement by creating three periodic interfaces: two interfaces between two blades and two small rotating circles, and one interface between a rotating circle with large radius and outer stationary part. The two small rotating circles covering the blades individually have the radius of  $c$  and they have the rotating and pitching movements simultaneously. The large rotating circle, which has a radius of  $3c$ , only has the rotating motion.

The particle image velocimetry (PIV) measurements conducted in a closed-section wind tunnel were used to validate our simulations, in terms of the velocity and vorticity contours. The wind tunnel has a maximal velocity speed of 45m/s and the turbulence level is about 0.25%. The lift, propulsive force and shaft torque of the cycloidal rotor were measured by a precise 3-component wind tunnel force balance. The information of the experimental setup and the measurement precision accuracy is included in reference [86].

The mesh distribution is critical to the laminar-turbulence transition, massive flow separation and unsteady wake. In the commercial code STARCCM +, the hybrid mesh, including the trimmed cell in the external region and prism layer cell near the blade surface, is employed in this work. To capture more scales near the blade and in the wake region, a cone with sufficient cells is also employed, as is presented in figure 2.16a. Table 2.6 shows the mesh distributions in two rotating parts covering two blades and near the blade surface at  $\lambda=0.52$ . The aspect ratio of 1.15 and prism layer thickness of  $2 \times 10^{-3}$  m are unchanged (shown in figure 2.16c) and the mesh arrangement near the wall depends on the number of prism layer  $n_p$  (from case 1 to case 4). In all tested cases, the target size has the same value with minimum size because of its weak effect. Case 2, 5 and 6 are used to check the influence of streamwise mesh distribution by changing the target size  $T_f$  and minimum size  $M_f$  near the blade surface while the effect of mesh in two rotating parts (RP) are presented by case 2, 7 and 8. The time-averaged lift  $F_L$  and propulsive force  $F_{PF}$  of the rotating system in last five rotations for different sets of meshes are compared with the available experiments [86]. It can be seen that there is a significant change of lift and propulsive force when the prism layer increases to 70 and 75. In order to explain this particular event, the instantaneous vertical force coefficient  $C_{VF}$  ( $C_{VF}=F_{VF}/(0.5*\rho*U_0^2*c)$ , where  $F_{VF}$  is the vertical force) and propulsive force coefficient  $C_{PF}$  ( $C_{PF}=F_{PF}/(0.5*\rho*U_0^2*c)$ , where  $F_{PF}$  is the propulsive force) of one blade in the last rotation is plotted in figure 2.17. It seems that the discrepancy of the globe performance obtained by different meshes becomes larger as the number of prism layer increases. Therefore, an instant, at  $\psi=140^\circ$  for right blade, is selected to study the detailed near-wall flow structures. The spanwise vorticity contours of different tested cases are presented in figure 2.18 and the results show that there are massive vorticity shedding on both sides of the blade. The distributions of vorticity for case 1 and 2 are almost the same, but it varies considerably for case 3 and 4, especially on the right surface. In figure 2.19, the velocity profiles on the right side at four locations are plotted and it shows that the results keep nearly same for case 1 and 2, but a little difference at the blade trailing edge where the flow separation occurs. However, the velocity profiles of case 3 and 4 are totally different, due to the vorticity distributions in figure 2.18. There are several reasons for that: (1) there is a little distortion of near-wall meshes in case 3 and 4; (2) this is presumably induced by the large value of specific turbulence frequency  $\omega$ , which scales with the first grid point height [87]; (3) Very small  $y^+$  ( $y^+=yu_\tau/\nu$ , where  $y$  is the distance to the wall,  $u_\tau$  is the friction velocity and  $\nu$  is the kinematic viscosity) leads to the SST blending function switching to  $k-\epsilon$  in the boundary layer, which is also observed in a compressor tested case [87]. Furthermore, by the comparison of meshes in case 2, 5 and 6, it can be seen that increasing the cells in the streamwise direction has a better performance. Then, the results of case 2, 7 and 8 show that further reduction of the mesh size in two rotating parts has a little deterioration of performance, possibly due to the more resolved vortical flows. In conclusion, according to the above information, the mesh of case 7 is applied directly to all the following simulations.

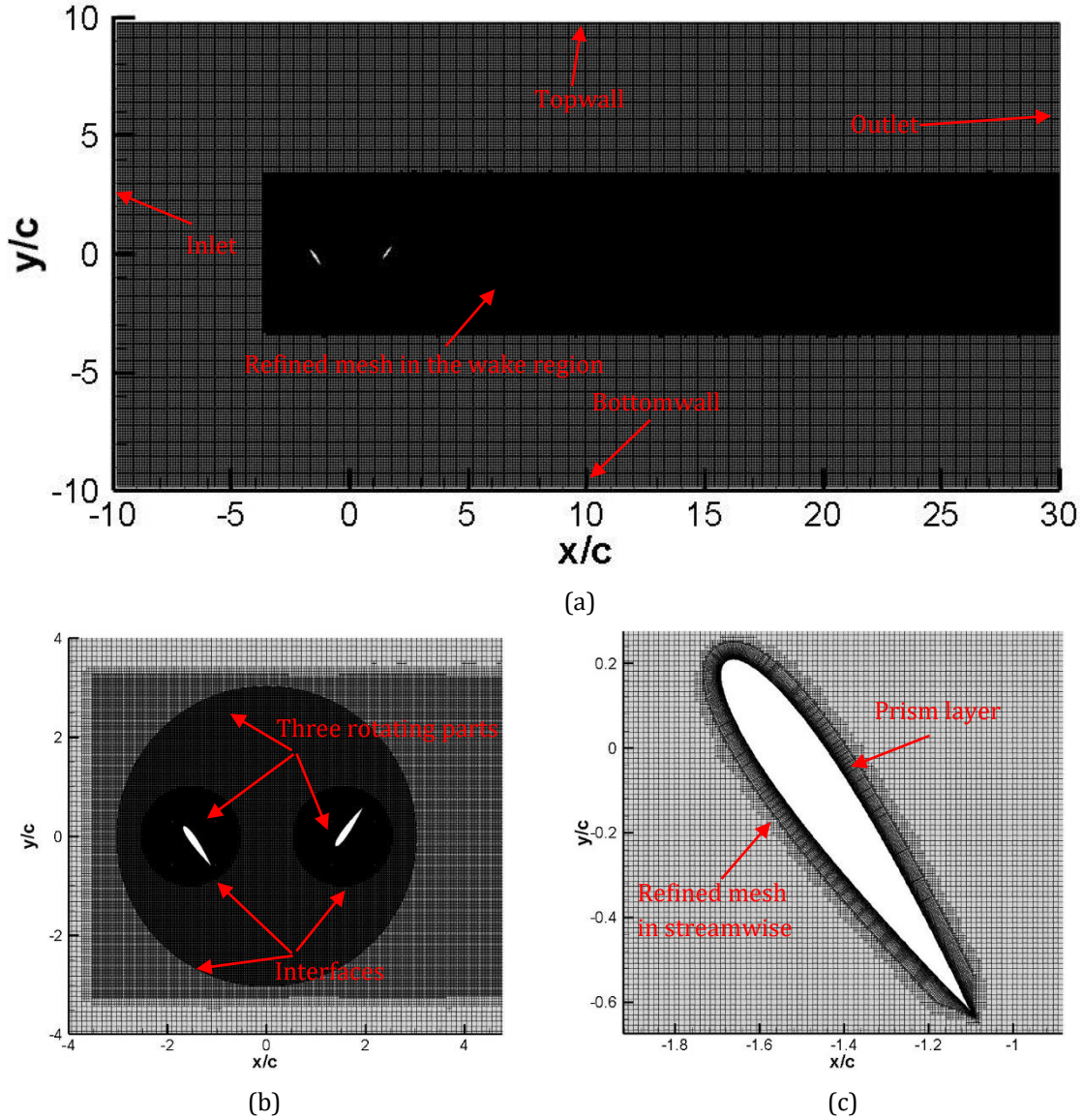


**Fig.2.16** Computational configuration and mesh distributions. (a) Mesh in computational domain; (b) Mesh in three rotating parts; (c) Mesh near the blade surface.

**Table 2.6** Mesh distributions of tested cases

	$T_{RP}$ (m)	$M_{RP}$ (m)	$T_f$ (m)	$M_f$ (m)	$n_p$	$y$ (m)	$F_L$ (N)	$F_{PF}$ (N)
Case 1	$7 \times 10^{-7}$	$7 \times 10^{-7}$	$2 \times 10^{-7}$	$2 \times 10^{-7}$	60	$6.8 \times 10^{-8}$	0.452	0.241
Case 2	$7 \times 10^{-7}$	$7 \times 10^{-7}$	$2 \times 10^{-7}$	$2 \times 10^{-7}$	65	$3.4 \times 10^{-8}$	0.489	0.245
Case 3	$7 \times 10^{-7}$	$7 \times 10^{-7}$	$2 \times 10^{-7}$	$2 \times 10^{-7}$	70	$1.7 \times 10^{-8}$	0.570	0.245
Case 4	$7 \times 10^{-7}$	$7 \times 10^{-7}$	$2 \times 10^{-7}$	$2 \times 10^{-7}$	75	$8.4 \times 10^{-9}$	0.716	0.217
Case 5	$7 \times 10^{-7}$	$7 \times 10^{-7}$	$8 \times 10^{-7}$	$8 \times 10^{-7}$	65	$3.4 \times 10^{-8}$	0.528	0.207
Case 6	$7 \times 10^{-7}$	$7 \times 10^{-7}$	$5 \times 10^{-7}$	$5 \times 10^{-7}$	65	$3.4 \times 10^{-8}$	0.507	0.248
Case 7	$6 \times 10^{-7}$	$6 \times 10^{-7}$	$2 \times 10^{-7}$	$2 \times 10^{-7}$	65	$3.4 \times 10^{-8}$	0.494	0.247
Case 8	$5 \times 10^{-7}$	$5 \times 10^{-7}$	$2 \times 10^{-7}$	$2 \times 10^{-7}$	65	$3.4 \times 10^{-8}$	0.473	0.246
EXP	--	--	--	--	--	--	0.490	0.260

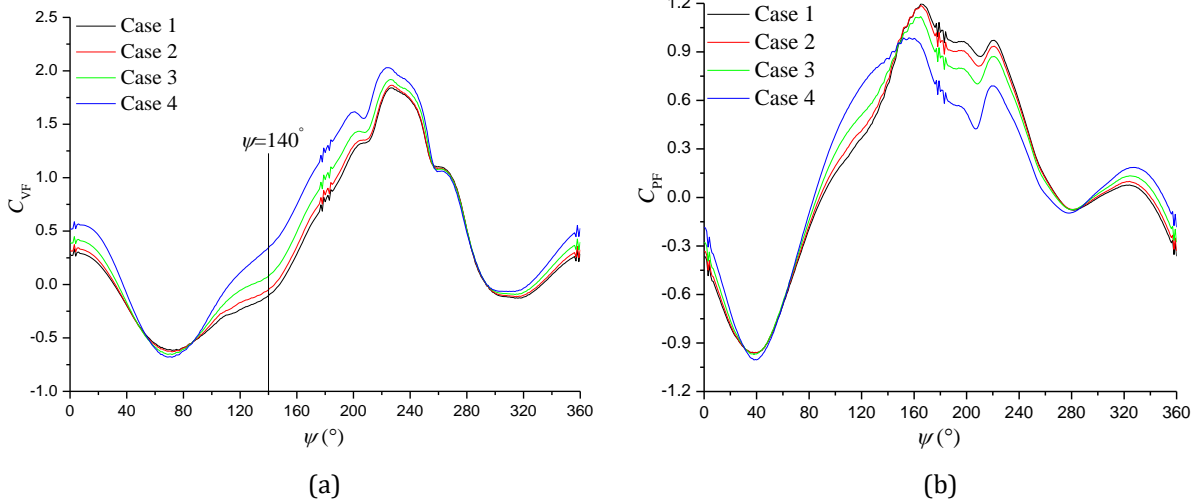


**Fig.2.17** Instantaneous performance of one blade in a revolution. (a) Vertical force coefficient; (b) Propulsive force coefficient.

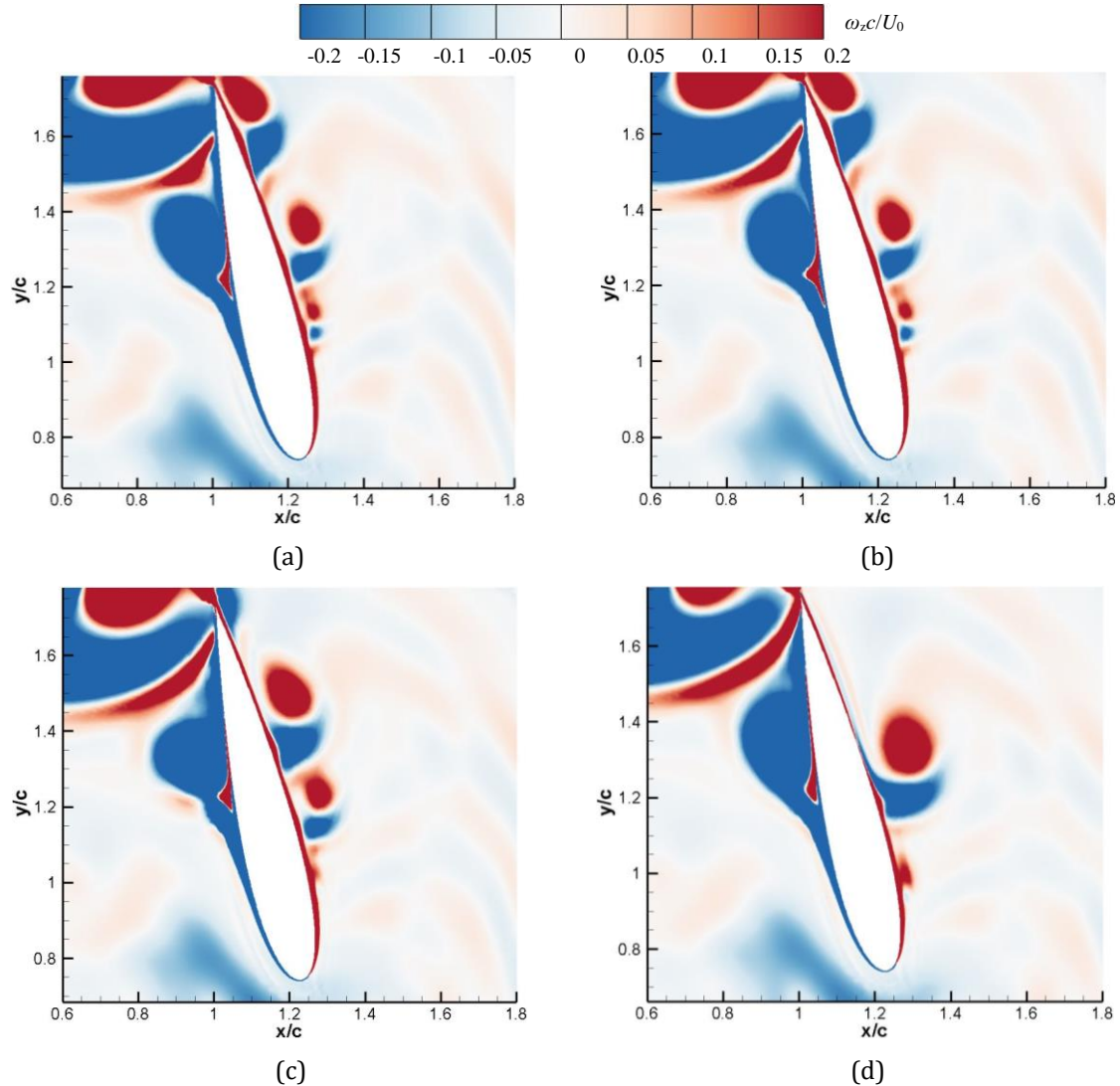


**Fig.2.18** Spanwise vorticity contours at  $\psi=140^\circ$ . (a) Case 1; (b) Case 2; (c) Case 3; (d) Case 4.

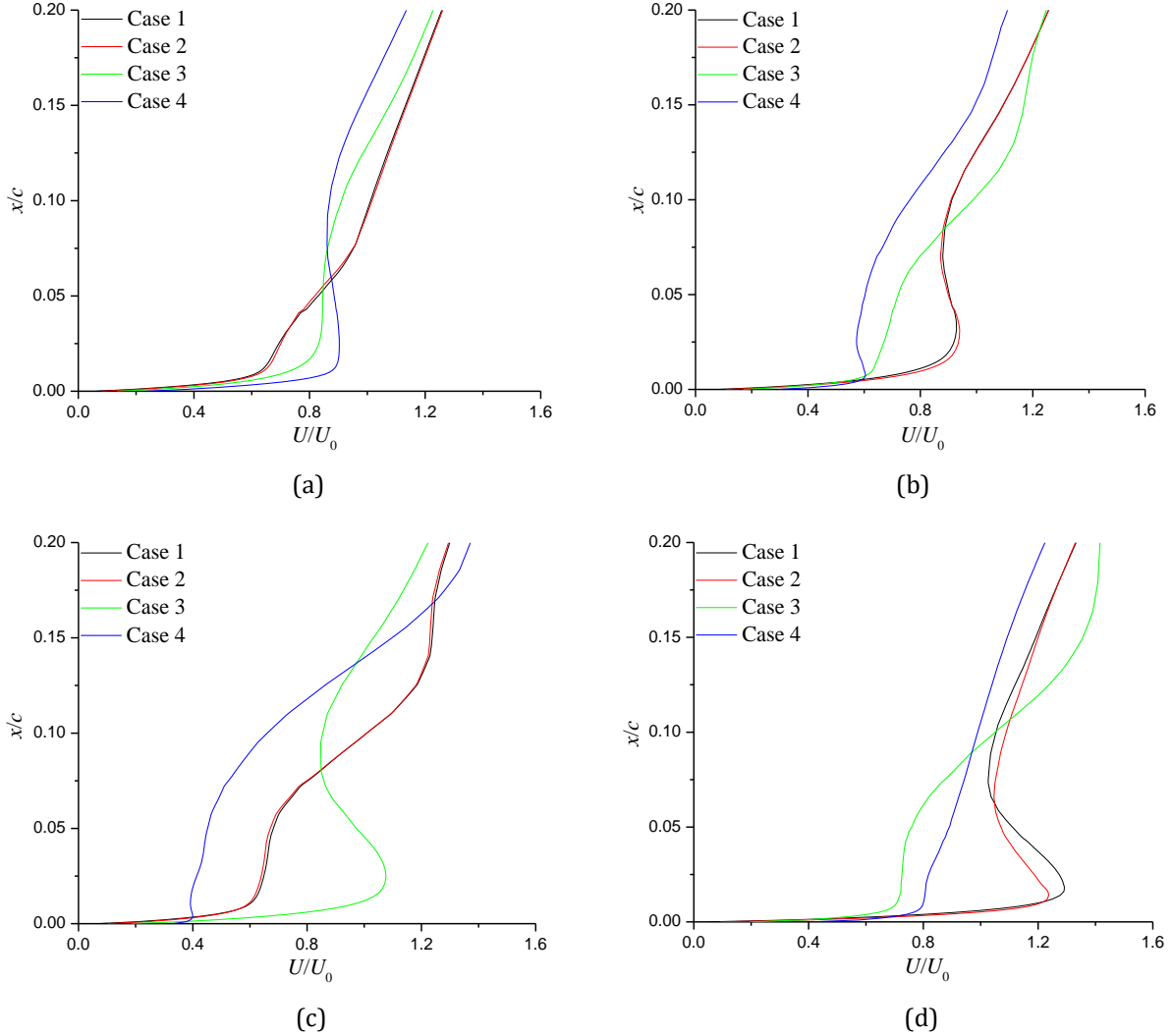


**Fig.2.19** Velocity profiles at  $\psi=140^\circ$ . (a)  $y/c=0.4$ ; (b)  $y/c=0.5$ ; (c)  $y/c=0.6$ ; (d)  $y/c=0.8$ .

When given the boundary conditions, the classical one, velocity imposed on the inlet section and pressure assigned on the outlet part, is adopted to the present computations. The top-wall and bottom-wall are set as symmetry planes to eliminate the sidewall effect. The blade surface is regarded as no-slip wall condition. The finite-volume-based segregated flow solver is utilized to simulate the unsteady vortical flows. In the simulations, the second-order upwind spatial discretization is used for the convective flux and the second-order central discretization is employed to the diffusion term. The previous studies show that the freestream turbulence level has great impact on the transition [15-16]. In this work, the inflow turbulence intensity of 0.25% is chosen, which is consistent with the experimental measurement [86]. Simultaneously, the influence of eddy viscosity ratio  $\mu_t/\mu$  ( $\mu_t$  is the eddy viscosity and  $\mu$  is the dynamic viscosity of the working fluid) is tested. In figure 2.20, on basis of the instantaneous vertical force and propulsive force coefficients in the last revolution, it seems that the results stay the same as the eddy viscosity ratio changes from 10 to 0.01, but a little difference when it decreases to 0.001. It is reasonable to choose a low value of eddy viscosity ratio because of relatively low Reynolds number. Gauthier et al. [88] and Kinsey and Dumars [89] analyzed the unsteady flows around tandem oscillating hydrofoils of hydrokinetic turbine, with the eddy viscosity ratio of 0.001 at Reynolds number  $5 \times 10^5$ . In addition, the

propulsive force of the cycloidal rotor has a slight improvement when  $\mu_t/\mu=0.001$  is selected.

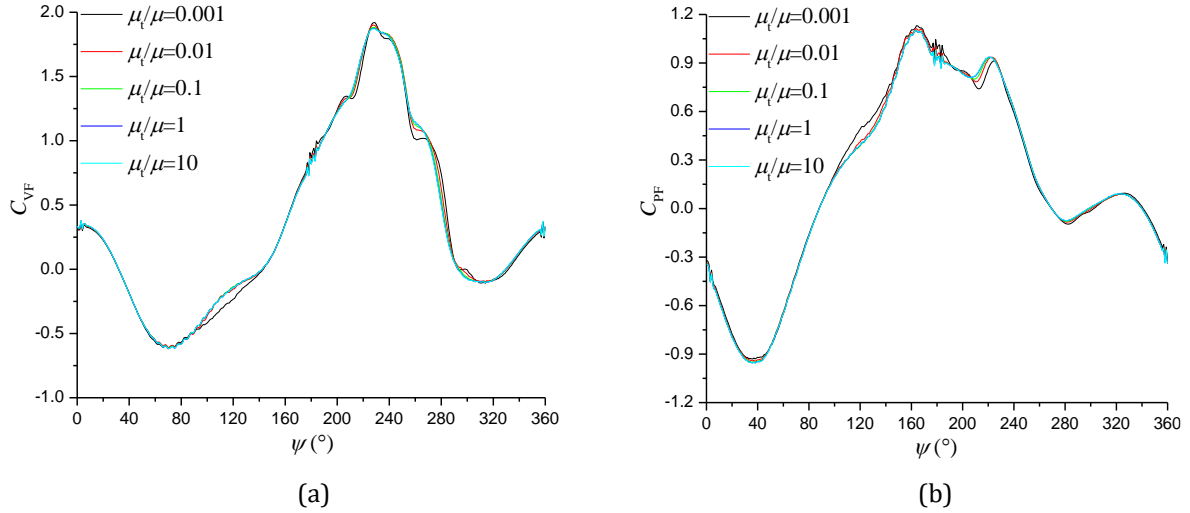


**Fig.2.20** Instantaneous performance of one blade in a revolution. (a) Vertical force coefficient; (b) Propulsive force coefficient.

The time-step, which has close relationship with the simulation stability, has also remarkable influence on the numerical accuracy. The instantaneous vertical force and propulsive force coefficients of a single blade in the last cycle are displayed in figure 2.21. Compared with the smallest one, using a relatively large value of time-step leads to a large discrepancy of performance in some regions, for examples, vertical force coefficient at  $280^\circ \sim 340^\circ$  and propulsive force coefficient at  $160^\circ \sim 220^\circ$ . However, when the time-step is  $0.5^\circ$ , there are some large flow oscillations and the globe performance has a slight decrease because of the more complicated vortical flows. Therefore, the time-step of  $1^\circ$  is adopted with the consideration of the computational resources and numerical stability.

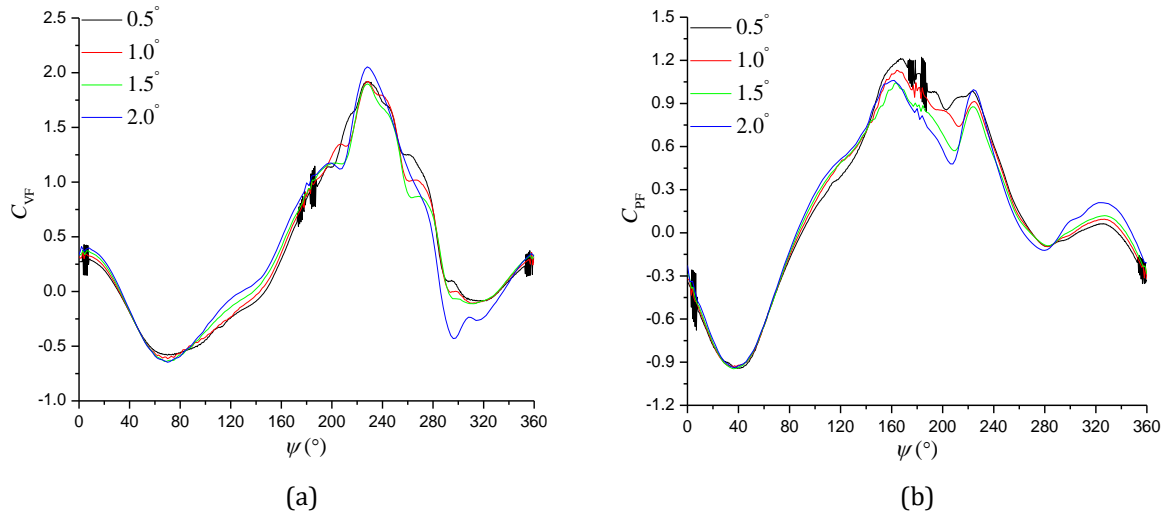


**Fig.2.21** Instantaneous performance of one blade in a revolution. (a) Vertical force coefficient; (b) Propulsive force coefficient.

The selection of convergence target is also essential to the numerical accuracy. The effect of different convergence-iteration loops on the performance of single blade is displayed in figure 2.22. It is observed that the iteration loop of 30 has an

overprediction/underprediction of the instantaneous performance in some regions, for instances, at  $\psi=100^\circ$ - $140^\circ$  and  $\psi=160^\circ$ - $220^\circ$ . Then, if the iteration loop reaches to a value of 50, the convergence target has no evident influence on the results. Thus, the combination of  $10^{-4}$ -50 is adopted in all the cases.

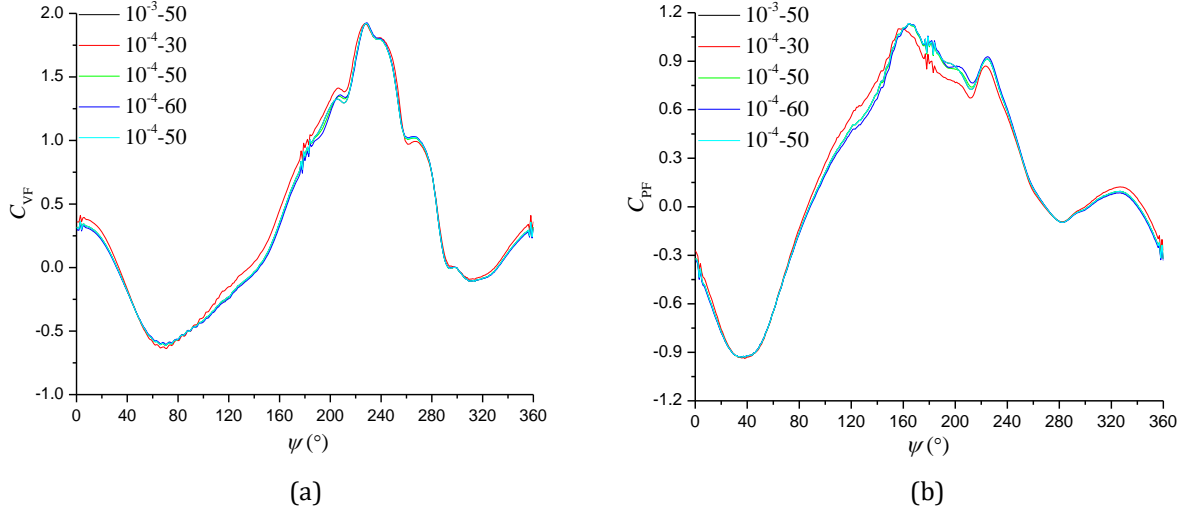


**Fig.2.22** Instantaneous performance of one blade in a revolution. (a) Vertical force coefficient; (b) Propulsive force coefficient.

The other points that should be paid attention to are the use of wall function and numerical convergence. The all  $y^+$  wall treatment is used in the current work, for the reason that it combines the low  $y^+$  wall treatment for the fine mesh and high  $y^+$  wall treatment for the coarse mesh. In addition, it also has reasonable answers for intermediate mesh which falls within the buffer region of the boundary layer. As a consequence, it is suitable for a wide range of near-wall mesh densities. Actually, it proves that there is no distinction in performance achieved by low  $y^+$  and all  $y^+$  wall treatments. Moreover, the maximal  $y^+$  does not exceed the value of 0.5 at any locations in a rotating cycle. What is more, in unsteady computations, 15 rotations are necessary to get the periodic results, as is shown in figure 2.23. Both the vertical force and propulsive force coefficients in last 5 rotations show no difference.

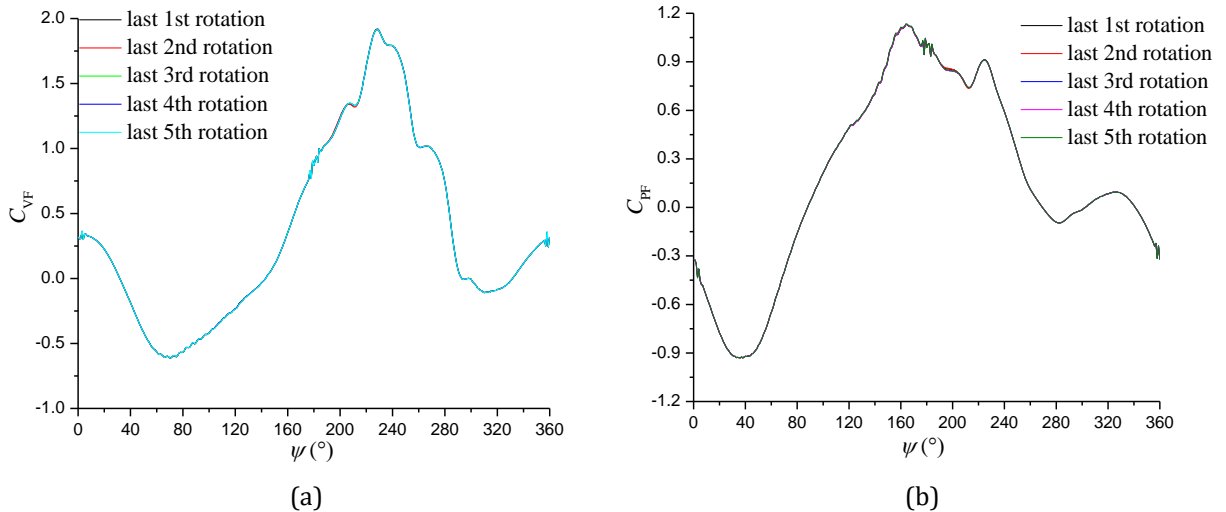


**Fig.2.23** Instantaneous performance of one blade in last 5 cycles. (a) Vertical force coefficient; (b) Propulsive force coefficient.

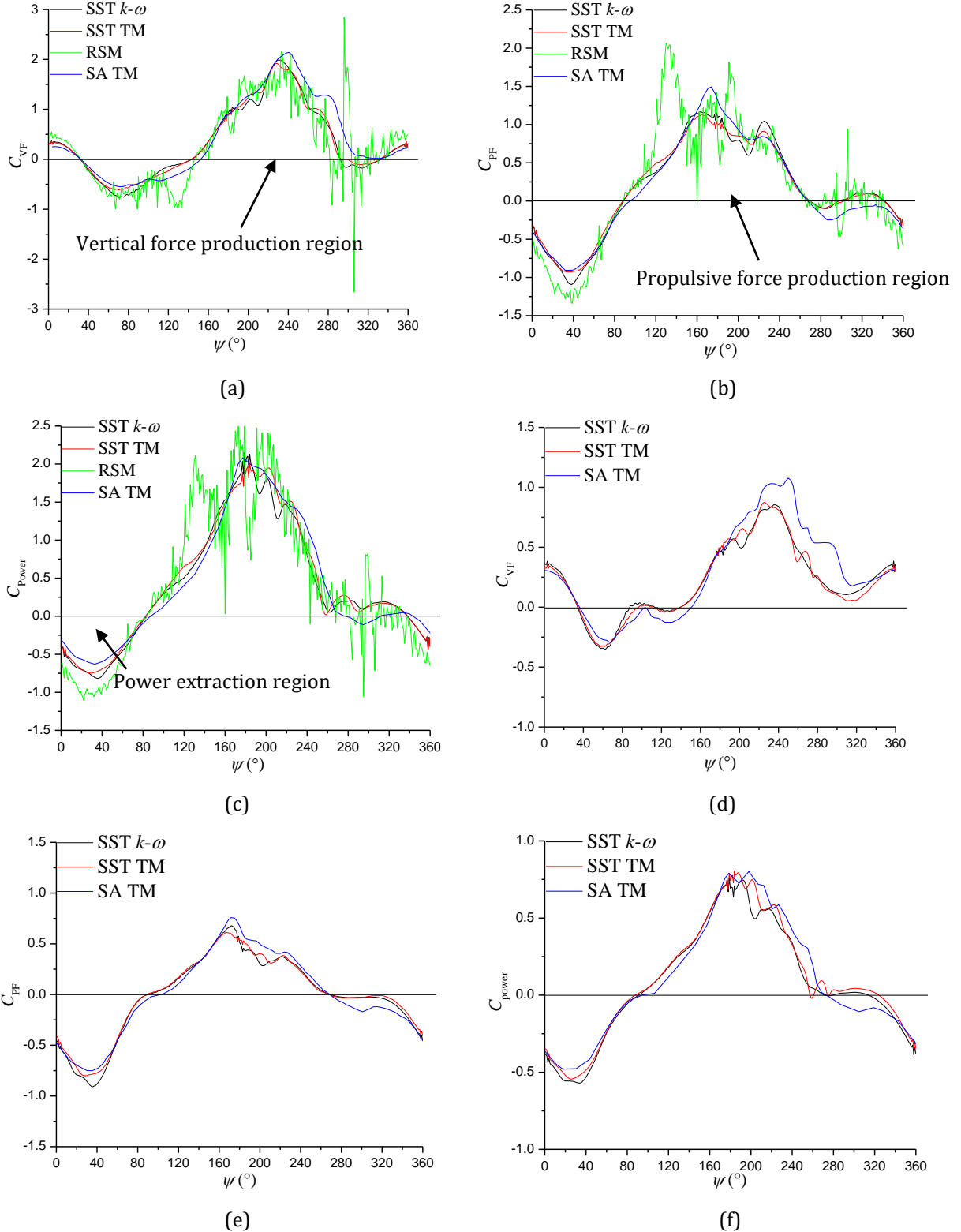
### 2.2.3 Analysis of unsteady vortical flows

The computational results, involving the time-averaged lift, propulsive force, power and calculated efficiency of the rotating system, are displayed in Table 2.7 for different turbulence models, at two  $\lambda$ . The efficiency is defined as  $\eta = (F_x \times U_0) / P$  ( $F_x$  is propulsive force and  $P$  is the power). At  $\lambda=0.52$ , the lift, propulsive force and efficiency obtained by SST  $\gamma$ - $Re_{\theta t}$  transition model (SST TM) are very close to the experiments. The power predicted by different turbulence models is always lower than the experimental measurement, largely induced by the neglect of the power-consumption of the shaft and other mechanical components. In addition, the Reynolds stress model (RSM) underpredicts the lift while it overpredicts the propulsive force. Then, when  $\lambda$  is 0.73, both the SST  $k-\omega$  model and SST TM underpredict the propulsive force because of its small value, but the power and efficiency obtained by SST TM has relatively small discrepancy compared with the experiments.

The instantaneous vertical force, propulsive force and power coefficients ( $C_{\text{power}} = P / (0.5 * \rho * U_0^3 * c)$ ) of single blade for three turbulence models, namely SST  $k-\omega$  model, SST TM and RSM, are plotted in figure 2.24 at two  $\lambda$ . The performance obtained by RSM is only presented at  $\lambda=0.52$  and the results show a noticeable fluctuation, which is owing to the disordered flow structures caused by resolving more equations in RSM with fine mesh and small timestep. The present work is also compared with the computational results using SA  $\gamma$ - $Re_{\theta t}$  transition model (SA TM) [86]. At two  $\lambda$ , it is observed that the large difference of the performance occurs at the lower half cycle when the blade is undergoing the advancing side, which may be due to the choice of turbulence model and the numerical solver. The critical locations where the values of forces and power have the transition, are listed in table 2.8 for different turbulence models. It concludes that increasing  $\lambda$  has no obvious effect on the force production regions, but has little influence on the peaks of these variables. Besides, the influence of turbulence model on the performance of single blade is also not obvious.

**Table 2.7** Results of different turbulence models

$\lambda=0.52$	$F_L$ (N)	$F_{PF}$ (N)	$P$ (W)	$\eta$ (%)
Laminar model	0.574	0.181	2.517	35.96
Spalart-Allmaras (SA) model	0.485	0.187	2.032	46.01
Realizable $k-\epsilon$ model	0.588	0.234	2.299	50.89
SST $k-\omega$ model	0.475	0.236	2.823	41.80
SST TM	0.494	0.247	3.136	39.38
RSM	0.469	0.306	3.408	44.89
EXP	0.49	0.26	3.55	36.6
$\lambda=0.73$				
SST $k-\omega$ model	0.619	-0.0566	1.44	-27.49
SST TM	0.614	-0.00489	1.99	-1.72
EXP	0.64	0.06	2.50	16.8



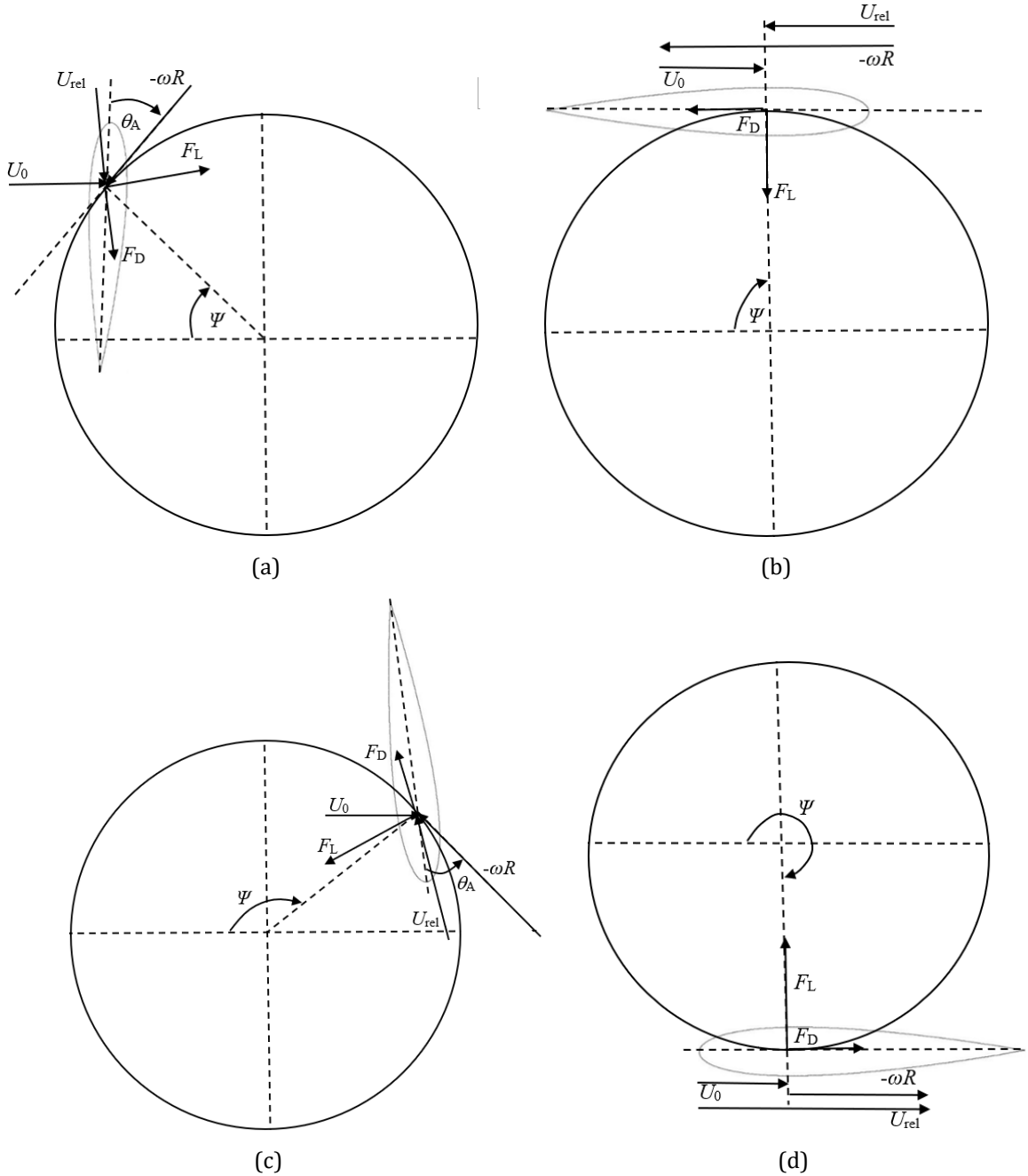
**Fig.2.24** Instantaneous vertical force, propulsive force and power coefficients of one blade in a revolution at two  $\lambda$ . (a), (b) and (c) at  $\lambda=0.52$ ; (d), (e) and (f) at  $\lambda=0.73$ .

Figure 2.25 shows the main forces (lift and drag) acting on one blade at different  $\psi$  when  $\lambda$  is 0.52. At  $\psi=32^\circ$ , the blade is nearly vertical and it is experiencing the retreating side. At this moment, the components of lift and drag are generated in the positive X axis, leading to the production of the large negative propulsive force, which is shown in figure

2.24b. Moreover, the component of lift is almost balanced by the component of the drag in Y axis. Consequently, the vertical force of this blade approaches to zero. This situation is quite similar with that at  $\psi=144^\circ$ . However, the components of lift and drag in negative X axis are responsible for the creation of the large positive propulsive force. For the propulsive force transition, the critical moment is when the blade is almost located at  $\psi=90^\circ$  and  $\psi=270^\circ$ . At these two positions, the lift  $F_L$  provides the vertical force of the blade totally, but the direction is contrary, as is shown in figure 2.24a. Simultaneously, the drag  $F_D$  makes the contribution to the propulsive force at  $\psi=90^\circ$  and  $270^\circ$ , but its magnitude is extremely small because the relative angle-of-attack is nearly equal to zero. Actually, without considering the relative velocity induced by the blade pitching motion, the stagnation point is not located on the leading edge, and there exists a deflection, which leads to the lift and drag that are not produced in the vertical and horizontal directions. As a consequence, the propulsive force generated from lift and drag is balanced in X axis.

**Table 2.8** Main production regions of forces and power

$\lambda=0.52$	Negative vertical force region ( $^\circ$ )	Positive vertical force region ( $^\circ$ )	Negative propulsive force region ( $^\circ$ )	Positive propulsive force region ( $^\circ$ )	Negative power region ( $^\circ$ )	Positive power region ( $^\circ$ )
SST $k-\omega$	32-144	144-360	0-89	89-269	0-83	83-338
SST TM	32-144	144-360	0-89	89-269	0-83	83-338
SA TM [87]	32-153	153-360	0-96	96-267	0-87	87-344
$\lambda=0.73$						
SST $k-\omega$	34-140	140-360	0-90	90-269	0-92	92-312
SST TM	34-140	140-360	0-90	90-269	0-88	88-323
SA TM [87]	36-151	151-360	0-103	103-269	0-100	100-272



**Fig.2.25** Sketch of main forces acting on one blade at different  $\psi$ . (a)  $\psi=32^\circ$ ; (b)  $\psi=90^\circ$ ; (c)  $\psi=144^\circ$ ; (d)  $\psi=270^\circ$ .

The detailed flow structures achieved by two turbulence models, including the velocity and vorticity contours, are shown in figure 2.26 and 2.27 at  $\psi=0^\circ$  when  $\lambda$  is 0.52. The numerical simulations are compared with the experimental measurements [86]. At this instant, both two blades have the largest relative incidence. Compared with the experiments, it seems that the present computations can capture the gross feature of the internal flow structures, such as the trajectory of wakes shedding from two blades and the interaction of blade B with its own wake. By the comparison of velocity and vorticity distributions, it is observed that the vortical flows dissipate quickly for SST TM, particularly in the wake region, which infers that the earlier onset of vortex shedding due to the susceptibility of disturbances [58]. To clarify the difference of near-wall flows for two turbulence models, the pressure coefficient  $C_p$  and relative velocity contours of blade

B are plotted in figure 2.28 and 2.29. Based on the pressure distributions, it is observed that there is almost no difference for blade A, but has evident dissimilarity for blade B, especially near the leading edge ( $x/c=0\sim0.35$ ) and the trailing edge ( $x/c=0.65\sim1.0$ ) on the suction surface. The pressure difference near the leading edge is primarily due to the low-pressure region induced by the prediction of the stagnation point, but it recovers quickly at  $x/c=0.35$ . Then, downstream from  $x/c=0.65$ , the onset of boundary layer separation is evident, which is earlier and more violent for SST TM, causing the significant pressure degradation.

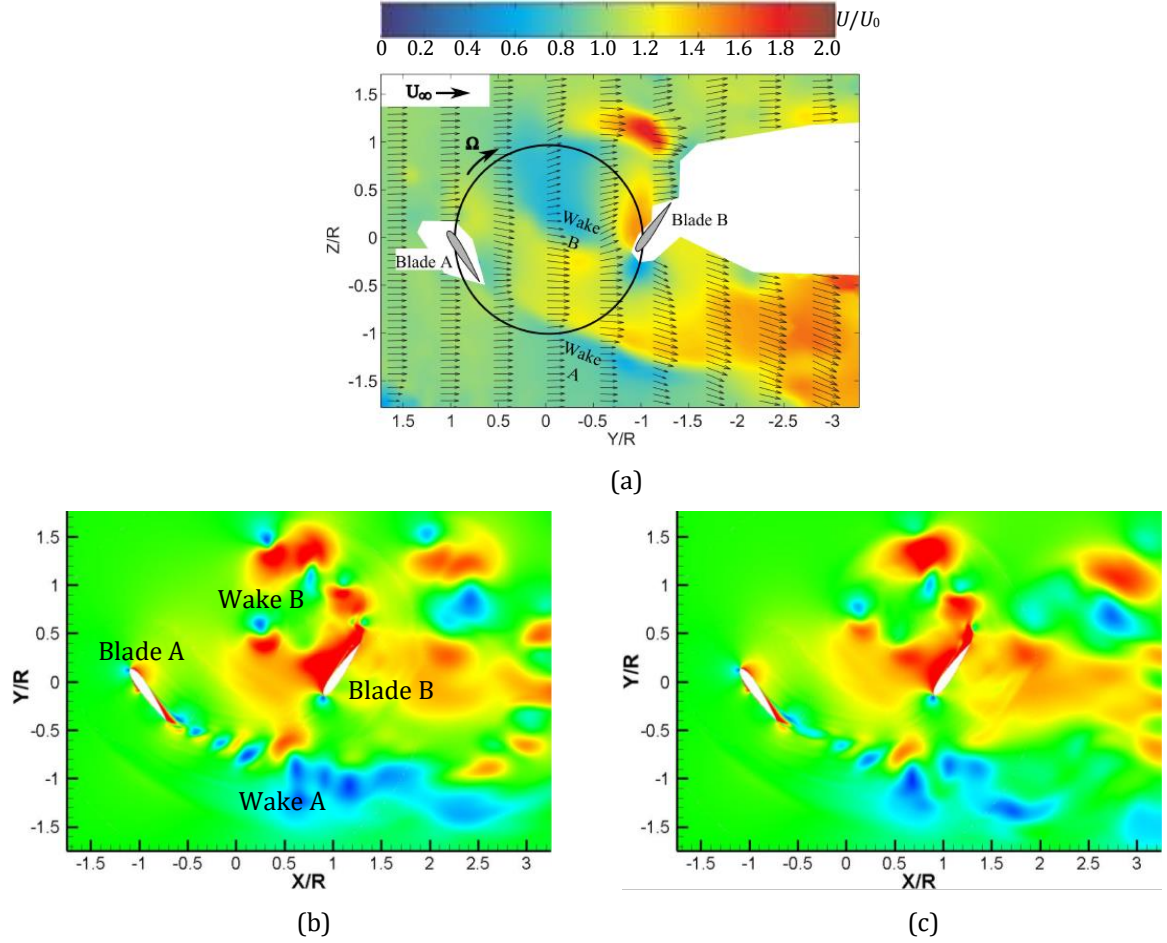


**Fig.2.26** Velocity contours. (a) Experiment; (b) SST  $k-\omega$ ; (c) SST TM.

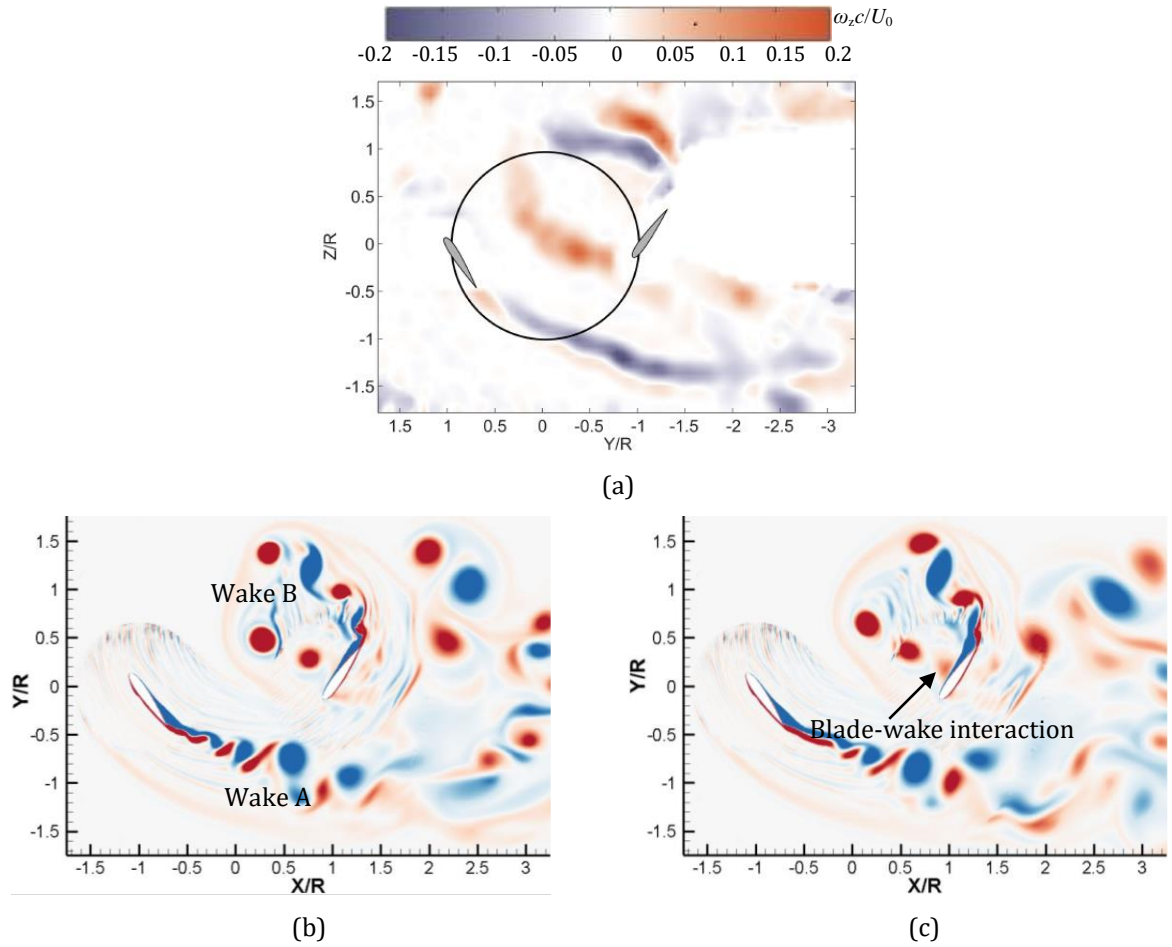


**Fig.2.27** vorticity contours. (a) Experiment; (b) SST  $k-\omega$ ; (c) SST TM.

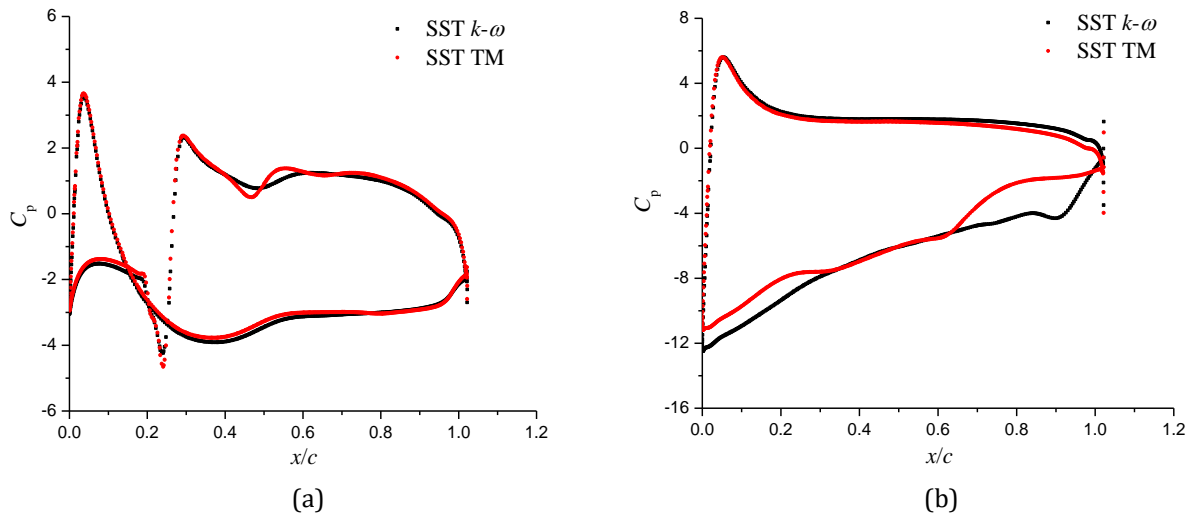


**Fig.2.28** Pressure distributions. (a) Pressure of blade A; (b) Pressure of blade B.

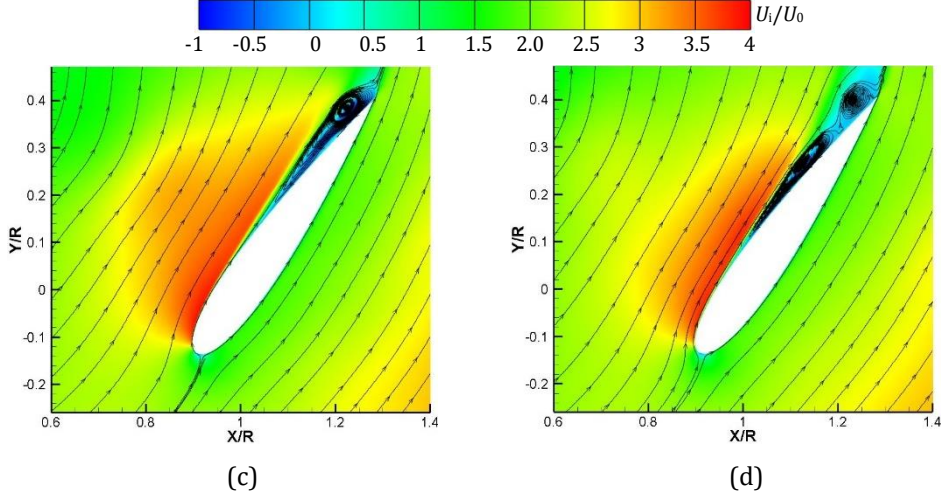
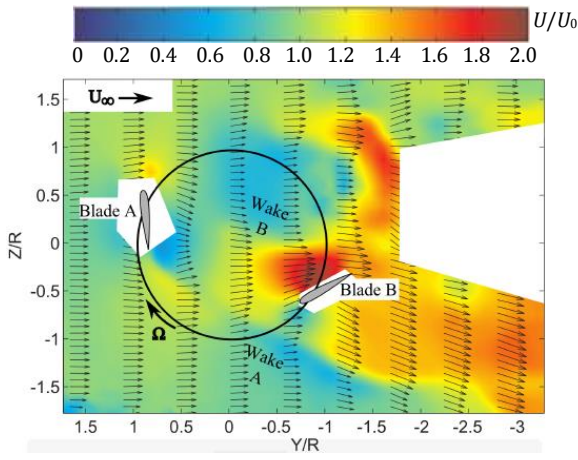
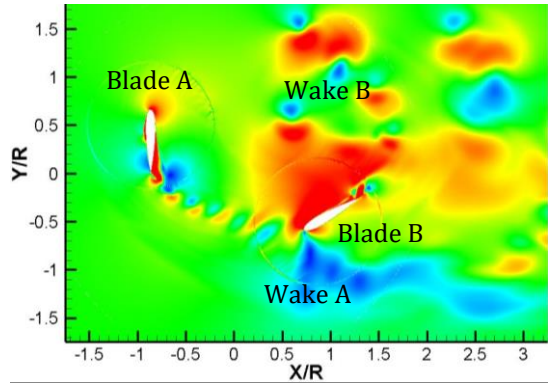


**Fig.2.29** Relative velocity of blade B. (a) SST  $k-\omega$ ; (b) SST TM.

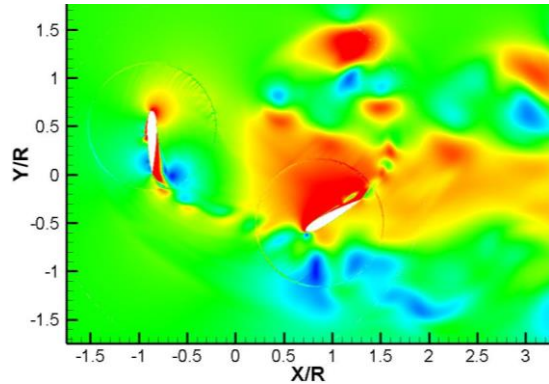
When  $\psi$  is  $30^\circ$ , the flow field is more complicated than that at  $\psi=0^\circ$ , shown by the distributions of velocity and vorticity contours in figure 2.30 and 2.31. It is obvious that the wake of blade A has a strong interaction with blade B, which is quite different from that in figure 2.26 where the blade B interacts with its own wake. In addition, the wake of blade B also has a strong interaction with wake B itself. Then, the detailed flow structures of two blades are displayed in figure 2.32 and 2.33, including the pressure coefficients, velocity contours of two blades and velocity profiles. For blade A, the main difference of pressure predicted by two turbulence models is at  $x/c=0.25\sim0.5$ , due to the existence of many small-scale vortices inside the boundary layer. Clearly, the SST TM resolves more scales near the wall, even a small vortex near the trailing edge causing the pressure drop on the pressure side, as is shown in figure 2.32a. Afterwards, the flow over the blade B is more complicated. There are three obvious distinctions for two turbulence models: (1) the low-pressure region near the leading edge on the suction side; (2) the flow separation after the middle chord; (3) the high-pressure region near the leading edge on the pressure surface. The pressure difference near the leading edge both on two sides is as a result of the stagnation point deviation. Certainly, the blade-wake interaction also more or less leads to this difference. Near the blade trailing edge, the flow separation predicted by SST TM is more intensive, which has great impact on the blade loading. What is more, in figure 2.31b, 2.32b and 2.33c, it is found that the blade-wake interaction has a significant effect on the external flow field near the leading edge, especially for SST  $k-\omega$  model, presented by the velocity profiles near the leading edge of the pressure side, which are shown in figure 2.33e and 2.33f.



(a)



(b)



(c)

**Fig.2.30** Velocity contours. (a) Experiment; (b) SST  $k-\omega$ ; (c) SST TM.

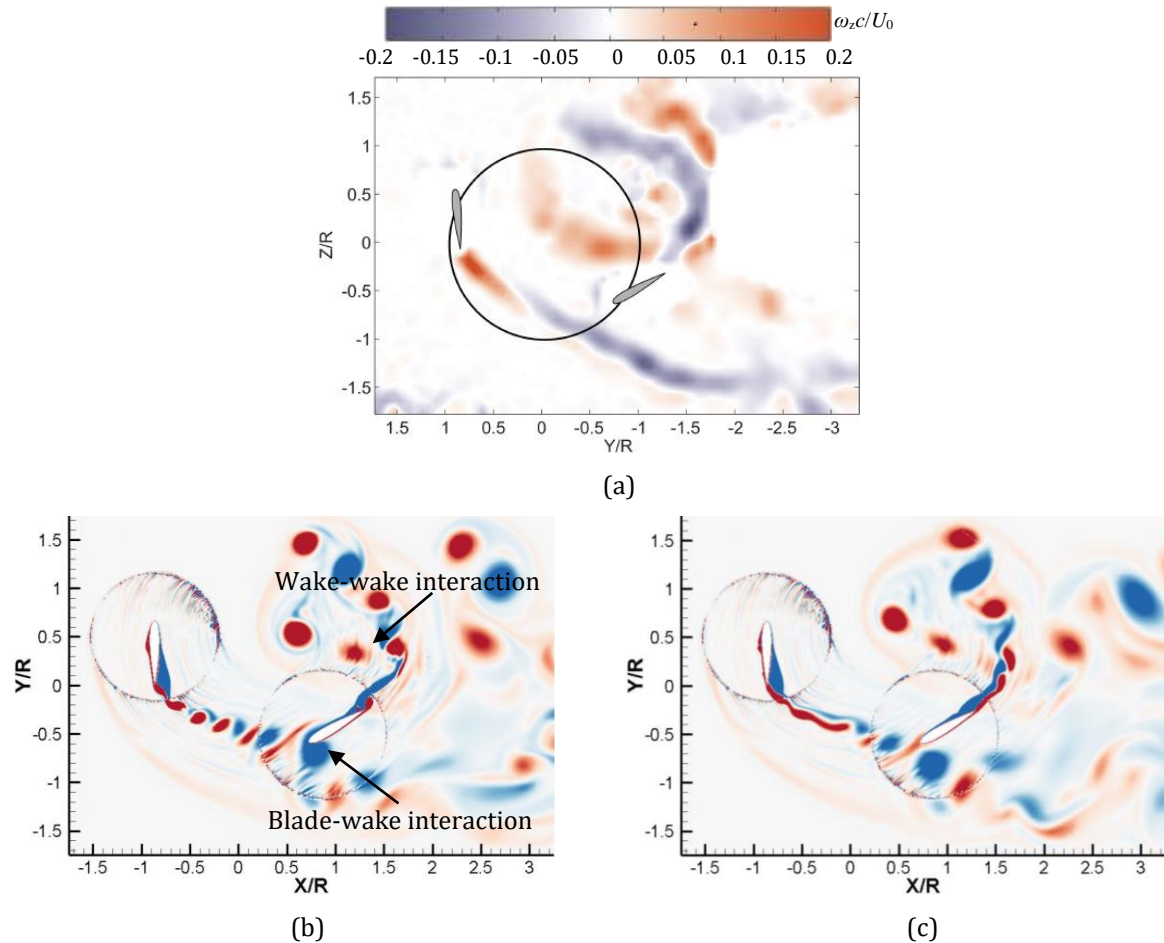


**Fig.2.31** Vorticity contours. (a) Experiment; (b) SST  $k-\omega$ ; (c) SST TM.

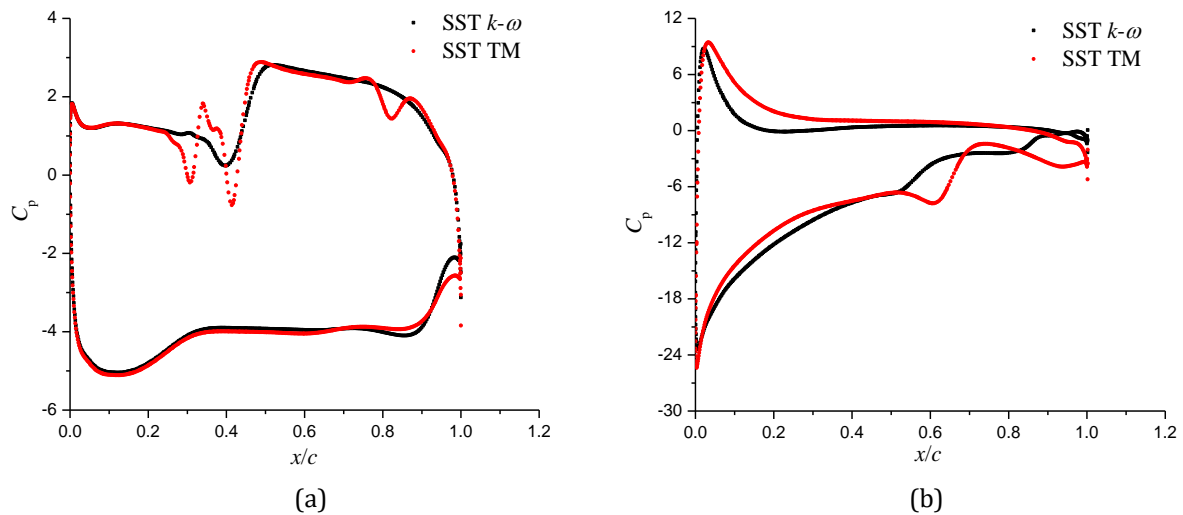


**Fig.2.32** Pressure distributions. (a) Pressure of blade A; (b) Pressure of blade B.

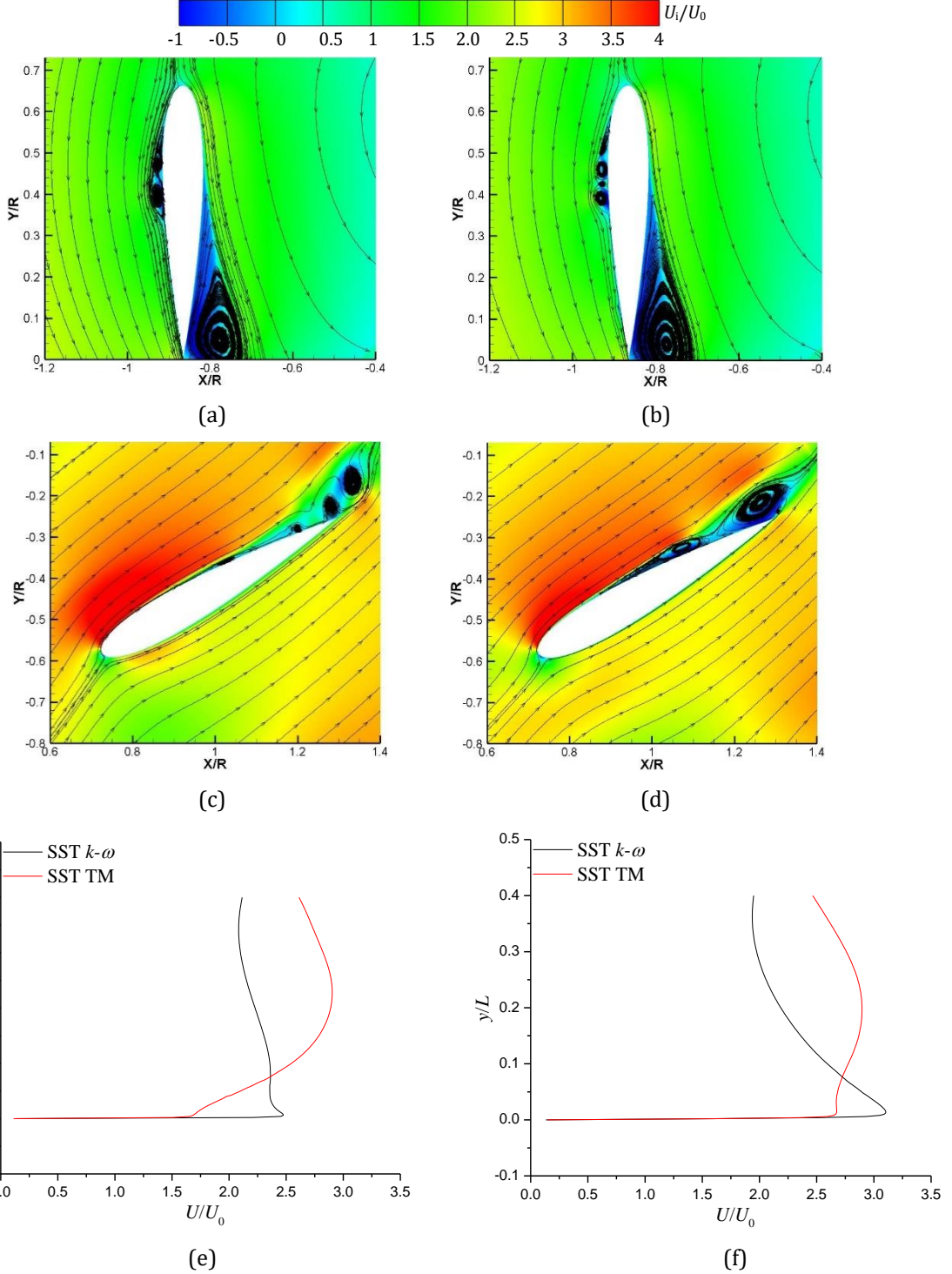


**Fig.2.33** Relative velocity of two blades and velocity profiles. (a) and (c) SST  $k-\omega$ ; (b) and (d) SST TM; (e) Velocity profile of blade B at  $x/c=0.05$  on lower surface; (f) Velocity profile of blade B at  $x/c=0.1$  on lower surface.

In the next moment, at  $\psi=60^\circ$ , blade B has already come across the wake shedding from blade A, but it contacts with wake B near the trailing edge of blade B. Besides, the wake of blade B also has an interaction with itself, indicating a wake-wake interaction. The trajectory of wake shedding from blade A in the experiments has a little difference compared with the simulations, which impacts directly on the upper surface of blade B, shown in figure 2.35a. However, the computations can still seize the gross feature of

unsteady vortical flows. The detailed description of flow field near the blade surface is shown in figure 2.36 and 2.37, using the pressure coefficients and velocity contours. The pressure of blade A predicted by SST  $k-\omega$  model has some difference compared with that obtained by SST TM, in regions where the small-scale vortex attaches on the pressure side and the flow separation emerges near the trailing edge of suction side. At azimuthal angle of  $30^\circ$ , the unstable area of pressure on the pressure side is at  $x/c=0.25\sim0.5$ , but it extends to  $x/c=0.3\sim0.7$  with the development of the attached vortex. The SST TM resolves the discrete vortices inside the boundary layer, resulting in the pressure fluctuation, as is shown in figure 2.36a. Near the trailing edge of suction side, the pressure is greatly influenced by the large-scale flow separation vortex, especially for SST  $k-\omega$  model. For blade B, the laminar separation bubble is formed near the leading edge. After LSB, the flow would reattach on the blade surface and then the turbulent boundary layer separation appears, shown in figure 2.37d. But the SST  $k-\omega$  model only captures the fully turbulent boundary layer after LSB and no reattachment point is observed, which will be discussed later in detail. Generally, it concludes that the considerable difference of pressure on the suction side of blade B is mostly due to the laminar-turbulence transition and turbulent boundary layer separation.

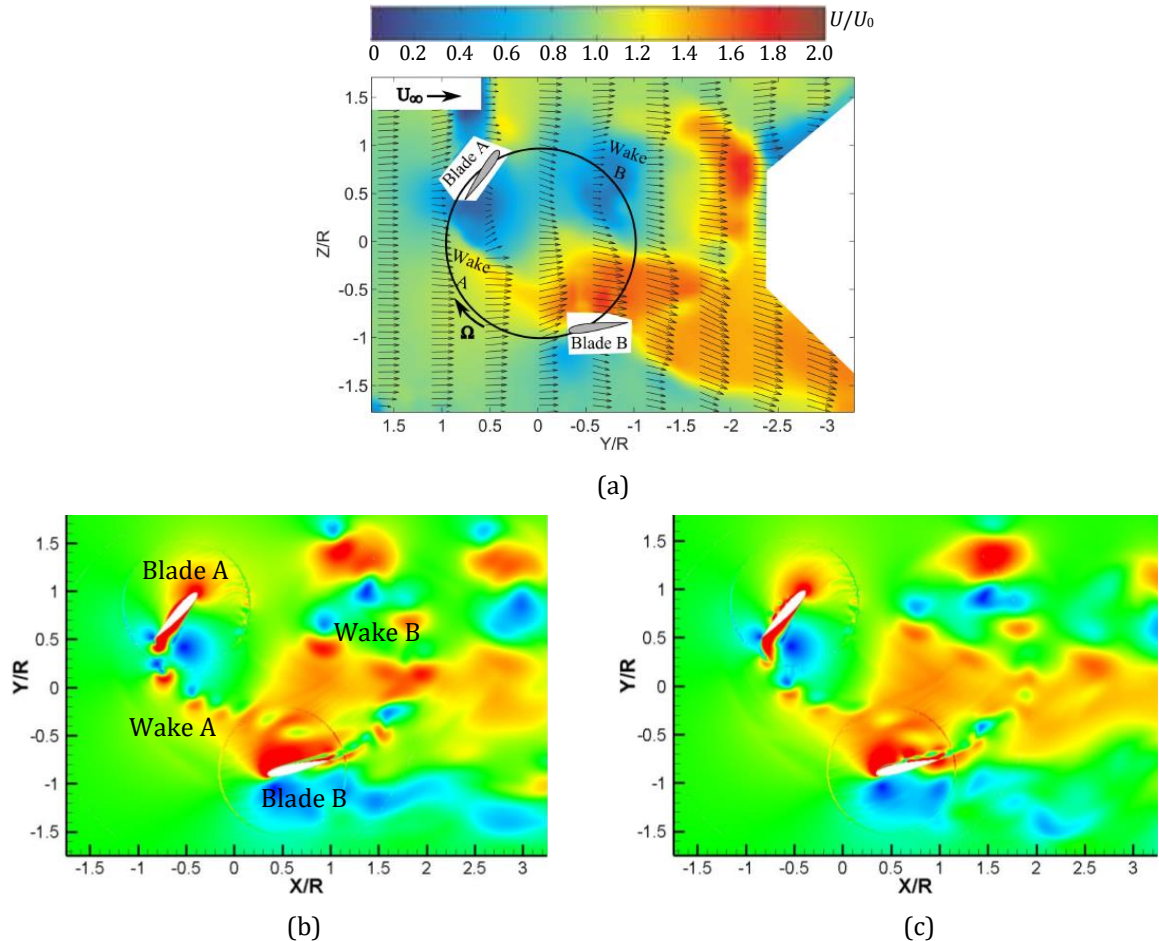


**Fig.2.34** Velocity contours. (a) Experiment; (b) SST  $k-\omega$ ; (c) SST TM.

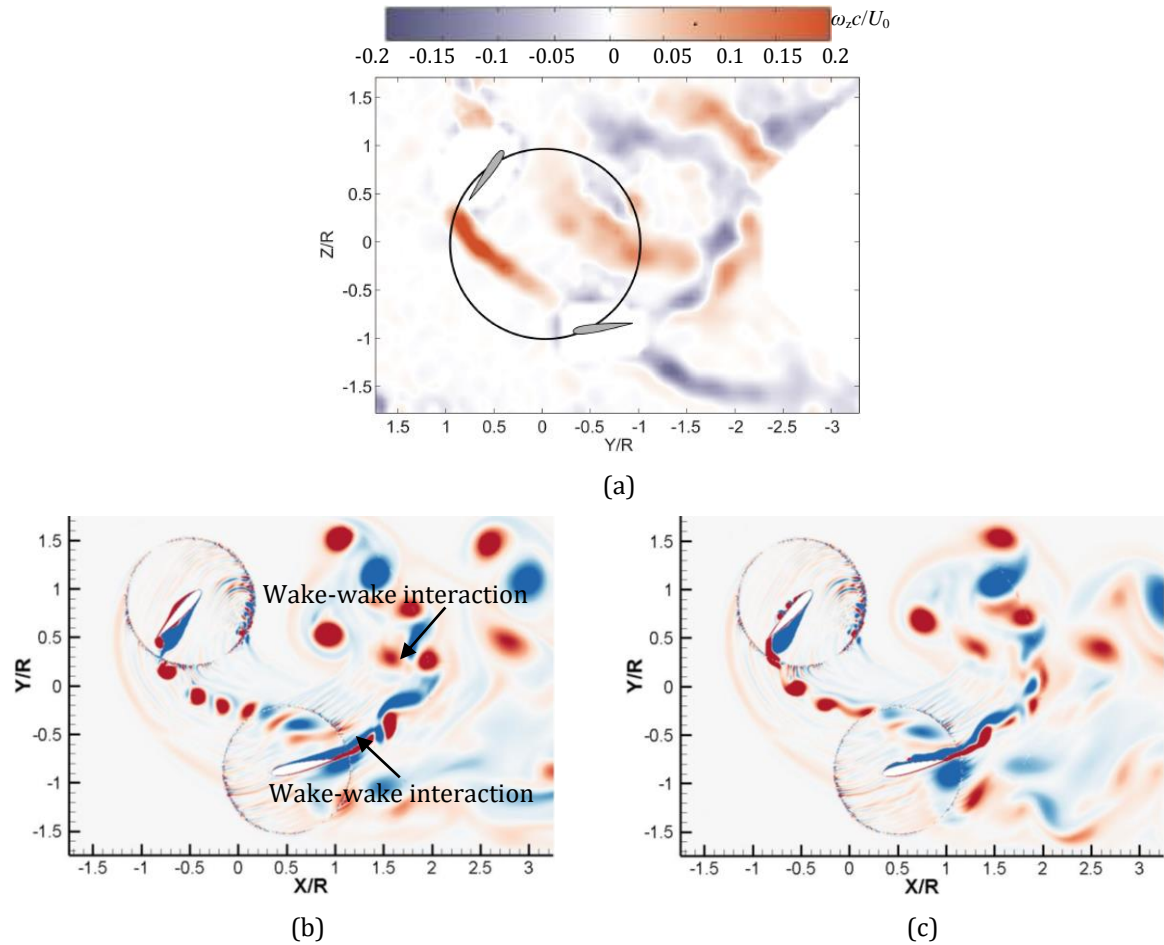


**Fig.2.35** Vorticity contours. (a) Experiment; (b) SST  $k-\omega$ ; (c) SST TM.

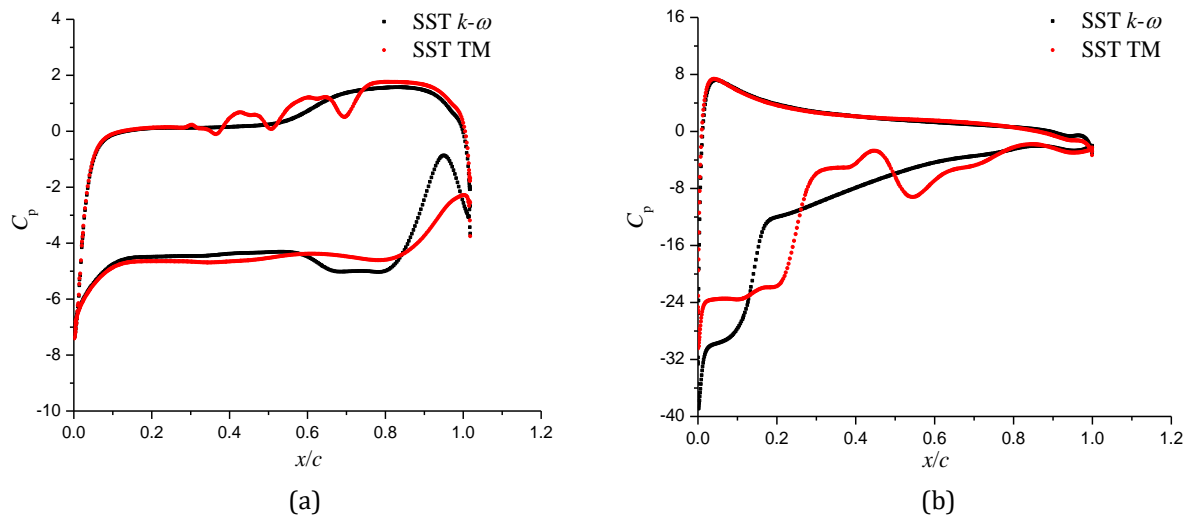


**Fig.2.36** Pressure distributions. (a) Pressure of blade A; (b) Pressure of blade B.

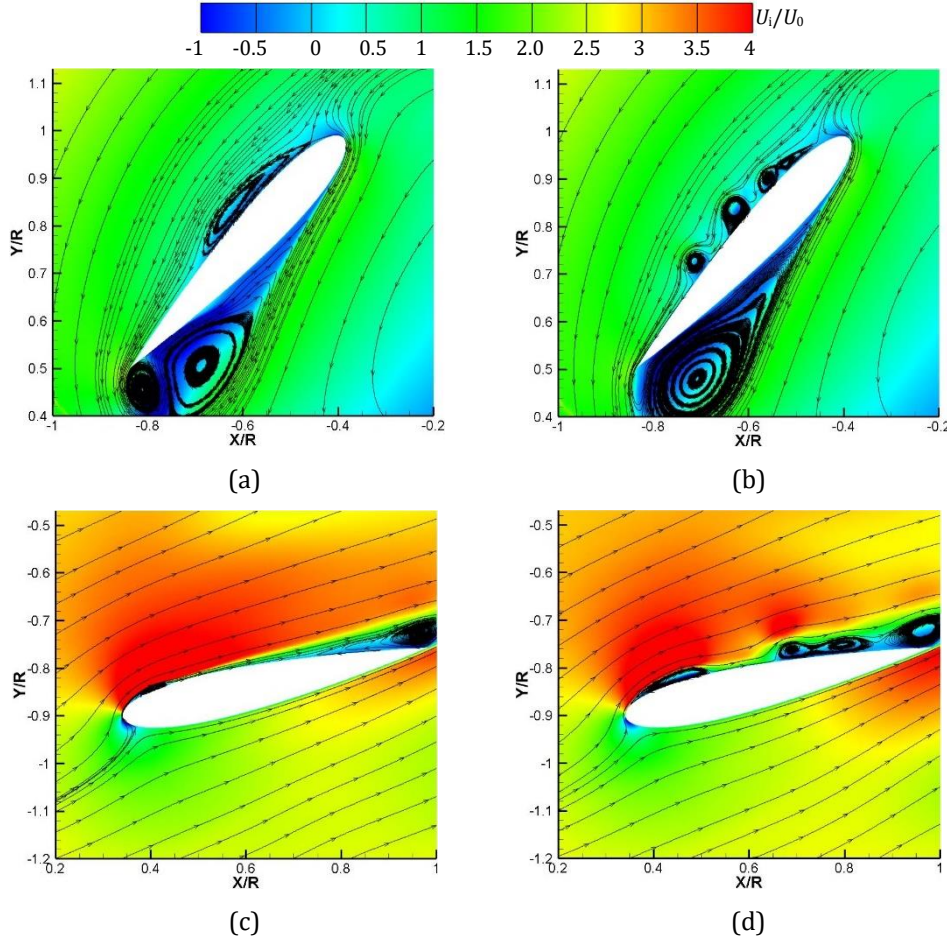


**Fig.2.37** Relative velocity of two blades. (a) and (c) SST  $k-\omega$ ; (b) and (d) SST TM.

As is shown in figure 2.38 and 2.39, the velocity and vorticity contours at  $\lambda=0.73$  are displayed and the computational results are compared with the experimental data. At  $\psi=0^\circ$ , the wake of blade A has no contact with blade B. But blade B has a visible interaction near the leading edge with the wake shedding from itself. Compared with that in figure 2.26, the interaction position is much closer to the leading edge, due to the change of velocity  $U_{\text{rel}}$ . It also can be seen that the blade-wake interaction predicted by SST  $k-\omega$  is more obvious. The pressure, relative velocity and velocity profiles are shown in figure 2.40 and 2.41, to study the near-wall flows and its impact on the performance of the single blade. According to the simulation results, it is found that the pressure distribution of blade B on the suction side has relatively large difference. The high level of relative velocity develops from the leading edge to the trailing edge for SST TM, leading to the performance enhancement because of the lower pressure, as is shown in figure 2.40b. This occurrence is due to the prediction of low-pressure region near the leading edge and less impact of blade-wake interaction for SST TM in figure 2.41d. In addition, the pressure has fluctuations for SST  $k-\omega$  model, as a result of many individual vortices. Very close to the wall, the reverse flow occurs earlier for SST TM, for the reason that it has the ability to detect the instability of boundary layer disturbed by the external environment. Moreover, near the leading edge of the pressure side, the external flow structure is strongly affected by the blade-wake interaction for SST  $k-\omega$  model, which is shown in figure 2.41c and 2.41d.

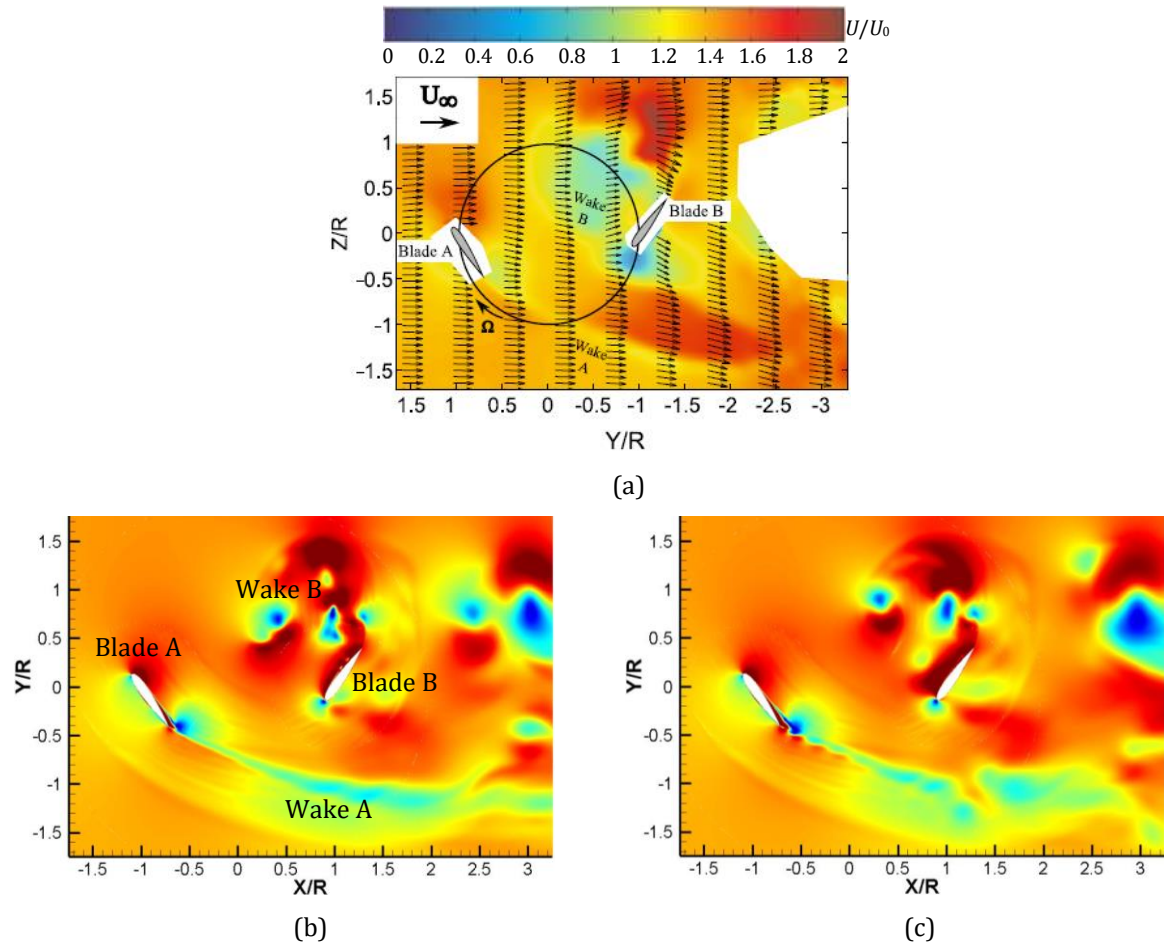


**Fig.2.38** Velocity contours. (a) Experiment; (b) SST  $k-\omega$ ; (c) SST TM.

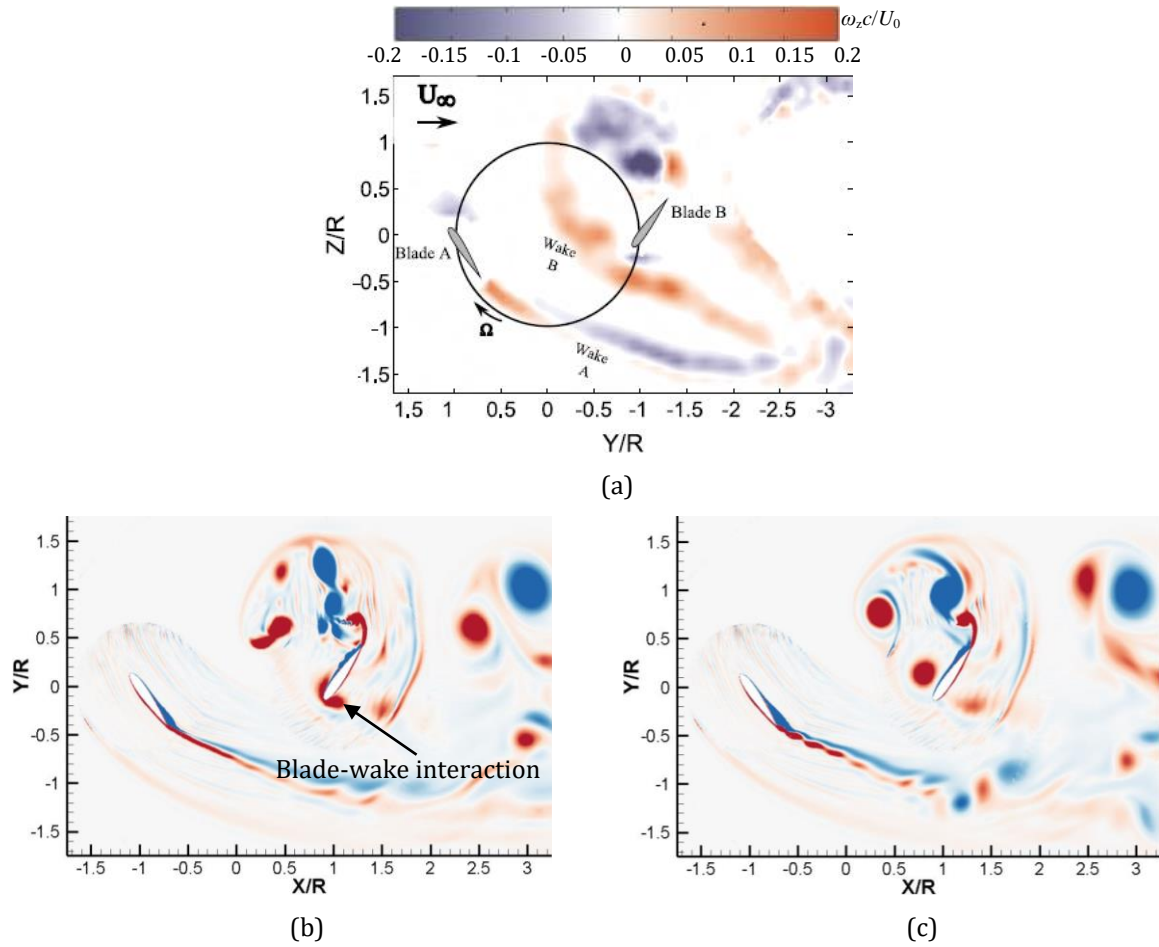


**Fig.2.39** Vorticity contours. (a) Experiment; (b) SST  $k-\omega$ ; (c) SST TM.

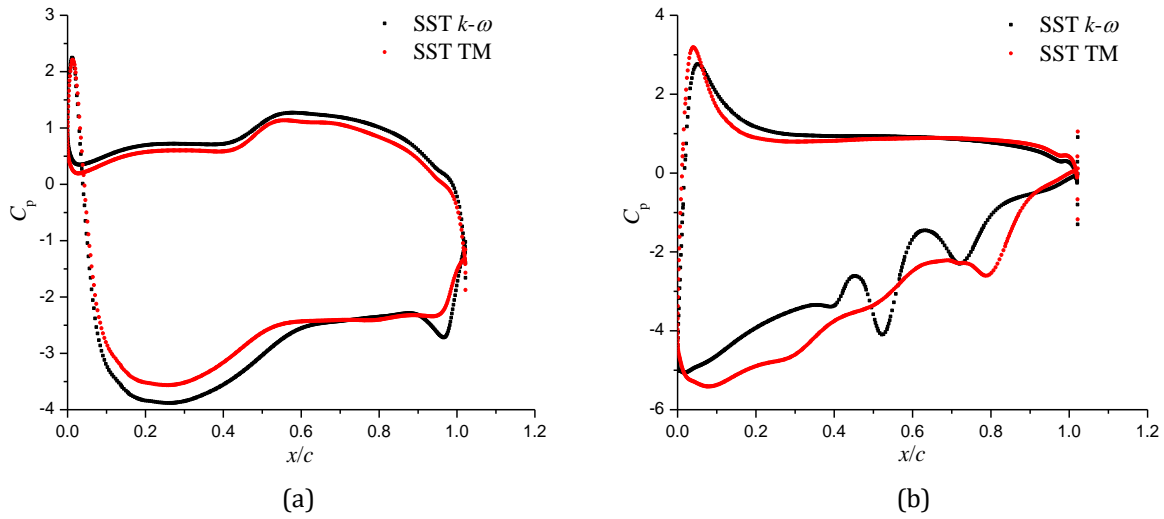


**Fig.2.40** Pressure distributions. (a) Pressure of blade A; (b) Pressure of blade B.

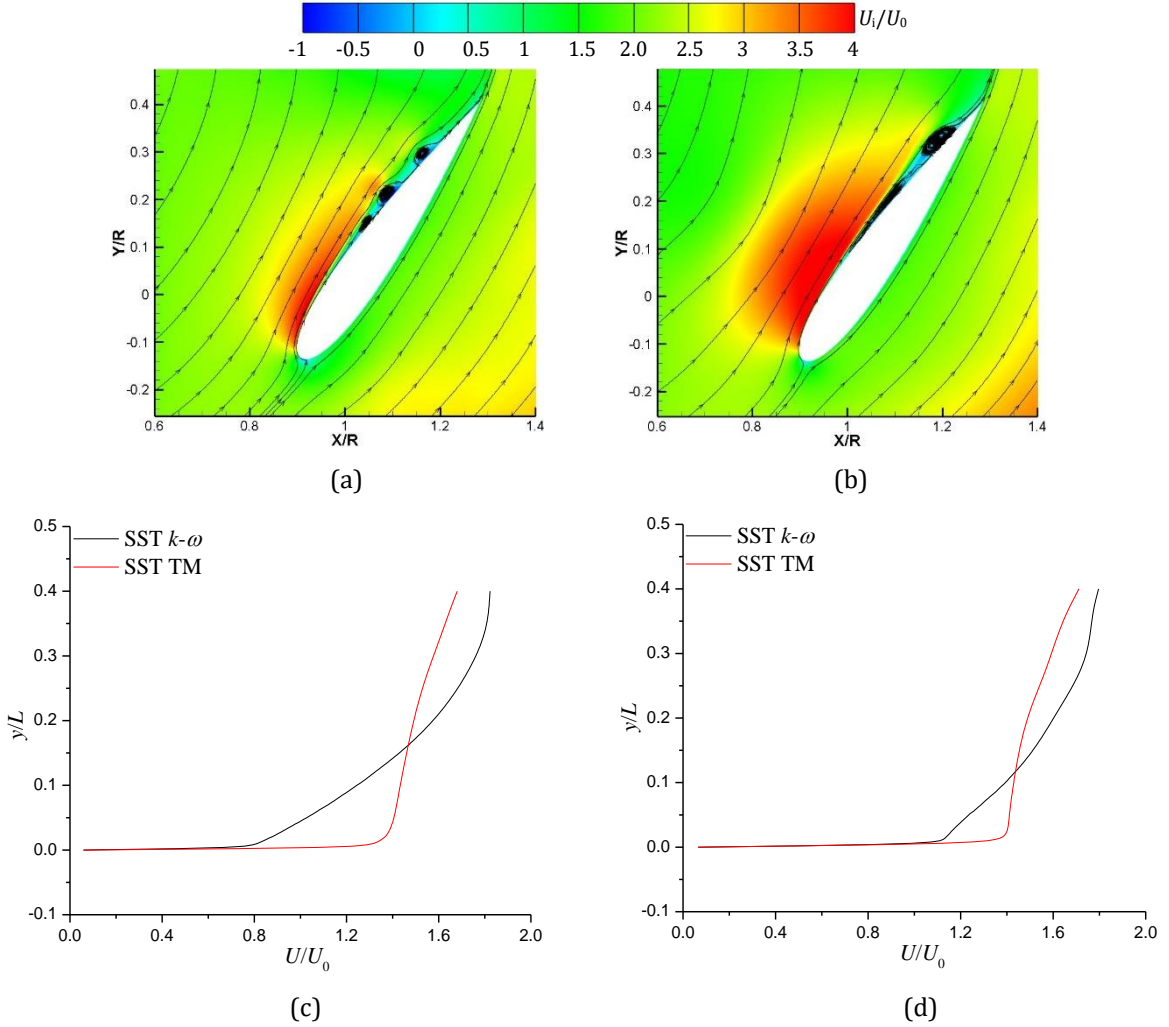
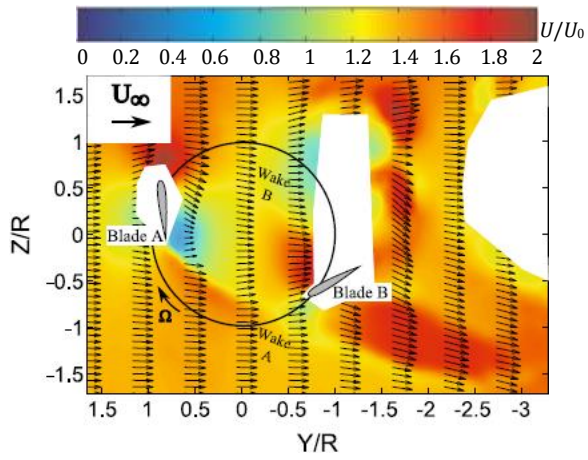
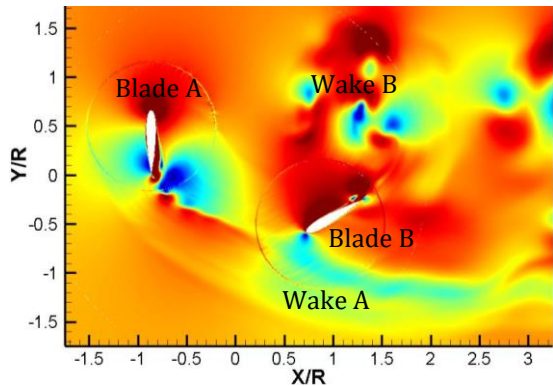


**Fig.2.41** Relative velocity of blade B and velocity profiles. (a) SST  $k-\omega$ ; (b) SST TM; (c) Velocity profile of blade B at  $x/c=0.05$  on pressure side; (d) Velocity profile of blade B at  $x/c=0.15$  on pressure side.

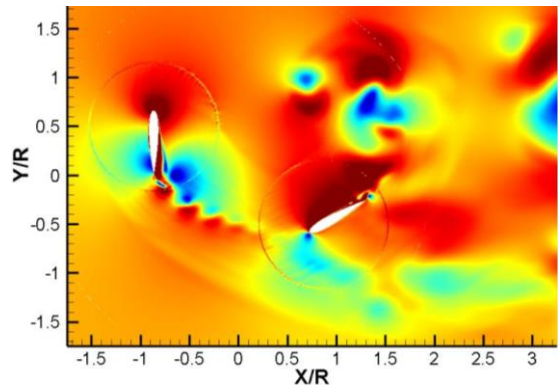
At  $\psi=30^\circ$ , the velocity and vorticity contours obtained by the simulations and experiments are shown in figure 2.42 and 2.43, when  $\lambda$  is 0.73. Although the flow structure is quite similar with that at  $\lambda=0.52$ , there is no blade-wake interaction at this time. The change of the relative velocity, due to the increase of the freestream velocity, modifies the trajectory of the wake shedding from blade A. But for blade B, the wake-wake interaction is still captured clearly by two turbulence models. To study the difference of flow structures near the blade surface, the blade loadings and velocity contours of two blades are shown in figure 2.44 and 2.45, respectively. The pressure distribution on the pressure side is quite similar for two turbulence models and a little difference is induced by the existence of a small-scale attached vortex. Then, on the suction side of blade A, flow separation occupying a large part of the blade surface occurs, particularly near the trailing edge, leading to the remarkable pressure difference. When it comes to the blade B, the turbulent boundary layer separation changes the blade loading evidently from the middle chord to the trailing edge, but this phenomenon becomes weak compared with that in figure 2.33. Ultimately, the results show that SST TM has the capability to capture more scales near the wall.



(a)



(b)



(c)

**Fig.2.42** Velocity contours. (a) Experiment; (b) SST  $k-\omega$ ; (c) SST TM.

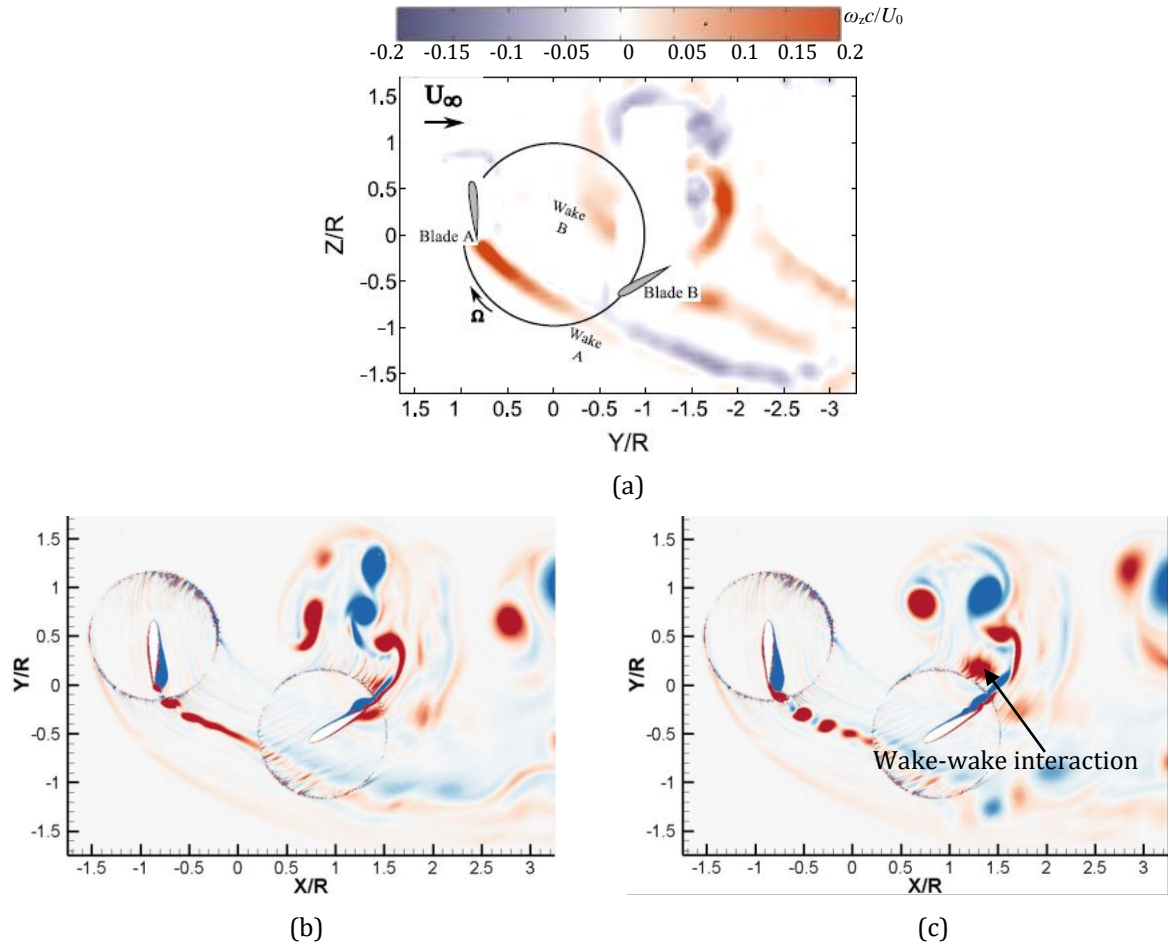


**Fig.2.43** Vorticity contours. (a) Experiment; (b) SST  $k-\omega$ ; (c) SST TM.

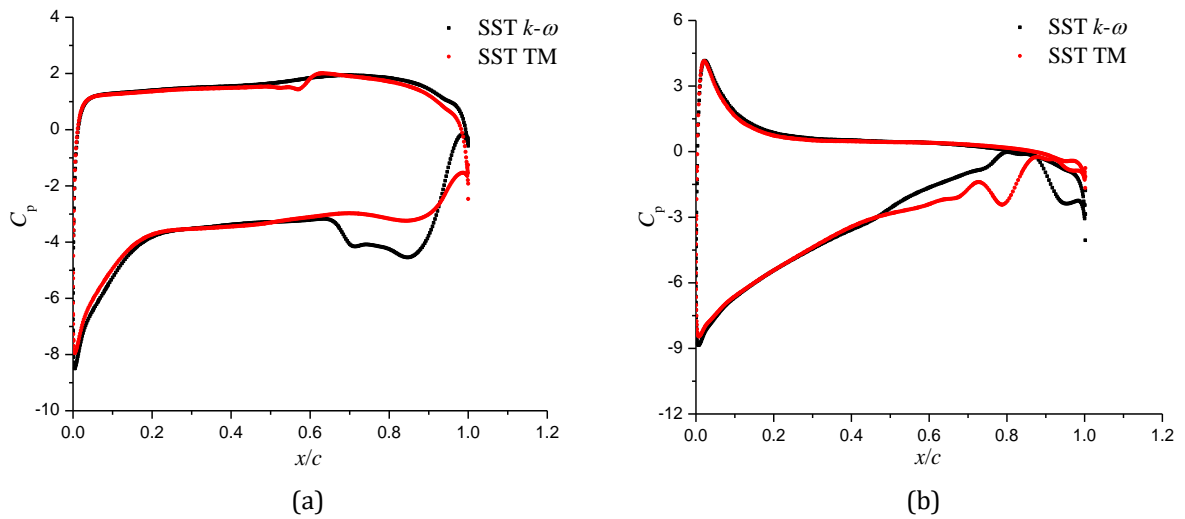


**Fig.2.44** Pressure distributions. (a) Pressure of blade A; (b) Pressure of blade B.

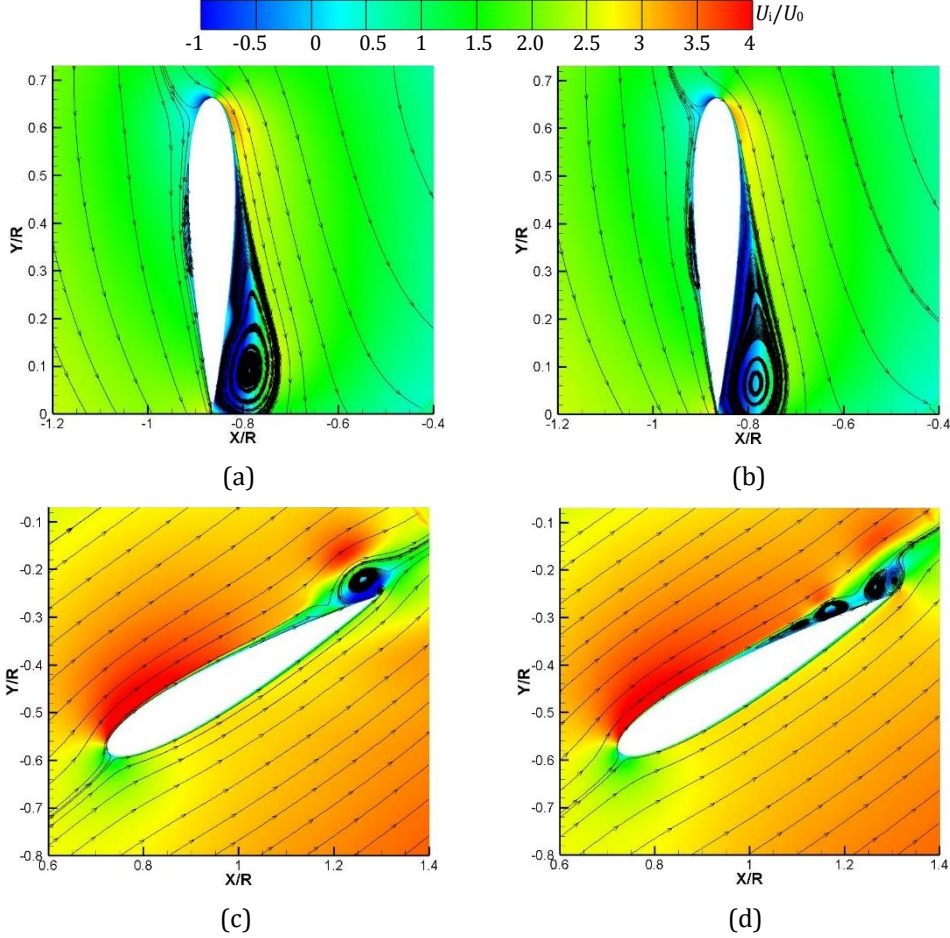


**Fig.2.45** Relative velocity of two blades. (a) and (c) SST  $k-\omega$ ; (b) and (d) SST TM.

When  $\psi$  increases to  $60^\circ$ , the wake of blade A has a weak interaction with the wake of blade B near the trailing edge, compared with that at  $\lambda=0.52$ . From the distributions of velocity and vorticity, it seems that the vortical flows obtained by SST TM are more unstable, characterized by more individual vortex in shedding wakes, as is shown in figure 2.47b and 2.47c. As a complementary, the pressure and velocity contours are presented in figure 2.48 and 2.49, to analyze the detailed near-wall flow structures. For blade A, it is undergoing the retreating side and massive flow separation nearly exists on the whole suction side, particularly from  $x/c=0.4\sim 1.0$ . There is a three-vortex-structure located at the leading edge. After the reattachment, the turbulent boundary layer separates and two vortices connecting with each other are generated. Evidently, the presence of the trailing edge flow separation causes a lower pressure for SST  $k-\omega$  model, leading to a better performance for blade A. On the suction side of blade B, there is only a small vortex attached on the blade trailing edge for SST  $k-\omega$  model, but SST TM captures the slender separation bubble, the reattachment and the turbulent boundary layer separation clearly.

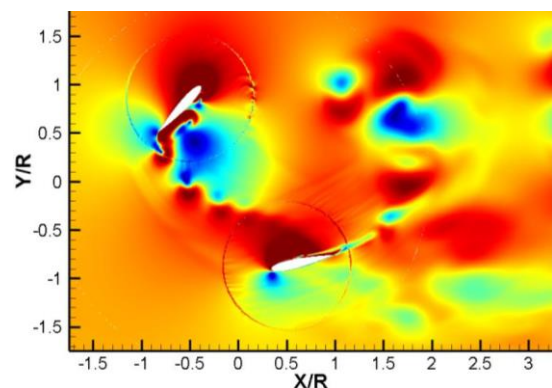
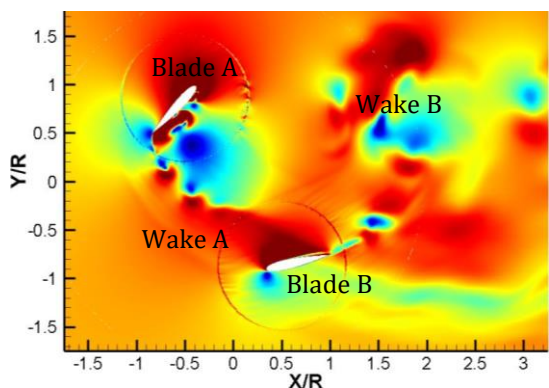
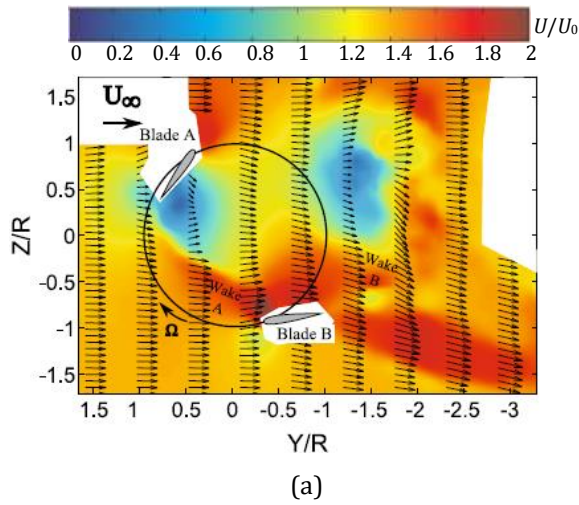


**Fig.2.46** Velocity contours. (a) Experiment; (b) SST  $k-\omega$ ; (c) SST TM.

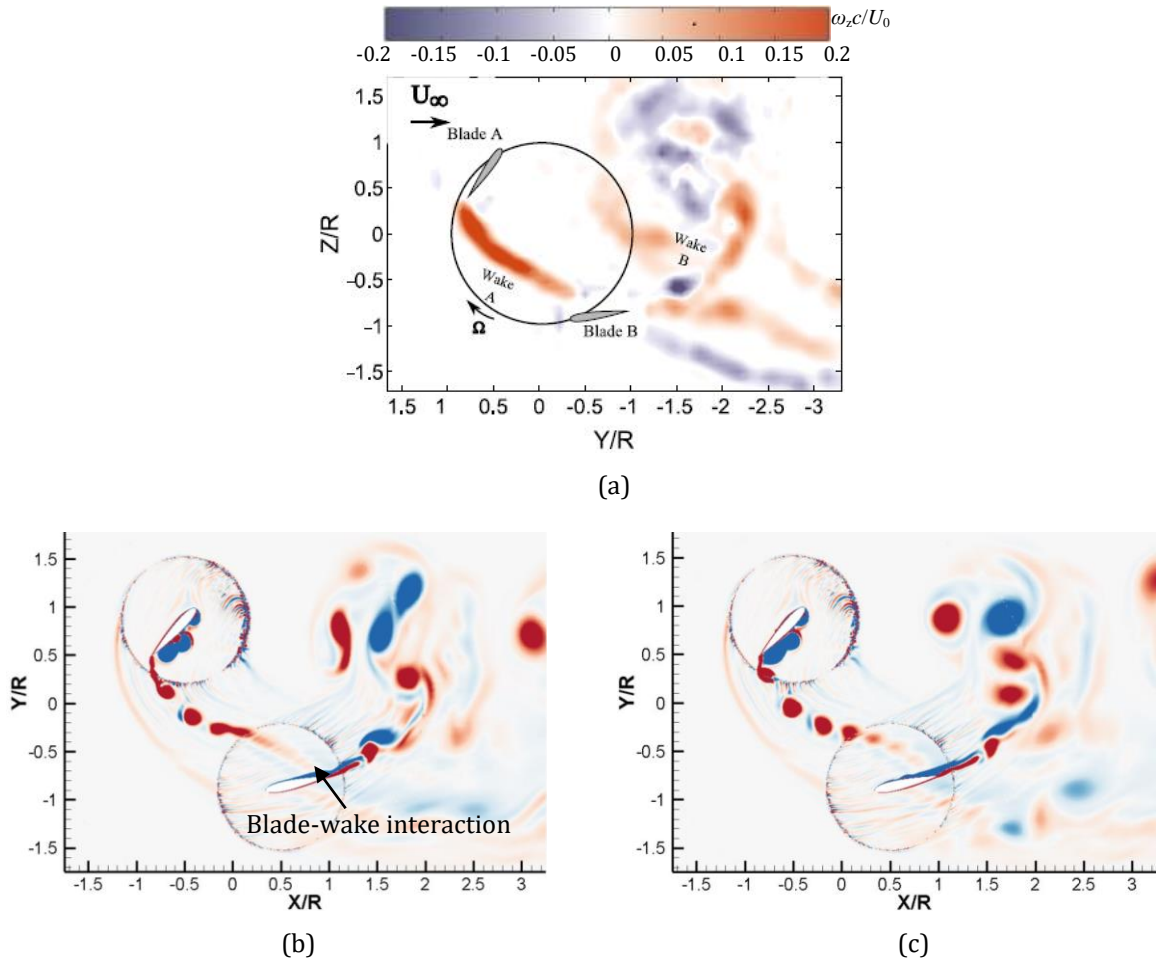


**Fig.2.47** Vorticity contours. (a) Experiment; (b) SST  $k-\omega$ ; (c) SST TM.

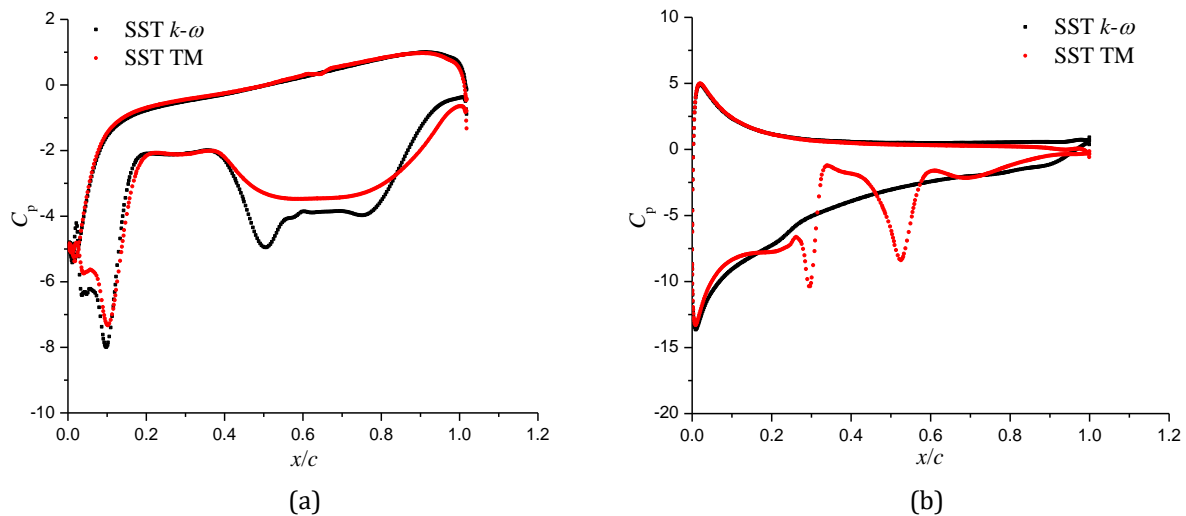


**Fig.2.48** Pressure distributions. (a) Pressure of blade A; (b) Pressure of blade B.

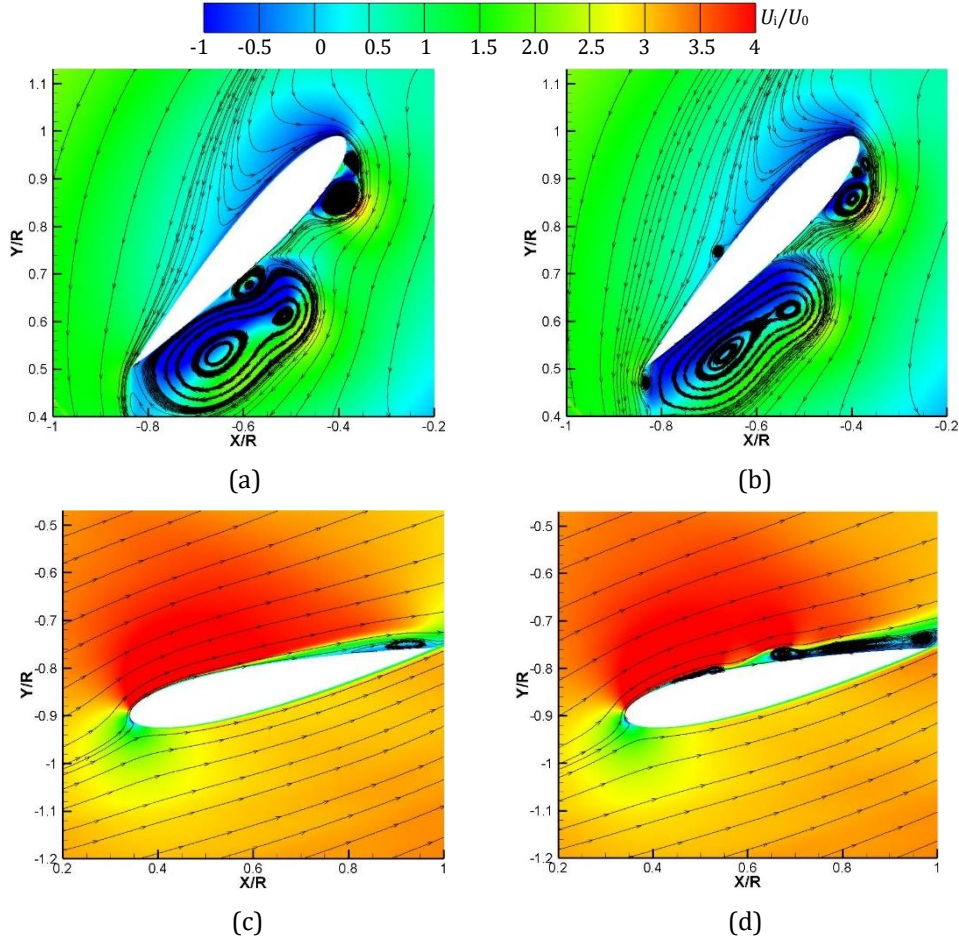


**Fig.2.49** Relative velocity of two blades. (a) and (c) SST  $k-\omega$ ; (b) and (d) SST TM.

The global performance of the cycloidal rotor at two  $\lambda$  are displayed in figure 2.50, to explain the difference of lift and propulsive force predicted by two different turbulence models. It can be seen that the main difference of lift is nearly at  $\psi=30^\circ$  and  $90^\circ$  while it is at  $\psi=30^\circ$  for propulsive force difference when  $\lambda$  is 0.52. At  $\psi=30^\circ$ , the blade A is almost vertical and the vertical force is almost equal to zero, which is shown in figure 2.24a. Due to the components of lift and drag in Y axis, the large magnitude of lift for the cycloidal system is provided by blade B. However, in figure 2.32b, the blade loading obtained by SST TM is larger than that of SST  $k-\omega$  model because of the earlier and more intensive flow separation near the trailing edge, resulting in the larger lift of the cycloidal rotor. Furthermore, the blade B can provide the positive propulsive force, but its magnitude is larger for SST TM as a consequence of the larger blade loading in figure 2.32b. Simultaneously, the blade A produces the negative propulsive force due to the components of lift and drag in X axis, which is shown in figure 2.25a. As a result, according to the propulsive force generated by two blades, SST  $k-\omega$  model achieves the negative propulsive force with large value.

Then, at  $\psi=90^\circ$ , based on the force sketch in figure 2.25b and 2.25d, each blade can generate the vertical force completely provided by the lift, but with different values shown in figure 2.51a and 2.51b. Obviously, the vertical force of blade B is much larger than the blade A, which brings about the positive lift of the cycloidal rotor. For blade A, the pressure difference predicted by two turbulence models is due to the large flow separation on the trailing edge of the suction side. However, the impact is more apparent for SST  $k-\omega$  model. In addition, on the pressure side, the flow state is also extremely

different, as is presented in 2.51c and 2.51d. The blade B also makes the contribution to the lift difference of the rotating system, and the blade loading obtained by SST TM is much larger than SST  $k-\omega$  model, resulting from the attached large-scale laminar separation bubble. Generally, it concludes that the massive flow separation on the suction side of blade A has greater impact on the blade loading for SST  $k-\omega$  model, while the laminar separation bubble with large size predicted by SST TM is the main contributor to the large pressure difference of blade B.

As  $\lambda$  increases to 0.73, the noticeable phenomenon is the negative propulsive force with large magnitude at  $\psi=30^\circ$ , compared with that at  $\lambda=0.52$ . By the comparison of pressure distributions in figure 2.32a and 2.44a, there is no much difference for blade A, which means that the negative propulsive force created by blade A is quite similar with the increase of  $\lambda$ . However, for blade B, the positive propulsive force at  $\lambda=0.52$  is much larger than that at  $\lambda=0.73$ , because of the larger blade loading shown in figure 2.32b, compared with that in figure 2.44b.

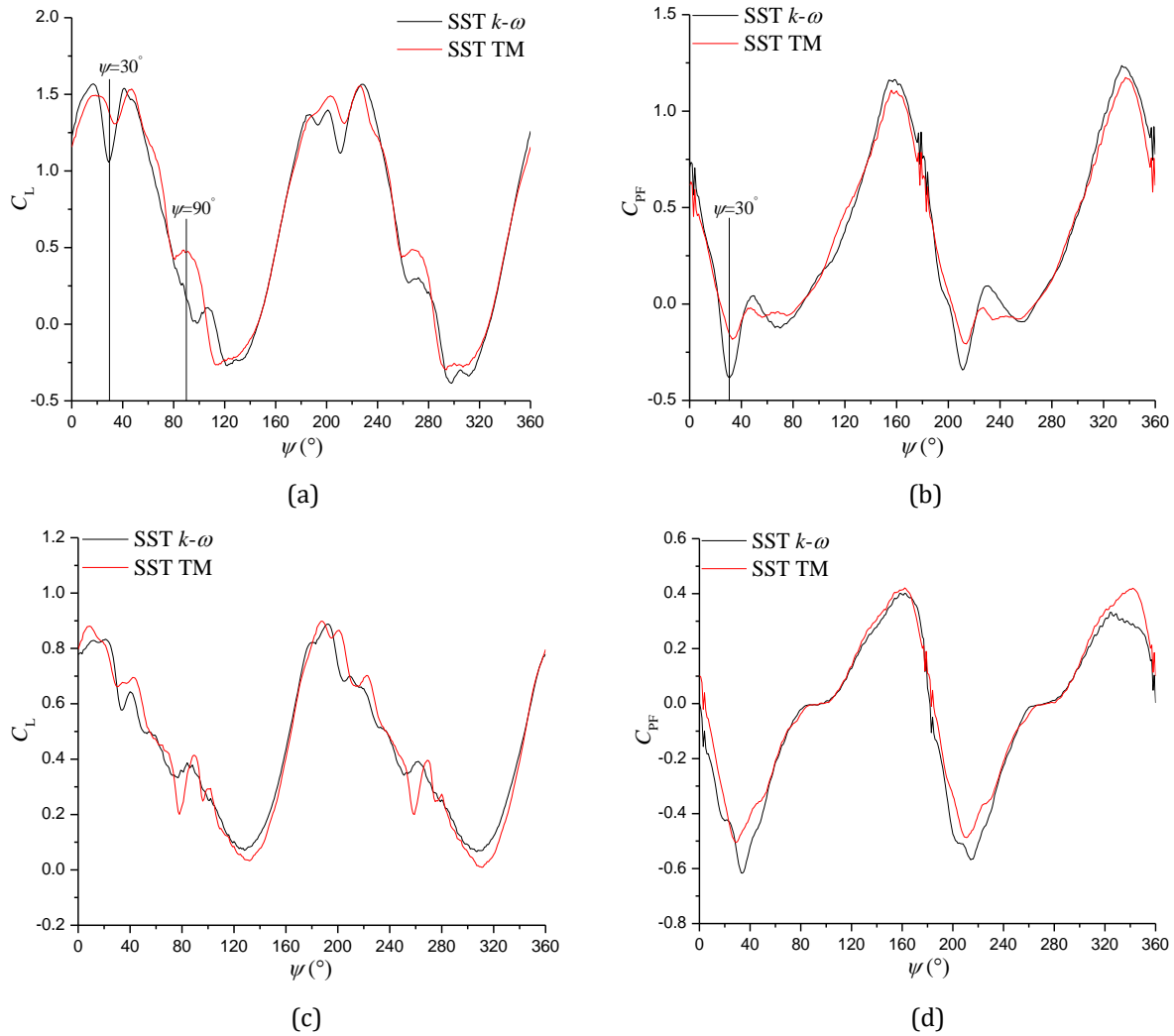


**Fig.2.50** Instantaneous performance of the rotating system. (a) and (b) Lift and propulsive force coefficients at  $\lambda=0.52$ ; (c) and (d) Lift and propulsive force coefficients at  $\lambda=0.73$ .

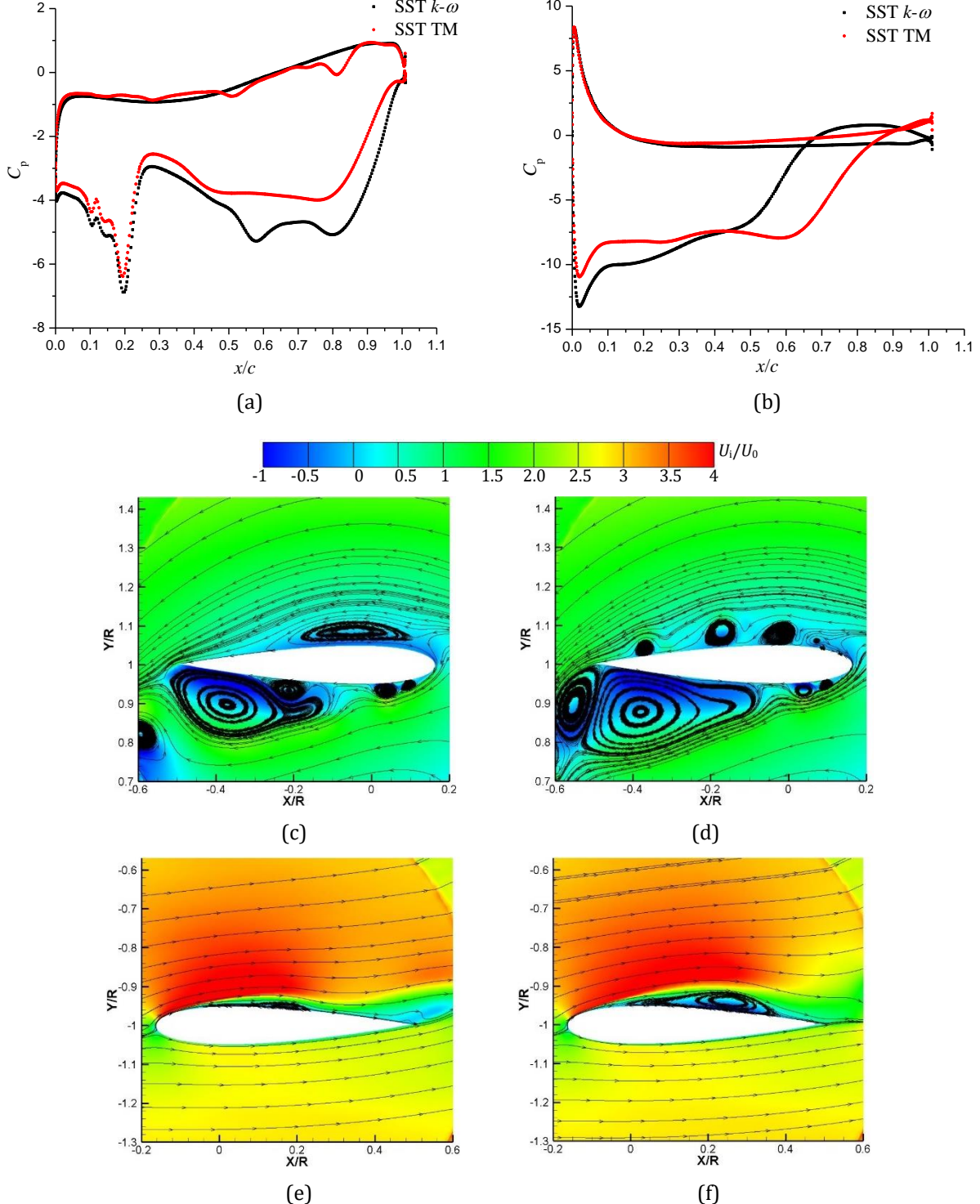


**Fig.2.51** Pressure and relative velocity. (a) Pressure of blade A; (b) Pressure of blade B; (c) and (e) SST  $k-\omega$ ; (d) and (f) SST TM.

#### 2.2.4 Main features of laminar-turbulence transition

In this section, the characteristics of laminar-turbulence transition over the blade surface at two  $\lambda$  for SST  $k-\omega$  model and SST TM are discussed thoroughly. Several positions at advancing side are selected to clarify the transition evolution. The distributions of turbulent kinetic energy at  $\lambda=0.52$  and the corresponding skin friction coefficients  $C_f$  are

displayed in figure 2.52 and 2.53, respectively. In this work, it is found that both two turbulence models can capture the existence of separation bubble, due to the extremely low Reynolds number. But the boundary layer after the separation bubble is fully turbulent for SST  $k-\omega$  model, which indicates that the bubble is a turbulent separation bubble. The Winslow et al. [85] pointed out that there is a large-scale flow separation vortex from the leading edge and the lift curves becomes highly nonlinear because of premature flow separation and failure to reattach, when the Reynolds number is below  $5 \times 10^4$ . However, compared with the SST  $k-\omega$  model, the separation bubble size is larger and it is composed of multiple vortices at the initial stage for SST TM. Dong et al. [38] observed that a nonclassical laminar separation bubble structure, which includes two vortices with the cores locating around the transition point, is evident with the increase of Reynolds number to  $5 \times 10^5$ . For the oscillating airfoil, Negi et al. [90] used the large eddy simulation to investigate the transition over a pitching airfoil with small amplitude, and the main results reveal that there is spatially growing wave of laminar boundary layer when the LSB is absent. These growing waves are amplified gradually with the increases of LSB size, which indicates that the transition is triggered by this laminar boundary layer instability. Usually, after the reattachment, the boundary layer would become fully turbulent until the occurrence of turbulent boundary layer separation, which is often detected over the stationary objectives. However, in figure 2.52b, the boundary layer is still laminar after the reattachment in the inception time, which is presumably ascribed to the laminar flows occupying large portion of upper surface and the delayed transition resulting from the oscillating airfoil [91]. Then, at  $\psi=60^\circ$ , the separation bubble has already formed and it expands towards the middle chord and the separated flow near the trailing edge sheds into the wake gradually. In general, the bubble size obtained by SST TM is relatively larger and the development of transition is predicted more clearly. From the distributions of skin friction coefficients in figure 2.53, it is evident that the laminar flow separation is always near the leading edge and the reattachment point moves downstream with the increase of  $\psi$ . This is because the transition is normally located at the trailing edge when the attack-of-angle is small. Additionally, it is discovered that there is no difference in flow separation point for two turbulence models, but the transition and reattachment locations are more upstream for SST  $k-\omega$  model, as a consequence of the separation bubble size.

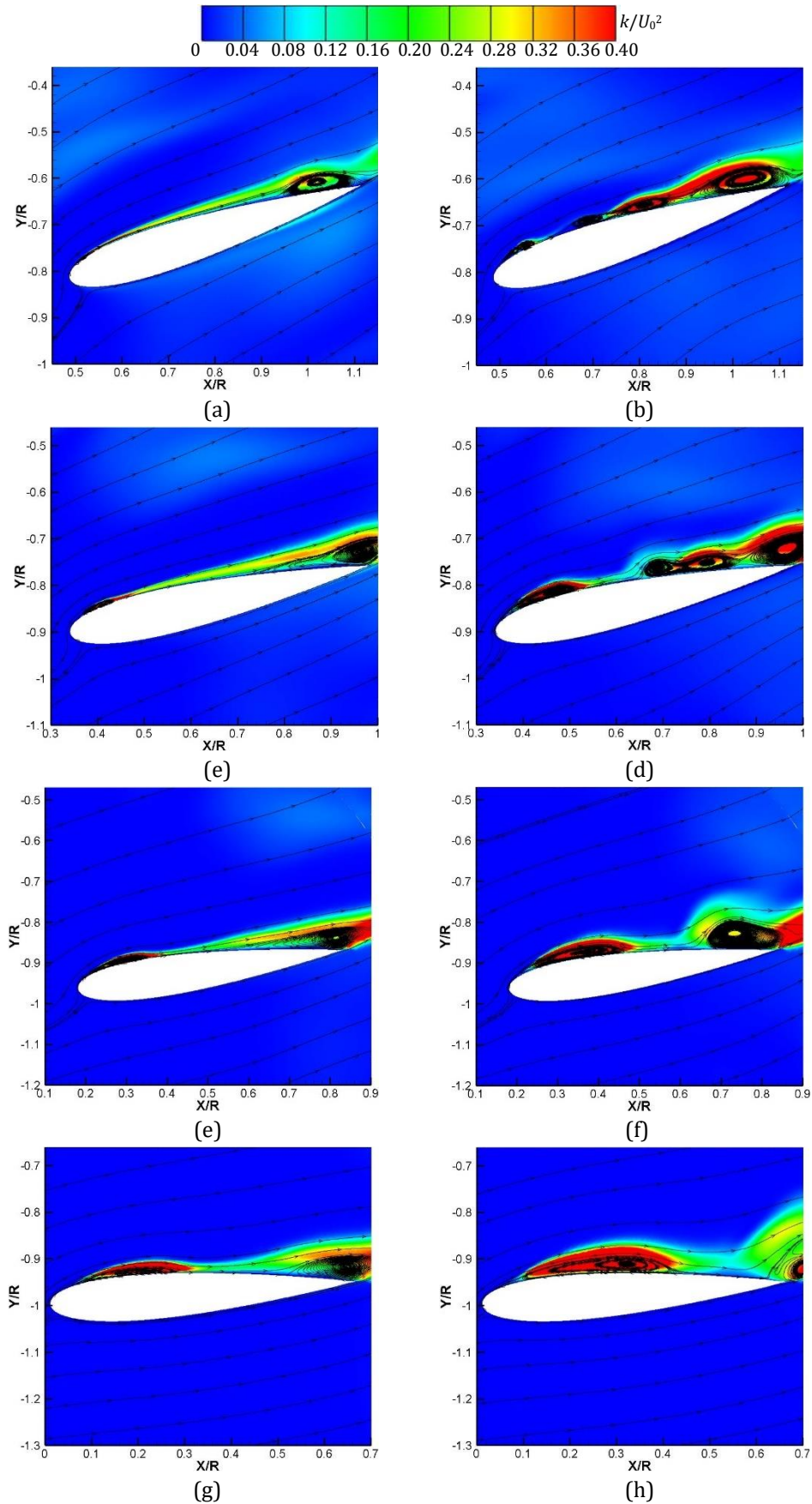


**Fig.2.52** Distributions of turbulent kinetic energy. (a) SST  $k-\omega$  at  $\psi=50^\circ$ ; (b) SST TM at  $\psi=50^\circ$ ; (c) SST  $k-\omega$  at  $\psi=60^\circ$ ; (d) SST TM at  $\psi=60^\circ$ ; (e) SST  $k-\omega$  at  $\psi=70^\circ$ ; (f) SST TM at  $\psi=70^\circ$ ; (g) SST  $k-\omega$  at  $\psi=80^\circ$ ; (h) SST TM at  $\psi=80^\circ$ .

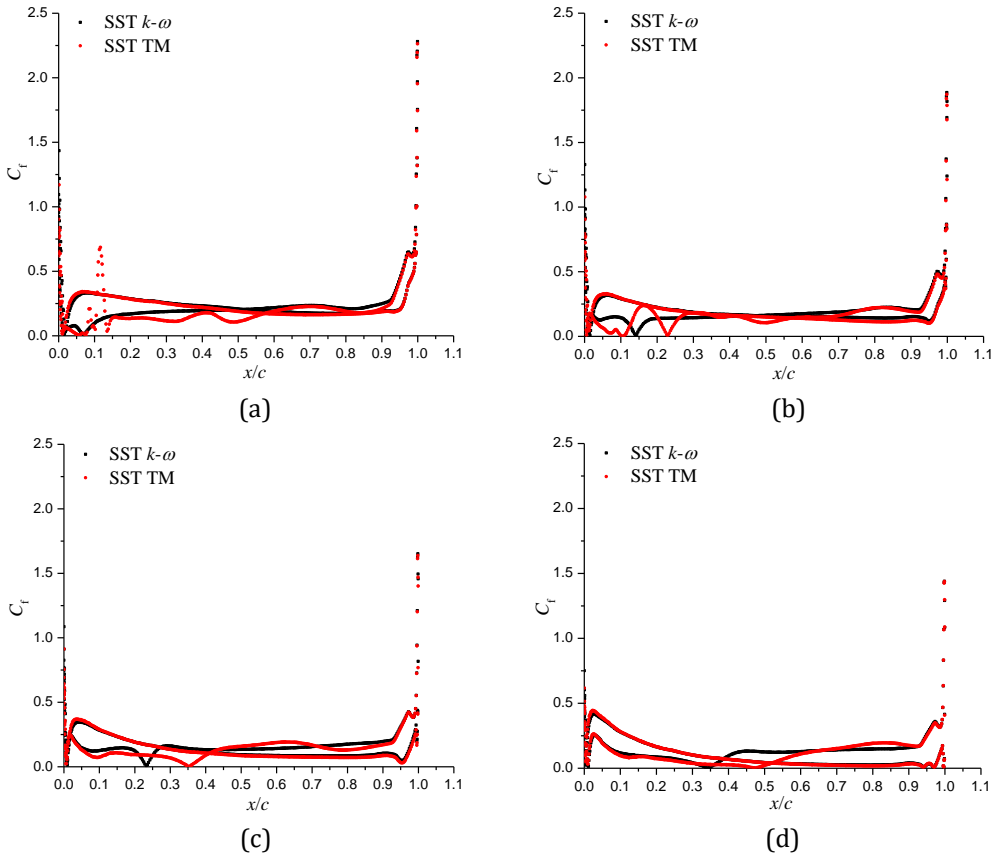


**Fig.2.53** Distributions of skin friction coefficients at different  $\psi$ . (a)  $\psi=50^\circ$ ; (b)  $\psi=60^\circ$ ; (c)  $\psi=70^\circ$ ; (d)  $\psi=80^\circ$ .

Afterwards, the distributions of turbulence kinetic energy and skin friction coefficients at  $\lambda=0.73$  are shown in figure 2.54 and 2.55, respectively. In figure 2.54b, the roll-up vortices cause the growing wave of laminar boundary layer when the separation bubble does not occur. Obviously, the shape of roll-up vortices is much slenderer than that at  $\lambda=0.52$ , due to the change of the relative velocity. When the flow separation appears near the trailing edge, the level of turbulence kinetic energy becomes very high. However, for SST  $k-\omega$  model, the fully turbulent boundary layer is observed after a point and no separation bubble is detected, which means that the formation of separation bubble is delayed as the relative Reynolds number increases. At next moment, as shown in figure 2.54c, the separation bubble emerges and it moves towards the middle chord gradually as the relative attack-of-angle becomes smaller. Then, in figure 2.54f, the region where two vortices co-exist has high level of turbulence kinetic energy, leading to the local transition onset. Downstream from the reattachment point, the boundary layer is still laminar and a vortex is evident, leading to a small change of skin friction coefficient shown in figure 2.55c. Finally, at the incidence where the relative velocity coincides with the foil leading edge, a separation bubble is totally formed by two vortices and the vortex after the reattachment of separation bubble is located near the trailing edge. Generally, it concludes that the roll-up vortices lead to the growing wave of laminar boundary layer and then the local transition onset is induced by two distinctive vortices. Consequently, the single separation bubble is generated by these two vortices and it develops towards the trailing edge. In figure 2.55, it is observed that the roll-up vortices cause the jump of wall shear stress. Increasing the freestream velocity leads to the flow separation, transition and reattachment points moving downstream, especially for reattachment location.

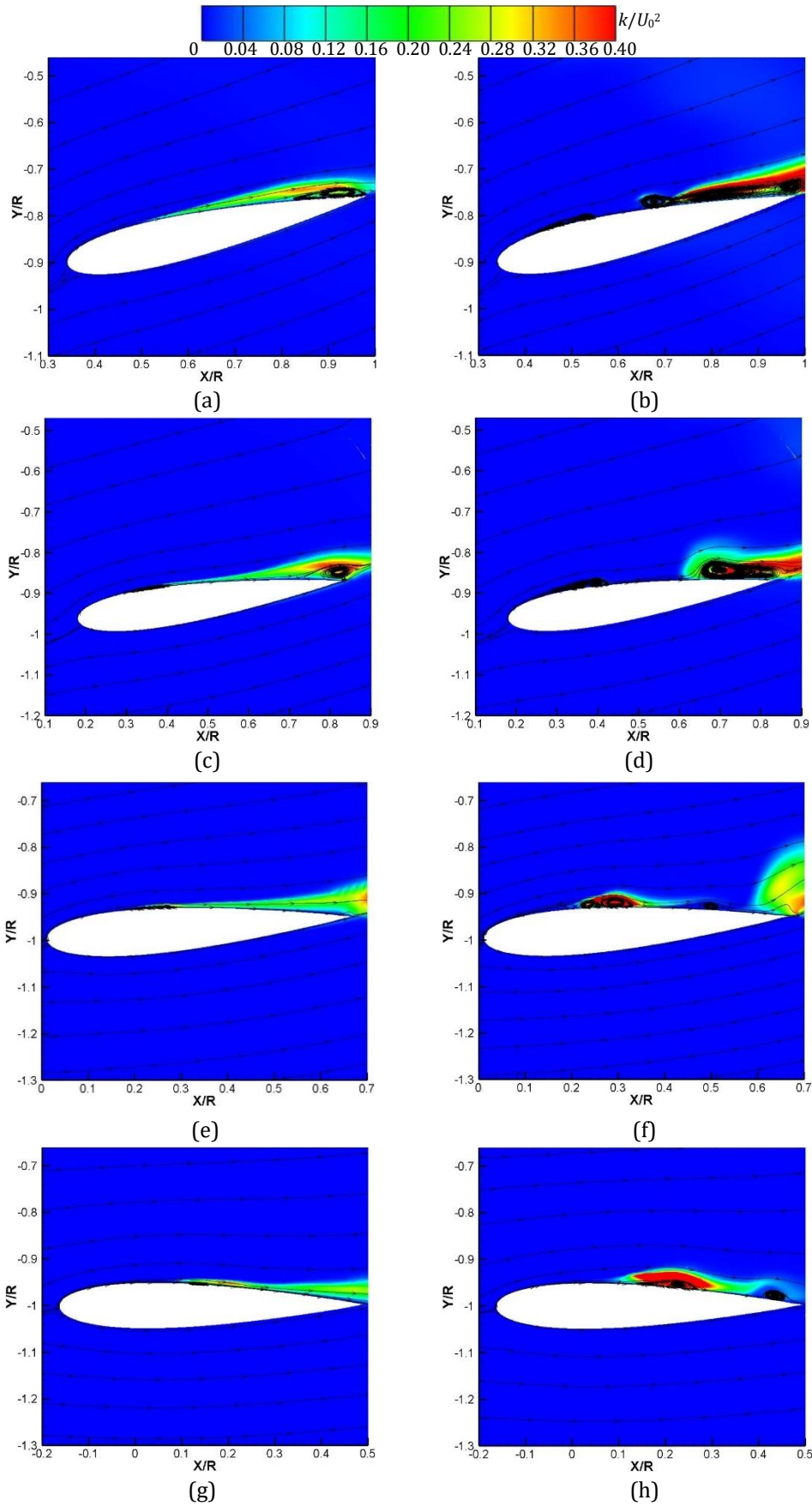


**Fig.2.54** Distributions of turbulent kinetic energy. (a) SST  $k-\omega$  at  $\psi=60^\circ$ ; (b) SST TM at  $\psi=60^\circ$ ; (c) SST  $k-\omega$  at  $\psi=70^\circ$ ; (d) SST TM at  $\psi=70^\circ$ ; (e) SST  $k-\omega$  at  $\psi=80^\circ$ ; (f) SST TM at  $\psi=80^\circ$ ; (g) SST  $k-\omega$  at  $\psi=90^\circ$ ; (h) SST TM at  $\psi=90^\circ$ .

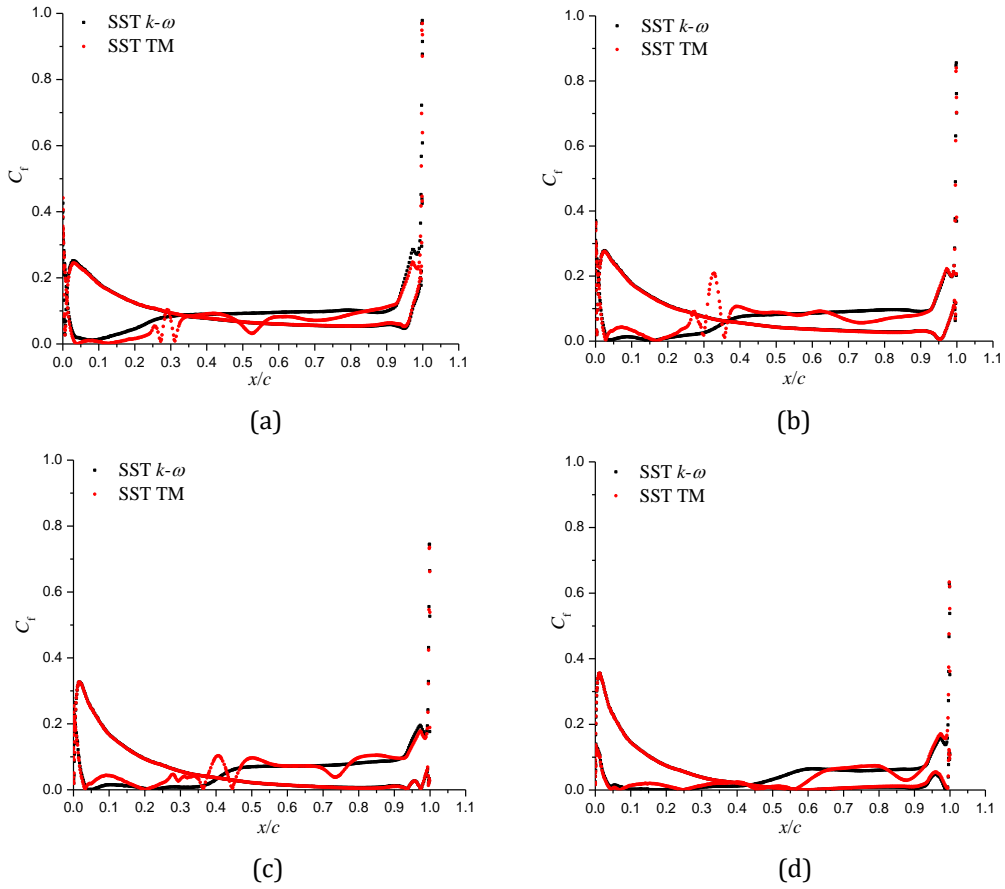


**Fig.2.55** Distributions of skin friction coefficients at different  $\psi$ . (a)  $\psi=60^\circ$ ; (b)  $\psi=70^\circ$ ; (c)  $\psi=80^\circ$ ; (d)  $\psi=90^\circ$ .

## 2.2.5 Conclusions

The unsteady vortical flows and laminar-turbulence transition of a two-bladed cycloidal rotor is investigated using the original SST  $k-\omega$  model and optimized SST TM. The obtained results are compared with the available numerical and experimental data. The main conclusions are listed as follows:

- (1) Among different turbulence models, the SST TM has the superiority in predicting the global performance of the cycloidal rotor, and the results obtained by RSM have large fluctuations due to the very refined mesh and small timestep.
- (2) The transition of the forces and power for one blade is analyzed using the force distributions, which shows that increasing/decreasing  $\lambda$  has no impact on that. The transition of the vertical force is mainly at  $\psi=32^\circ$  and  $144^\circ$ , where the blade profile is almost perpendicular to the horizontal axis, while the propulsive force transition occurs at  $\psi=90^\circ$  and  $270^\circ$  when the blade geometry is parallel to the horizontal axis.
- (3) Near the airfoil surface, the low-pressure and high-pressure zones near the blade leading edge due to the stagnation point deviation, the existence of the attached vortex, the massive flow separation and laminar-turbulence transition induced by the separation bubble, have a great impact on the performance of the cycloidal rotor and single blade. In addition, the blade-wake and wake-wake interactions has a strong effect on the external flow field.
- (4) The main difference of the lift is at  $\psi=30^\circ$  and  $90^\circ$  while it exists at  $\psi=30^\circ$  for the propulsive force, because of the force direction and single blade loading. When analyzing

the force difference of the cycloidal rotor, the force (vertical force and propulsive force) distribution of the single blade, the forces (lift and drag) acting on the blade and the pressure difference of each blade are necessary.

(5) The transition induced by the separation bubble at two  $\lambda$  when the blade undergoes the advancing side are revealed. It concludes that SST TM is highly sensitive to the disturbances and has the capability to capture the evolution of transition, from the growing wave of laminar boundary layer to the fully development of the separation bubble. However, the SST  $k-\omega$  model only resolves the turbulent flows after the formation of the separation bubble.

### 3 PARAMETRICAL STUDY AND OPTIMIZATION OF A CYCLOIDAL ROTOR

#### 3.1 INFLUENCE OF THE PITCHING KINEMATIC

##### 3.1.1 Introduction

In the previous studies, most research employed the symmetrical pitching kinematic for vertical-axis turbines and propellers, which means that the blade has the opposite magnitude of the relative incidence between the blade chord line and tangential direction of the rotating trajectory, at  $\psi=0^\circ$  and  $180^\circ$ . However, if the mean pitch angle is considered, the relative incidences at these two positions are different. In a rotating cycle, due to the variation of the relative incidence, the vortex trajectory and performance of the cycloidal rotor and single blade also change significantly, for cases with various pitching kinematics. Therefore, in this section, the influence of symmetrical and asymmetrical pitching kinematic on the unsteady vortical flows and global performance is investigated.

##### 3.1.2 Symmetrical/asymmetrical pitching kinematics

The 2-blade cycloidal rotor presented previously is considered here, for different rotating speeds and freestream velocity conditions. The symmetrical pitching is defined as  $\theta_A = \theta_{amp}\sin(\psi+\Phi)$  (where  $\theta_{amp}$  is the pitching amplitude set to  $35^\circ$ ), while the asymmetrical pitching kinematic is  $\theta=\theta_0+\theta_{A\sin}(\psi+\Phi)$ . For the asymmetrical pitching kinematic, several values are considered for the mean pitch angle  $\theta_0: 15^\circ, -10^\circ, -5^\circ, 5^\circ, 10^\circ$  and  $15^\circ$ . The results obtained with these different values are compared hereafter to the performance of the symmetrical pitching kinematics.

The symmetrical pitching is considered firstly, for various inlet velocities and rotating speeds. The performance curves (i.e. the time-averaged lift, propulsive force, power coefficients, and efficiency) are shown in figure 3.1. The tested cases have the blade chord length of 0.0495m and the chord-to-radius ratio of 0.65. When  $\lambda$  is increased at constant inlet velocity, the lift, propulsive force and power coefficients decrease significantly, while the efficiency firstly improves and then decreases, which means that the combination of inlet velocity and rotating speed should be in a specific range to obtain the best performance.

For  $\lambda$  varying between 0.47 and 0.56, the efficiency of the cycloidal rotor system improves remarkably from 28.82% to 41.63%, when the inlet velocity is increased. In addition, with a low inlet velocity, although the propulsive force at low advanced coefficient is large, the efficiency remains quite low because of the large power that is consumed. Simultaneously, it is also observed that the lift coefficient has some difference at small advance coefficient condition, especially for the cases with low inlet velocity. Six points with the best efficiency, including at  $\lambda=0.47$  for  $U_0=3\text{m/s}$ ,  $\lambda=0.50$  for  $U_0=4\text{m/s}$ ,  $\lambda=0.52$  for  $U_0=5\text{m/s}$ ,  $\lambda=0.54$  for  $U_0=6\text{m/s}$ ,  $\lambda=0.55$  for  $U_0=7\text{m/s}$  and  $\lambda=0.56$  for  $U_0=8\text{m/s}$ , are selected to study the influence of the pitching kinematic on the performance and flow structures of the rotating system and the single blade.

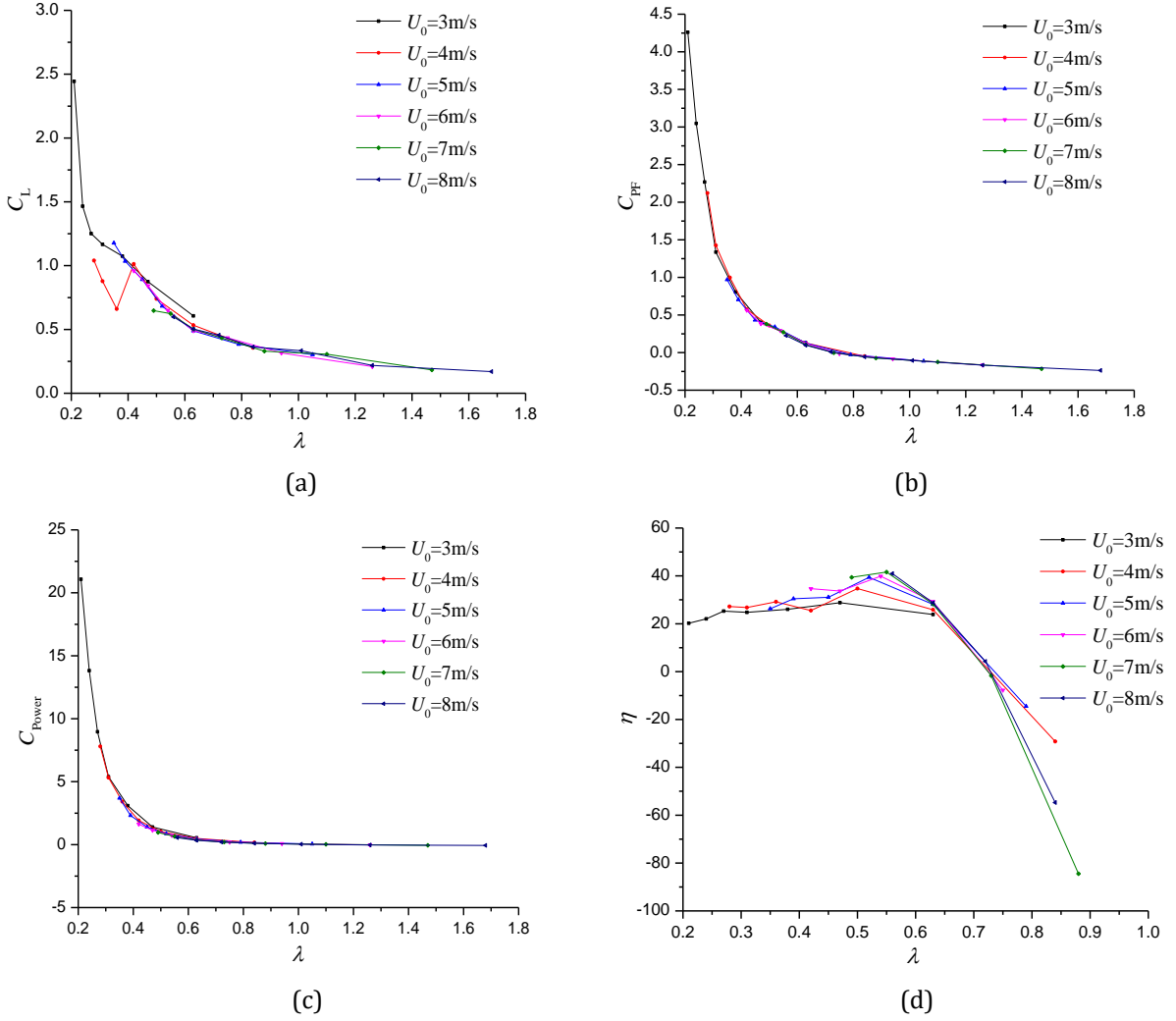


**Fig.3.1** Performance curves at different  $\lambda$ . (a) Lift coefficient; (b) Propulsive force coefficient; (c) Power coefficient; (d) Efficiency.

In figure 3.2, the performance curves are plotted at the best efficiency conditions shown in figure 3.1d, for different pitching kinematics. For a better understanding, the variation of the angle-of-attack for several cases are also presented in figure 3.2e. In these figures, ‘ $5^\circ$ - $35^\circ$ ’ indicates the combination of the mean pitch angle and the pitching amplitude. For the symmetrical pitching, the lift coefficient exhibits no significant change at different  $\lambda$  when the pitching amplitude does not exceed the value of  $35^\circ$ . For the pitching amplitude between  $35^\circ$  and  $55^\circ$ , the lift coefficient increases dramatically when  $\lambda$  is larger than 0.5. When the mean pitch angle is negative, the lift coefficient shows an evident increase, while the trend is opposite in cases with the positive mean pitch angle. It can be observed that the symmetrical pitching with amplitudes of  $45^\circ$  and  $55^\circ$  produce a large propulsive force coefficient, which increases significantly with  $\lambda$ . Conversely, pitching amplitudes lower than  $25^\circ$  generate the lowest propulsive force coefficient, which even decrease more at large  $\lambda$ . At fixed amplitude, the propulsive force coefficient obtained with a positive mean pitch angle increases slowly with  $\lambda$  while it shows the opposite trend for a negative mean pitch angle. Figure 3.2c shows that the symmetrical pitching with large amplitude and the asymmetrical pitching with large negative mean pitch angles are more power-consuming than other cases, which is related to the energy loss induced by the more complex internal flow structures. At the same  $\lambda$ , though the

propulsive force coefficient predicted by the symmetrical pitching with large amplitude is much larger, the efficiency is not improved, due to the large power. The asymmetrical pitching with negative mean pitch angle shows the worst efficiency, compared with the cases with a positive mean pitch angle. Globally, it can be concluded that the asymmetrical pitching with a positive mean pitch angle of  $5^\circ$  generates the best performance.

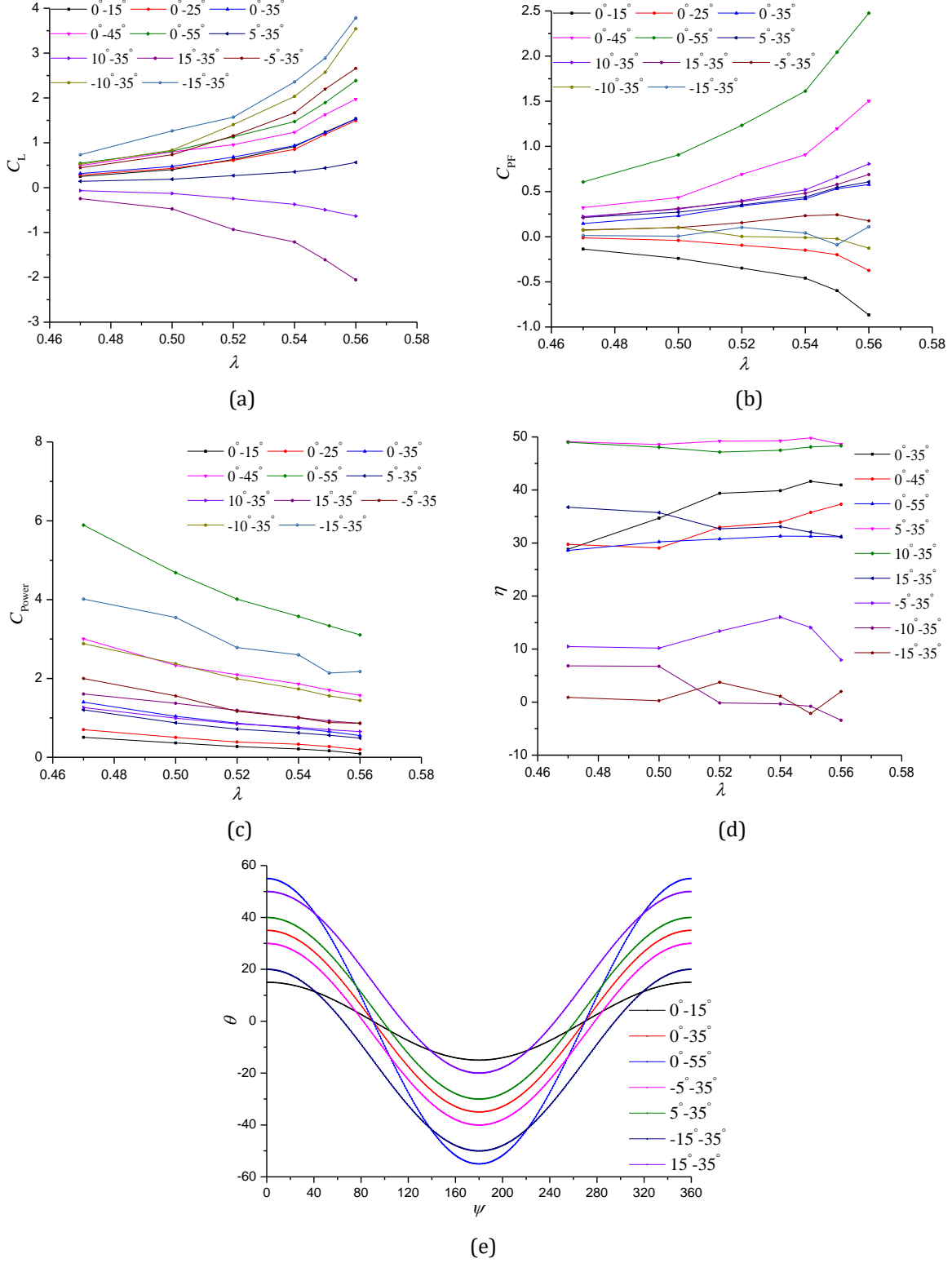


**Fig.3.2** Performance curves at different  $\lambda$  for various pitching kinematics. (a) Lift coefficient; (b) Propulsive force coefficient; (c) Power coefficient; (d) Efficiency; (e) Variation of incidence.

The distributions of spanwise vorticity obtained in the cases of symmetrical and asymmetrical pitching kinematics are displayed in figure 3.3 at  $\psi=0^\circ$ . The asymmetrical pitching is controlled by changing the mean pitch angle, while the pitching amplitude remains unchanged, equal to  $35^\circ$ . The inlet velocity is set to  $U_0=5\text{m/s}$ , and the corresponding advance coefficient is 0.52. For the symmetrical pitching, when the pitching amplitude is increased (figures 3.3a to 3.3c), vortices shed in the wake of blade A have a stronger interaction with blade B. Additionally, at a pitching amplitude of  $15^\circ$ , it is clear that wake B interacts with wake A. At high pitching amplitude, there is also an interaction between blade B and wake B, which indicates that there is a transition from wake A-wake B to wake A-blade B, and finally wake B-blade B interactions. Besides, the massive flow separation is visible on the left side of blade A when the pitching amplitude is  $55^\circ$ , which certainly greatly impacts the blade loading. When the mean pitch angle is equal to  $5^\circ$  (the amplitude being the same), the global flow pattern remains similar (see figures 3.3b and 3.3d), but the flow starts to separate at the leading edge of blade A, on its left side. With a mean pitch angle of  $-5^\circ$ , blade B has a large risk of interaction with the vortices shed in the wake of blade A. Moreover, on the right side of blade A, there is a substantial flow separation. Finally, as the mean pitch angle increases to  $15^\circ$  or  $-15^\circ$ , wake A is more likely to interact with blade B and there is also an obvious interaction between the leading edge and the trail vortices of blade B. Globally, the flow structures over the two blades are much different in these different configurations. For example, some flow separation is detected on the left side of blade A in figure 3.3f, while it is on the right side of the blade in figure 3.3g, where it also occurs on blade B. Thus, it can be concluded that the complicated flow field within a cycloidal rotor, involving different kinds of blade-wake, wake-wake interactions and massive flow separation over the two blades, depends considerably on the pitching kinematics, especially for the symmetrical pitching with large amplitude and asymmetrical pitching with large mean pitch angle.

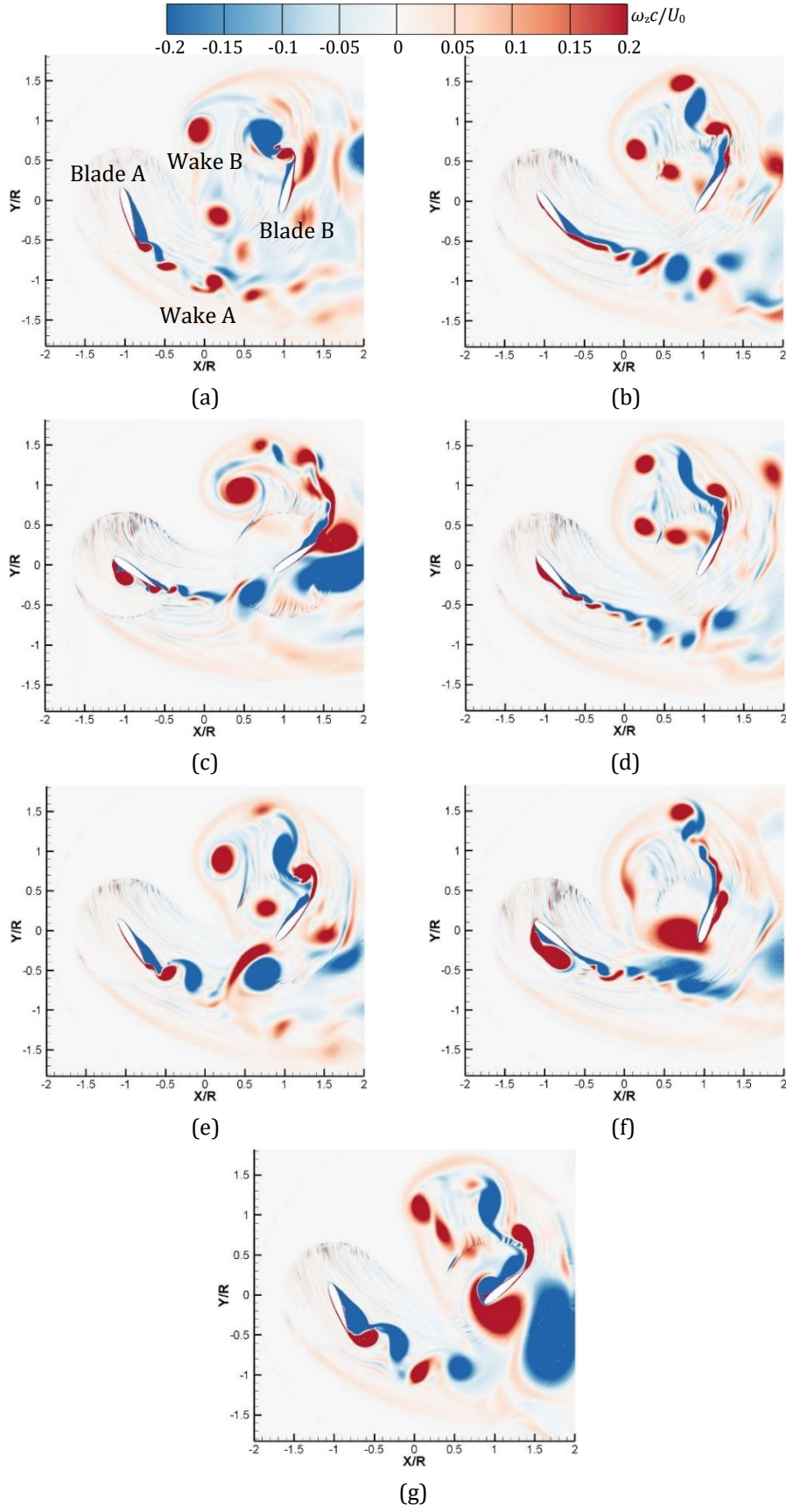


**Fig.3.3** Flow structures for different pitching kinematics. (a)  $\theta=15^\circ \sin(\psi+\pi/2)$ ; (b)  $\theta=35^\circ \sin(\psi+\pi/2)$ ; (c)  $\theta=55^\circ \sin(\psi+\pi/2)$ ; (d)  $\theta=5^\circ + 35^\circ \sin(\psi+\pi/2)$ ; (e)  $\theta=-5^\circ + 35^\circ \sin(\psi+\pi/2)$ ; (f)  $\theta=15^\circ + 35^\circ \sin(\psi+\pi/2)$ ; (g)  $\theta=-15^\circ + 35^\circ \sin(\psi+\pi/2)$ .

Two cases with symmetrical pitching and three cases with asymmetrical pitching at  $\lambda=0.52$ , are considered to investigate the performance of both the propeller and a single blade during one rotation, as shown in figure 3.4. It is found that the symmetrical pitching with an amplitude of  $55^\circ$  produces the largest lift and propulsive force coefficients. Relatively high values of lift coefficients are obtained by the asymmetrical pitching with negative mean pitch angle, followed by the symmetrical pitching with amplitude of  $35^\circ$ . Evidently, the cases with a positive mean pitch angle generate the lowest lift coefficient, but a higher propulsive force coefficient, as shown in figure 3.4b. Based on the performance evolution of the single blade, it can be seen that the difference of vertical force coefficient production for different cases becomes larger gradually when the azimuthal angle exceeds  $160^\circ$ , which is closely associated with the distribution of relative incidence shown in figure 3.2e. Simultaneously, the differences in the propulsive force coefficient are observed during almost all the cycle. Consequently, two azimuthal angles of  $35^\circ$  and  $123^\circ$ , coupled with two positions at  $\psi=35^\circ$  and  $160^\circ$ , are analyzed in more detail to explain the difference of vertical force and propulsive force coefficients, respectively, for five pitching kinematics. At the same time, the locations of  $15^\circ$ ,  $75^\circ$  and  $147^\circ$ , represented by the dash lines in figure 3.4b, are employed to describe the large variation of propulsive force coefficient for the symmetrical pitching with amplitude of  $55^\circ$ .

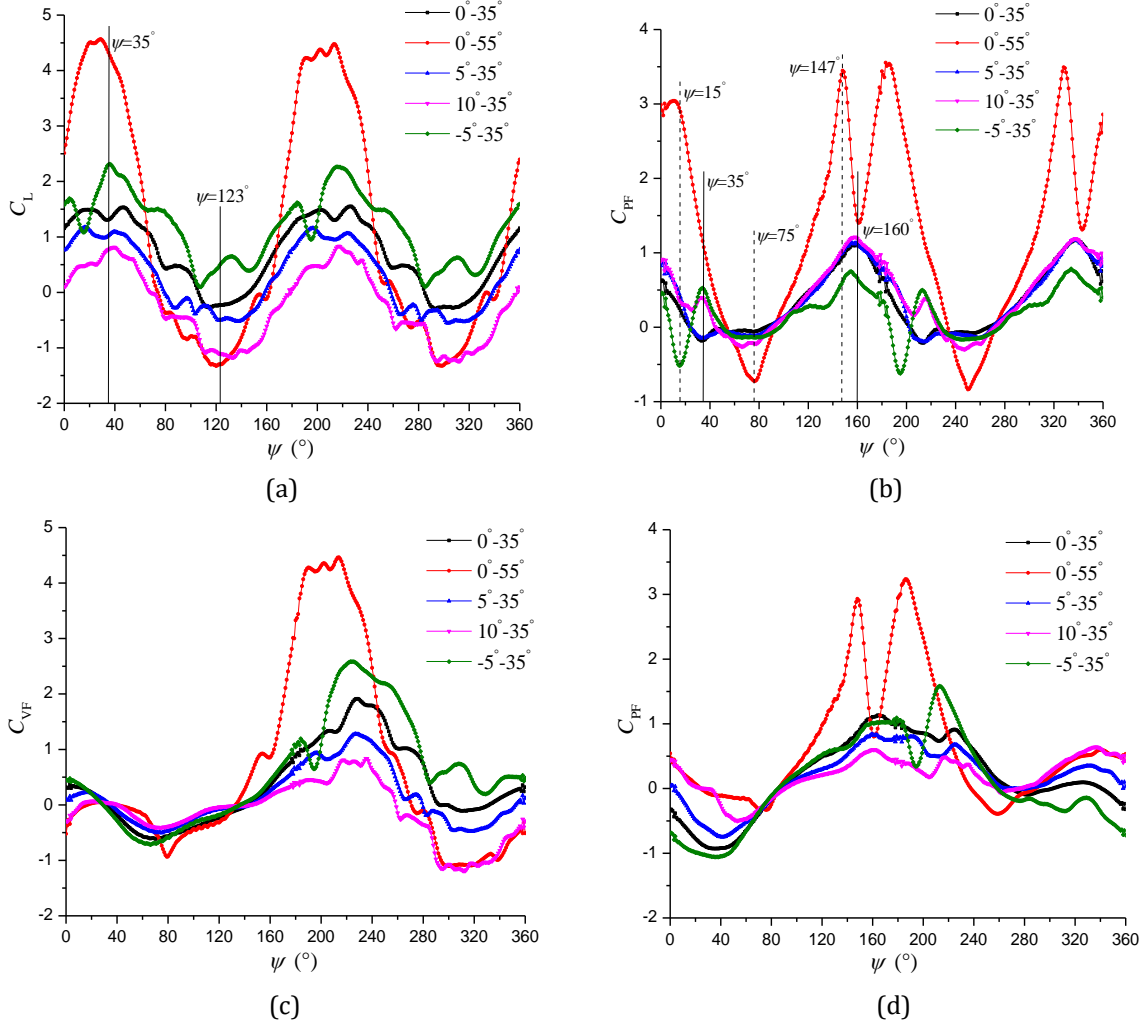
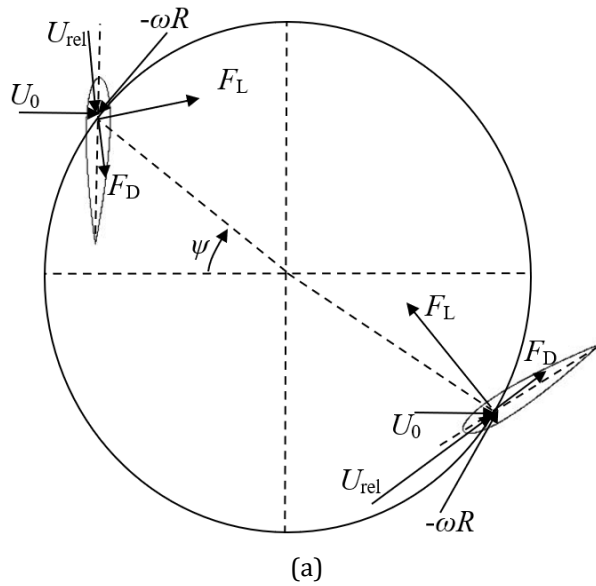


**Fig.3.4** Performance curves for various pitching kinematics in a revolution. (a) Lift coefficient of the rotating system; (b) Propulsive force coefficient of the rotating system; (c) Vertical force coefficient of single blade; (d) Propulsive force coefficient of single blade.

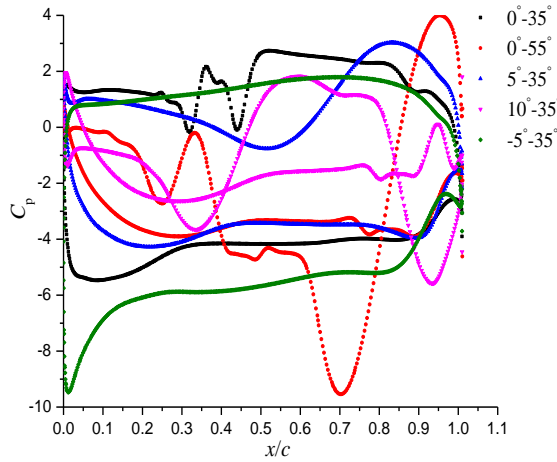
The pressure distributions and flow fields at  $\psi=35^\circ$  are displayed in figure 3.5, 3.6 and 3.7 for different cases. As a supplement, the forces (lift and drag) and pressure coefficients of two blades are also shown to describe the force difference in figure 3.4. For blade A (left blade), three distinctive vortex structures are attached on the left surface when the pitching amplitude is  $55^\circ$ , which was also observed by Choudhuri and Knight [92] on a pitching airfoil at  $Re=1\times 10^4$ . Recently, Tseng and Hu [33] applied Lagrangian coherent structures (LCS) to a pitching airfoil operating at  $Re=4.5\times 10^3$  and captured the co-existence of the leading-edge vortex (LEV), vortex A and B. They clarified that the generation of vortex B is due to the existence of vortex A which separates the connection between the shear layer and the LEV. Moreover, vortex A rotating in the opposite direction compared with vortex B and LEV, is mainly formed by the reverse flow from the other side and the fluid flow around the outer edge of LEV. In figure 3.6a, a series of roll-up vortices emerge in the laminar boundary layer. On a pitching airfoil, Negi et al. [90] found that these vortices are the main sources of laminar boundary layer instability when LSB is absent. In addition, it is reasonable that the transition model is easily subjected to the disturbances. When the positive mean pitch angle is small, vortex B occupies a large part of blade surface and LEV has already shed into the wake. However, as the mean pitch angle increases to  $10^\circ$ , vortex B is at the development stage and the LEV still remains near the trailing edge. For the case with a mean pitch angle of  $-5^\circ$ , only a small scale is visible on the left side. Based on the velocity figures, it seems that the flow structures on the two sides of blade A depend on the position of the stagnation point due to the relative angle-of-attack. For an instance, in figure 3.6b, the stagnation point shifts towards the right side, leading to a relatively weak flow separation, compared with the case in figure 3.6a. However, the flow separation on the left side is stronger. Although the flow over blade A is more complex, the vertical force shown in figure 3.4c for different cases are almost the same. This is related to the balance of lift and drag components, presented by the force analysis in figure 3.5a.

On the suction side of blade B (right blade) in figure 3.7b, there is a large amount of vortex, like on the left side of blade A, resulting in the extremely low pressure. Because the lift of the rotating system is mainly produced by blade B, the vertical force provided by symmetrical pitching with large amplitude has the largest value. Meanwhile, due to the relatively small pressure difference in figure 3.5c for the case with mean pitch angle of  $10^\circ$ , the lift of the rotating system is the smallest. When the mean pitch angle is negative, a laminar separation bubble (LSB) is detected near the leading edge.

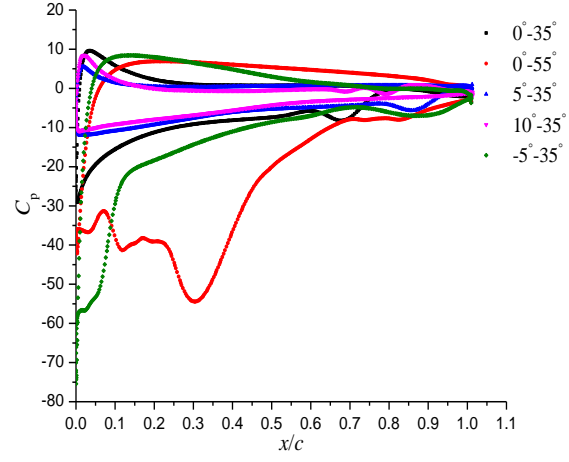
Then, the propulsive force at this location also exhibits much difference in various cases. Blade A generates a negative propulsive force while a positive propulsive force is produced by blade B, shown in figure 3.4d and 3.5a. For the case with a mean pitch angle of  $-5^\circ$ , blade A has the largest pressure difference, resulting in a large negative propulsive force. Simultaneously, the positive propulsive force provided by blade B is also large due to the large pressure difference in figure 3.5c. Therefore, the propulsive force of the rotating system has a relatively large magnitude. Similarly, for the symmetrical pitching with an amplitude of  $35^\circ$ , because of the small lift generated by blade B, the positive propulsive force is smaller than the negative propulsive force produced by blade A, so the total propulsive force has the lowest value. In general, it can be concluded that the lift of the rotating system is determined by blade B while both blade A and B are responsible for the propulsive force at  $\psi=35^\circ$ , which is closely associated with the pressure difference of two blades.



(a)



(b)



(c)

**Fig.3.5** Pressure distributions for various pitching kinematics at  $\psi=35^\circ$ . (a) Sketch of force; (b) Pressure distribution of blade A; (c) Pressure distribution of blade B.

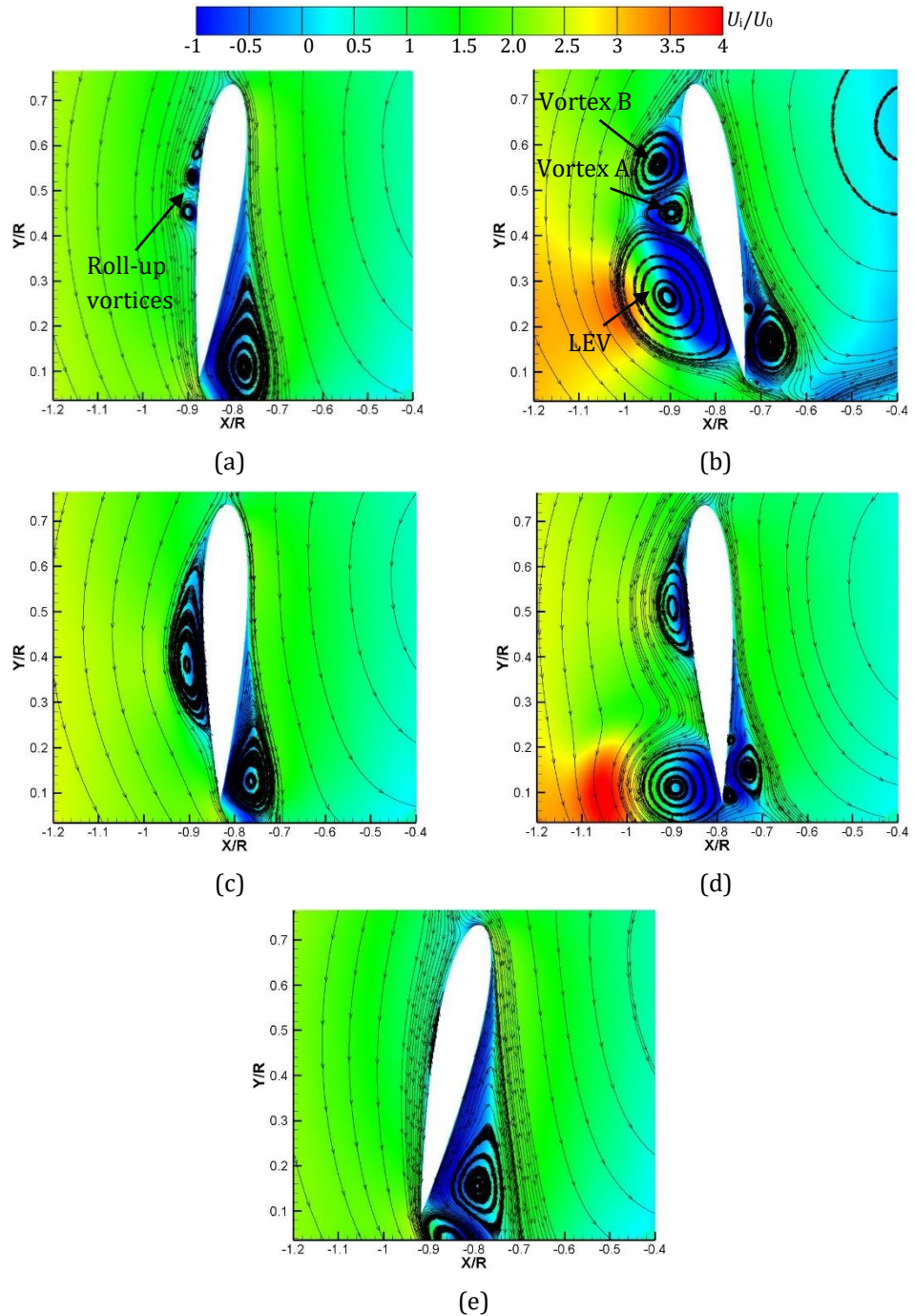


**Fig.3.6** Flow structures of blade A for various pitching kinematics at  $\psi=35^\circ$ . (a)  $0^\circ-35^\circ$ ; (b)  $0^\circ-55^\circ$ ; (c)  $5^\circ-35^\circ$ ; (d)  $10^\circ-35^\circ$ ; (e)  $-5^\circ-35^\circ$ .

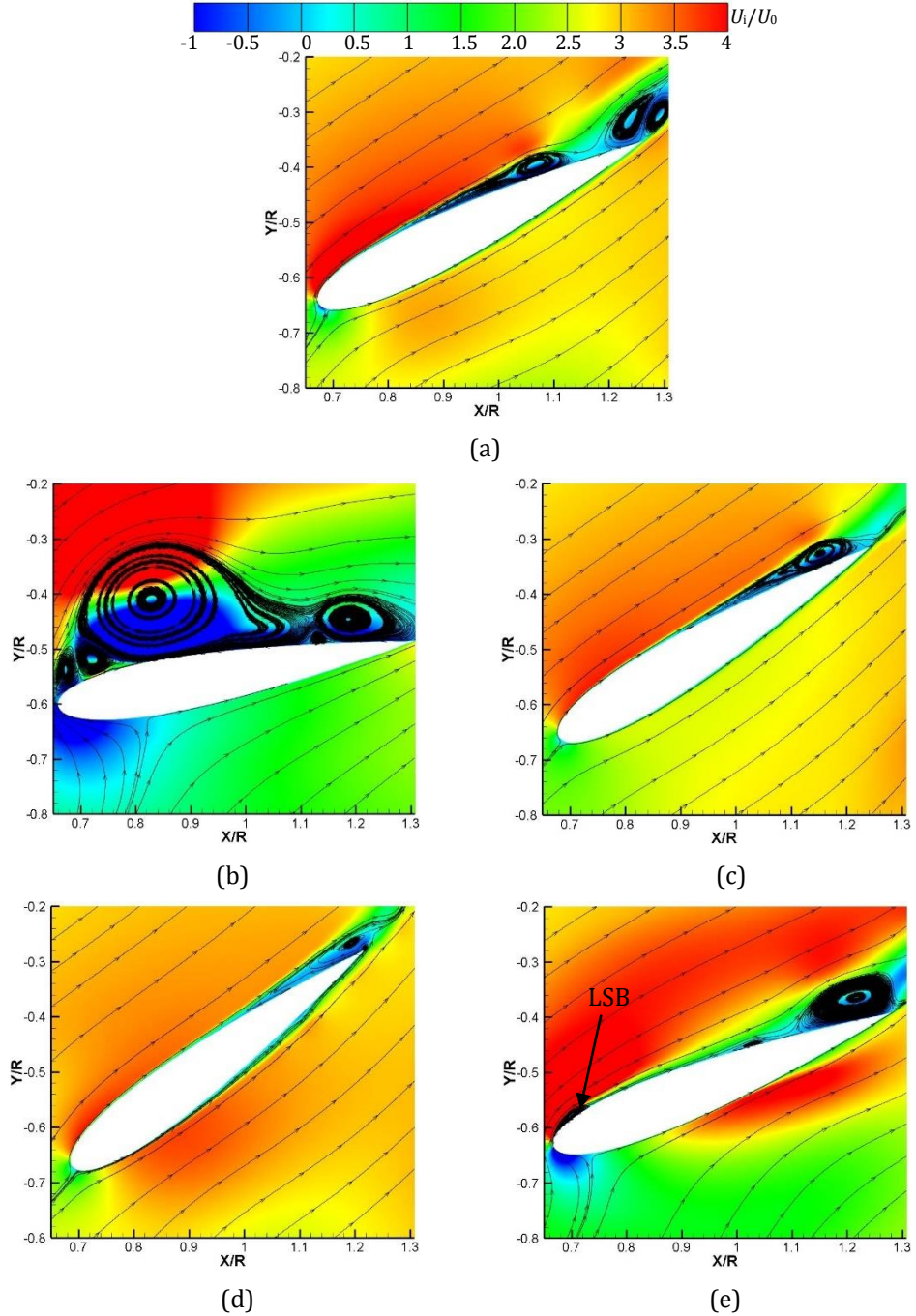


**Fig.3.7** Flow structures of blade B for various pitching kinematics at  $\psi=35^\circ$ . (a)  $0^\circ-35^\circ$ ; (b)  $0^\circ-55^\circ$ ; (c)  $5^\circ-35^\circ$ ; (d)  $10^\circ-35^\circ$ ; (e)  $-5^\circ-35^\circ$ .

Then, figure 3.8, 3.9 and 3.10 show the flow field over the surfaces of two blades at  $\psi=123^\circ$ , when the lift of the rotating system is dropping as shown in figure 3.4a. At this position, the blade A is experiencing the retreating side, and the flow separation mainly emerges on the suction side at the trailing edge, where the trailing edge vortex (TEV) interacts with the LEV, especially for the case in figure 3.9c. For the symmetrical pitching with an amplitude of  $55^\circ$ , the flow is relatively smooth on the suction side, but the pressure is sufficiently low due to the large relative incidence. When the mean pitch angle is  $10^\circ$ , a large-scale vortex remains near the trailing edge on the pressure side, resulting in the pressure drop visible in figure 3.8b. According to the force sketch in figure 3.8a, the lift component is larger than the drag component, especially for the symmetrical pitching

with an amplitude of  $55^\circ$ , which is producing the large blade loading, resulting in the negative vertical force of blade A shown in figure 3.4c.

The lift of blade B has not the same direction for various pitching kinematics. For example, for the case in figure 3.10e, due to the presence of the LEV on the upper surface, the resultant lift of blade B is upward (the opposite direction in figure 3.8a). However, when the blade operates with the symmetrical pitching with an amplitude of  $55^\circ$  or an asymmetrical pitching with positive mean pitch angles, the lift of blade B is downward, as shown in figure 3.8a, creating the negative vertical force. When the mean pitch angle is  $10^\circ$ , the large pressure difference in figure 3.8c leads to the generation of a large lift on blade B, so the vertical force in figure 3.4c has a large negative value. It can be seen that the lift direction of blade B has a close relationship with the stagnation point location. When the stagnation point shifts towards the upper surface, the flow separation occurs on the lower surface, resulting in the downward lift. Finally, it can be concluded that the lift difference of the rotating system for various cases is generally caused by the lift direction of blade B because of the stagnation point location.

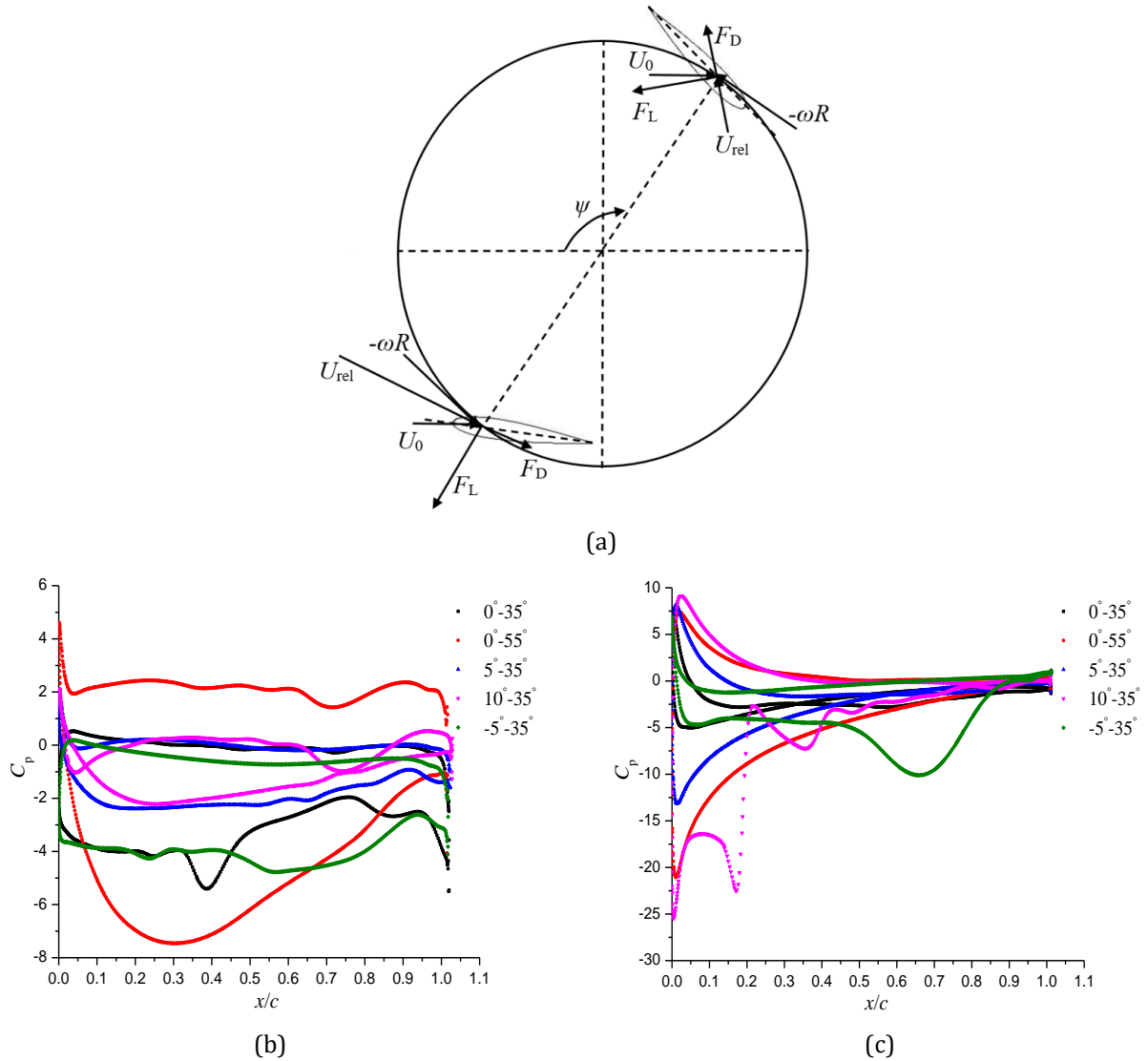


**Fig.3.8** Pressure distributions for various pitching kinematics at  $\psi=123^\circ$ . (a) Sketch of force; (b) Pressure distribution of blade A; (c) Pressure distribution of blade B.

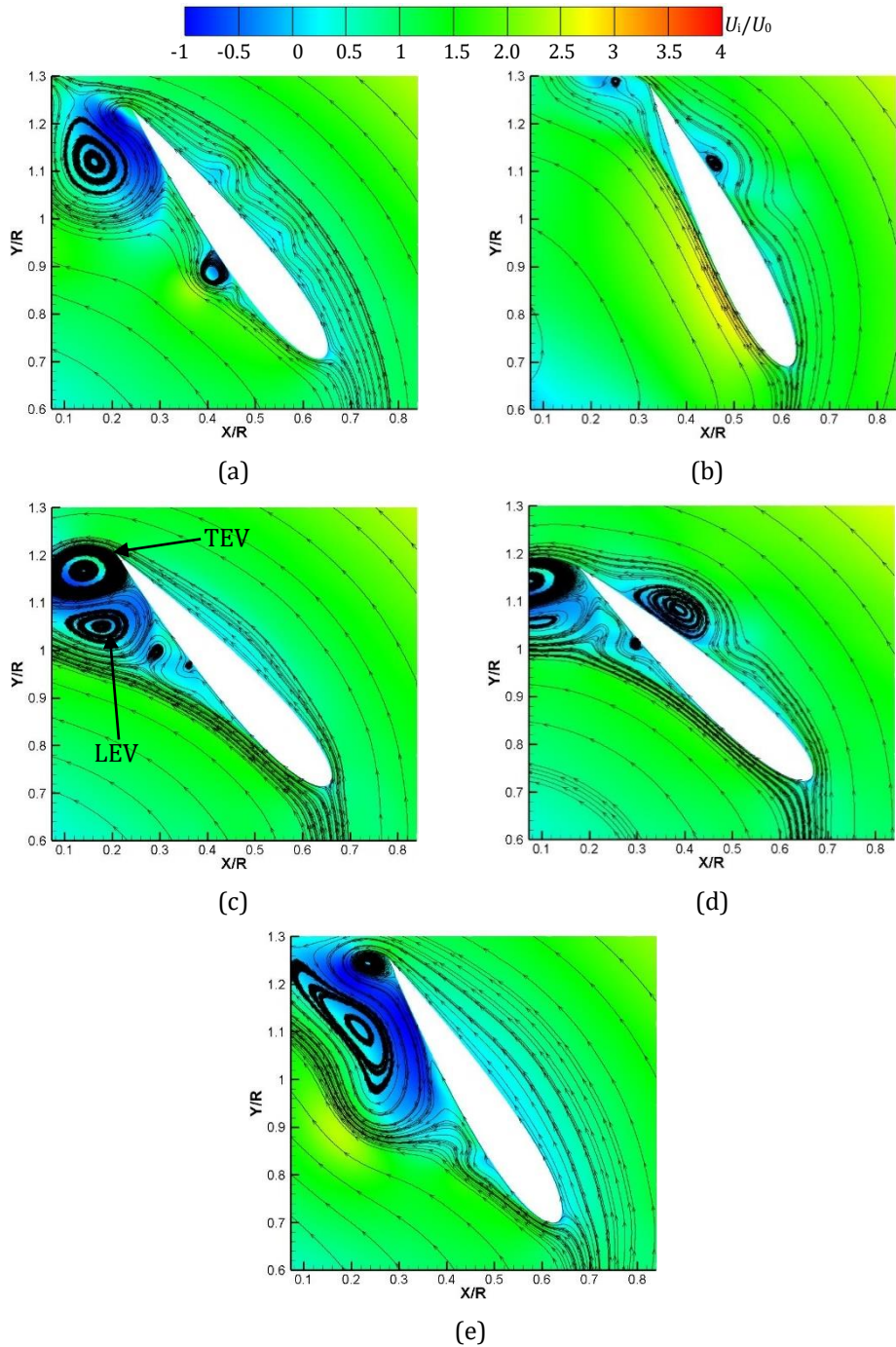


**Fig.3.9** Flow structures of blade A for various pitching kinematics at  $\psi=123^\circ$ . (a)  $0^\circ$ - $35^\circ$ ; (b)  $0^\circ$ - $55^\circ$ ; (c)  $5^\circ$ - $35^\circ$ ; (d)  $10^\circ$ - $35^\circ$ ; (e)  $-5^\circ$ - $35^\circ$ .

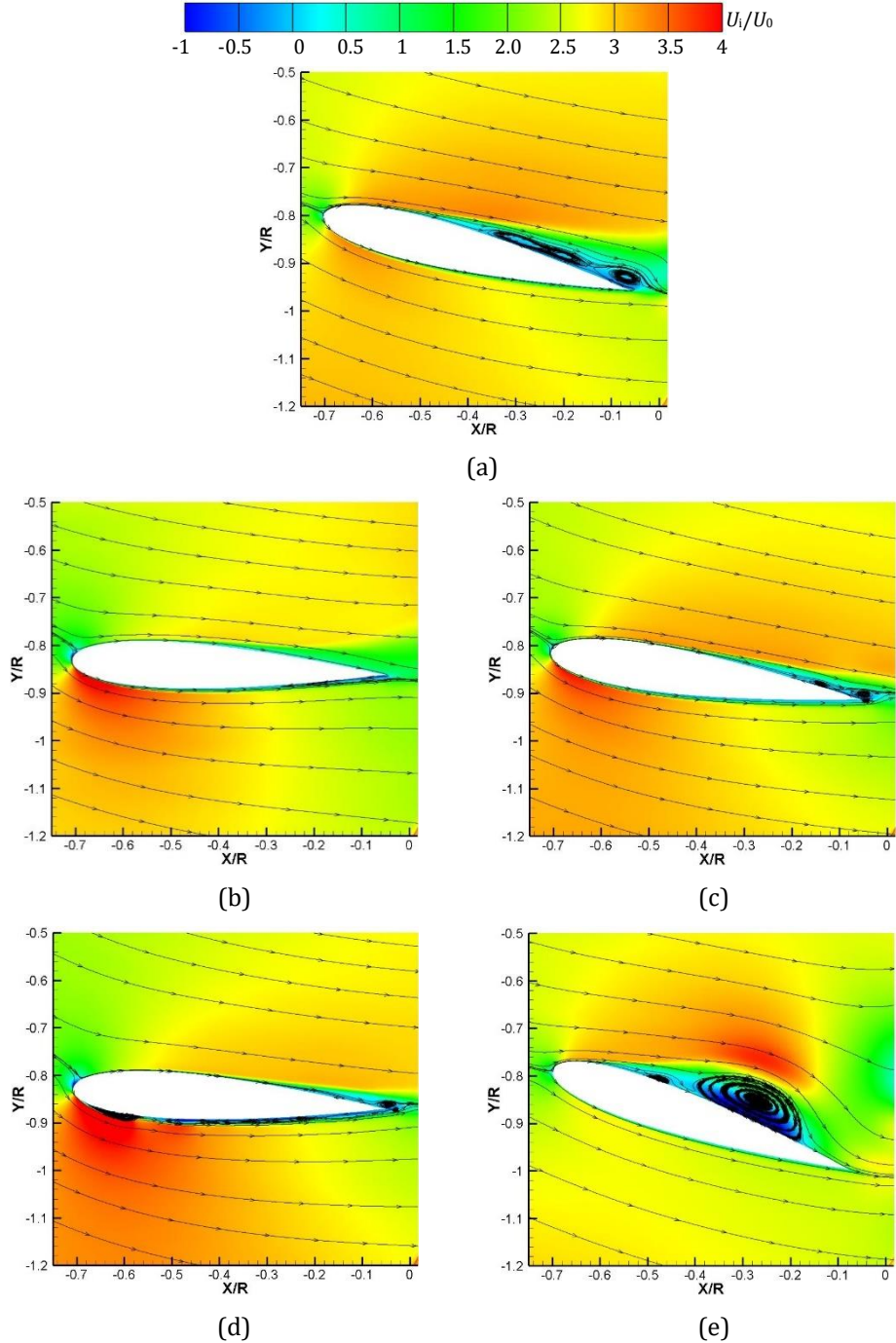
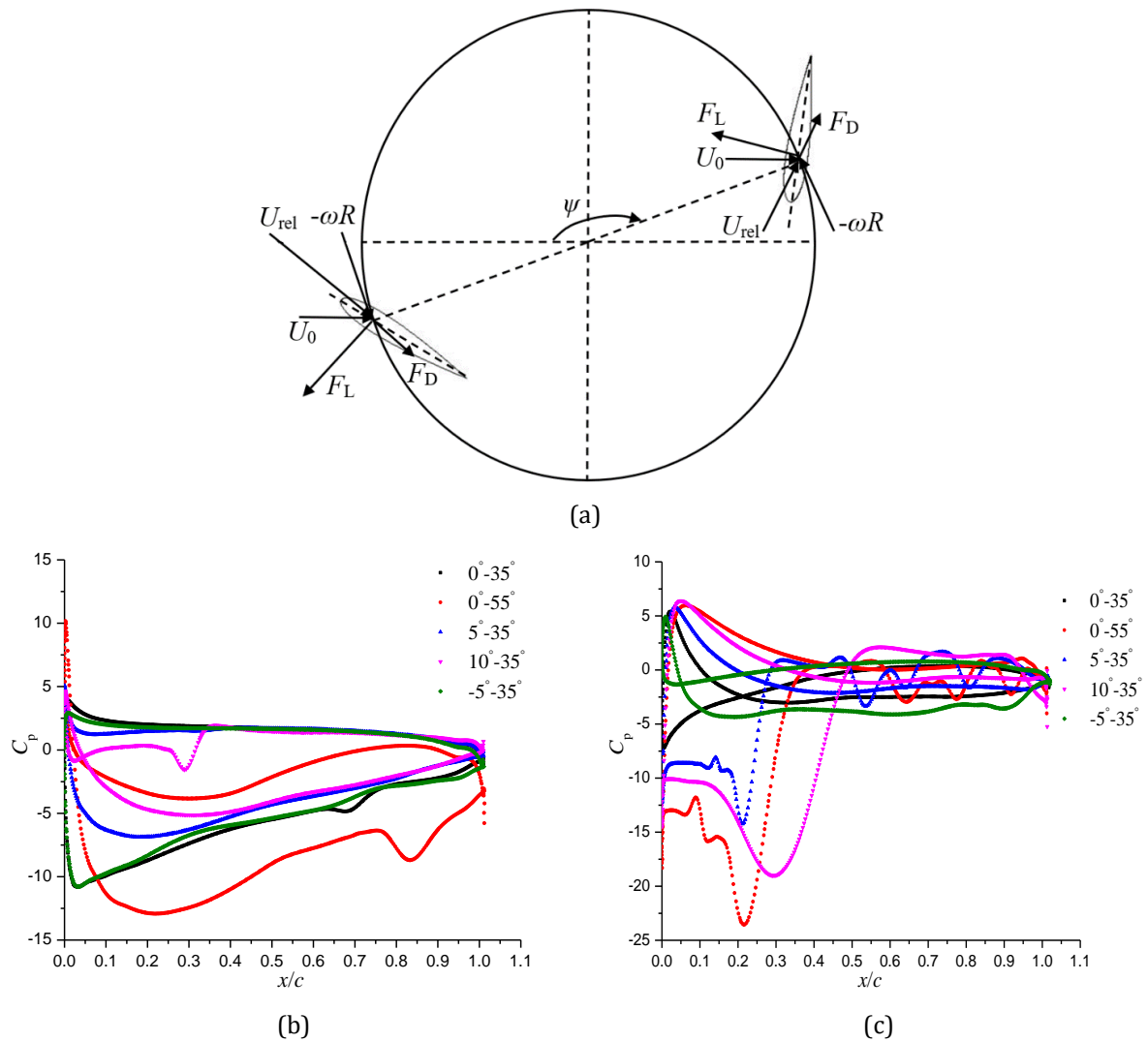


**Fig.3.10** Flow structures of blade B for various pitching kinematics at  $\psi=123^\circ$ . (a)  $0^\circ$ - $35^\circ$ ; (b)  $0^\circ$ - $55^\circ$ ; (c)  $5^\circ$ - $35^\circ$ ; (d)  $10^\circ$ - $35^\circ$ ; (e)  $-5^\circ$ - $35^\circ$ .

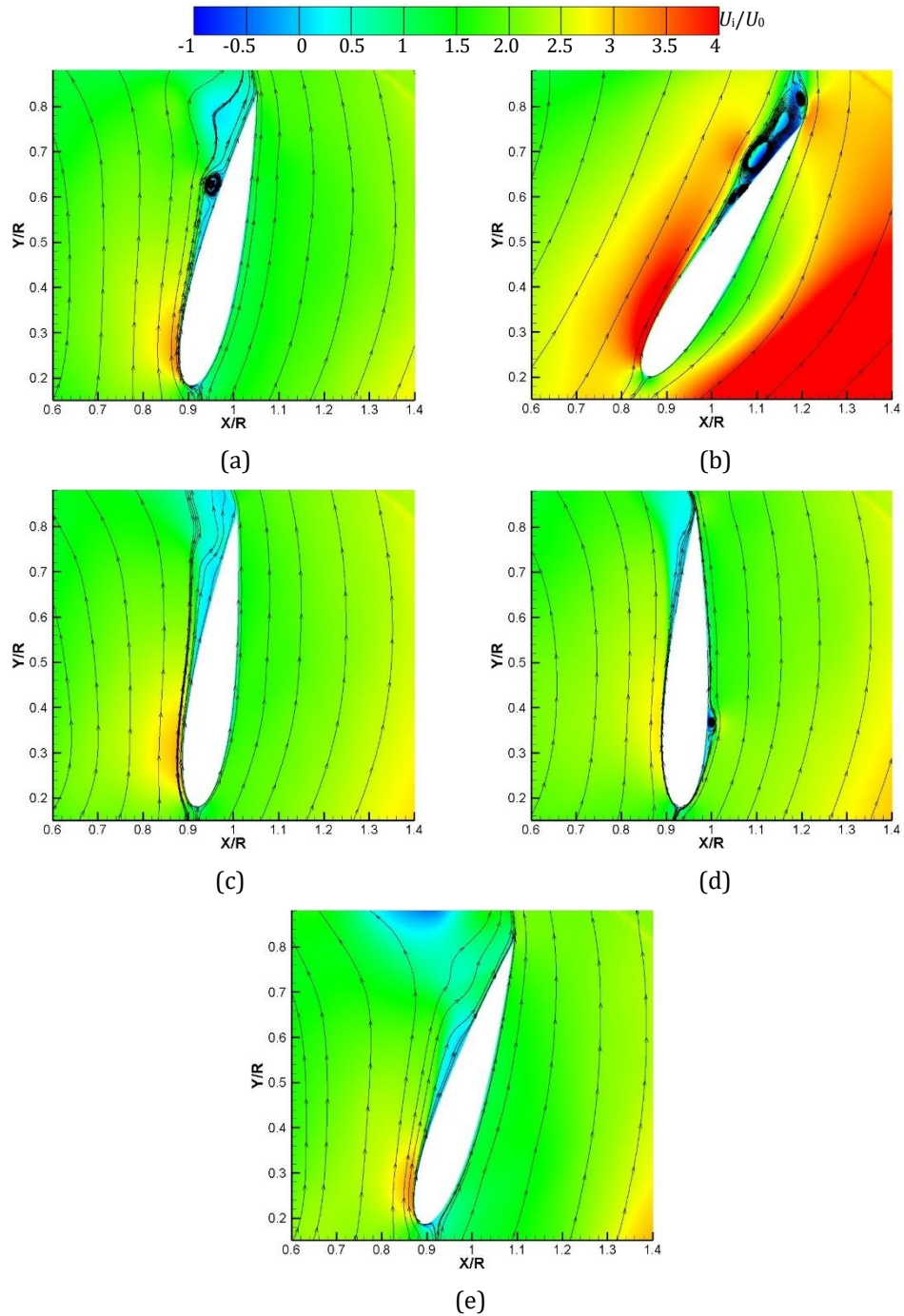
At  $\psi=160^\circ$ , in figure 3.4b, the propulsive force shows large differences between the symmetrical pitching with an amplitude of  $55^\circ$  and the asymmetrical pitching with a negative mean pitch angle. Thus, the flows over the two blade surfaces are displayed in figure 3.11, 3.12 and 3.13. The separation flow only appears on the suction side of blade A when the blade has the symmetrical pitching. With the increase of the pitching amplitude, the flow separation is more obvious in figure 3.12b due to the relatively large incidence. From the pressure distribution in figure 3.11b, it seems that the pressure on both sides for the symmetrical pitching with large amplitude differ from that for other cases, as a consequence of the incidence and stagnation point location. At this position,

the propulsive force of blade A is positive because of the upward lift, but its value is relatively small for the case with mean pitch angle of  $10^\circ$ , as shown in figure 3.11b.

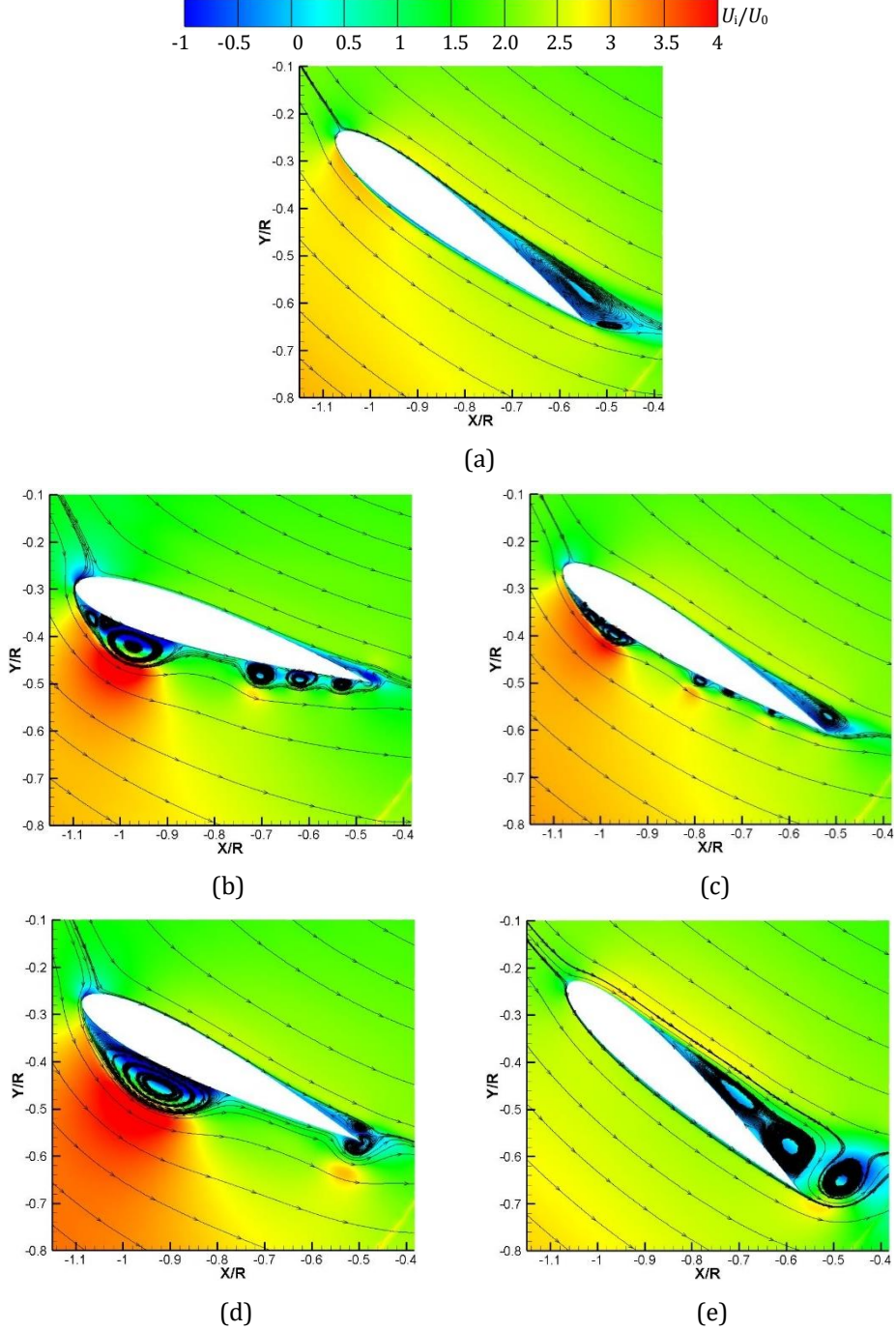
Then, because the stagnation point is moving towards the upper side, the vortex structures mentioned in figure 3.6 occur on the lower surface for the symmetrical pitching with large amplitude and the asymmetrical pitching with positive mean pitch angles. Therefore, the lower pressure on the suction side produces the downward lift, creating the positive propulsive force of blade B, which is shown in figure 3.11a. Due to the large pressure difference in figure 3.11c, the propulsive force of the rotating system for symmetrical pitching with large amplitude and asymmetrical pitching with large positive mean pitch angle, has the largest magnitude. But for asymmetrical pitching with negative mean pitch angle, the flow separation is on the upper side and the resultant lift is upward, leading to the generation of negative propulsive force. Therefore, although the blade A can produce the relatively large positive propulsive force, the total propulsive force for the rotating system is the smallest. In general, the total propulsive force is determined by the two blades, especially for blade B, because the lift direction is different for various pitching kinematics, depending on the angle of attack, which changes the stagnation point and flow structures significantly.



**Fig.3.11** Pressure distributions for various pitching kinematics at  $\psi=160^\circ$ . (a) Sketch of force; (b) Pressure distribution of blade A; (c) Pressure distribution of blade B.



**Fig.3.12** Flow structures of blade A for various pitching kinematics at  $\psi=160^\circ$ . (a)  $0^\circ-35^\circ$ ; (b)  $0^\circ-55^\circ$ ; (c)  $5^\circ-35^\circ$ ; (d)  $10^\circ-35^\circ$ ; (e)  $-5^\circ-35^\circ$ .



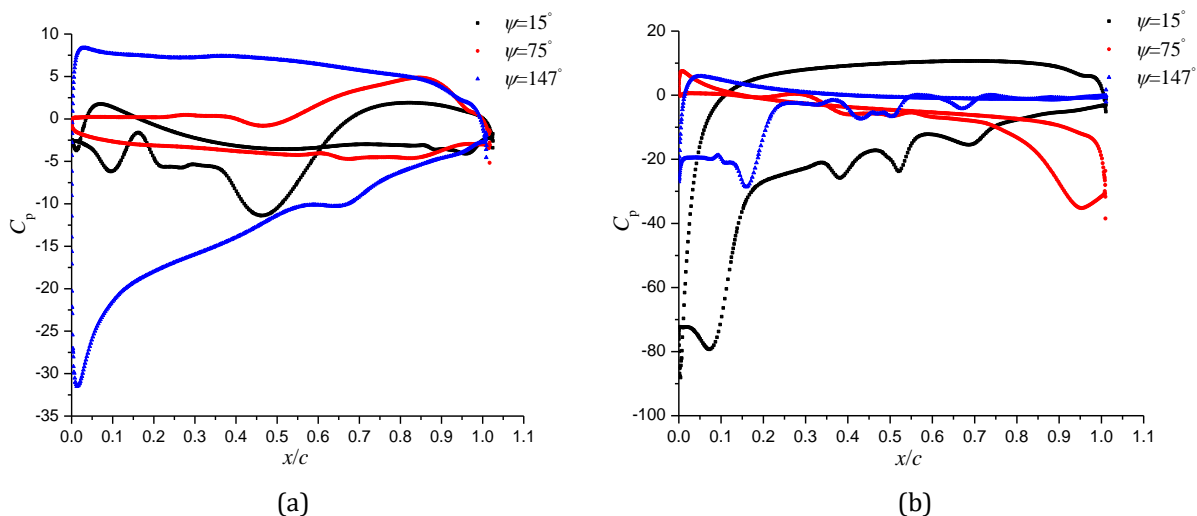
**Fig.3.13** Flow structures of blade B for various pitching kinematics at  $\psi=160^\circ$ . (a)  $0^\circ$ - $35^\circ$ ; (b)  $0^\circ$ - $55^\circ$ ; (c)  $5^\circ$ - $35^\circ$ ; (d)  $10^\circ$ - $35^\circ$ ; (e)  $-5^\circ$ - $35^\circ$ .

Figure 3.14 and 3.15 show the flow structures for the symmetrical pitching with an amplitude of  $55^\circ$  at three azimuthal angles, namely  $15^\circ$ ,  $75^\circ$  and  $147^\circ$ , to clarify why the total propulsive force has large variations at these positions. At  $\psi=15^\circ$ , the pressure difference on blade B is much larger than that on blade A, as shown in figures 3.14a and 3.14b. On the left side of blade A, three kinds of vortex nearly cover the large part of the surface, but the low pressure on the aft part recovers obviously. Furthermore, the LSB, triggering the transition, is located near the leading edge of blade B and then the flow separation occurs near the trailing edge. At this instant, due to the large pressure

difference of blade B, the positive propulsive force of the rotating system has the maximal value.

As  $\psi$  increases to  $75^\circ$ , on both sides of blade A, the massive flow separation is evident. The component of lift produces a negative propulsive force, but its magnitude is relatively small due to the blade loading in figure 3.14a. Meanwhile, the blade B can still produce the upward lift owing to the pressure drop on the trailing edge of upper surface, leading to the negative propulsive force. Consequently, the rotating system has the peak of negative propulsive force.

Finally, at  $\psi=147^\circ$ , the rotating system has the positive peak of propulsive force, as a consequence of the large positive propulsive force generated by blade A because of the large blade loading in figure 3.14a, which is quite similar to the situation at  $\psi=160^\circ$ . At the same time, blade B creates a downward lift, which can produce the positive propulsive force. However, the loading is smaller on blade B than on blade A, so the positive propulsive force of blade B is much smaller.



**Fig.3.14** Pressure distributions of two blades for symmetrical pitching with amplitude of  $55^\circ$  at different  $\psi$ . (a) Blade A; (b) Blade B;

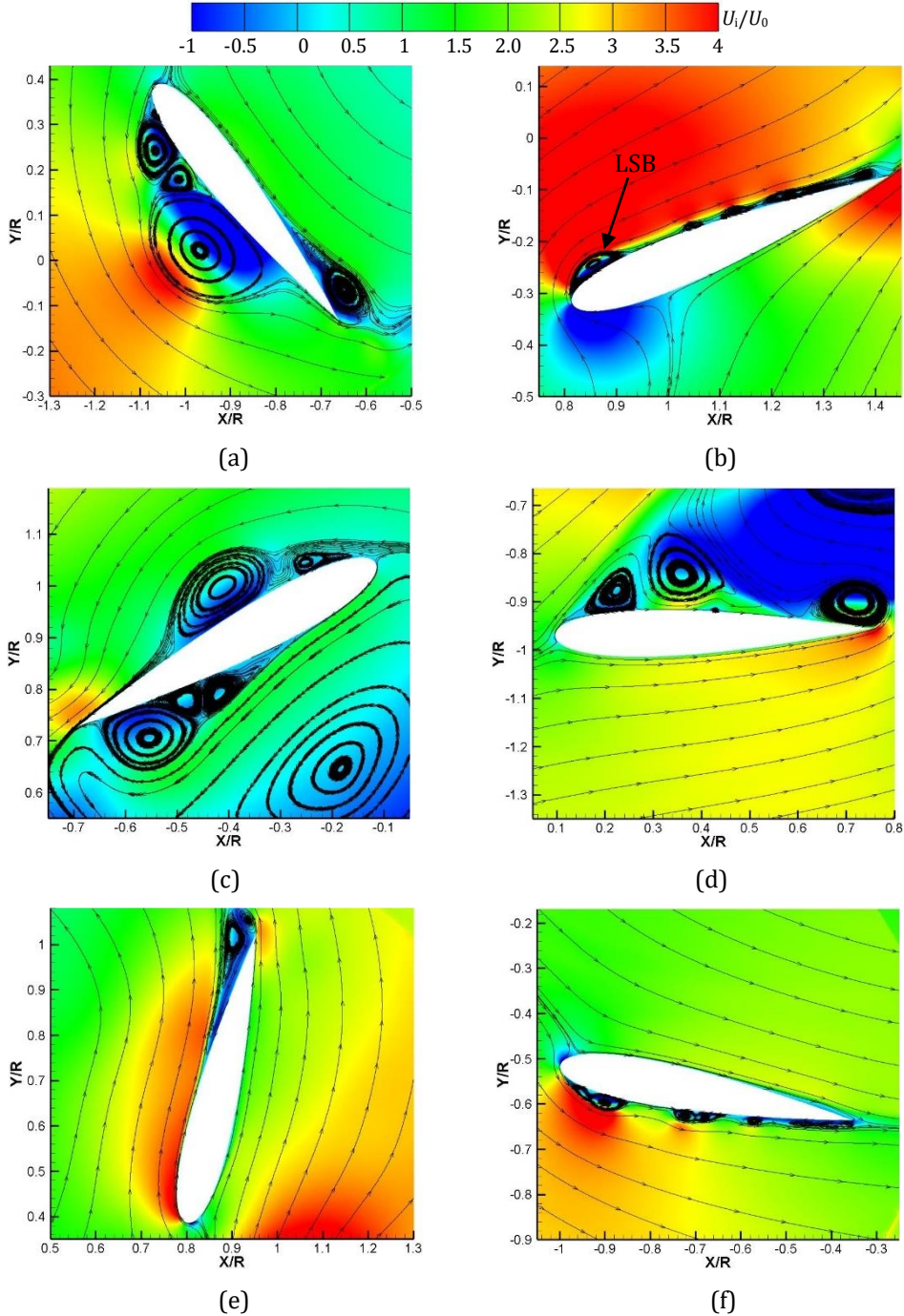


**Fig.3.15** Flow structures of two blades for symmetrical pitching with amplitude of  $55^\circ$  at different  $\psi$ . (a) and (b)  $\psi=15^\circ$ ; (c) and (d)  $\psi=75^\circ$ ; (e) and (f)  $\psi=147^\circ$ .

### 3.1.3 Conclusions

(1) The asymmetrical pitching kinematic with a small positive mean pitch angle results in the best performance regarding the efficiency of the cycloidal rotor, which results from the moderate propulsive force and low power. Conversely, although the symmetrical pitching with large amplitude and the asymmetrical pitching with large mean pitch angle generate a high propulsive force, the efficiency is quite low as a result of the complicated vortical flows leading to the higher power. Moreover, the asymmetrical pitching with a negative mean pitch angle produces the high lift coefficient with  $\lambda$ , but a

decrease of the propulsive force coefficient.

(2) Generally, the performance of the single blade shows that the difference of the lift coefficient is mainly caused by blade B at advancing side, while it is induced by the two blades for the difference of the propulsive force coefficient. Near the airfoil surface, the flow structures are rich, including three vortex structures, roll-up vortices, flow separation vortex at the trailing edge, LSB, LEV and TEV, and the pattern of these vortices depends on the incidence importantly. When analyzing the forces on the single blade, it is interesting that when the blade undergoes the left side of the advancing side, the lift direction is opposite for the asymmetrical pitching with negative mean pitch angles compared with that in other cases, as a consequence of the stagnation point location caused by the different relative incidences.

## 3.2 INFLUENCE OF THE CHORD-TO-RADIUS RATIO

### 3.2.1 Introduction

The chord-to-radius ratio ( $c/R$ ) is also a critical parameter to the optimization of cycloidal propeller performance, but it is seldom investigated previously. Additionally, in most cases,  $c/R$  is varied by changing the blade chord length, and the influence of the rotating radius is always neglected. Thus, in this section, to study the influence of  $c/R$ , both the rotating speed and the rotor radius are changed to keep the Reynolds number and the advance coefficient constant. Then, the effect of the Reynolds number and the advance coefficient are analyzed for various  $c/R$ , respectively.

### 3.2.2 Effect of $c/R$

Firstly, the influence of the blade chord length  $c$  is evaluated at the same  $\lambda$  and  $Re$ . In figure 3.16, it seems that with the increase of  $c/R$  until the value below 0.65, the lift coefficient of the rotating system increases, which is almost the same for different blade chord lengths. After that, it has a rapid rise for  $c=0.0495\text{m}$ . The propulsive force coefficient obtained with different blade chords is quite similar, characterized by the curves that have a rise from  $c/R=0.30$  to 0.45 initially and an obvious drop after that. Then, the power coefficient increases firstly and then has a slight decrease, and finally increases again significantly at relatively large  $c/R$ , which is due to the more complicated flow structures when the two blades are quite close caused by the decrease of  $R$ . As a result, the best efficiency is around  $c/R=0.45$ , but the magnitude increases with the blade chord length. As  $c/R$  increases, due to the increase of the power and decrease of the propulsive force, the efficiency of the rotating system decreases obviously. Generally, a too small or too large rotor radius is not beneficial to the global performance, so an appropriate value of  $c/R$  is necessary to achieve a high efficiency.

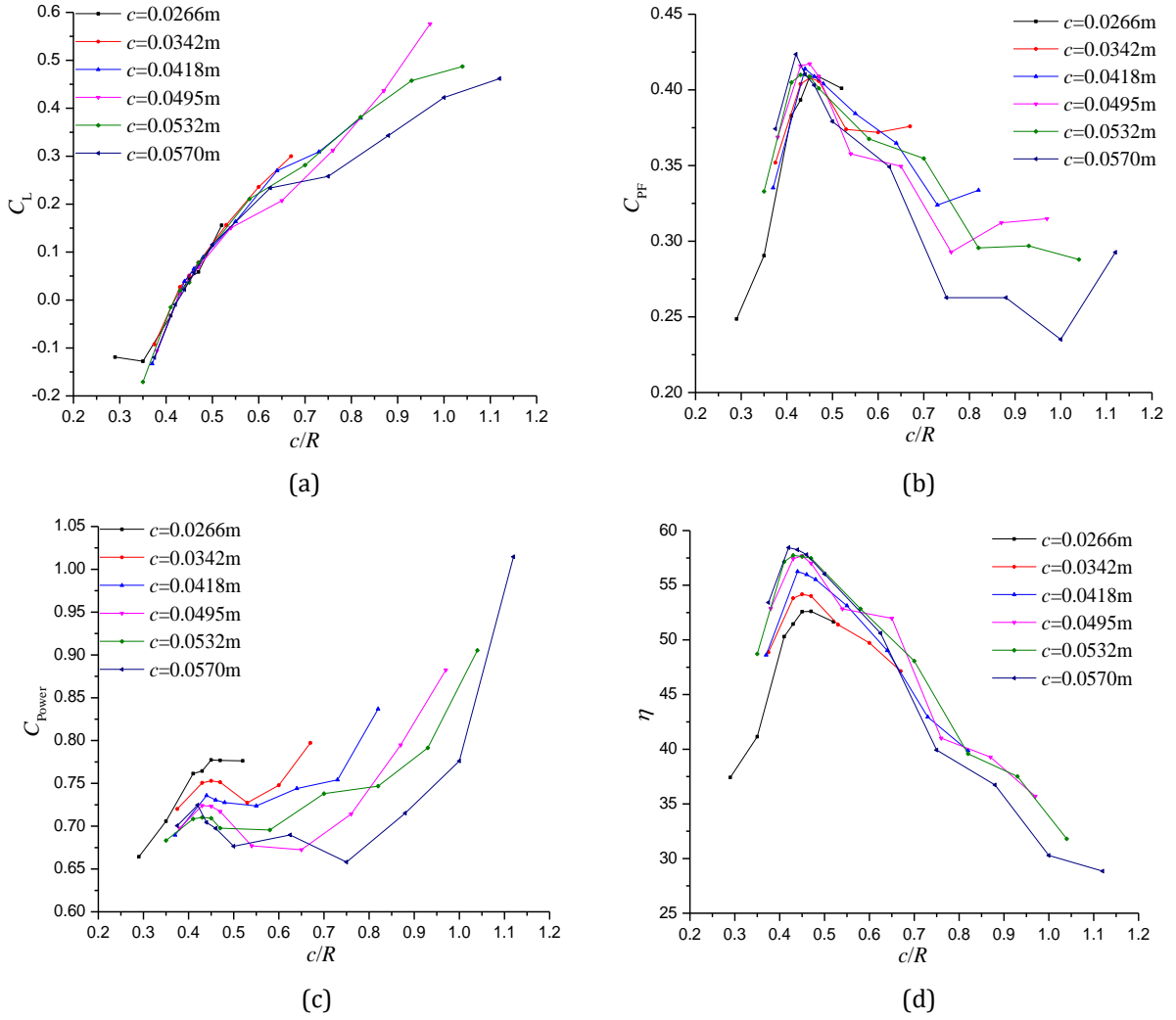


**Fig.3.16** Performance curves at  $\lambda=0.52$  and  $Re=2.46\times 10^4$ . (a) Lift coefficient; (b) Propulsive force coefficient; (c) Power coefficient; (d) Efficiency.

Three cases with  $c/R=0.375$ ,  $0.45$  and  $0.60$ , at  $\lambda=0.52$  and  $Re=2.46\times 10^4$ , are selected to study the detailed flow structures and their influence on the performance of the rotating system and the single blade. The forces of the cycloidal rotor and single blade are plotted in figure 3.17, for a fixed blade chord length equal to  $0.0342\text{m}$ . The results show that the lift coefficient of the rotating system increases with  $c/R$ , while the propulsive force coefficient predicted by the case with  $c/R=0.45$  is the largest, as a result of the large propulsive force coefficient produced from  $\psi=10^\circ$  to  $90^\circ$  and  $\psi=190^\circ$  to  $270^\circ$ . Moreover, in figure 3.17c and 3.17d, it can be seen that the vertical force coefficient of cases with  $c/R=0.375$  and  $0.45$  is nearly the same in a rotating cycle, but has much difference compared with the case with  $c/R=0.6$ . Similarly, except the region of  $\psi=0^\circ$ - $90^\circ$ , the propulsive force coefficient obtained by the case with  $c/R=0.6$  has significant difference compared with other two cases. Thus, two specific blade positions at  $\psi=45^\circ$  and  $142^\circ$ , corresponding to the positive and negative peaks of the lift coefficient, are adopted to analyze the internal flows. Additionally, regarding the difference of propulsive force coefficient, the flow structures obtained in the cases  $c/R=0.375$  and  $0.45$  at  $\psi=180^\circ$  and in the case  $c/R=0.60$  at  $160^\circ$  (presented by the dash line), are investigated in detail.

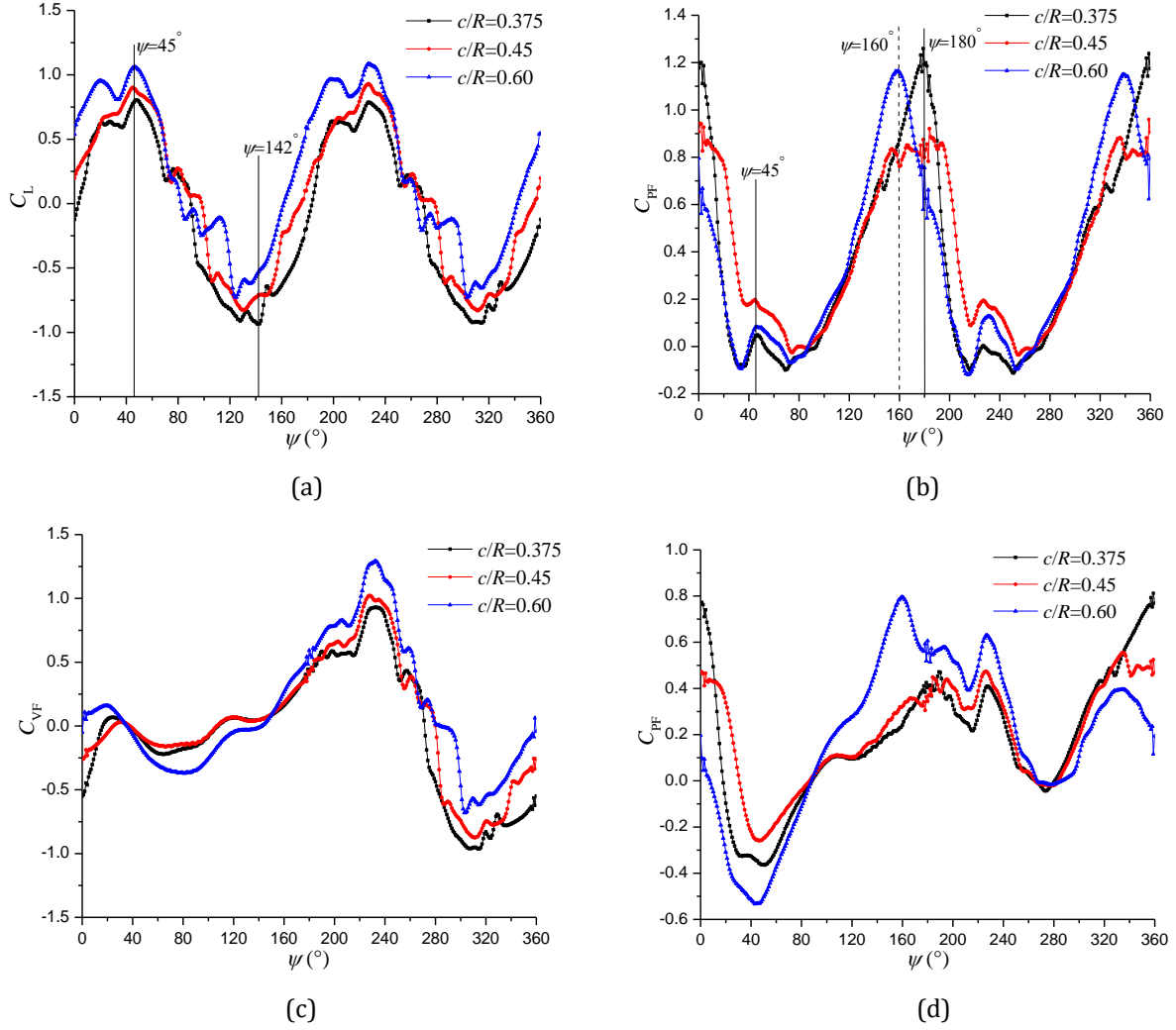


**Fig.3.17** Performance curves for various  $c/R$  in a revolution. (a) Lift coefficient of the rotating system; (b) Propulsive force coefficient of the rotating system; (c) Vertical force coefficient of single blade; (d) Propulsive force coefficient of single blade.

In figure 3.18 and 3.19, with the combination of global flow morphology, pressure distributions and relative velocity contours on the two blades, the lift differences at  $\psi=45^\circ$  are explained for various  $c/R$ . At this moment, wake A interacts with blade B, which is more obvious with the increase of  $c/R$  because of the narrow distance between the two blades. Similarly, wake B also has large possibility to contact with itself. In general, as  $c/R$  increases, the vortex flow is more violent because it does not have enough time to dissipate for two close blades. According to the pressure distribution in figure 3.19a, it can be seen that due to the vortex attachment on the left side of blade A, the blade loading for three cases have a remarkable difference. However, the vertical force produced by blade A is almost the same, which is caused by the balance of the lift and drag components, as shown in figure 3.17c. Therefore, blade B becomes the main contributor to the global lift for the rotating system. It should be mentioned that the pressure on the suction side changes considerably if the rotating speed changes, which is equivalent to the change of pitching rate. Kim et al. [93] reported that the reduced frequency of the pitching airfoil is the main factor determining the unsteady boundary layer under low Reynolds number condition. The stagnation point location changes the pressure distribution on both two sides for the case  $c/R=0.60$ , which is shown in figure 3.19b. The resultant large pressure

difference leads to the large lift generated by blade B, leading to the large lift of the rotating system.

The propulsive force created by blade A and B varies a lot in the three cases. The components of both lift and drag of blade A produce a negative propulsive force, especially for the case  $c/R=0.60$ , due to the large pressure difference visible in figure 3.19a. Then, blade B produces the upward lift, leading to the generation of a positive propulsive force. The largest propulsive force of blade B results from the largest pressure difference shown in figure 3.19b. By the combination of two blades, the case with  $c/R=0.45$  shows the best performance regarding the positive propulsive force.

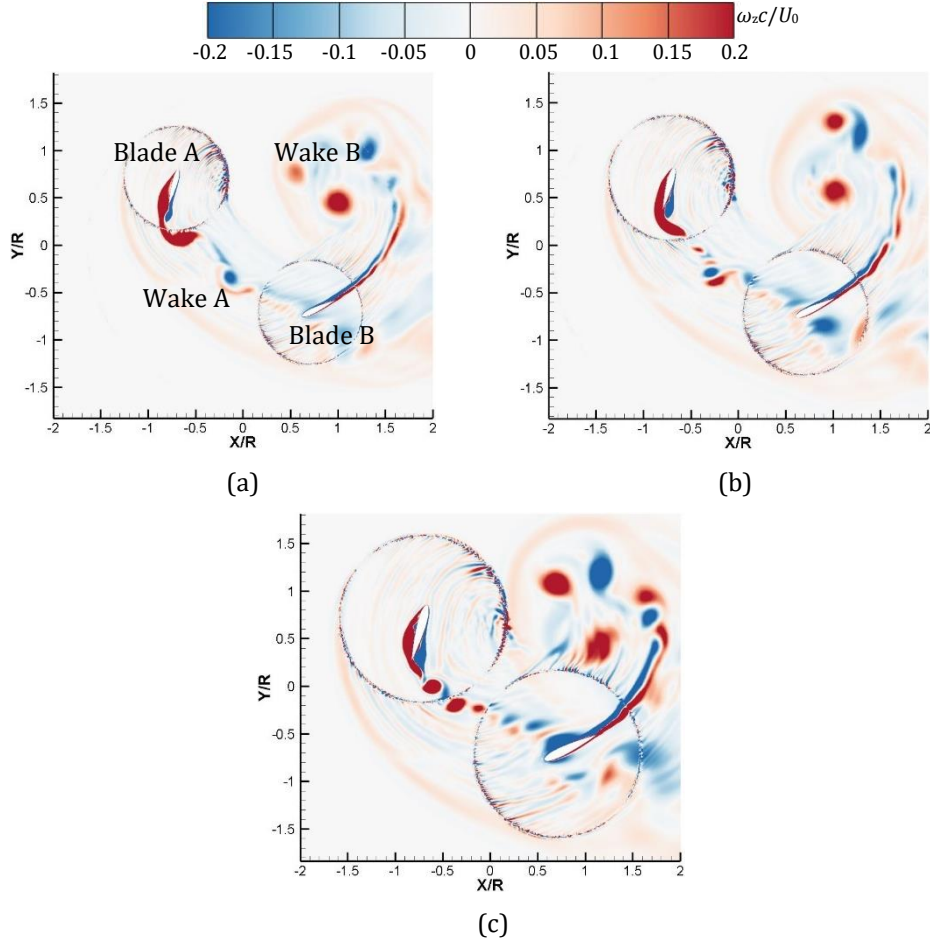


**Fig.3.18** Global flow structures for various  $c/R$  at  $\psi=45^\circ$ . (a)  $c/R=0.375$ ; (b)  $c/R=0.45$ ; (c)  $c/R=0.60$ .

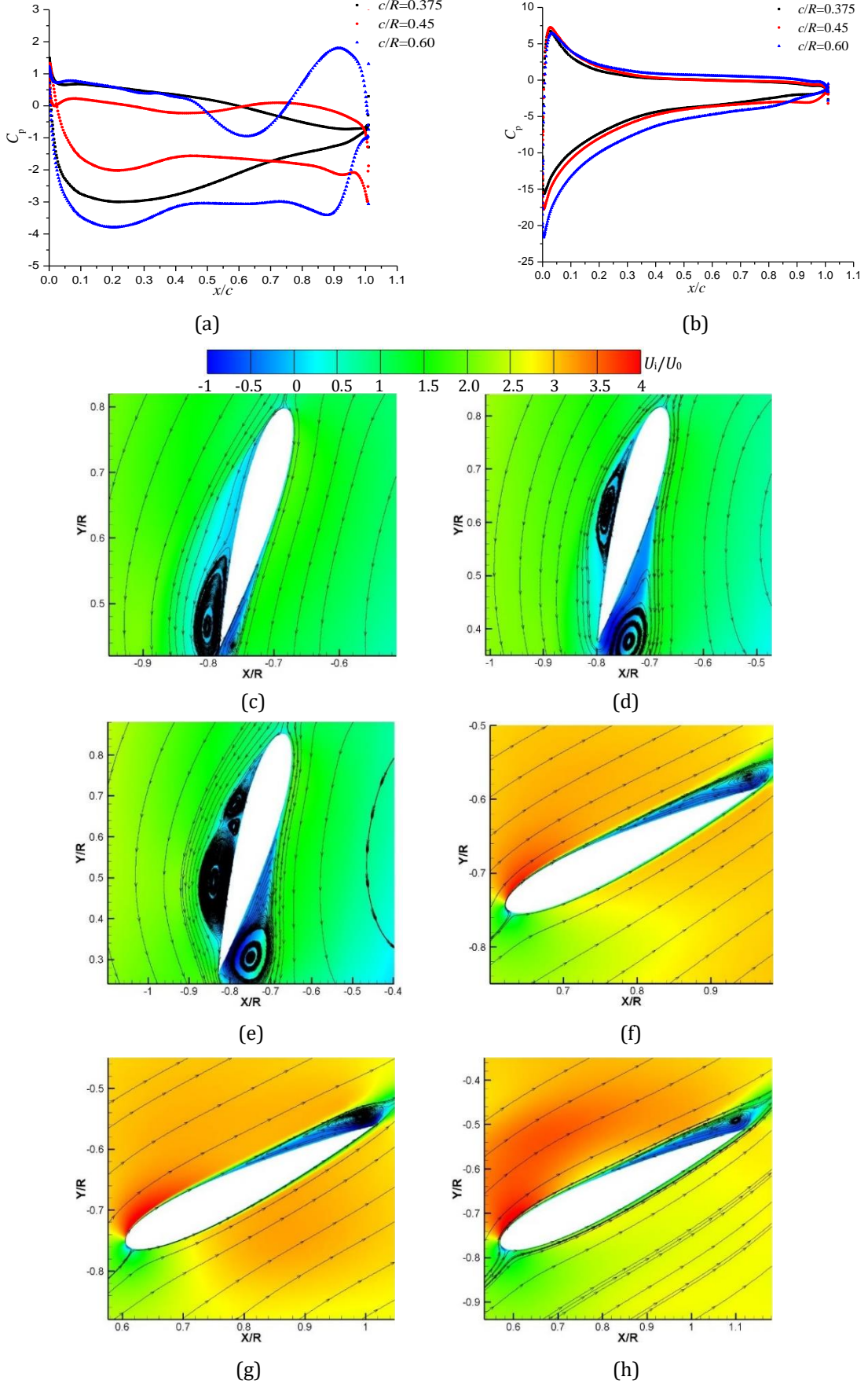


**Fig.3.19** Near-wall flow structures for various  $c/R$  at  $\psi=45^\circ$ . (a) Pressure distribution of blade A; (b) Pressure distribution of blade B; (c) and (f)  $c/R=0.375$ ; (d) and (g)  $c/R=0.45$ ; (e) and (h)  $c/R=0.60$ .

As  $\psi$  increases up to  $142^\circ$ , the lift coefficient of the rotating system experiences a negative peak. The global flow structures for different cases are relatively smooth, but the wake shedding from blade A will likely interact with wake B when  $c/R$  is large (see figure 3.20c). The flows on two sides of blade A are quite smooth, and only small-scale vortices are observed on the pressure side. But the pressure difference on blade A in the case  $c/R=0.60$  is very large, causing a large negative vertical force on blade A, which is shown in figure 3.17c. Then, blade B is the main contributor to the total lift. On suction side of blade B, the three-vortex-structure and other scales are attached, which has a great impact on the pressure distribution. At this instant, blade B generates the downward lift, resulting in the negative lift of the rotating system. Meanwhile, because of the large pressure difference in the case  $c/R=0.375$  (figure 3.21b), blade B has the largest negative vertical force compared with the other cases, causing the production of the largest negative lift of the rotating system. By comparing the two blades, it is concluded that blade B still generates most of the lift of the rotating system.

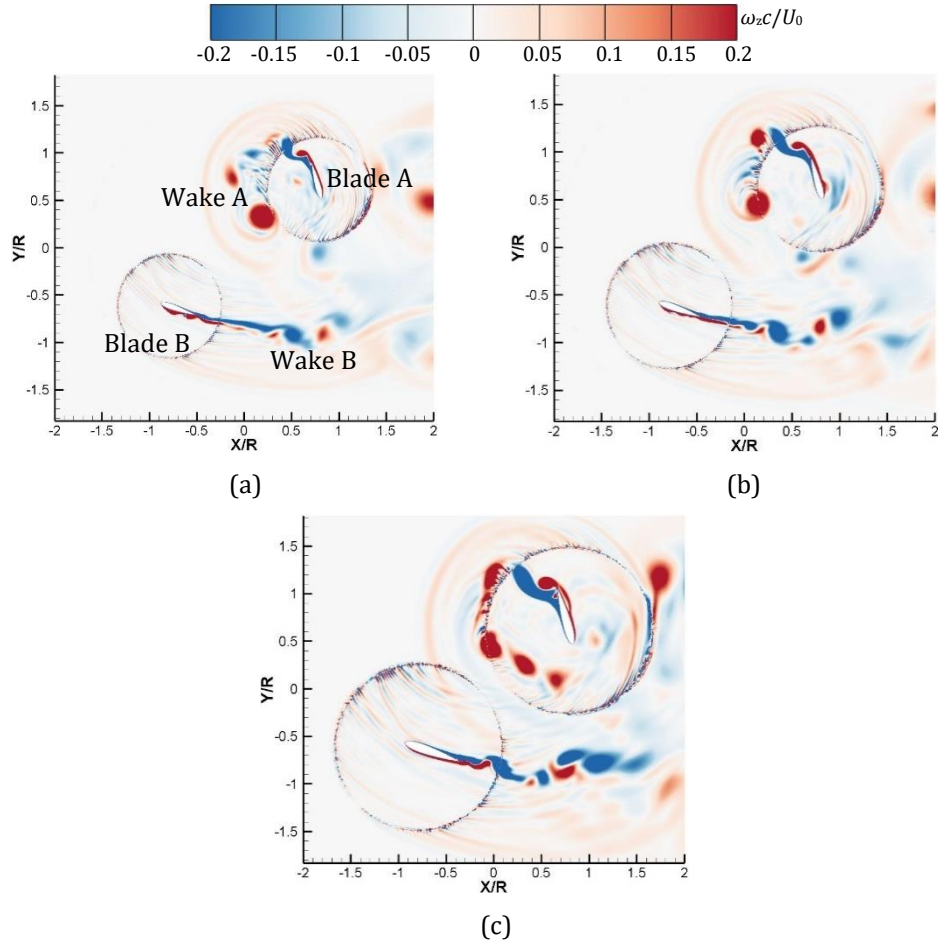


**Fig.3.20** Global flow structures for various  $c/R$  at  $\psi=142^\circ$ . (a)  $c/R=0.375$ ; (b)  $c/R=0.45$ ; (c)  $c/R=0.60$ .

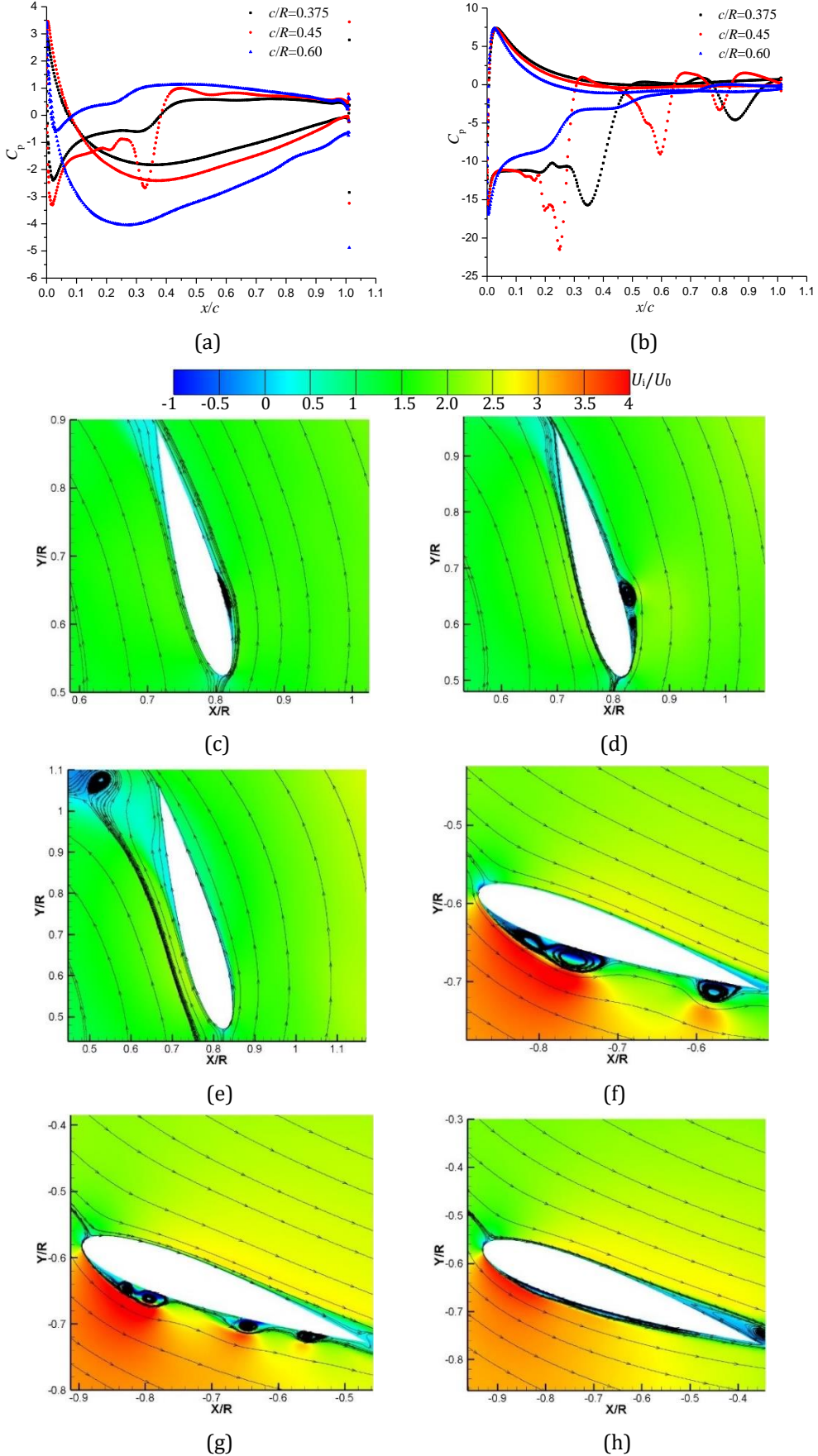


**Fig.3.21** Near-wall flow structures for various  $c/R$  at  $\psi=142^\circ$ . (a) Pressure distribution of blade A; (b) Pressure distribution of blade B; (c) and (f)  $c/R=0.375$ ; (d) and (g)  $c/R=0.45$ ; (e) and (h)  $c/R=0.60$ .

In figure 3.22 and 3.23, the flow structures at positions  $\psi=160^\circ$  (case  $c/R=0.6$ ) and  $\psi=180^\circ$  (cases  $c/R=0.375$  and  $0.45$ ) are presented. Globally, the flows obtained with  $c/R=0.375$  and  $0.45$  are extremely similar, as well as the pressure distribution and near-wall flow around blade A. However, the flow structures for the case  $c/R=0.60$  differ from the other two cases, due to the different azimuthal angles. In figure 3.22c, wake A has already contacted with the leading edge of blade A and the wake B is more intense. Blade A generates the upward lift, which can produce the positive propulsive force, but its magnitude is quite similar in cases  $c/R=0.375$  and  $0.45$ , due to the pressure distribution in figure 3.23a. However, the attached vortex on the suction side of blade B has a great impact on the pressure, especially for the case  $c/R=0.375$ , leading to the larger propulsive force of the rotating system, compared with the case  $c/R=0.45$ . Thus, for these two cases, blade B is still dominant due to the influence of the large-scale vortex attached on the suction side.

For the case  $c/R=0.60$  at  $\psi=160^\circ$ , the high lift of the rotating system is mainly created by blade A, due to the large blade loading (figure 3.23a). Here, blade A is almost vertical, so the lift can provide the positive propulsive force. In addition, blade B can also produce the positive propulsive force as a consequence of the downward lift, but its magnitude is smaller than that the one given by blade A, as shown in 3.17d. For the single blade performance, the existence of the three-vortex -structure near the airfoil leading edge results in the low pressure and then the significant pressure recovery is observed after the reattachment. Afterwards, several small-size vortices bring about the pressure fluctuations, as shown figure 3.23b and 3.23h.

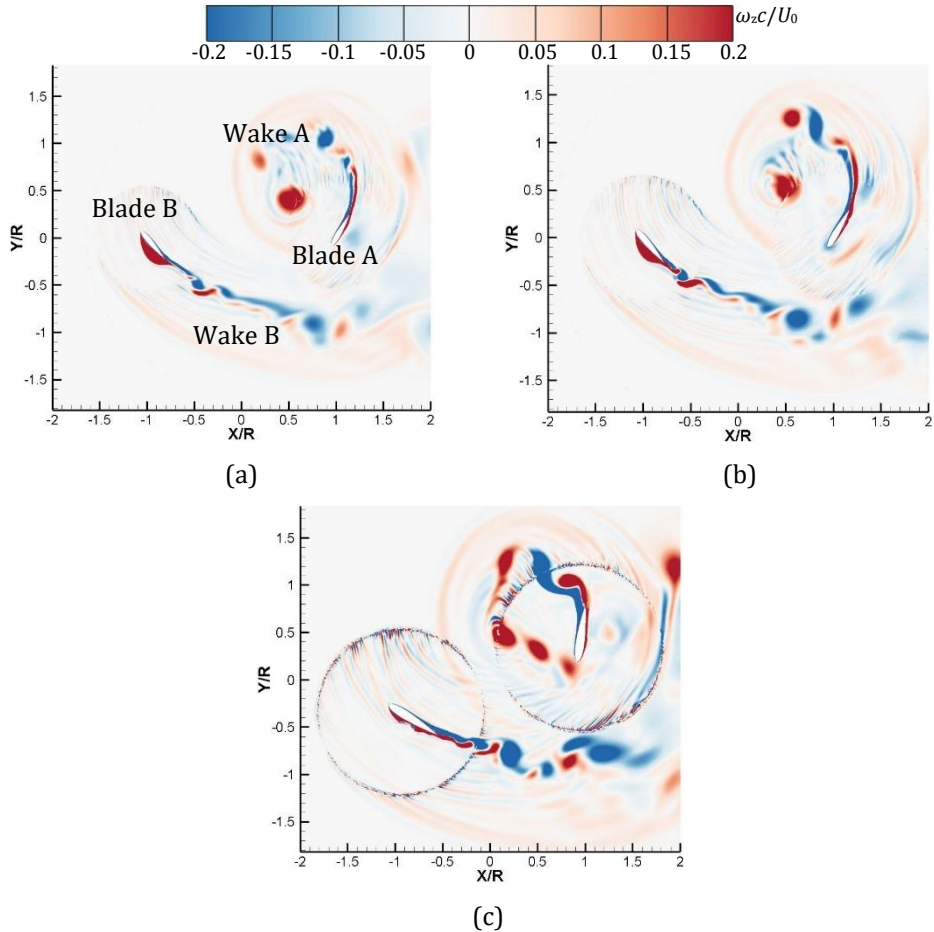


**Fig.3.22** Global flow structures for various  $c/R$ . (a)  $c/R=0.375$  at  $\psi=180^\circ$ ; (b)  $c/R=0.45$  at  $\psi=180^\circ$ ; (c)  $c/R=0.60$  at  $\psi=160^\circ$ .

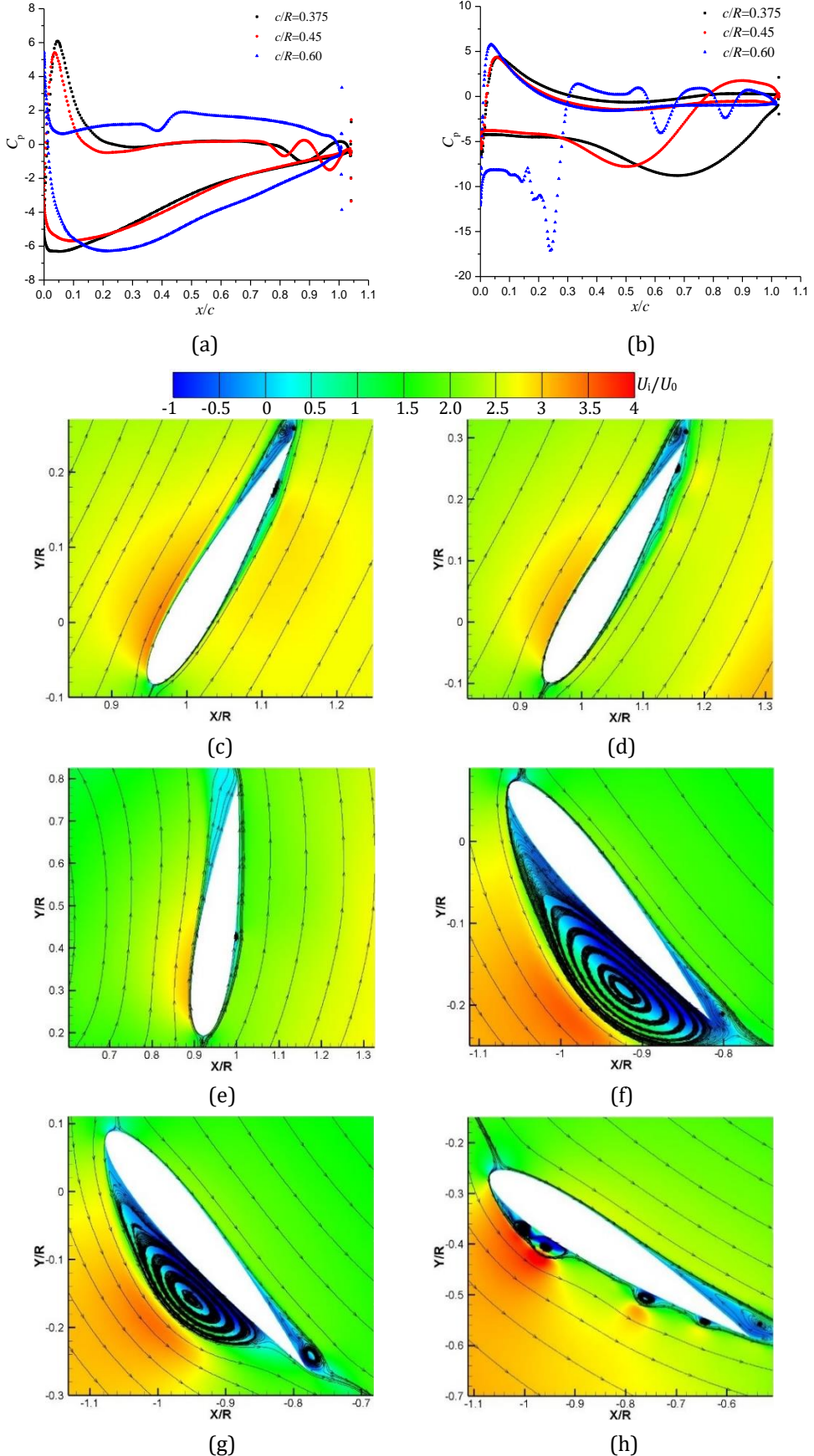


**Fig.3.23** Flow structures for various  $c/R$ . (a) Pressure distribution of blade A; (b) Pressure distribution of blade B; (c) and (f)  $c/R=0.375$  at  $\psi=180^\circ$ ; (b) and (e)  $c/R=0.45$  at  $\psi=180^\circ$ ; (c) and (h)  $c/R=0.60$  at  $\psi=160^\circ$ .

### 3.2.3 Effect of $Re$

The influence of the Reynolds number on the global performance is investigated at  $\lambda=0.52$  by changing the inlet velocity and rotating speed. Figure 3.24 presents the performance curves at various  $Re$  for different  $c/R$ . When  $c/R$  is constant, the lift coefficient increases slowly with  $Re$ , while it is more obvious at a fixed  $Re$  as  $c/R$  increases. For the distribution of propulsive force coefficient, it seems that the highest values are obtained in cases with  $c/R=0.43$ , 0.45 and 0.47, especially at extremely low Reynolds number. The power coefficient in the case  $c/R=0.67$  has the largest magnitude, leading to the lowest efficiency (figure 3.24d). Then, the power coefficient for the cases  $c/R=0.43$ , 0.45 and 0.47 decreases significantly with the Reynolds number. Consequently, the efficiency increases obviously with  $Re$  because of the slight decrease of the propulsive force coefficient.

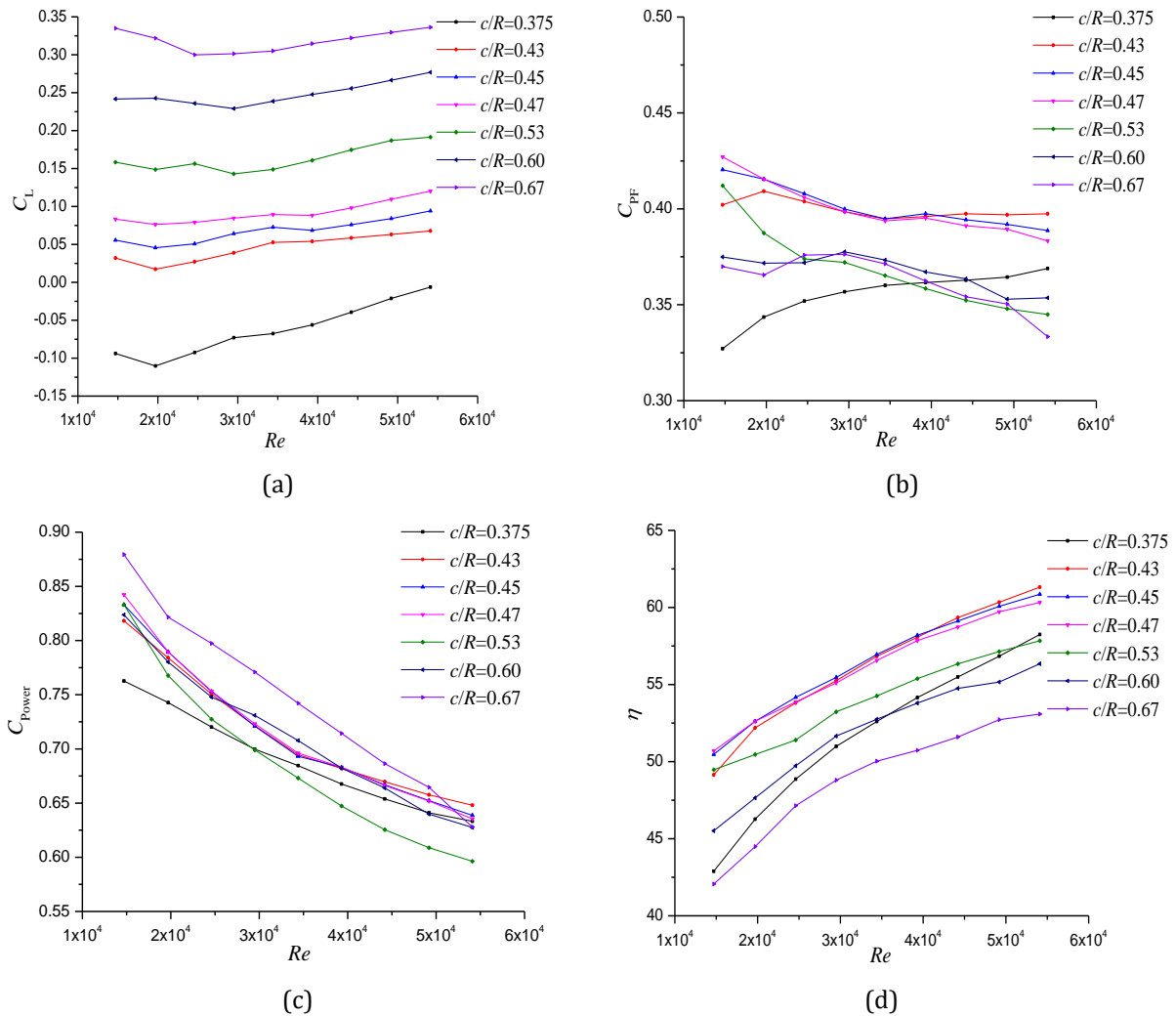


**Fig.3.24** Performance curves at different  $Re$ . (a) Lift coefficient; (b) Propulsive force coefficient; (c) Power coefficient; (d) Efficiency.

In figure 3.25, three cases with  $c/R=0.45$ , at different Reynolds numbers, are selected to demonstrate the force difference generated by both the rotating system and the single blade. It can be seen that there is not much difference of lift coefficient between three cases during a cycle, but the propulsive force coefficient shows some differences at

some positions. Evidently, the performance of the cycloidal rotor and single blade obtained at low  $Re$  is very different from the two other cases. Therefore, the lift coefficient at  $\psi=110^\circ$  and the propulsive force coefficient  $\psi=35^\circ$  and  $180^\circ$ , are adopted to perform a deeper analysis of the flow structures.

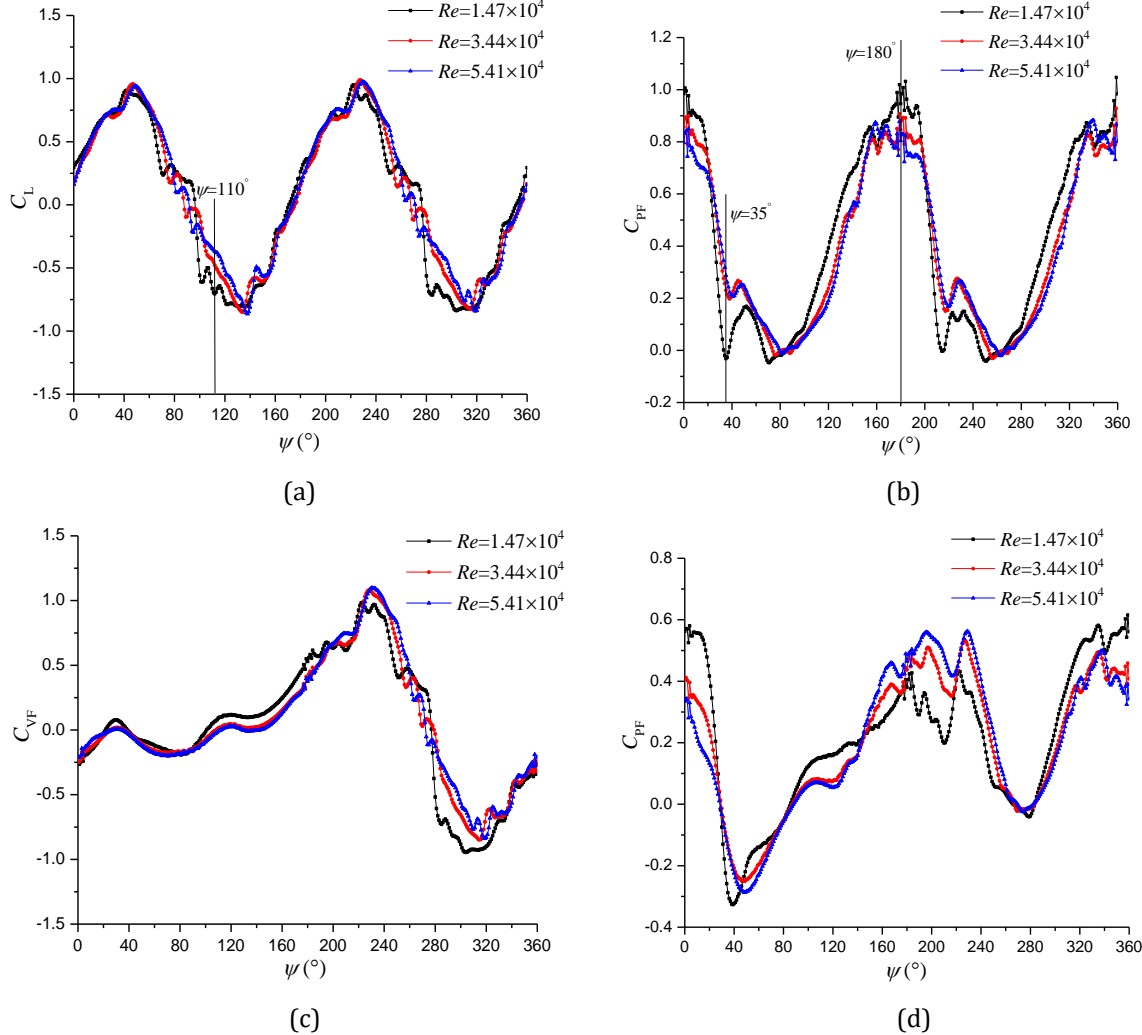


**Fig.3.25** Performance curves at different  $Re$  in a revolution. (a) Lift coefficient of the rotating system; (b) Propulsive force coefficient of the rotating system; (c) Vertical force coefficient of single blade; (d) Propulsive force coefficient of single blade.

Figure 3.26 and 3.27 show the flow structures at  $\psi=110^\circ$  for cases at different  $Re$ . Inside the cycloidal rotor, the most noticeable event is the wake A-wake B interaction, which is stronger at high  $Re$ . The complicated vortical flows at large  $Re$  is responsible for the higher power consumption observed in figure 3.24 (the actual value of the power increases with  $Re$ ). Then, at this position, the vertical force of blade A is very small, because of the small pressure difference (figure 3.27a) and the balance between the lift and drag components in the vertical direction. The flow on blade A is relatively smooth and the flow separation only occurs at the trailing edge on the suction side. Thus, it indicates that the lift of the rotating system is mainly generated by blade B because of the downward lift, especially for the case  $Re=1.47 \times 10^4$ , due to the large pressure difference induced by the stagnation point location in figure 3.27b.

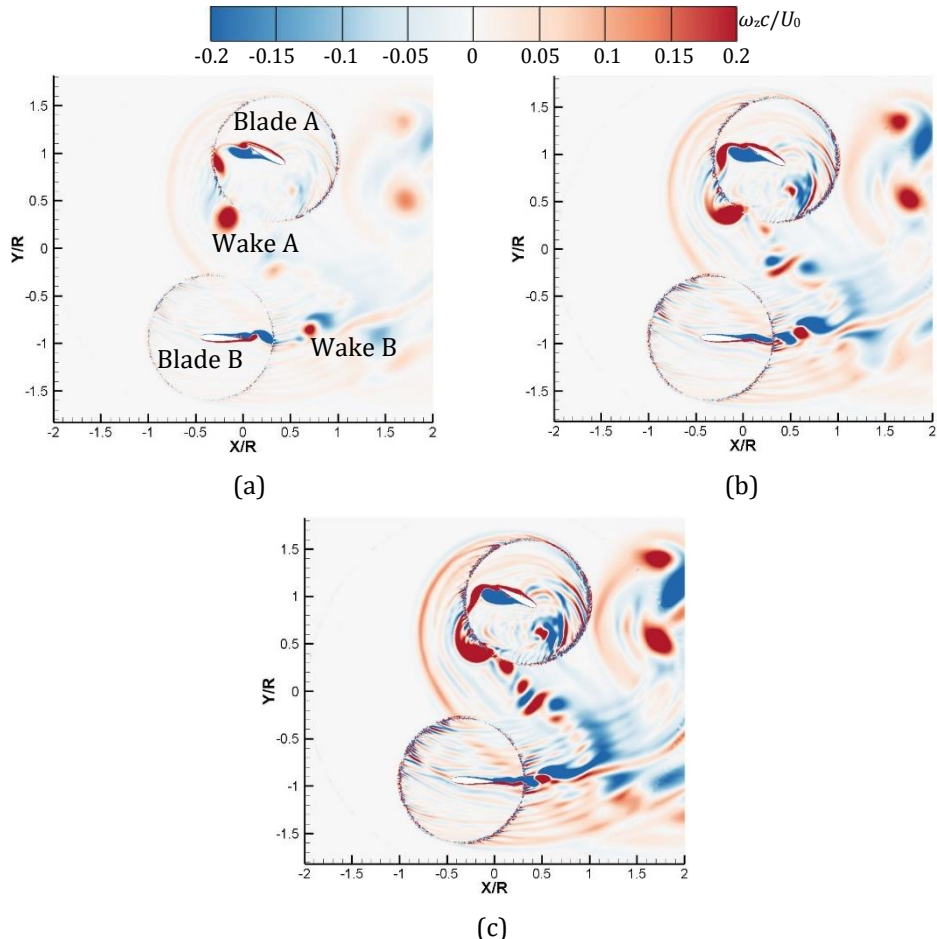


**Fig.3.26** Global flow structures for various  $Re$  at  $\psi=110^\circ$ . (a)  $Re=1.47\times 10^4$ ; (b)  $Re=3.44\times 10^4$ ; (c)  $Re=5.41\times 10^4$ .

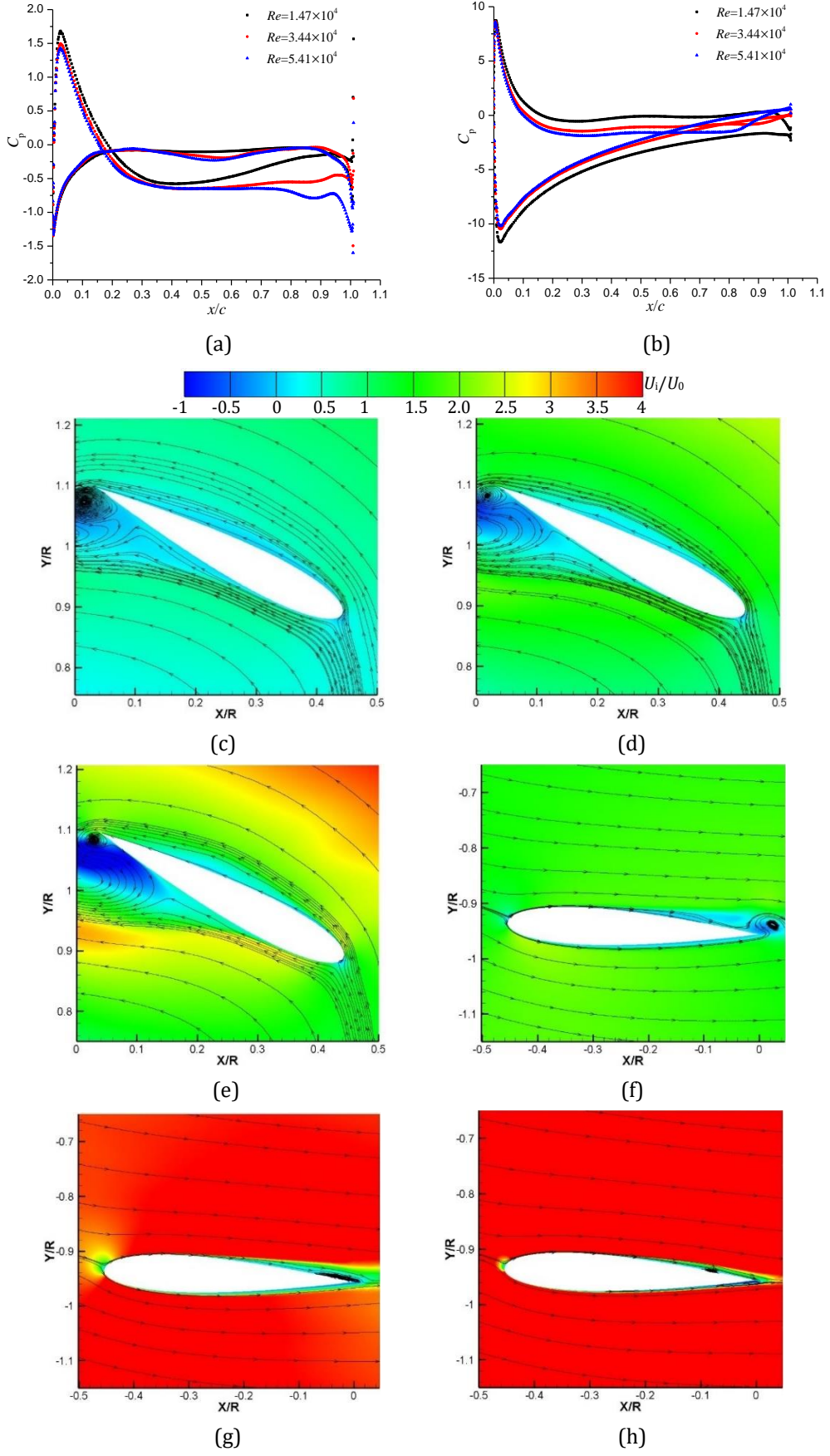


**Fig.3.27** Flow structures for various  $Re$  at  $\psi=110^\circ$ . (a) Pressure distribution of blade A; (b) Pressure distribution of blade B; (c) and (f)  $Re=1.47\times 10^4$ ; (d) and (g)  $Re=3.44\times 10^4$ ; (e) and (h)  $Re=5.41\times 10^4$ .

At position  $\psi=35^\circ$ , the global propulsive force coefficient for the cases  $Re=3.44\times10^4$  and  $5.41\times10^4$  is almost the same, but not anymore when the Reynolds number is  $1.47\times10^4$ . Consequently, the flow structures are displayed in figure 3.28. At this position, wake A has a high risk of colliding with the leading edge of blade B, especially at high  $Re$ . Simultaneously, wake B rolls up, resulting in the wake B-wake B interaction. Then, on the pressure side of blade A, a large-scale separation vortex is attached at  $Re=1.47\times10^4$ , but it splits into two connecting vortices when  $Re$  increases. After the reattachment point, the pressure recovery is obvious at low  $Re$ . Simultaneously, the flow separation at the trailing edge on the suction side, has a great effect on the pressure, resulting in the large pressure difference at low  $Re$ . As a result, the large amplitude upward lift is generated on blade A, producing the negative propulsive force. For blade B, the upward lift towards the suction side creates a positive propulsive force, but the magnitude is relatively small at low  $Re$ , because of the blade loading (figure 3.29b). Finally, by the combination of two blades, it concludes that the total propulsive force obtained at  $Re=1.47\times10^4$  is the smallest, compared with that of two other cases.

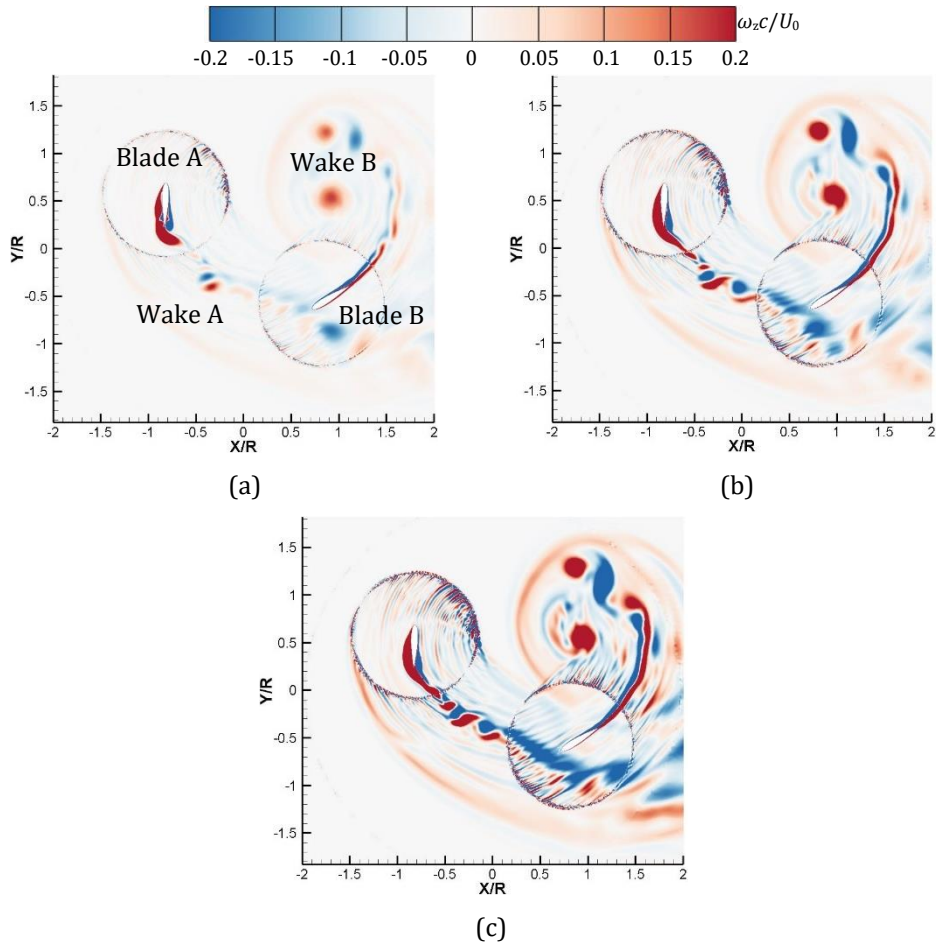


**Fig.3.28** Global flow structures for various  $Re$  at  $\psi=35^\circ$ . (a)  $Re=1.47\times10^4$ ; (b)  $Re=3.44\times10^4$ ; (c)  $Re=5.41\times10^4$ .

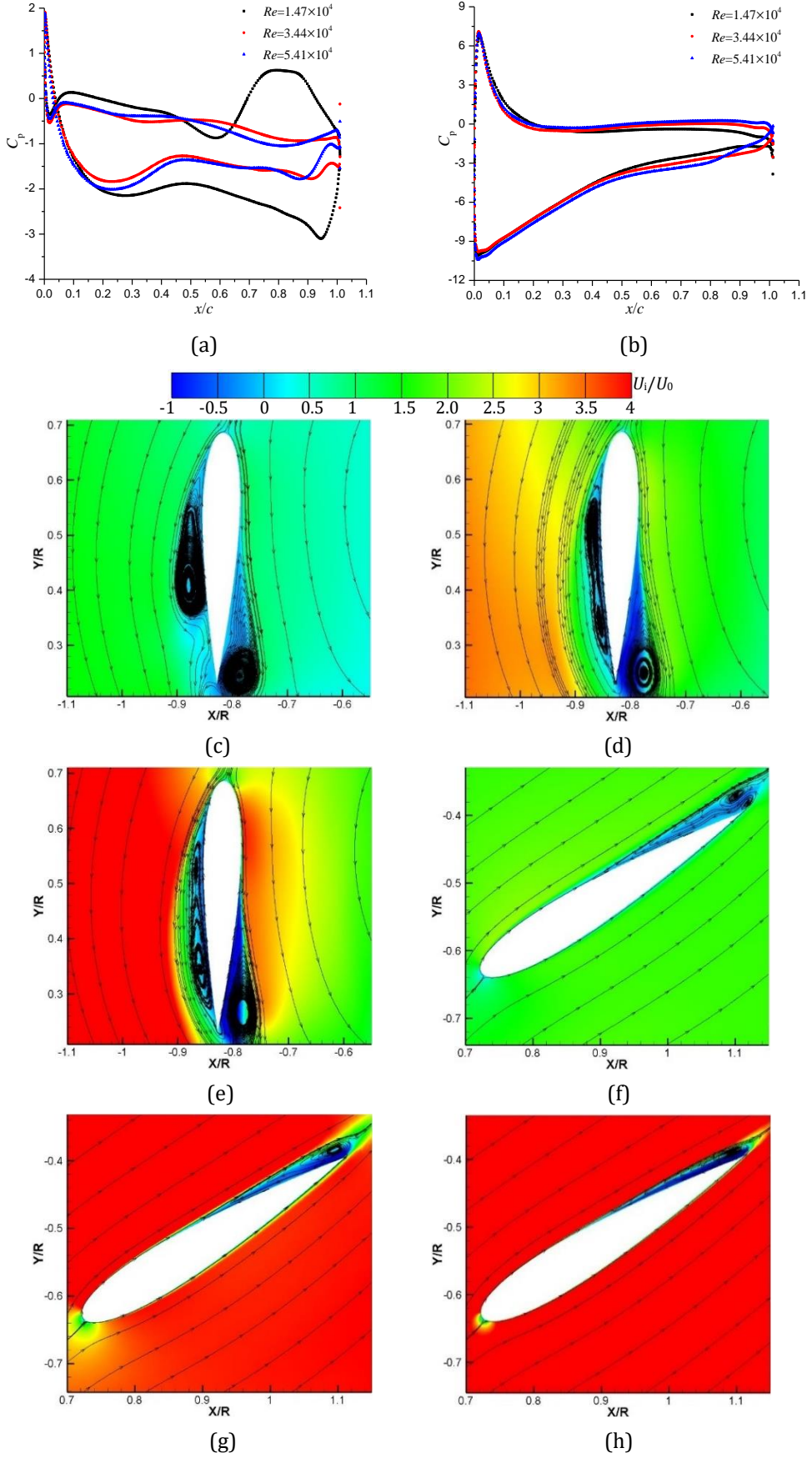


**Fig.3.29** Flow structures for various  $Re$  at  $\psi=35^\circ$ . (a) Pressure distribution of blade A; (b) Pressure distribution of blade B; (c) and (f)  $Re=1.47\times 10^4$ ; (d) and (g)  $Re=3.44\times 10^4$ ; (e) and (h)  $Re=5.41\times 10^4$ .

When approaching the position  $\psi=180^\circ$ , the two blades change the initial position each other. The global propulsive force obtained with various Reynolds numbers has a positive peak, but it is the largest for  $Re=1.47\times10^4$ . Therefore, the flow field is shown in figure 3.30 and 3.31. At high Reynolds number, the flow is more disordered, characterized by the complex shedding in the wake of the two blades and wake A-blade A interaction. Although there is flow separation near the trailing edge on blade A at  $Re=1.47\times10^4$  and  $3.44\times10^4$ , the blade loadings are nearly the same for the three cases (figure 3.31a). Thus, the predicted propulsive force generated by blade A is quite the same at three  $Re$  in figure 3.25d. However, the flow pattern over the suction side of blade B is different in the three cases, especially at low  $Re$ , when three distinct vortex structures attach on the suction side, leading to the very low pressure, as shown in figure 3.31b. Hence, the downward lift generated by blade B is responsible for the large value of the positive propulsive force. Finally, the propulsive force of the rotating system is the largest at low  $Re$ .

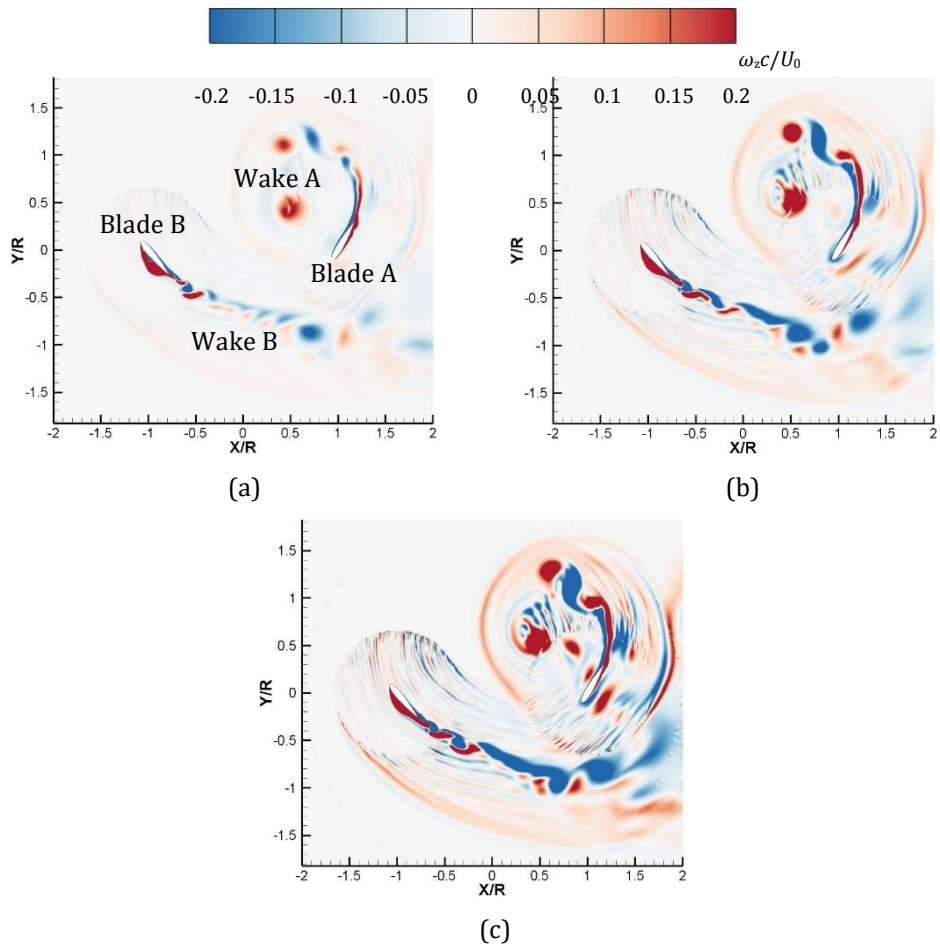


**Fig.3.30** Global flow structures for various  $Re$  at  $\psi=180^\circ$ . (a)  $Re=1.47\times10^4$ ; (b)  $Re=3.44\times10^4$ ; (c)  $Re=5.41\times10^4$ .

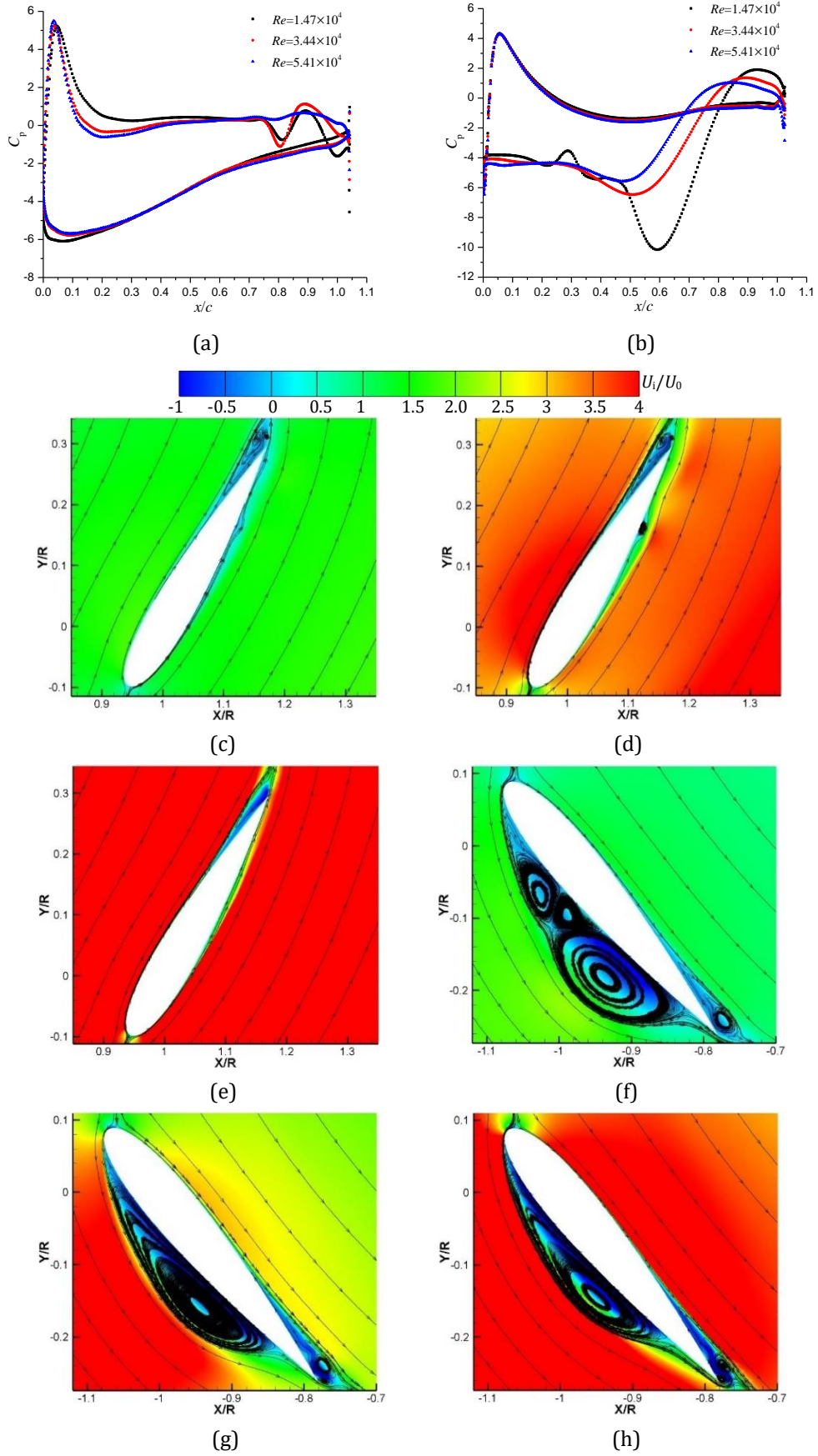


**Fig.3.31** Flow structures for various  $Re$  at  $\psi = 180^\circ$ . (a) Pressure distribution of blade A; (b) Pressure distribution of blade B; (c) and (f)  $Re = 1.47 \times 10^4$ ; (d) and (g)  $Re = 3.44 \times 10^4$ ; (e) and (h)  $Re = 5.41 \times 10^4$ .

### 3.2.4 Effect of $\lambda$

The influence of the advance coefficient  $\lambda$  on the performance and the flow structures for different  $c/R$  is discussed in the following section only by changing the rotating speed. The performance curves are plotted in figure 3.32. For a fixed  $c/R$ , the lift coefficient decreases with the increase of  $\lambda$ , while it increases with  $c/R$  at a constant  $\lambda$ . The propulsive force and power coefficients show the same trend, i.e. a decrease when  $\lambda$  increases, but it only slightly depends on  $c/R$ . The efficiency exhibits a slight increase initially and then decreases dramatically with the increase of  $\lambda$ , which indicates that the decrease rate of the propulsive force is larger than the power. Generally, it is observed that the best efficiency is achieved around  $\lambda=0.45$  for the case  $c/R=0.45$ .

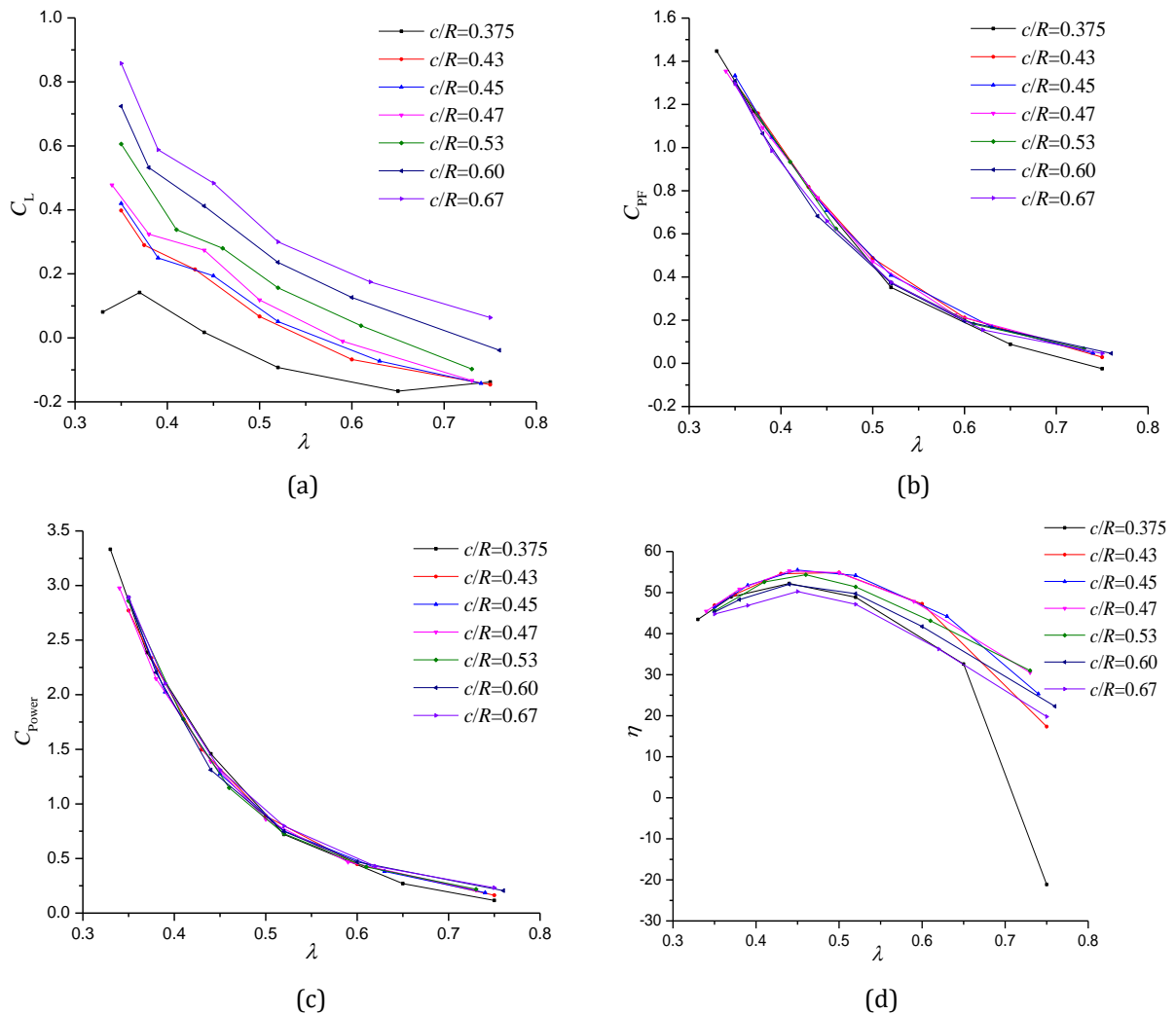


**Fig.3.32** Performance curves at different  $\lambda$ . (a) Lift coefficient; (b) Propulsive force coefficient; (c) Power coefficient; (d) Efficiency.

The performance curves of both the rotating system and single blade are displayed in figure 3.33, to investigate their differences for three  $\lambda$ . Compared with the Reynolds number effect, it seems that the influence of  $\lambda$  is more obvious. Actually, both  $\lambda$  and  $Re$  depends on the rotating speed, based on the definition of  $Re$ . However, the influence of  $Re$  on the performance is very small, except when  $Re$  is smaller than  $1.47 \times 10^4$ , which is observed in section 3.2.3. The  $Re$  in the tested cases in this section is much larger than

$1.47 \times 10^4$ . Based on the following figures, it is observed that both the lift and propulsive force coefficients are much larger at low  $\lambda$  caused by the large rotating speed. Additionally, the performance curves of the rotating system and single blade vary considerably during a cycle. Thus, two positions,  $\psi=45^\circ$  and  $135^\circ$ , are selected to study the flow structures when the lift coefficient has a positive and negative peak, respectively, while the azimuthal angle of  $12^\circ$  is used to clarify the difference of the propulsive force coefficient.

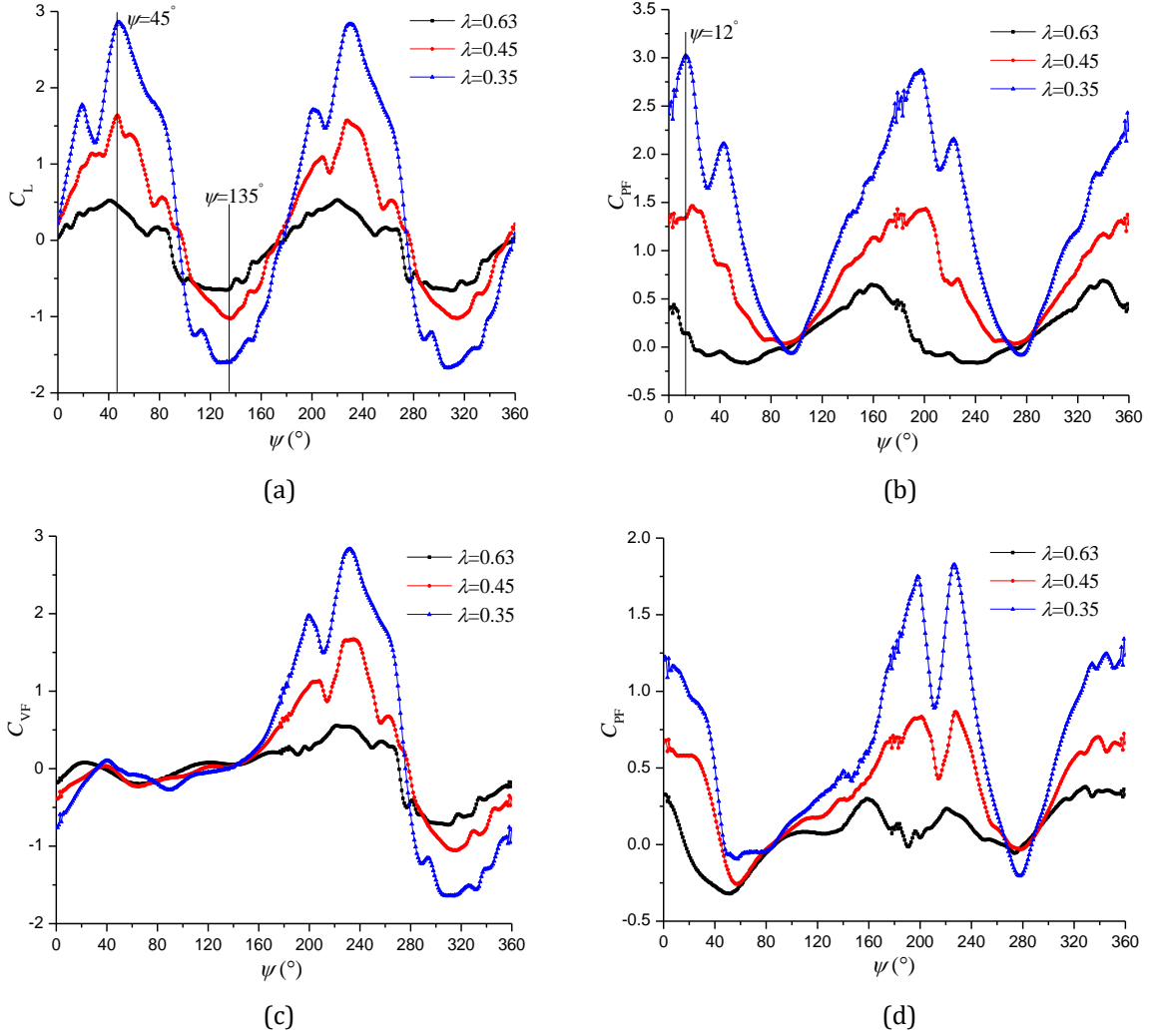


**Fig.3.33** Performance curves at different  $\lambda$  in a revolution. (a) Lift coefficient of the rotating system; (b) Propulsive force coefficient of the rotating system; (c) Vertical force coefficient of single blade; (d) Propulsive force coefficient of single blade.

The flow structures and pressure distributions on the two blades are presented in figure 3.34 and 3.35 at three  $\lambda$ . At  $\psi=45^\circ$ , the lift coefficient of the rotating system has a positive peak. At low  $\lambda$ , the flow field is more complex due to the large rotating speed and there is a clear wake A-blade B interaction. Besides, at high  $\lambda$ , the wake B also interacts with itself, because it has enough time to contact because of the low rotating speed. On the left side of blade A, there is a large flow separation vortex near the leading edge. After that, the flow reattaches and then a vortex structure appears near the trailing edge, which becomes weaker when  $\lambda$  decreases. Further decreasing the rotating speed makes the vortex structures nearly disappear. This phenomenon is mainly caused by the stagnation point location. For an instance, at high  $\lambda$ , the stagnation point is located on the left side,

leading to the relatively smooth near-wall flows. Although the attached vortex flows at  $\lambda=0.35$  modify the pressure obviously, as shown in figure 3.35a, the vertical force of blade A is almost the same for three cases. This is due to the balance of the lift and drag components in the vertical direction and the small pressure difference produced by blade A.

On the suction side of blade B, at  $\lambda=0.35$ , a LSB is observed near the leading edge. Then, after the reattachment location, the flow separation occurs near the trailing edge, leading to the slight decrease of the pressure. With the increase of  $\lambda$ , the flow on the suction side of blade B becomes gradually smoother. From the distribution of pressure in figure 3.35b, combined with the velocity contours, it seems that the stagnation point location is the main source for the pressure distribution on both sides, which is due to the change of the relative velocity caused by the change of the rotating speed. The blade B can produce the upward lift, resulting in the generation of positive vertical force. And the drag can also create the positive vertical force, so the rotating system has the largest positive lift at  $\lambda=0.35$ . Finally, the conclusion is that blade B is responsible for the lift difference of the rotating system, mainly caused by the stagnation point location.

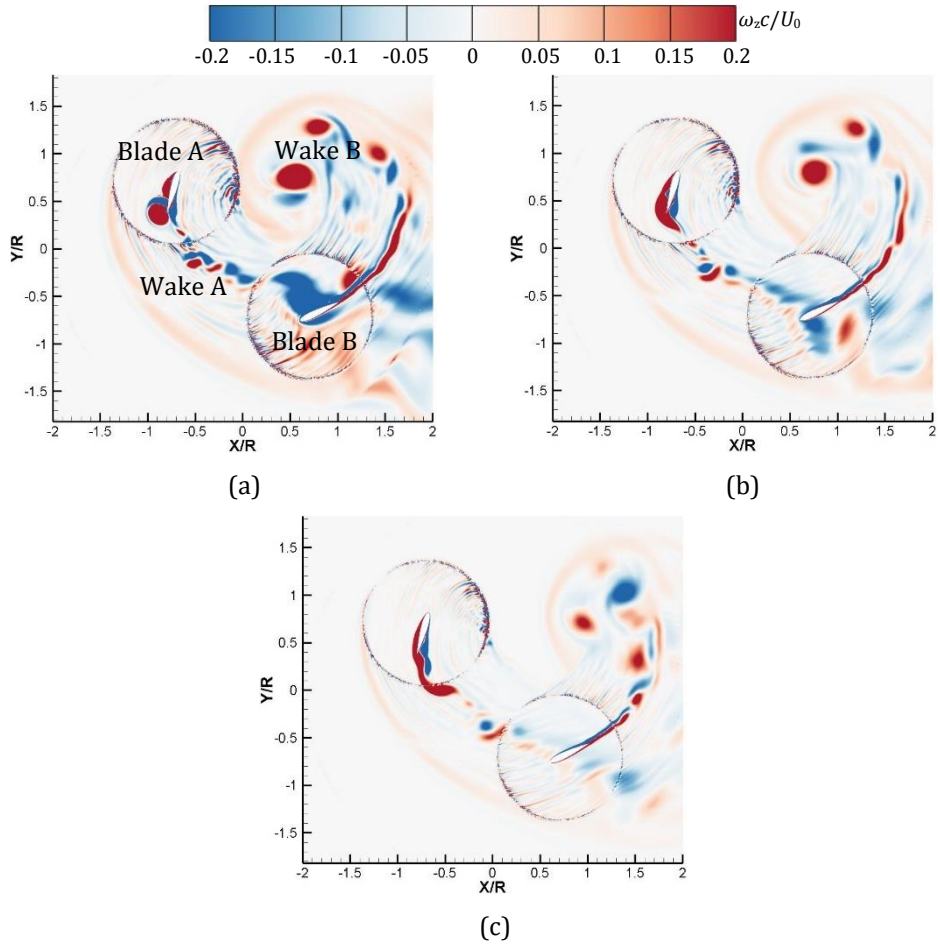


**Fig.3.34** Global flow structures for various  $\lambda$  at  $\psi=45^\circ$ . (a)  $\lambda=0.35$ ; (b)  $\lambda=0.45$ ; (c)  $\lambda=0.63$ .

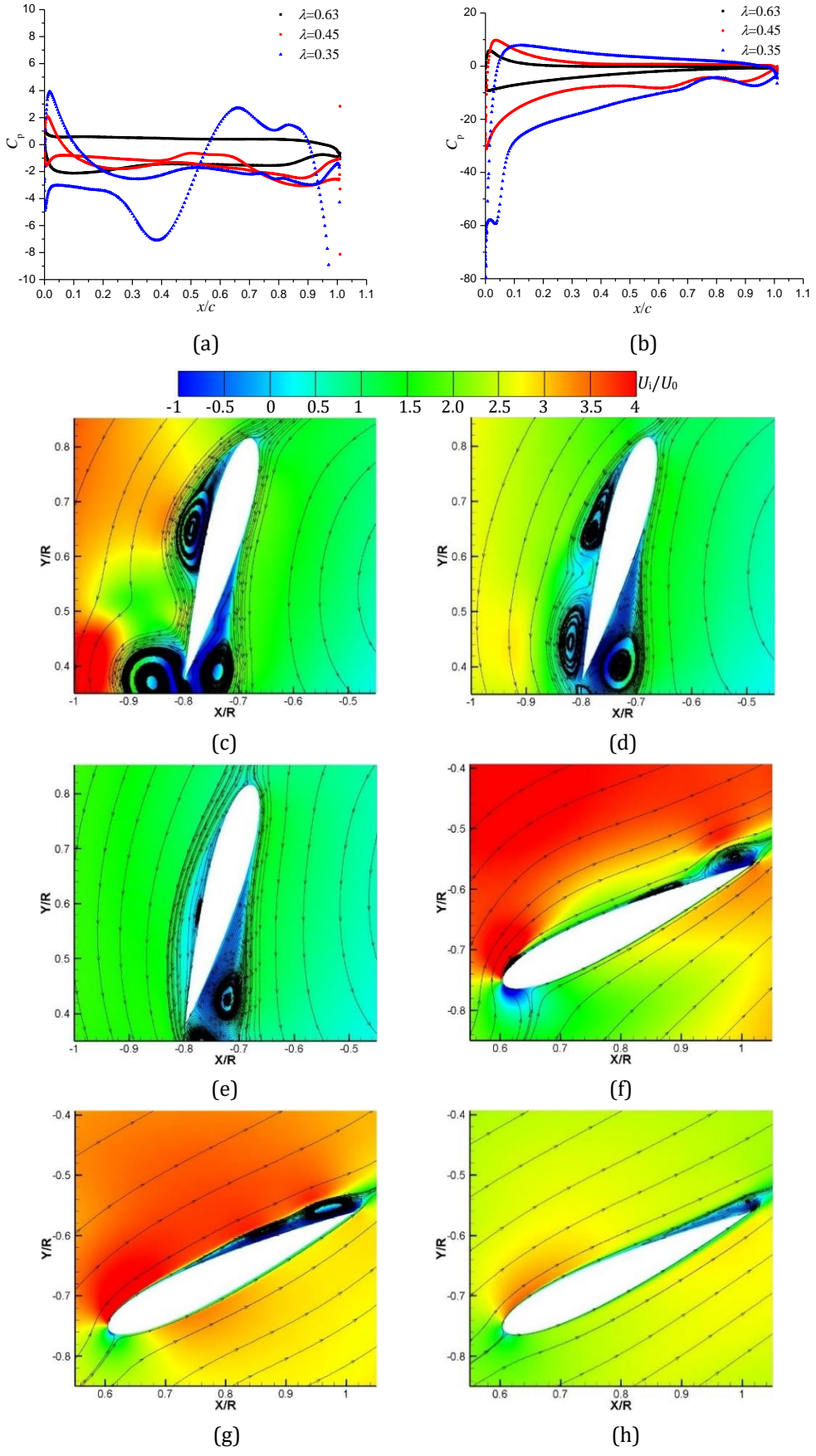


**Fig.3.35** Flow structures for various  $\lambda$  at  $\psi=45^\circ$ . (a) Pressure distribution of blade A; (b) Pressure distribution of blade B; (c) and (f)  $\lambda=0.35$ ; (d) and (g)  $\lambda=0.45$ ; (e) and (h)  $\lambda=0.63$ .

When the blade undergoes the retreating side, at  $\psi=135^\circ$ , the lift coefficient of the rotating system has a negative peak, especially for the case at  $\lambda=0.35$ . The flow structures at this instant are presented in figure 3.36 and 3.37. Globally, it shows no obvious interaction, however, the flow is more complex at low  $\lambda$ . It detects that there are some small-scale vortices inside the boundary layer on the pressure side of blade A, leading to the pressure fluctuations in figure 3.37a. The blade A produces the downward lift, whose component is balanced by the drag component in the vertical direction, resulting in the lift of the rotating system close to zero, as shown in figure 3.33c. For blade B, the main feature is that the vortices appear on the suction side, especially at  $\lambda=0.63$ , where the three vortex structures develop. The largest negative lift of the rotating system is obtained at  $\lambda=0.35$ , due to the downward lift generated by blade B and the large pressure difference (figure 3.37b).

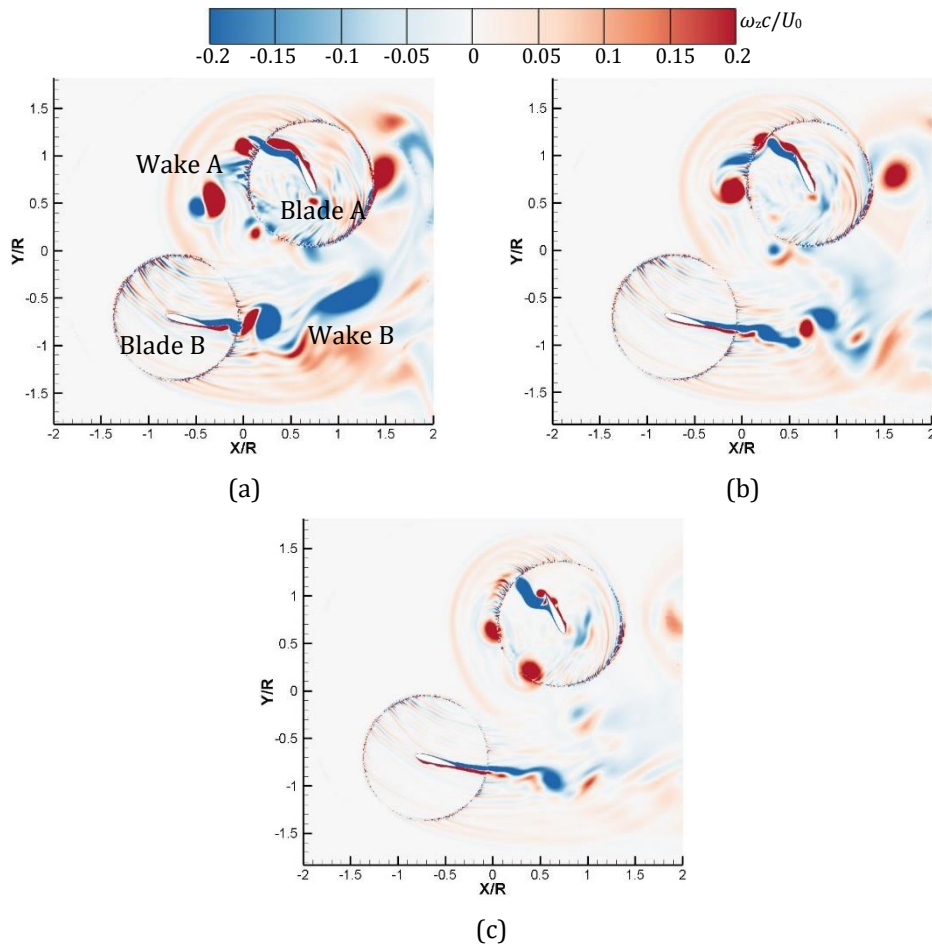


**Fig.3.36** Global flow structures for various  $\lambda$  at  $\psi=135^\circ$ . (a)  $\lambda=0.35$ ; (b)  $\lambda=0.45$ ; (c)  $\lambda=0.63$ .

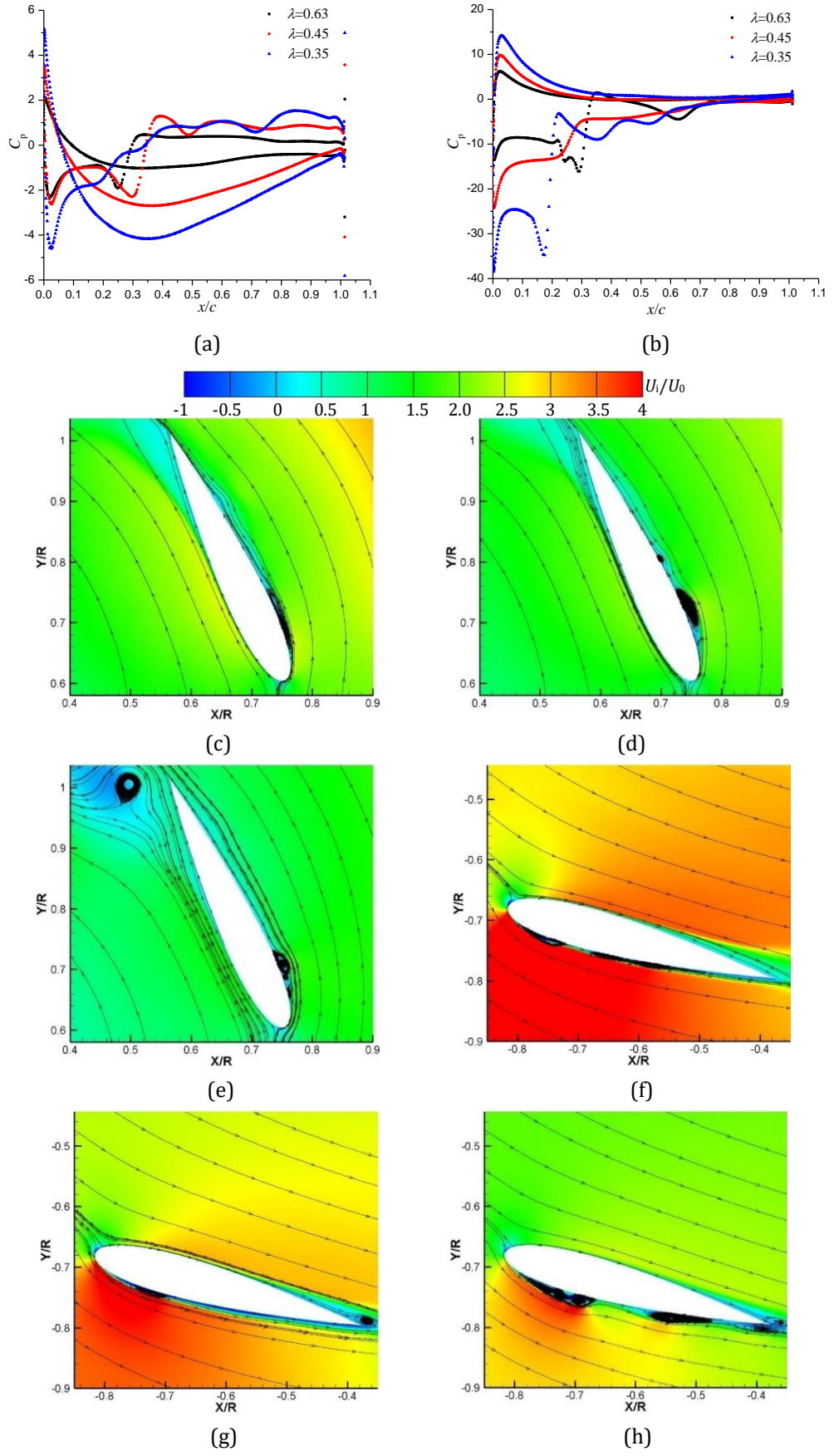


**Fig.3.37** Flow structures for various  $\lambda$  at  $\psi = 135^\circ$ . (a) Pressure distribution of blade A; (b) Pressure distribution of blade B; (c) and (f)  $\lambda = 0.35$ ; (d) and (g)  $\lambda = 0.45$ ; (e) and (h)  $\lambda = 0.63$ .

Finally, the impact of  $\lambda$  on the propulsive force difference of the rotating system is clarified at  $\psi=12^\circ$ , where it has a positive peak. At low  $\lambda$ , blade A is likely interacting with wake B, but this is not the case when  $\lambda$  increases. Moreover, at high  $\lambda$ , wake B has a strong interaction with itself because of the low rotation speed. When it comes to the single blade, the near-wall flow structure and blade loading are very different. The flow over blade A is relatively smooth and there is a flow separation only at the trailing edge on the suction side. However, due to the location of the stagnation point, the pressure on both two sides varies considerably according to  $\lambda$ . Because of the large blade loading at low  $\lambda$ , blade A can produce large upward lift, which is the main source of the large positive propulsive force of the rotating system. Then, on blade B, the flow is more complicated and many vortices are attached to the suction side. At low  $\lambda$ , the three-vortex-structure are obvious, nearly occupying the whole blade surface. With the increase of  $\lambda$ , the flow becomes relatively smooth and only a large-scale vortex appears on the suction side, which is attributed to the shift of the stagnation point towards the suction side. The existence of the vortex leads to a significant pressure drop, as shown in figure 3.39b, resulting in the large blade loading at low  $\lambda$ . The large downward lift creates a large positive propulsive force, which is beneficial to the large positive propulsive force of the rotating system, as shown in figure 3.33. Thus, the global propulsive force is determined by the two blades at this position.

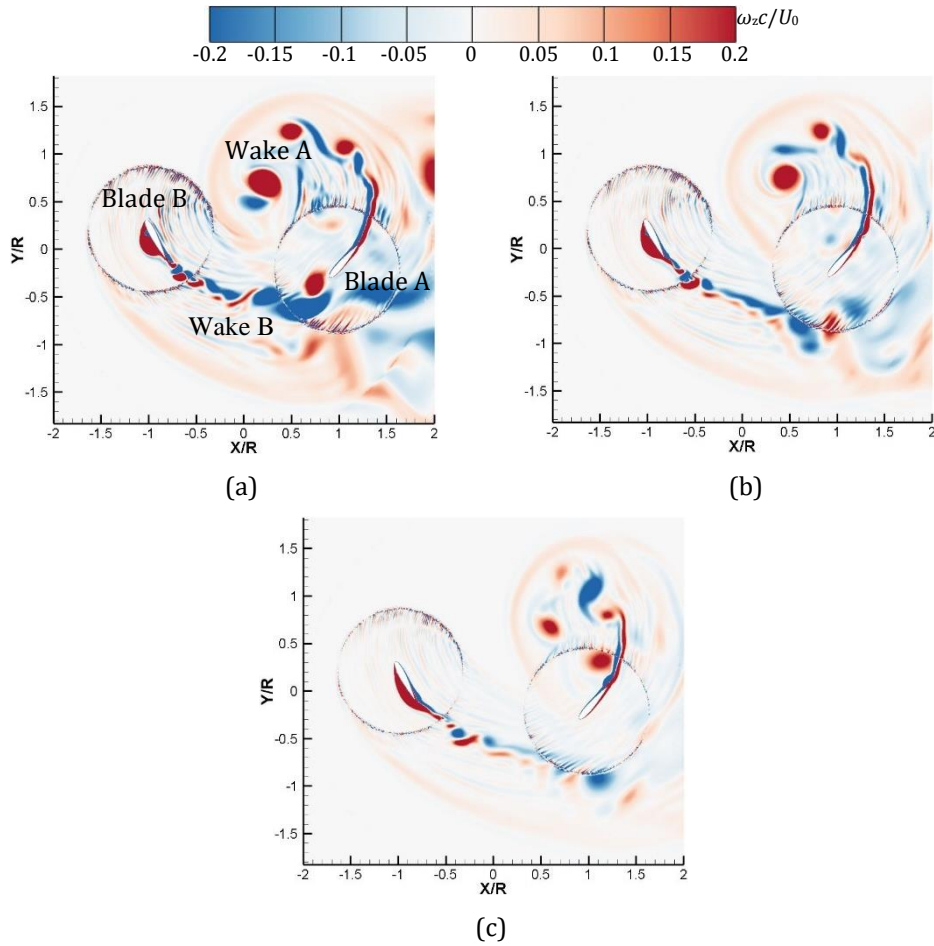


**Fig.3.38** Global flow structures for various  $\lambda$  at  $\psi=12^\circ$ . (a)  $\lambda=0.35$ ; (b)  $\lambda=0.45$ ; (c)  $\lambda=0.63$ .

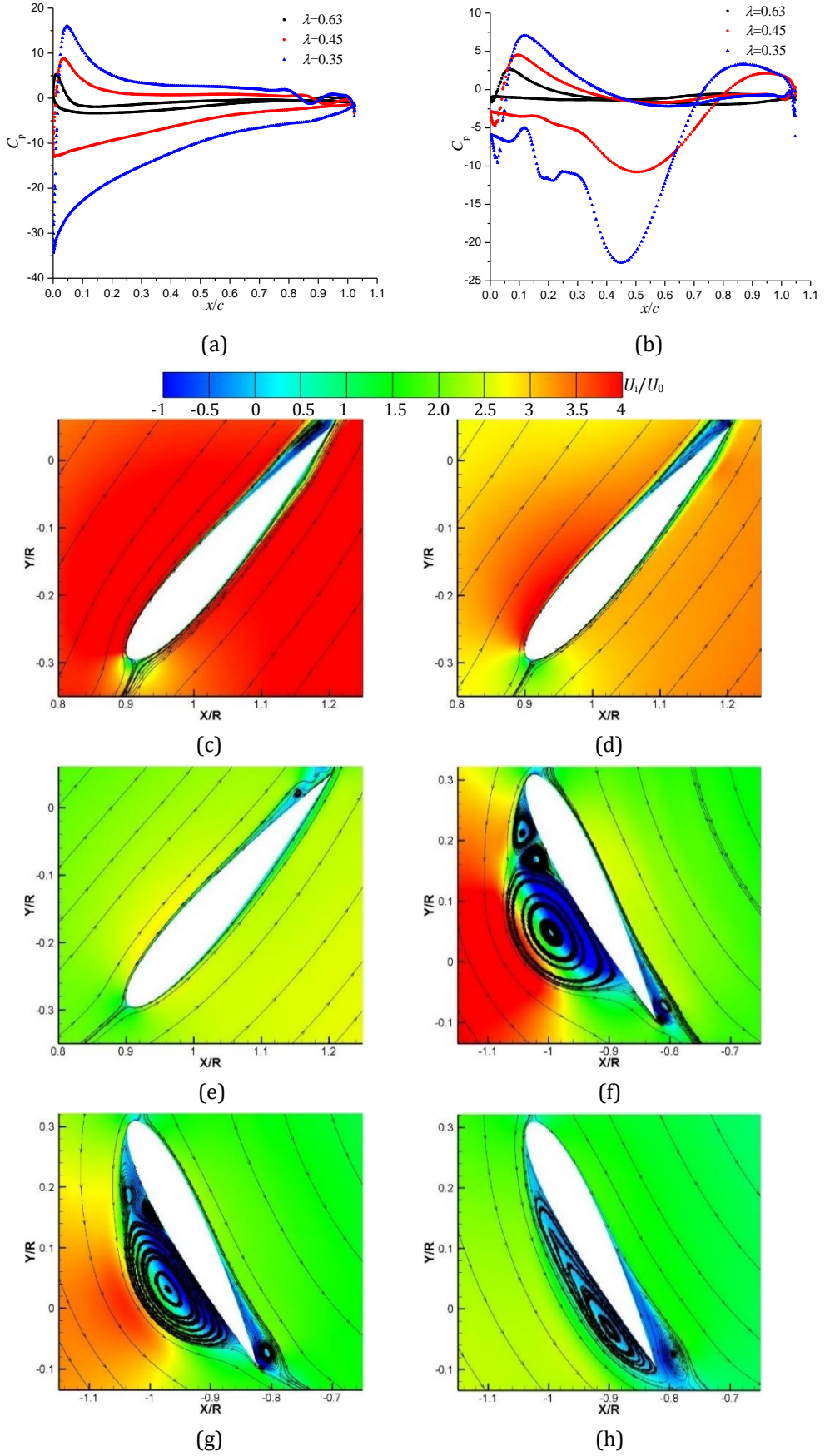


**Fig.3.39** Flow structures for various  $\lambda$  at  $\psi=12^\circ$ . (a) Pressure distribution of blade A; (b) Pressure distribution of blade B; (c) and (f)  $\lambda=0.35$ ; (d) and (g)  $\lambda=0.45$ ; (e) and (h)  $\lambda=0.63$ .

### 3.2.5 Conclusions

(1) For given  $\lambda$  and  $Re$ , the cases with  $c/R=0.45$  for different blade chord lengths achieve the best efficiency. Then, at large  $c/R$ , the global flow structure is more complicated and the performance is strongly impacted, due to the small distance between two adjacent blades.

(2) When it comes to the influence of  $Re$  and  $\lambda$ , it seems that the effect of  $Re$  on the performance is very small. However, at low  $Re$ , the propulsive force is significantly different from the one obtained at relatively high  $Re$ . The advance coefficient  $\lambda$  has a large impact on the flow structures and the global performance, especially at low  $\lambda$ , which is due to the large variation of the relative velocity induced by the change of the rotating speed. It seems that at high  $\lambda$ , the wake at right side of retreating side has a high risk in contacting with the blade, due to the low rotating speed. It is found that the cases with  $c/R=0.45$  at various  $Re$  or  $\lambda$  obtain the best efficiency.

(3) The flow structures inside a cycloidal rotor are extremely complex, including three vortex structures, roll-up vortices inside the boundary layer, LSB, flow separation vortex, wake-wake and blade-wake interactions, and depend on the operating conditions. In addition, except for the near-wall flow, the stagnation point location associated with the boundary layer development is very critical to each blade loading. Both changing  $Re$  and  $\lambda$  can modify the direction of the relative velocity, but it is less influential for  $Re$ , because of the change of the inlet velocity and rotation speed at the same time.

### 3.3 INFLUENCE OF THE PITCH-PIVOT-POINT

#### 3.3.1 Introduction

The location of pitching pivot has much effect on the performance and flow structures, which has been proved on pitching or flapping airfoils/hydrofoils previously. Yilmaz et al. [94] revealed that the appearance of leading-edge-vortex is delayed by the order of one-half convective time scale  $c/U$  as the pitch-pivot-point moves from the leading edge to the trailing edge. Visbal and Shang [95] observed that the pitch-axis position would determine the relative velocities at the leading edge and trailing edge. When it moves towards the leading edge, the effective incidence increases, as well as the relative velocity at the trailing edge. The increase of the effective angle-of-attack and maximal pressure lead to a higher pressure gradient, which can cause a higher vortex flux and resultant higher lift, since more counter-clockwise vortices are shed into wakes from the lower surface at the trailing edge. Besides, the location of pitch-pivot-point determines whether the airfoil imparts or extracts energy from the freestream flows. In this section, the influence of the pitch-pivot-point on the performance and unsteady vortical flows of the cycloidal propeller are studied, because of the rare investigations. The change of the pitch-axis location is from the leading edge to the middle chord, from  $x/c=0.1$  to 0.6. Initially, at the same  $\lambda$  and  $Re$ , the effect of the pitching point is evaluated. Furthermore, the influence of  $Re$  and  $\lambda$  are also included for the case with a specific pitch-pivot-point.

#### 3.3.2 Effect of $x/c$

Seven pitching locations from  $x/c=0.1$  to 0.6, are employed in the present work. Figure 3.40 shows the global performance of the rotating system at different  $Re$ , by changing the inlet velocity and rotating speed at the same time, to remain  $\lambda$  unchanged. It seems that increasing  $Re$  increases the lift coefficient, especially for the case with the pitch-pivot-point located near the leading edge, which was explained by Visbal and Shang [95]. In addition, the propulsive force and power coefficients decrease as  $Re$  increases. At a constant  $Re$ , the lift coefficient increases as the pitching pivot is closer to the leading edge, which shows the opposite trend for the propulsive force and power coefficients. It is observed that the system produces the largest propulsive force when the pitching pivot is at  $x/c=0.5$ , but the efficiency is relatively low due to the production of the large power. According to the distribution of efficiency, it can be seen that it has the best performance when the pitching pivot ranges from  $x/c=0.25$  to 0.3 under various  $Re$  conditions.

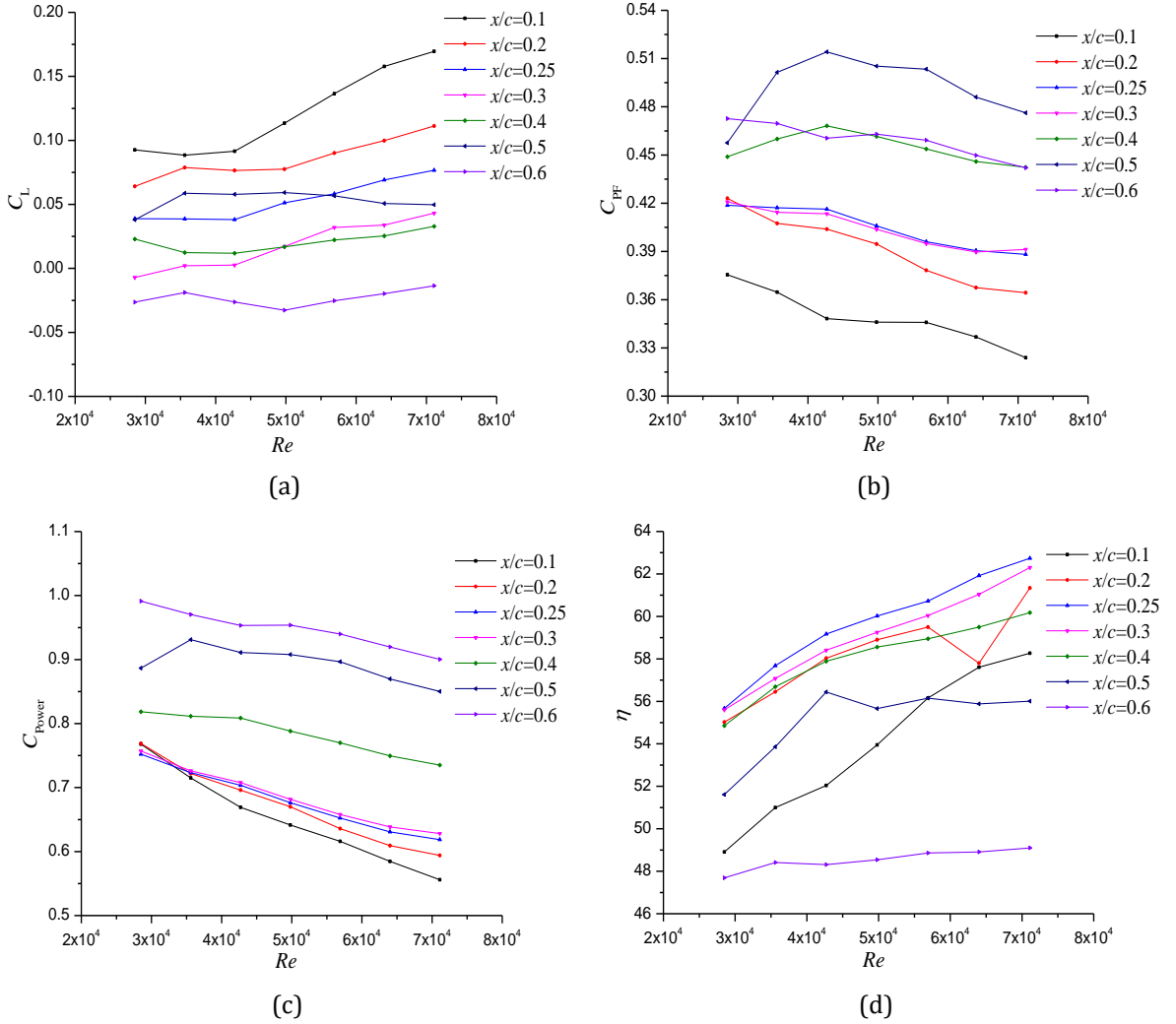


**Fig.3.40** Global performance of the cycloidal propeller. (a) Lift coefficient; (b) Propulsive force coefficient; (c) Power coefficient; (d) Efficiency.

At  $\lambda=0.52$  and  $Re=4.98\times10^4$ , three locations of  $x/c=0.25, 0.5$  and  $0.6$ , are adopted to study the effect of pitching pivot on the performance of the rotating system and single blade, as well as the internal flow structures. Figure 3.41 plots the performance curves of the cases with different pitch-pivot-points. When the pitching pivot is located at  $x/c=0.6$ , the lift coefficient is negative because of the large magnitude from  $\psi=120^\circ$  to  $180^\circ$ . The vertical force of the single blade with  $x/c=0.25$ , providing the lift to the rotating system, has much difference in some areas compared with other two cases, for examples, at  $\psi=30^\circ\text{-}160^\circ$  and  $\psi=280^\circ\text{-}360^\circ$ . Besides, the distributions of propulsive force coefficient are extremely different for three cases, especially when the pitch-pivot-point shifts to the airfoil middle chord. The propulsive force coefficient of the single blade presents that the difference for the case with  $x/c=0.25$  is relatively large in the whole rotating cycle by the comparison with two other cases. Thus, two locations at  $\psi=95^\circ$  and  $170^\circ$ , and three locations at  $\psi=47^\circ, 110^\circ$  and  $170^\circ$ , are chosen to clarify the difference of lift and propulsive force coefficients for three cases, respectively.

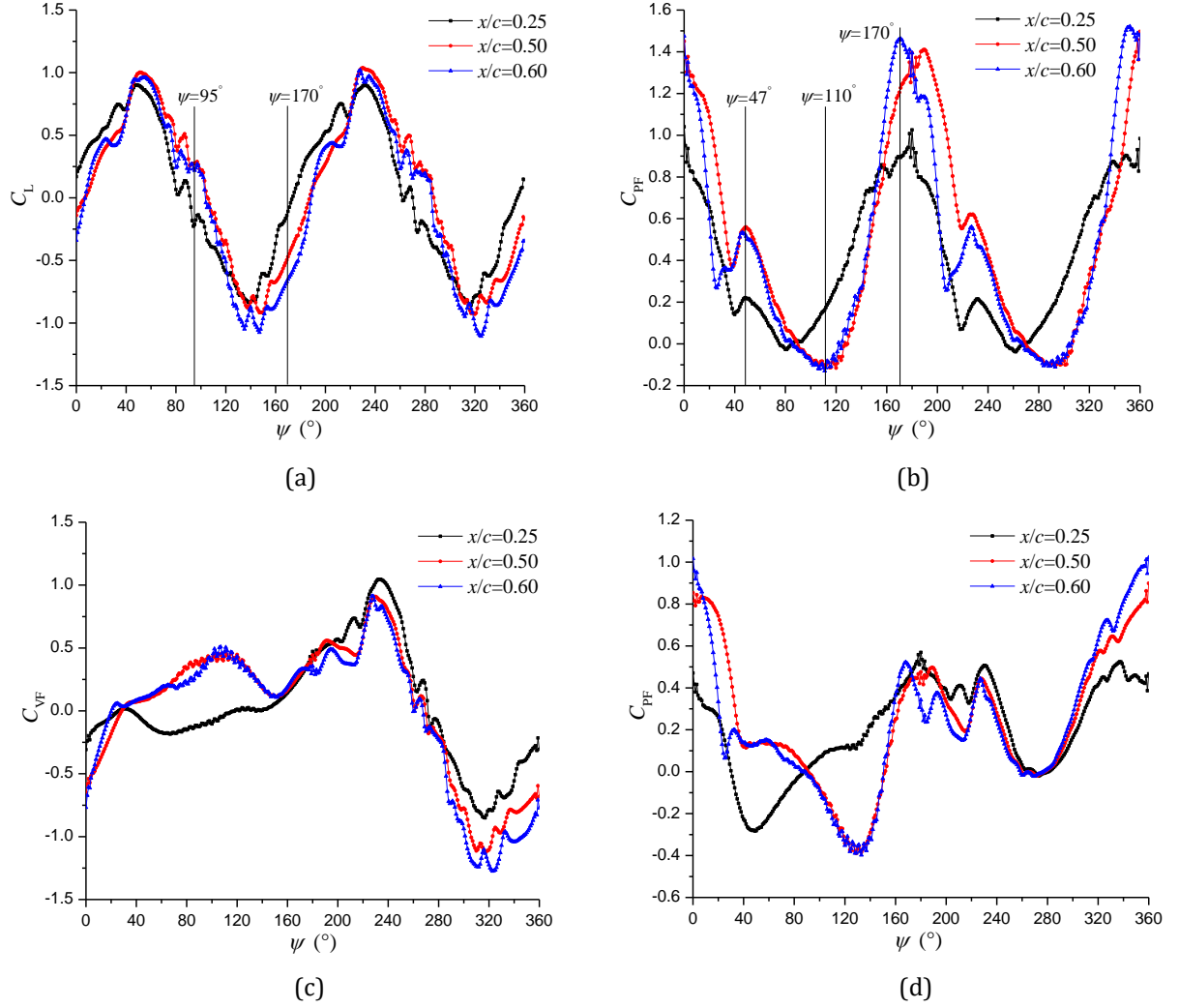


**Fig.3.41** Performance curves in a revolution. (a) Lift coefficient of the rotating system; (b) Propulsive force coefficient of the rotating system; (c) Vertical force coefficient of single blade; (d) Propulsive force coefficient of single blade.

The spanwise vorticity contours for the cases with different pitch-pivot-points are displayed in figure 3.42 to show the general flow field at  $\psi=0^\circ$ . At this position, blade B has the high level of risk in interacting with wake B, especially when the pitching pivot approaches to the blade middle chord. Moreover, the vortical flows become more complicated for the cases with  $x/c=0.4$ , 0.5 and 0.6, which makes the contribution to the large power in figure 3.40c. Besides, it is observed that the massive flow separation on the left side of blade A and right side of blade B appear violently, leading to the more disordered wakes. Consequently, it concludes that the general flow field becomes more complex as the pitching pivot moves towards the blade trailing edge, characterized by the substantial flow separation on one side of two blades and more unsteady wakes. Indeed, moving the pitch-pivot-point can be regarded as adding a plunging motion to the original pitching motion, which changes the resultant wake flows, as was reported by Tian et al. [96]. In addition, Li et al. [97] observed that the LEV occurs earlier and the lift coefficient becomes larger, when the pitching pivot moves towards the leading edge of a pitching airfoil during the upstroke process. However, in the cycloidal rotor, there still lacks the investigations associated with the pitch-pivot-point effect.

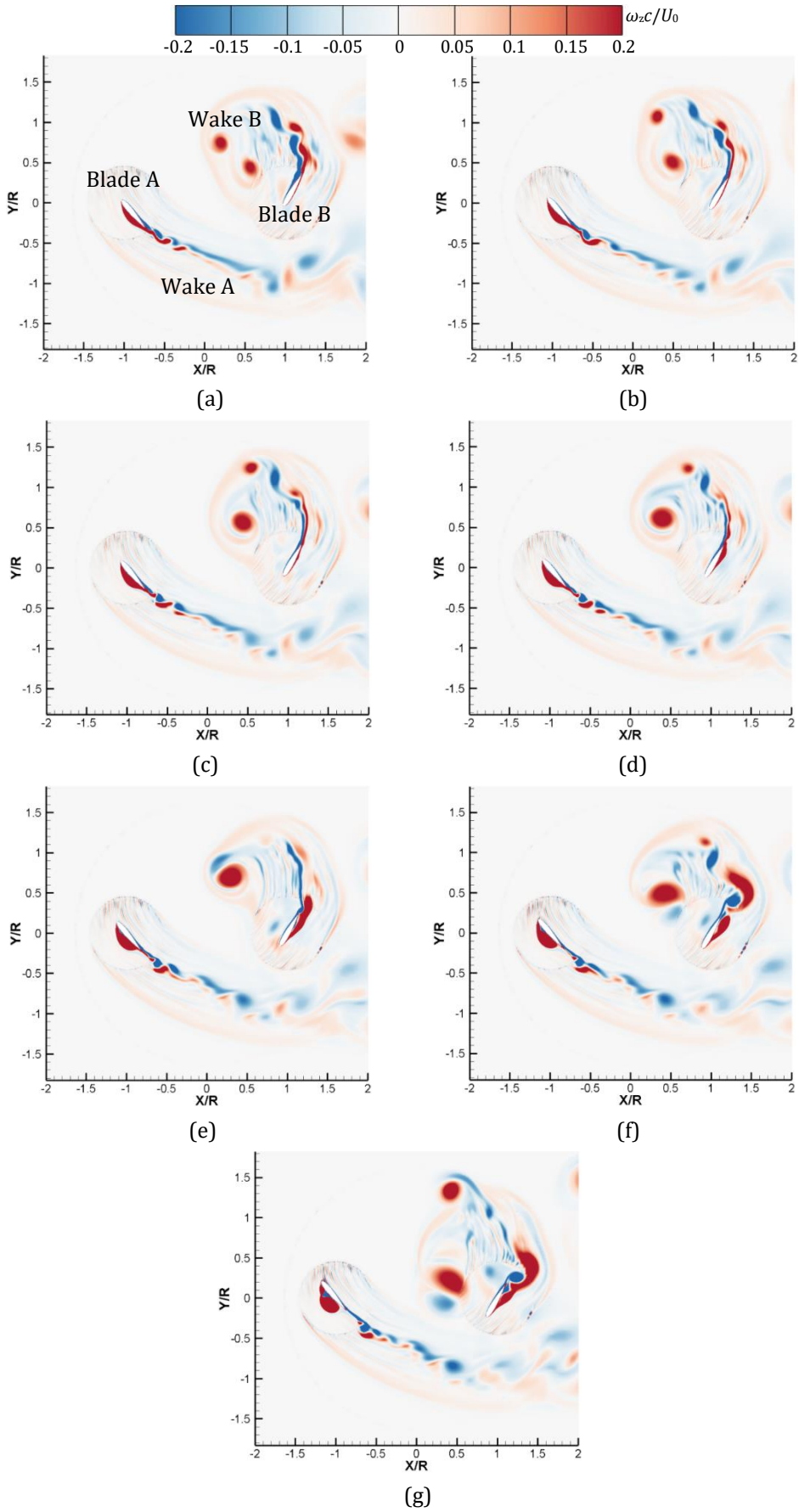


**Fig.3.42** Flow structures for cases with different pitch-pivot-points. (a)  $x/c=0.1$ ; (b)  $x/c=0.2$ ; (c)  $x/c=0.25$ ; (d)  $x/c=0.3$ ; (e)  $x/c=0.4$ ; (f)  $x/c=0.5$ ; (g)  $x/c=0.6$ .

At  $\psi=95^\circ$ , as is shown in figure 3.43 and 3.44, only two cases, in which the pitch-pivot-points are 0.25 and 0.5, are used to clarify the difference of global lift coefficient. The flow field shows the wake A-wake B interaction for two cases. However, for the case with  $x/c=0.5$ , the flow separation is more intensive, especially on two sides of blade A. Then, when it comes to the pressure distributions of two blades, it is observed that the pressure of blade A varies considerably, due to the complex near-wall flows. It seems that the vortical flows on the lower side for the case with  $x/c=0.25$  are more violent, leading to the downward lift. Conversely, as the pitch-pivot-point locates at the middle chord, the existence of the large-scale LEV is dominate in reducing the pressure on upper side, resulting in the upward lift. As a result, the vertical force of blade A is negative for the case with  $x/c=0.25$ , while it is positive for the other case, which is shown in figure 3.41c. This event is mainly ascribed to the stagnation point location, where it shifts towards the lower side for the case with  $x/c=0.5$ , generating the adequate time to develop the boundary layer flows fully on the upper side. The flow near the surface of blade B is similar for two cases, and a small-scale vortex is detected, which is closer to the trailing edge for the case with  $x/c=0.5$  and has more obvious impact on the pressure. Generally, blade A is the main contributor to the lift coefficient difference at this moment.

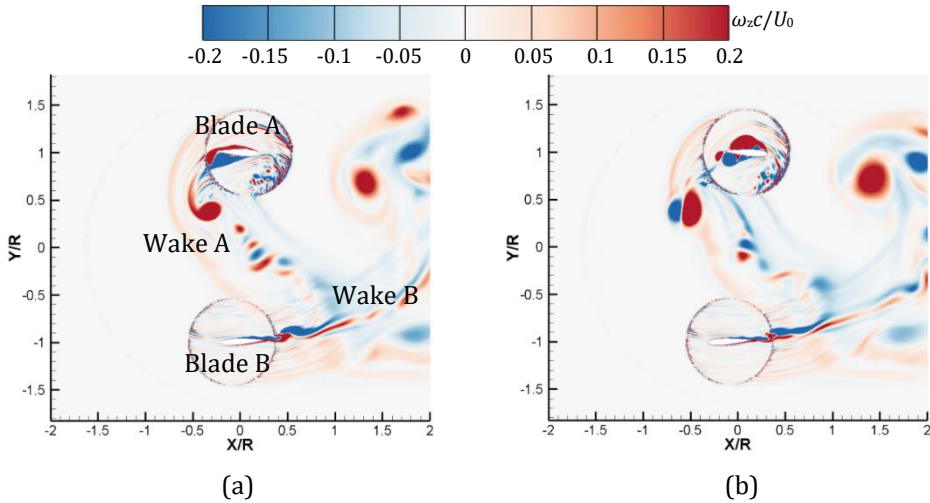


**Fig.3.43** Global flow structures at  $\psi=95^\circ$ . (a)  $x/c=0.25$ ; (b)  $x/c=0.5$ .

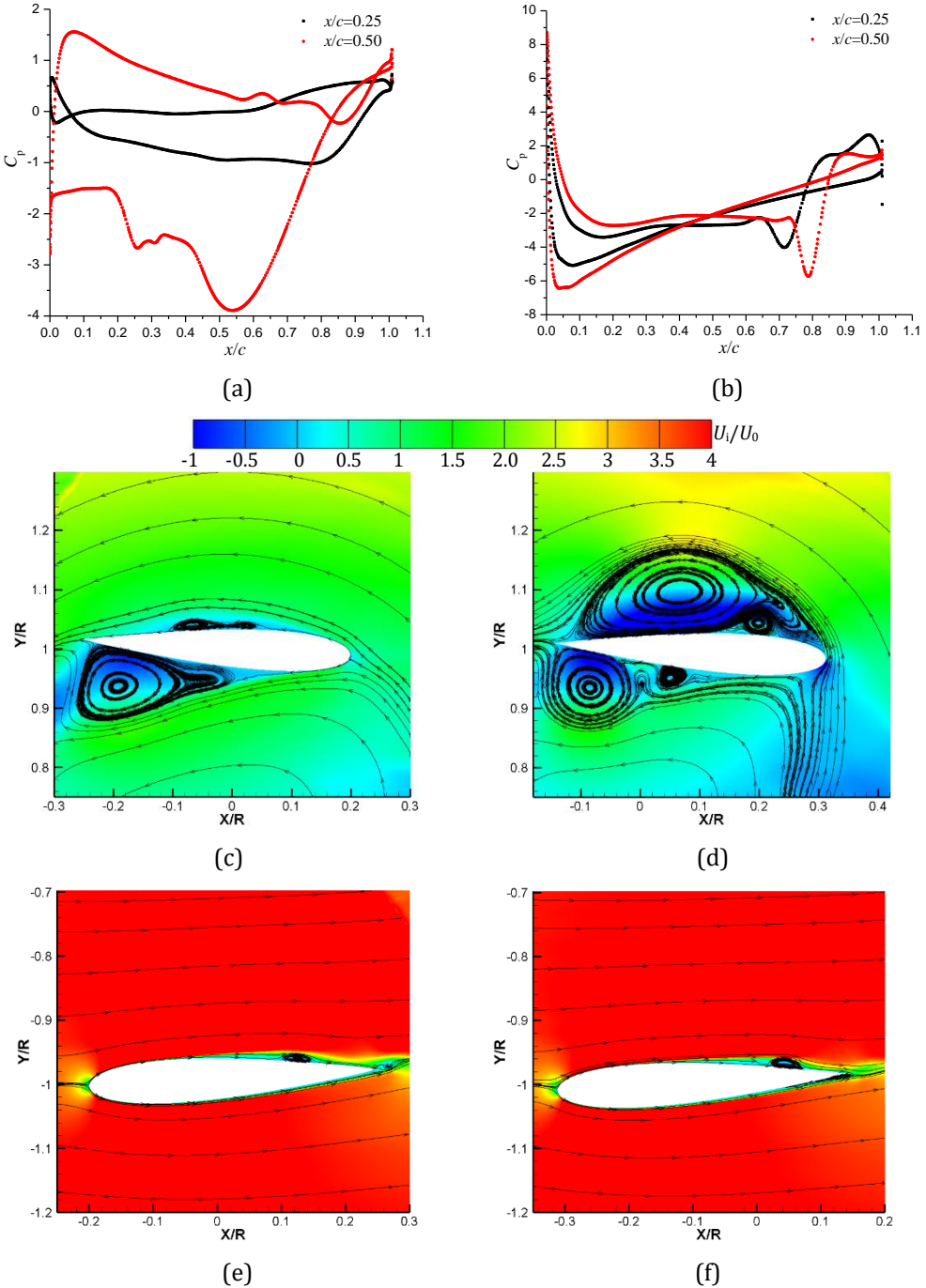


**Fig.3.44** Flow structures at  $\psi=95^\circ$ . (a) Pressure distribution of blade A; (b) Pressure distribution of blade B; (c) and (e)  $x/c=0.25$ ; (d) and (f)  $x/c=0.5$ .

Both the global lift and propulsive force coefficients have much difference at  $\psi=170^\circ$  for cases with three pitch-pivot-points. In figure 3.45, the general flow field shows that there is a strong blade A-wake A interaction as the pitch-pivot-point moves downstream. In addition, the massive flow separation is more obvious on the left side of blade B and right side of blade A, for cases with  $x/c=0.5$  and 0.6. When considering the pressure distributions of two blades, it seems that the main difference is the pressure on the left side of blade A due to the stagnation point deflection, and the pressure on the right side because of the attached vortex. Evidently, with the pitch-pivot-point moving to the middle chord, the size of this vortex structure becomes larger. Although the pressure

distributions and flow structures over the surface of blade A are different for three cases, the resultant vertical force in figure 3.41c is similar because of the relatively small blade loading. For blade B, the pressure difference is much larger than blade A, as is shown in figure 3.46b. The flow structures show that a large-scale LEV is attached on the suction side, which has great impact on the pressure there. The LEV has larger size as the pitching pivot moves towards the trailing edge, bringing about the large magnitude of negative vertical force in figure 3.41c. Thus, the lift coefficient difference for three cases is mainly induced by blade B, as a consequence of the attached large-scale LEV.

According to the variation of propulsive force coefficient for the rotating system and single blade, it can be seen that the contribution of blade A can be neglected because of the relatively small blade loading in figure 3.46a, although it can produce the positive propulsive force resulting from the upward lift. As a main contributor, blade B produces the large positive propulsive force induced by the downward lift with large magnitude, because of the large pressure difference in figure 3.46b. Therefore, the main conclusion is that blade B is responsible for the difference of both lift and propulsive force coefficients for three cases.

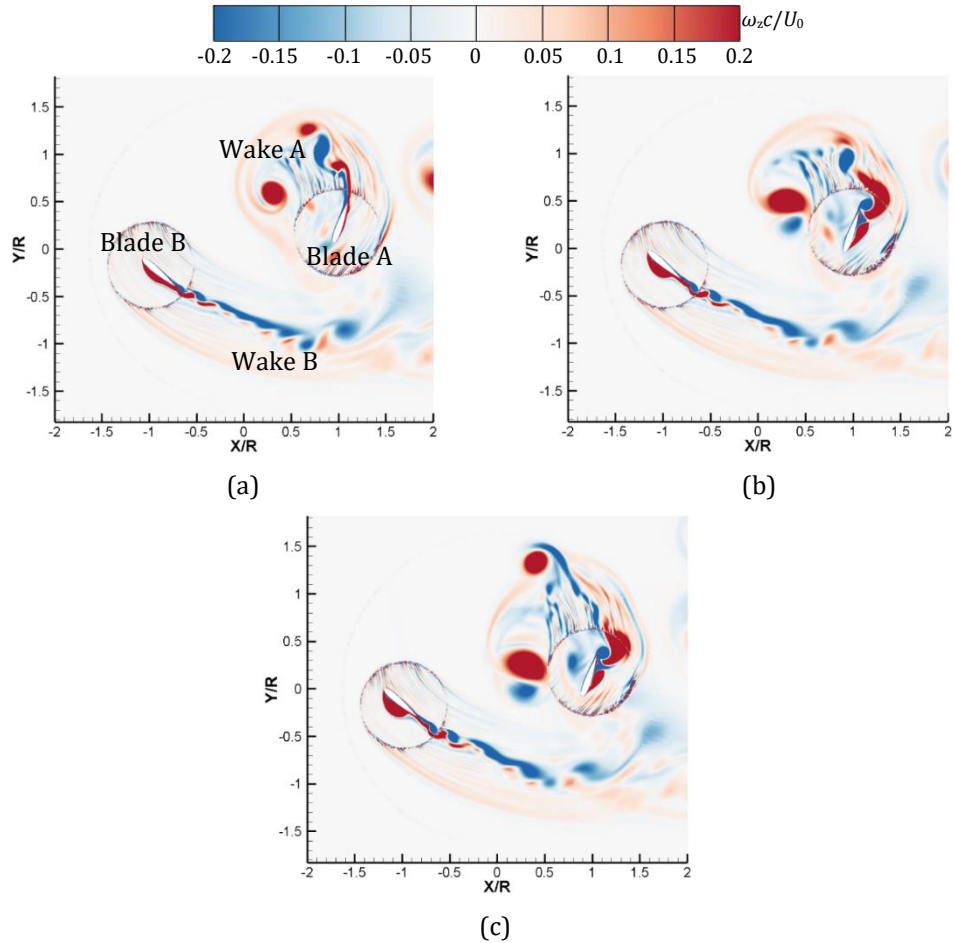


**Fig.3.45** Global flow structures at  $\psi=170^\circ$ . (a)  $x/c=0.25$ ; (b)  $x/c=0.5$ ; (c)  $x/c=0.6$ .

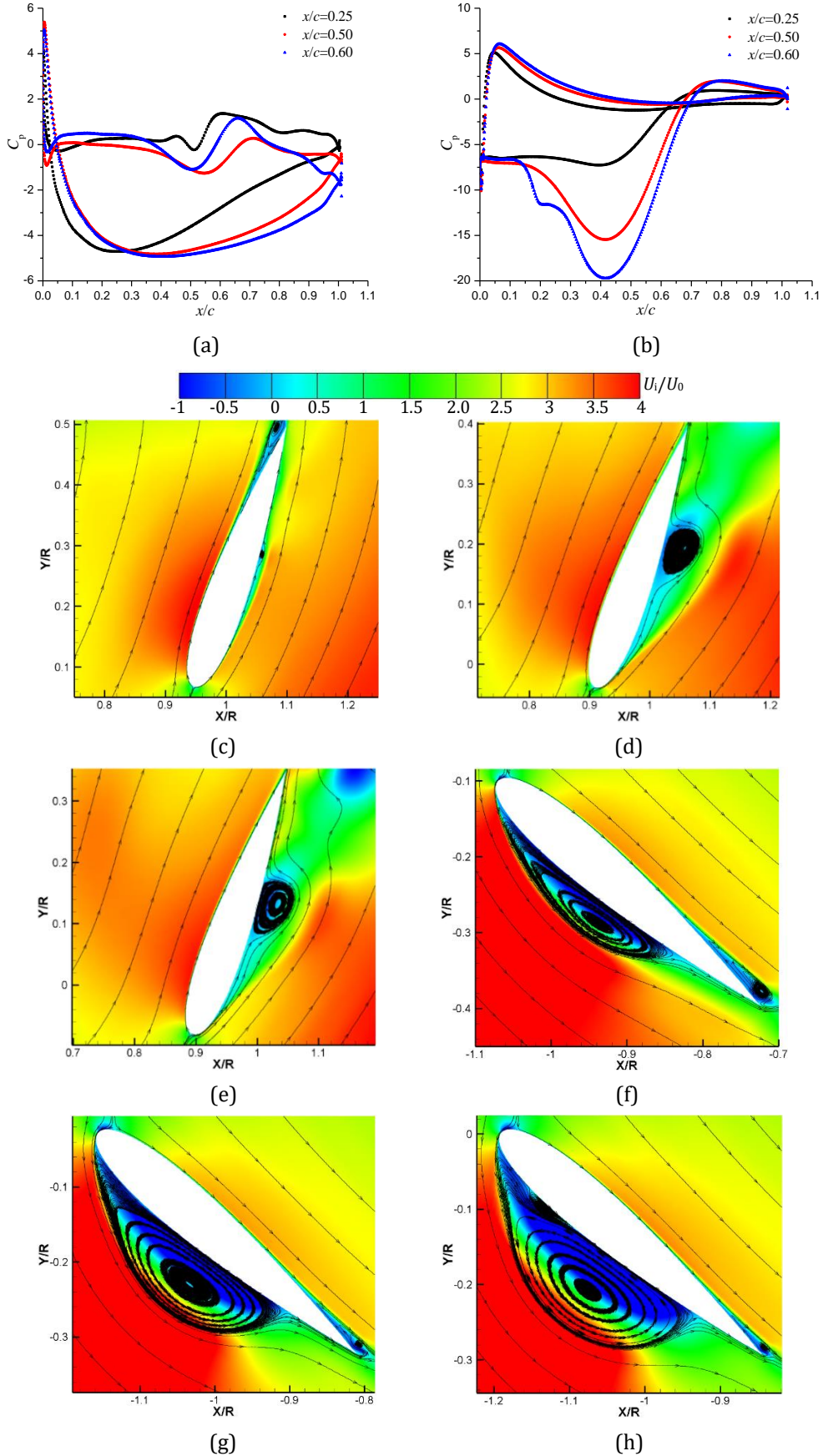


**Fig.3.46** Flow structures at  $\psi=170^\circ$ . (a) Pressure distribution of blade A; (b) Pressure distribution of blade B; (c) and (f)  $x/c=0.25$ ; (d) and (g)  $x/c=0.5$ ; (e) and (h)  $x/c=0.6$ .

In figure 3.41b, the difference of propulsive force coefficient is visible when the pitch-pivot-point is located at  $x/c=0.25$  and 0.5. Figure 3.47 and 3.48 presents the detailed flow structures and pressure distributions of two blades at  $\psi=47^\circ$ . At this location, the wake shedding from blade A interacts with blade B strongly and wake B has a high level of risk in colliding with itself. Additionally, a substantial flow separation on the surface of blade A and the more intensive wakes are observed for the case with  $x/c=0.5$ . By the comparison of pressure distributions of two blades, it seems that the pressure difference of blade B is much larger than that of blade A, but it is almost the same for two cases, as a result of the relatively smooth flows over the suction side, which is shown in figure 3.48b, 3.48e and 3.48f. Due to the upward lift, the propulsive force produced by blade B is positive with large value because of the large pressure difference. Around the blade A surface, there are a large-scale LEV attached on the left side and flow separation vortex near the trailing edge of right side. Interestingly, the presence of the large-scale LEV for the case with  $x/c=0.5$  drops the pressure significantly, leading to the positive propulsive force because of the upward lift towards the left side. However, for the case with  $x/c=0.25$ , the size of LEV is relatively small and the resultant lift is downward towards the right side, which causes the production of negative propulsive force, as is shown in figure 3.41d. This phenomenon is mainly induced by the stagnation point shift towards the right side for the case with  $x/c=0.5$  shown in figure 3.48d, resulting in the different development of the boundary layer flows. Thus, the difference of propulsive force coefficient for two cases should be analyzed based on the pressure distribution of blade A and the stagnation point location, leading to the different developments of the boundary layer flows, is the main contributor.

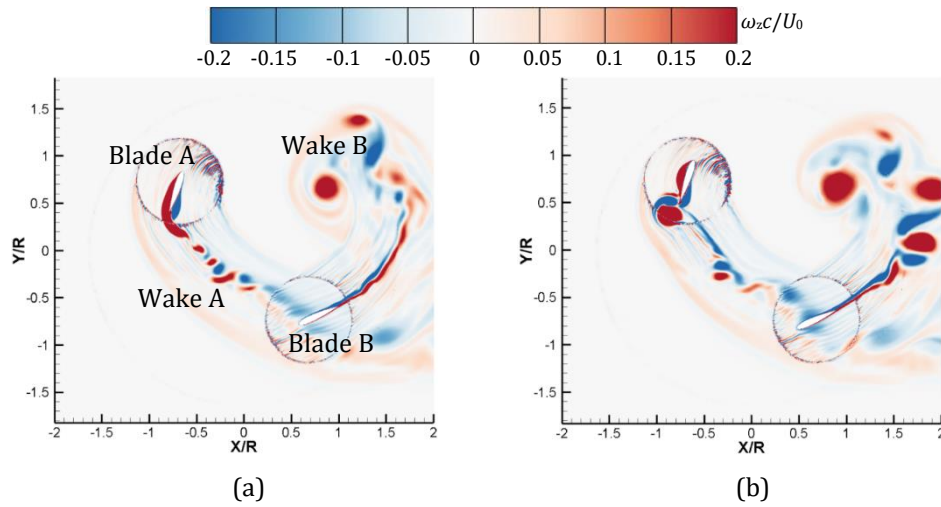


**Fig.3.47** Global flow structures at  $\psi=47^\circ$ . (a)  $x/c=0.25$ ; (b)  $x/c=0.5$ .

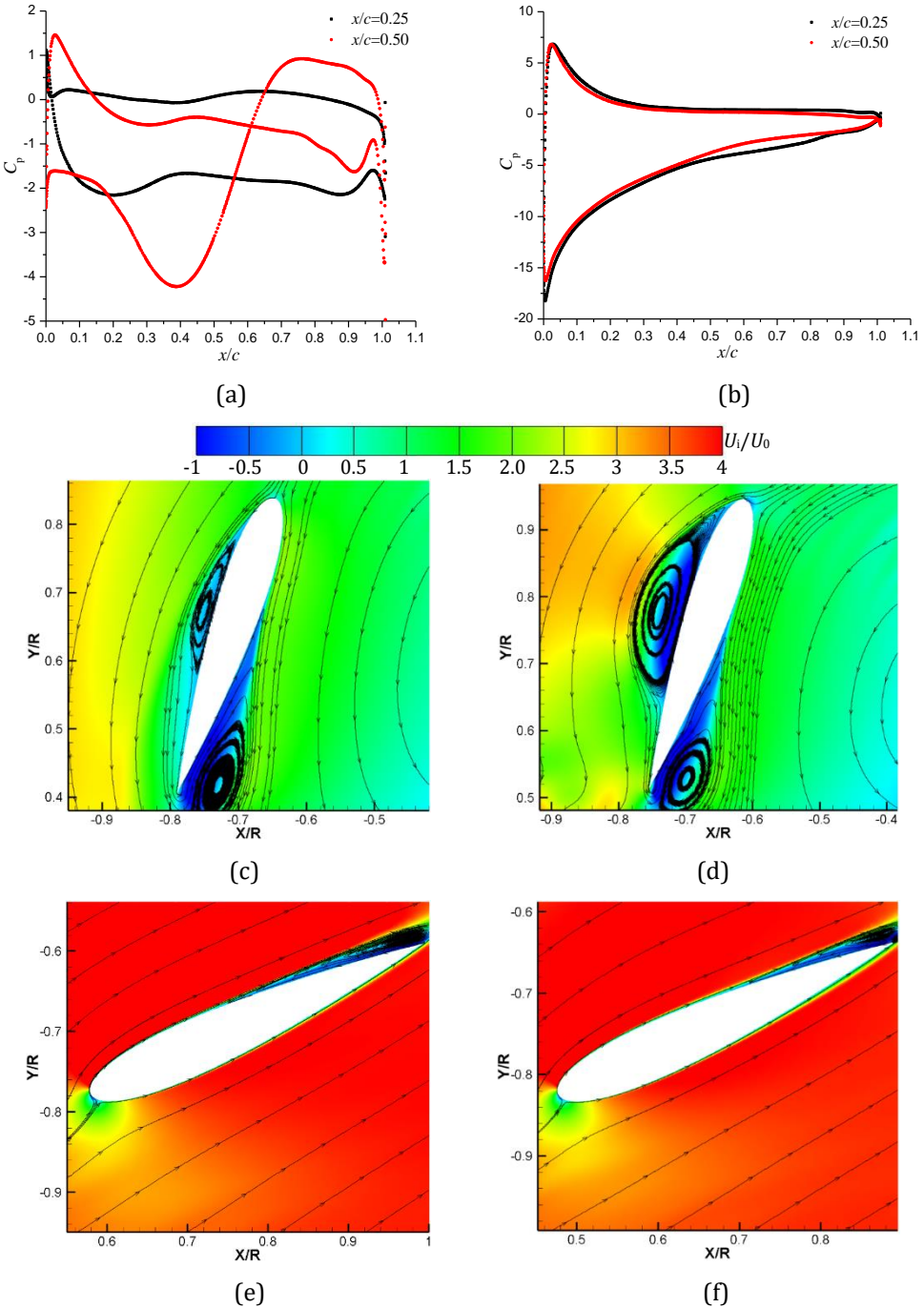


**Fig.3.48** Flow structures at  $\psi=47^\circ$ . (a) Pressure distribution of blade A; (b) Pressure distribution of blade B; (c) and (e)  $x/c=0.25$ ; (d) and (f)  $x/c=0.5$ .

As  $\psi$  increases to  $110^\circ$ , the global propulsive force coefficient for the case with  $x/c=0.25$  is much larger than that for the case with  $x/c=0.5$ , which shows the opposite trend compared with that at  $\psi=47^\circ$ . Consequently, the flow structures and pressure distributions of two blades are displayed in figure 3.49 and 3.50. The general flow is similar with that at  $\psi=95^\circ$  and the main feature is wake A-wake B interaction. Moreover, it seems that the flow separation on upper side of blade A is more violent when the pitch-pivot-point is located at the middle chord. In figure 3.50a, it is observed that the pressure distributions of blade A for two cases are extremely different, both on two sides. Due to the stagnation point close to the leading edge of the lower surface, the distinctive three-

vortex-structure is detected on the upper side for the case with  $x/c=0.5$ , generating the negative propulsive force because of the upward lift towards the upper side. But in figure 3.50c, the flow on the upper side is really smooth, resulting in the positive propulsive force due to the downward lift towards the lower side. The pressure distributions of blade B for two cases are almost the same, but a little difference near the leading edge. Therefore, because of the stagnation point location, the flow structures on upper side of blade A result in the opposite direction of lift, which causes the propulsive force difference for the cases with two pitch-pivot-points.

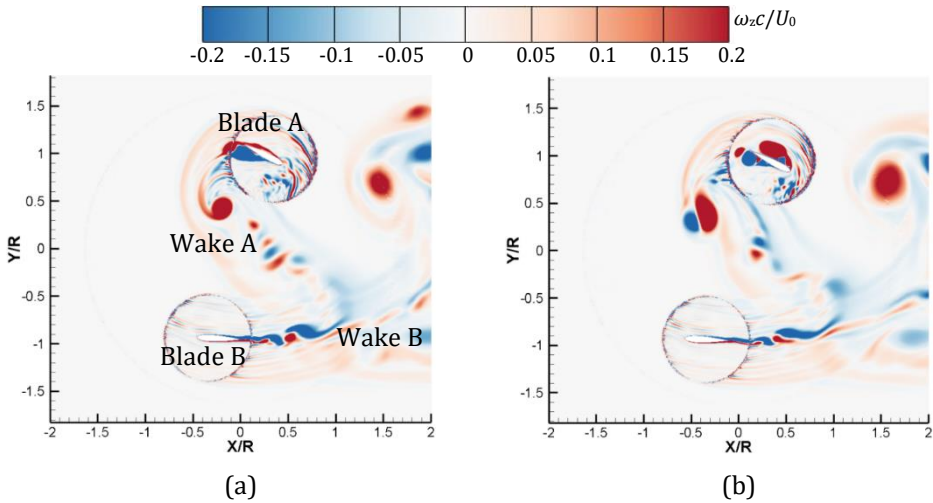


**Fig.3.49** Global flow structures at  $\psi=110^\circ$ . (a)  $x/c=0.25$ ; (b)  $x/c=0.5$ .

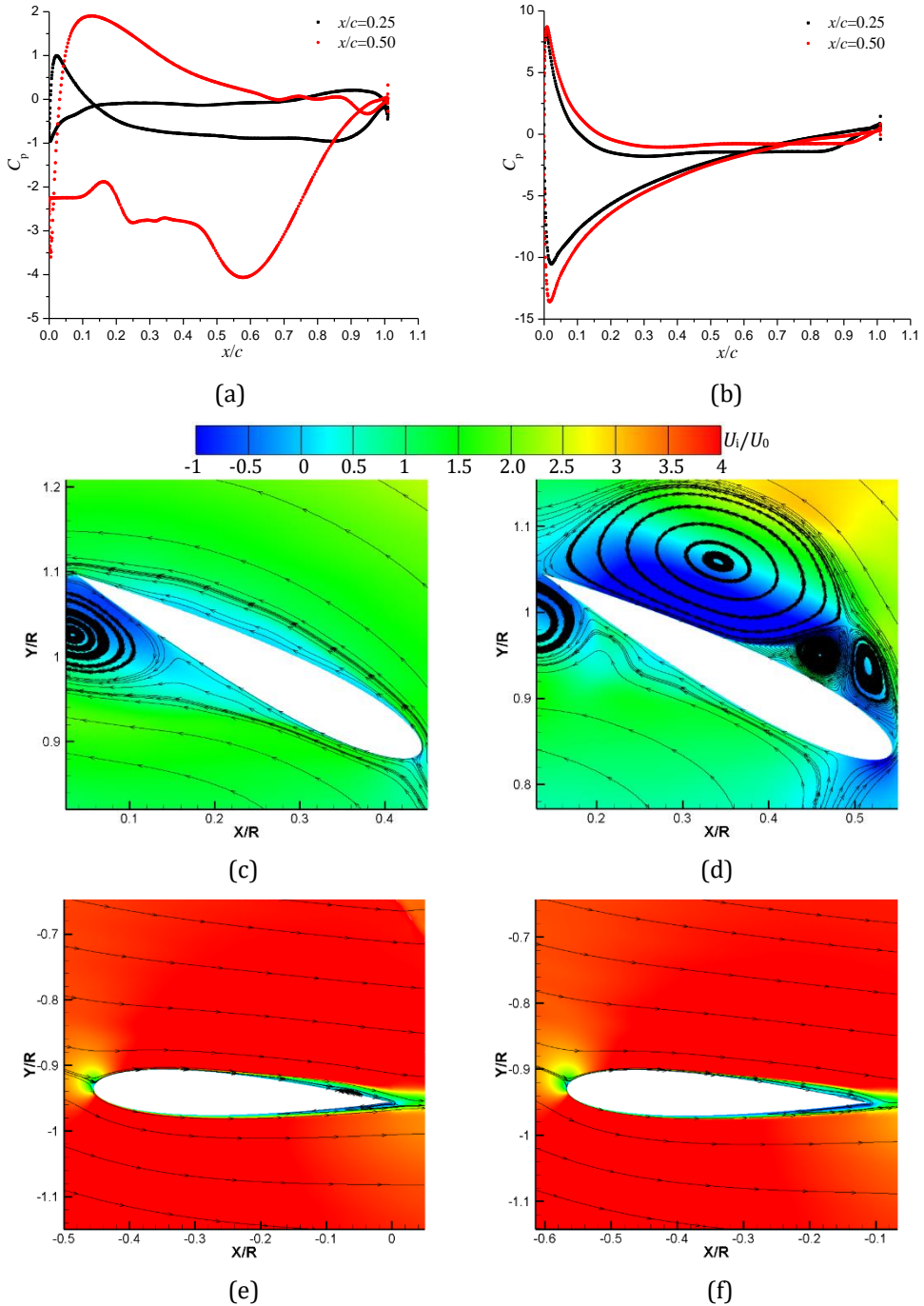


**Fig.3.50** Flow structures at  $\psi=47^\circ$ . (a) Pressure distribution of blade A; (b) Pressure distribution of blade B; (c) and (e)  $x/c=0.25$ ; (d) and (f)  $x/c=0.5$ .

### 3.3.3 Effect of $Re$

To take the Reynolds number effect into consideration, the advance coefficient  $\lambda$  is fixed by modifying the inlet velocity and rotating speed at the same time. When the pitching pivot is located at the blade middle chord, both the lift and propulsive force coefficients change significantly under different  $Re$  conditions, as is shown in figure 3.41a and 3.41b. As a consequence, the force distributions of the rotating system and single blade in a revolution at three  $Re$  are plotted in figure 3.51. It is evident that the force obtained under low  $Re$  condition differs from that at two other  $Re$ . The difference of lift

coefficient is mainly at  $\psi=90^\circ$ - $140^\circ$ , while it occurs in a wide range for the propulsive force coefficient. For the performance evolution of the single blade, the difference of propulsive force coefficient is more evident than the lift coefficient under various  $Re$  conditions. Hence, an azimuthal angle of  $105^\circ$  and two locations at  $\psi=30^\circ$  and  $170^\circ$ , are employed to clarify the difference of lift and propulsive force coefficients at two  $Re$ , respectively.

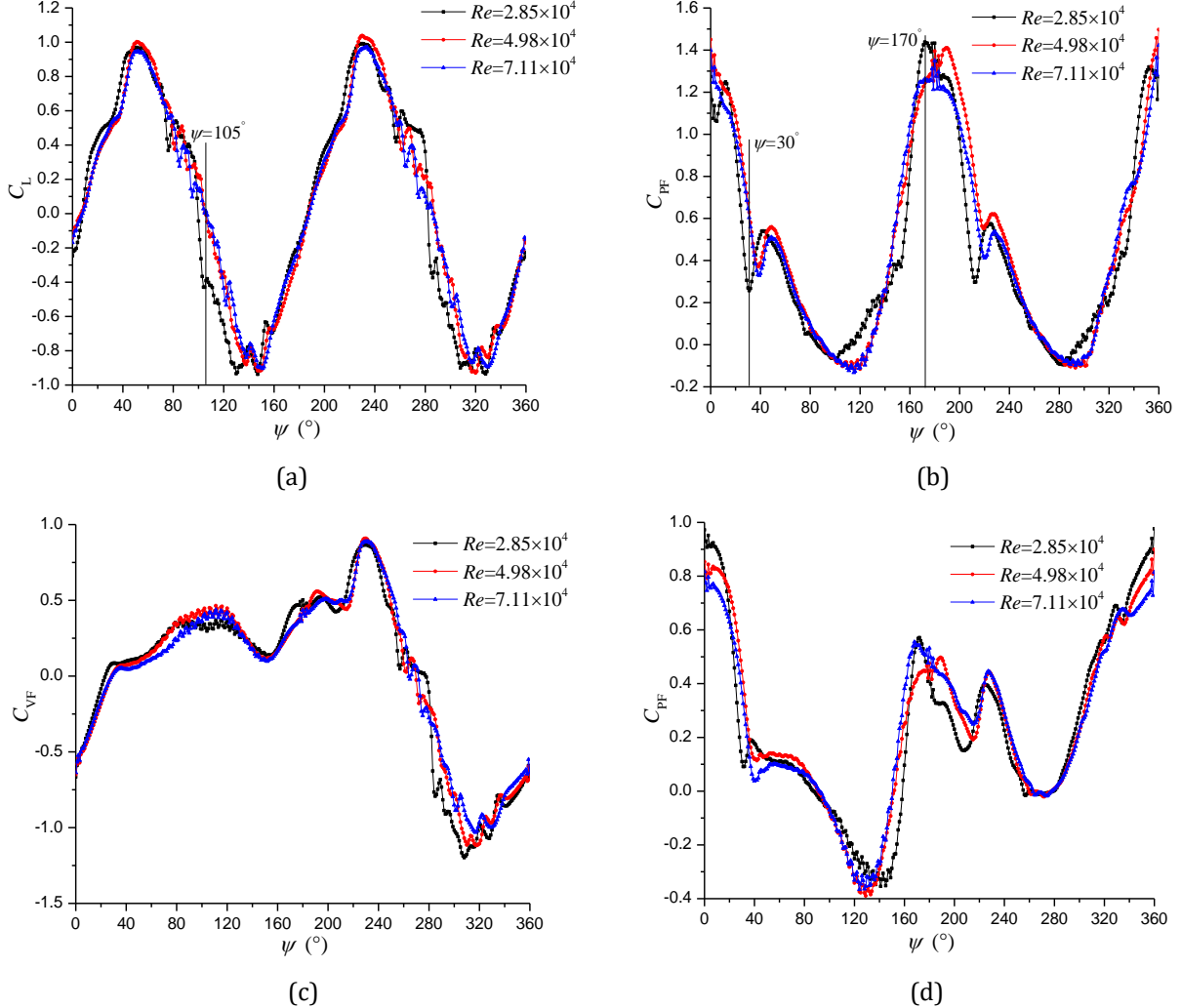


**Fig.3.51** Performance curves in a revolution. (a) Lift coefficient of the rotating system; (b) Propulsive force coefficient of the rotating system; (c) Vertical force coefficient of single blade; (d) Propulsive force coefficient of single blade.

At  $\psi=105^\circ$ , the flow structures used to describe the lift coefficient difference at two  $Re$  are shown in figure 3.52 and 3.53. It indicates that the global flow field is more disordered with the increase of  $Re$ , featured by the wake A-wake B interaction and massive flow separation on both sides of blade A. Obviously, the pressure difference of blade A is much smaller than that of blade B, although the vortical flows over the suction side of blade A is more complicated. The three-vortex-structure develops fully under high  $Re$  condition, affecting the pressure on the whole suction side. The lift of blade A is upward towards the upper side, leading to the production of positive vertical force and negative propulsive force. Due to the small blade loading in figure 3.53a, the vertical force of blade A has almost no difference at two  $Re$ . Thus, the lift difference is primarily from blade B, though the flows are very smooth on both two sides, which is shown in figure 3.53e and

3.53f. The pressure difference of blade B under low  $Re$  condition is larger than that at high  $Re$ . As a result, the downward lift generates the negative vertical force with large value. Generally, the difference of lift coefficient at two  $Re$  is induced by blade B, thanks to the different boundary layer flows caused by the change of the pitching rate.

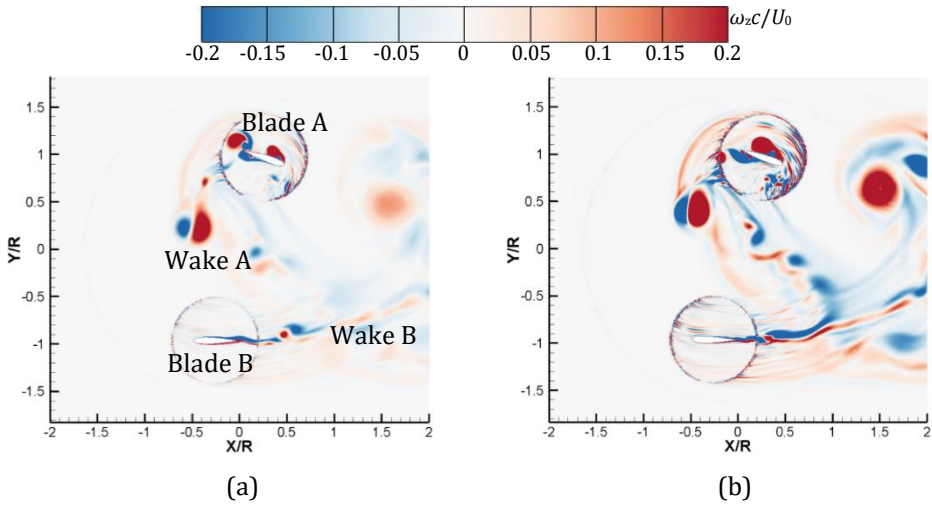


**Fig.3.52** Global flow structures at  $\psi=105^\circ$ . (a)  $Re=2.85\times 10^4$ ; (b)  $Re=7.11\times 10^4$ .

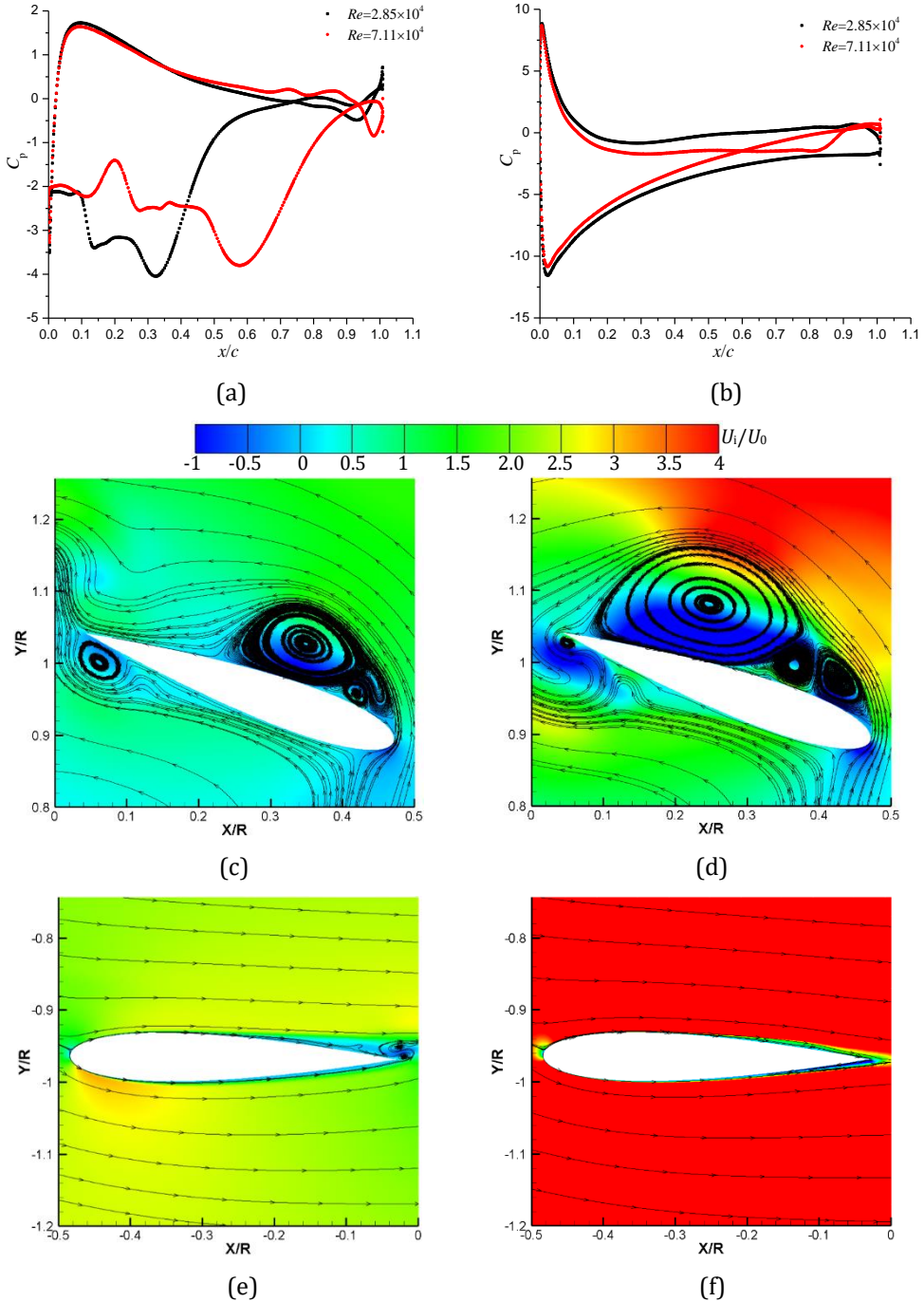


**Fig.3.53** Flow structures at  $\psi=105^\circ$ . (a) Pressure distribution of blade A; (b) Pressure distribution of blade B; (c) and (e)  $Re=2.85\times 10^4$ ; (d) and (f)  $Re=7.11\times 10^4$ .

When considering the difference of propulsive force coefficient at two  $Re$ , the detailed flow information at  $\psi=30^\circ$  is presented in figure 3.54 and 3.55. At high  $Re$ , the wakes shedding from two blades are more intensive. Simultaneously, the wake A has a high potential in contacting with the leading edge of blade B. Based on the pressure distribution and the near-wall flows of blade A in figure 3.55a, 3.55c and 3.55d, it is found that there are large-size vortex B and LEV over the suction side, as was shown in figure 3.6b, decreasing the pressure dramatically. However, the impact of vortex B on the pressure is more apparent for the case at low  $Re$ , but the LEV is less influential due to its shedding from the trailing edge. Consequently, the resultant upward lift towards the left

side produces the positive propulsive force, but the magnitude is larger because of the relatively large blade loading in figure 3.55a at high  $Re$ . Furthermore, blade B can also create the positive propulsive force because of the upward lift towards the upper side, but the magnitude is a little smaller at low  $Re$ , as a result of the blade loading in figure 3.55b. Therefore, the difference of propulsive force coefficient at this position should consider both two blades.

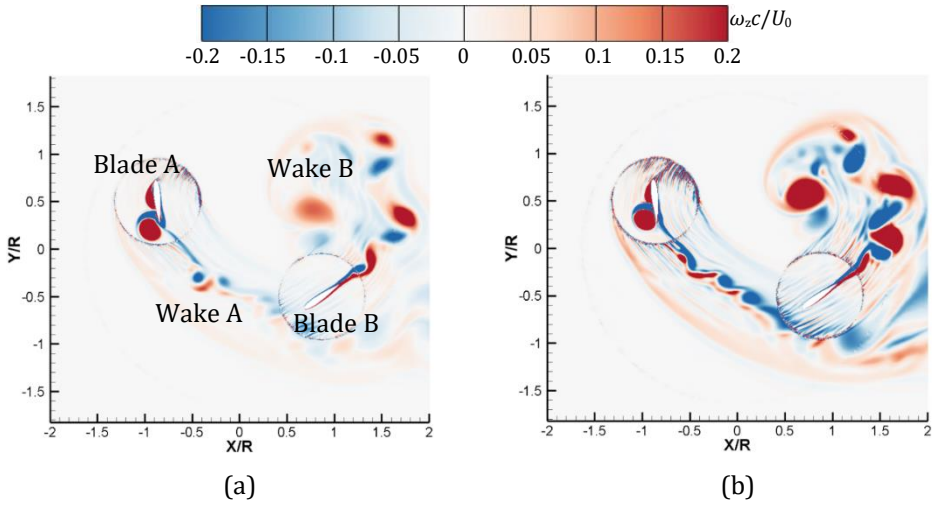


**Fig.3.54** Global flow structures at  $\psi=30^\circ$ . (a)  $Re=2.85\times 10^4$ ; (b)  $Re=7.11\times 10^4$ .

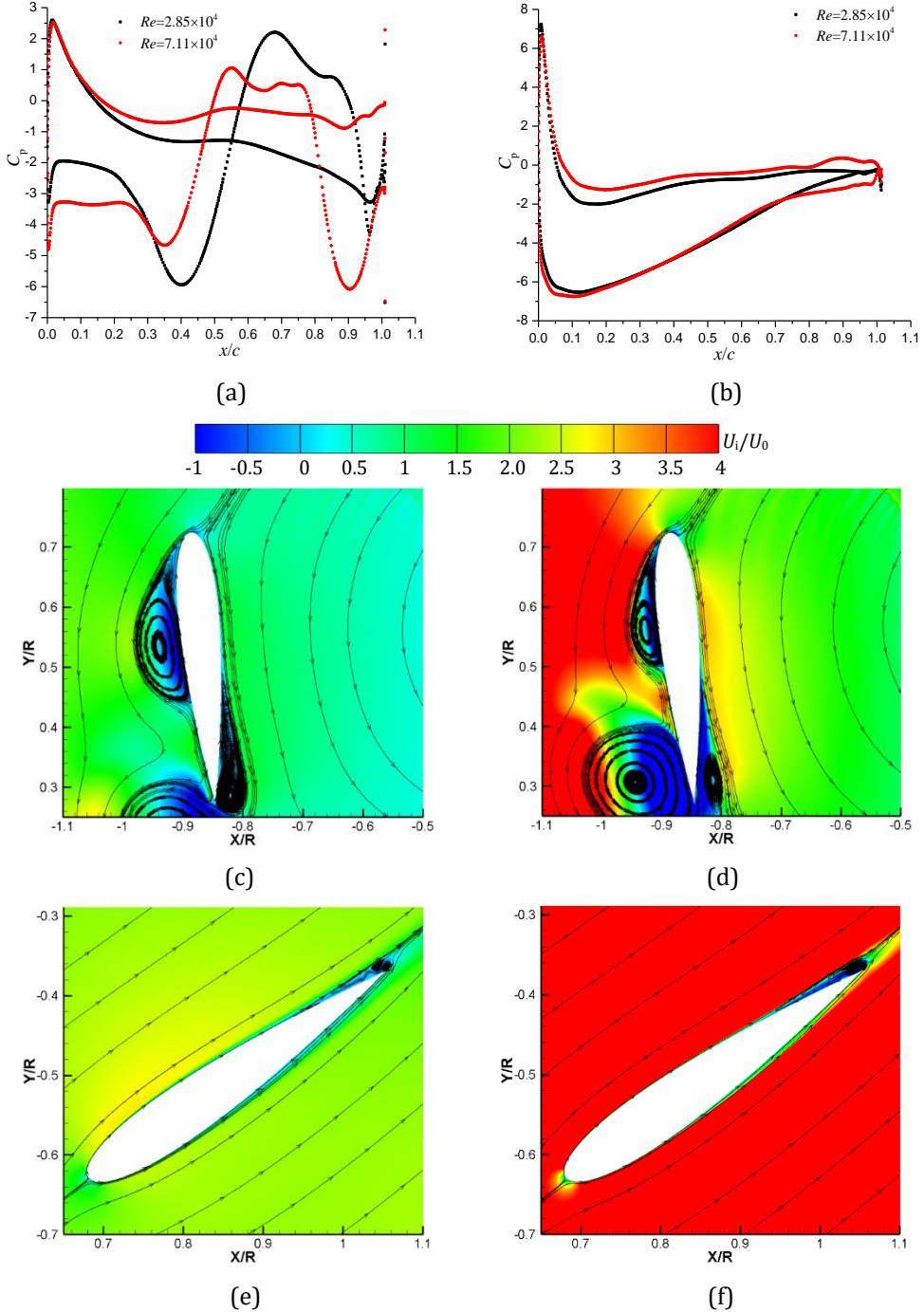


**Fig.3.55** Flow structures at  $\psi=30^\circ$ . (a) Pressure distribution of blade A; (b) Pressure distribution of blade B; (c) and (e)  $Re=2.85\times 10^4$ ; (d) and (f)  $Re=7.11\times 10^4$ .

Afterwards, when blade A nearly reaches to the initial position of blade B, the flow structures at two  $Re$  in figure 3.56 and 3.57 are used to explain the difference of propulsive force coefficient. At this location, the blade B interacts with its wakes. There exists substantial flow separation on the left side of blade A and right side of blade B, which is more evident at high  $Re$ . Over the surface of blade A, although the flow separation occurs on the right side, the pressure is still higher than that on the other side, leading to the positive propulsive force because of the upward lift towards the left side. However, it has the same magnitude of propulsive force for two cases, due to the same blade loading in figure 3.34c. Given the pressure distribution of blade B, it is observed that a large-scale

LEV is attached on the suction side, which is responsible for the generation of positive propulsive force because of the downward lift. By the comparison of the blade loading in figure 3.57b, it can be seen that the pressure on the suction side induced by the LEV under low  $Re$  condition is lower, creating the positive propulsive force with large magnitude, as is shown in figure 3.57e. The difference of propulsive force coefficient at two  $Re$  is mainly caused by blade B, because of the existence of LEV attached on the suction side, which further proves that the generation of LEV at low  $Re$  is earlier.

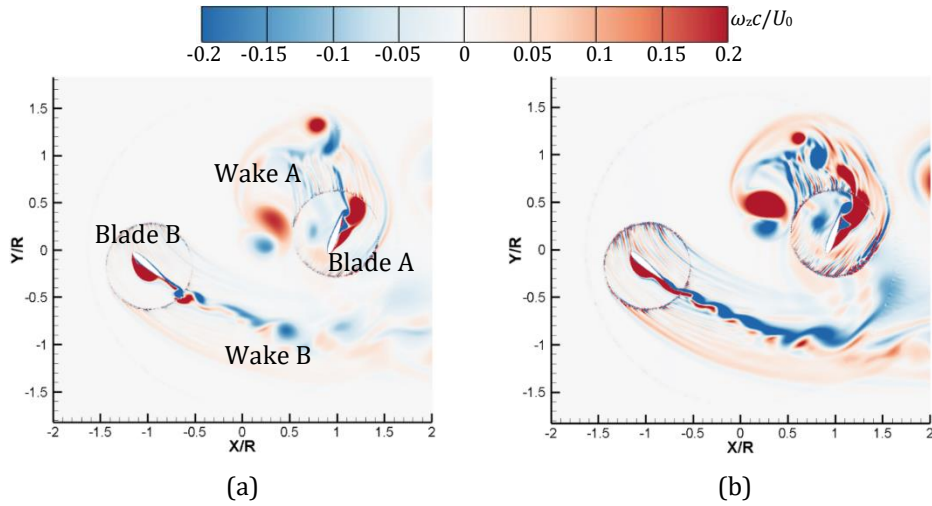


**Fig.3.56** Global flow structures at  $\psi=170^\circ$ . (a)  $Re=2.85\times 10^4$ ; (b)  $Re=7.11\times 10^4$ .

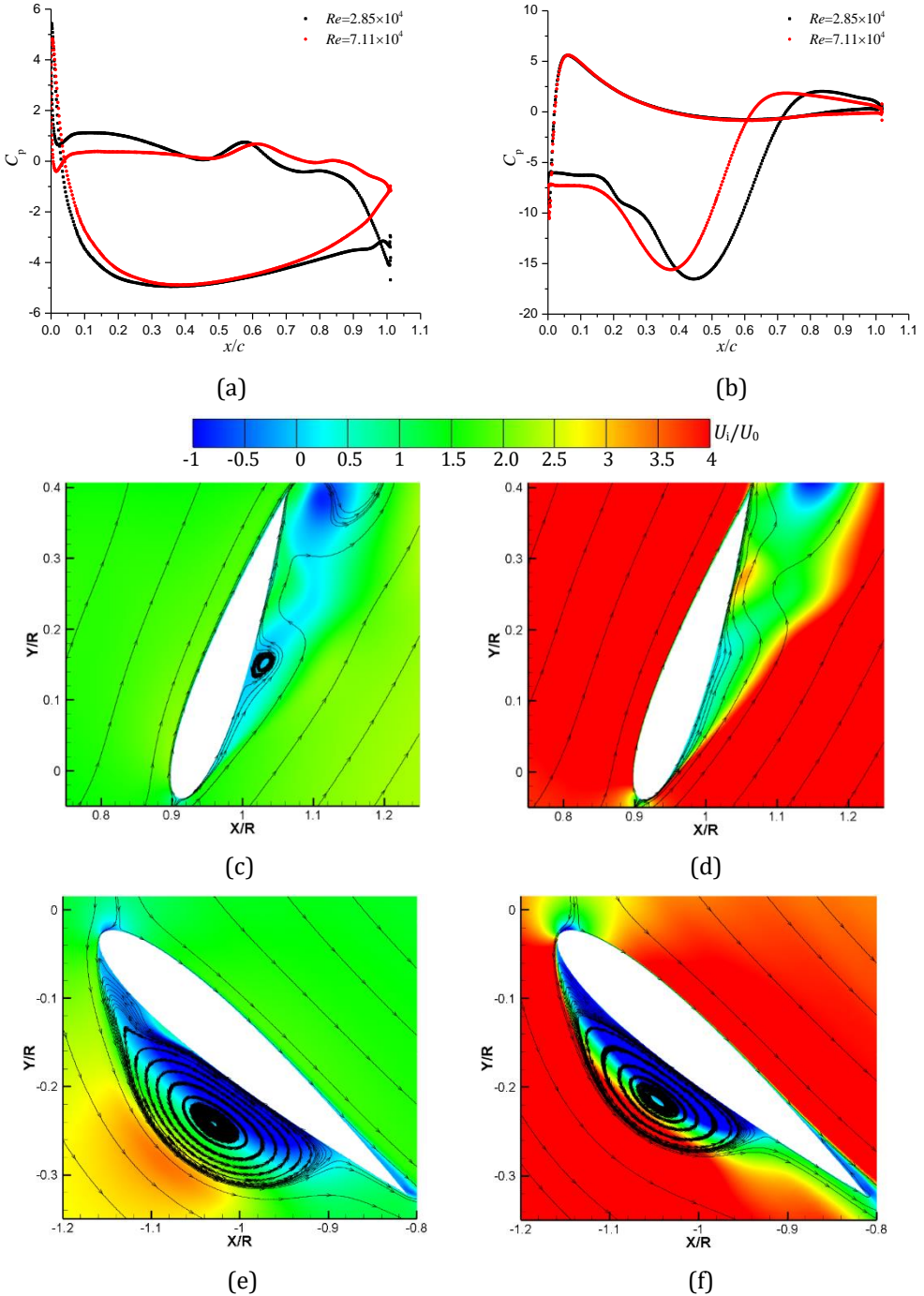


**Fig.3.57** Flow structures at  $\psi=170^\circ$ . (a) Pressure distribution of blade A; (b) Pressure distribution of blade B; (c) and (e)  $Re=2.85\times 10^4$ ; (d) and (f)  $Re=7.11\times 10^4$ .

### 3.3.4 Effect of $\lambda$

In order to investigate the advance coefficient effect, only the rotating speed is changed when the inlet velocity remains constant with the value of 5m/s. Figure 3.58 shows the global performance at various  $\lambda$  for the cases with different pitch-pivot-points. When the pitching pivot is fixed, the lift, propulsive force and power coefficients decrease obviously with the increase of  $\lambda$ , which indicates that the forces and power decrease with the rotating speed. Sometimes, the more complicated unsteady flows indeed improve the forces and the consumption of power. Based on the comparison of lift coefficient, it seems

that the magnitude is much larger at large  $\lambda$ , when the pitching pivot is located near the leading edge. At low  $\lambda$ , when the pitching pivot is at  $x/c=0.2$  and 0.25, the relatively large propulsive force is produced, while it is generated for the cases with  $x/c=0.5$  and 0.6 at high  $\lambda$ . The distribution of power coefficient indicates that it is more power-consuming as the pitching pivot is close to the middle chord, which can be used to explain why the efficiency of the cases with  $x/c=0.5$  and 0.6 is much lower compared with that of the cases with  $x/c=0.25$  and 0.3. Figure 3.58d also shows that the best efficiency is achieved at  $\lambda=0.48$  when the pitch-pivot-point is at  $x/c=0.25$ .

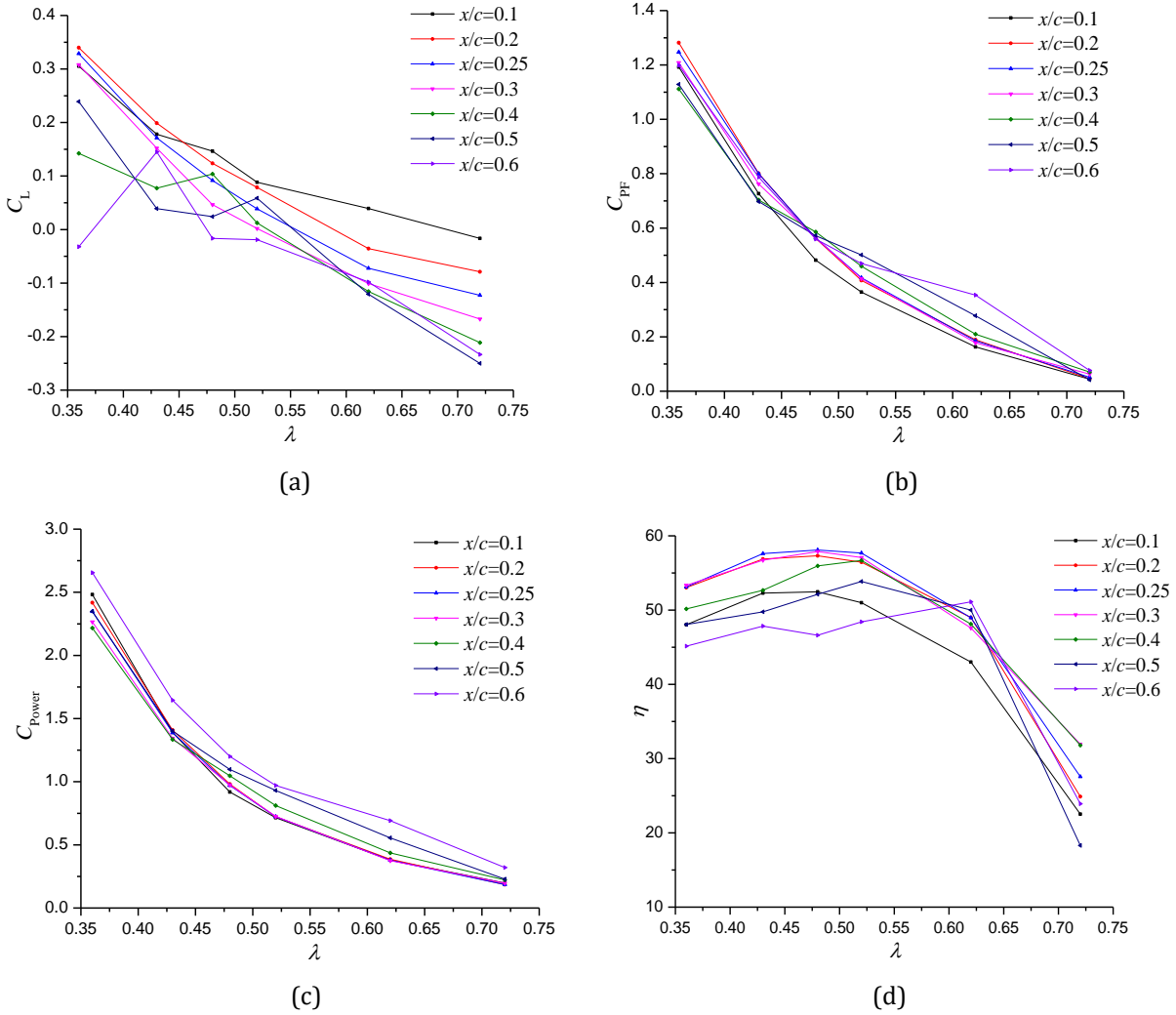


**Fig.3.58** Global performance of the cycloidal propeller. (a) Lift coefficient; (b) Propulsive force coefficient; (c) Power coefficient; (d) Efficiency.

Figure 3.59 presents the performance of the rotating system and single blade in a revolution at three  $\lambda$  for the case with  $x/c=0.25$ . The results show that the effect of  $\lambda$  is more obvious than the influence of  $Re$ . The time-averaged lift and propulsive force coefficients increases with the decrease of  $\lambda$  by increasing the rotating speed. Both the lift and propulsive force coefficients vary considerably in a rotating cycle for three cases, but the variation of propulsive force coefficient is much huge, even for the single blade. As a consequence, two positions, representing the peak and valley of lift coefficient, are adopted, while an azimuthal angle of  $160^\circ$  is used to clarify the difference of propulsive force coefficient.

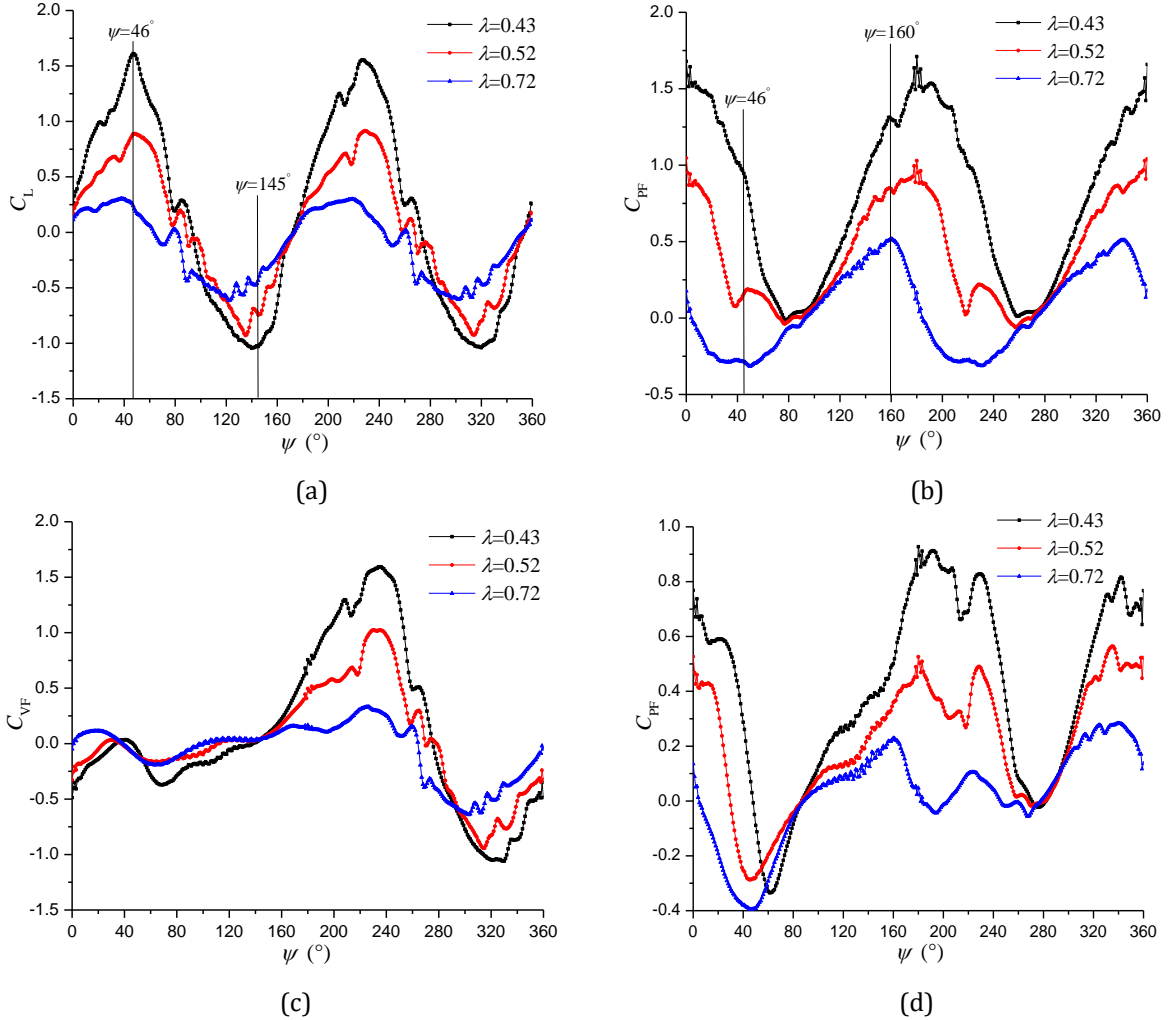


**Fig. 3.59** Performance curves. (a) Lift coefficient of the rotating system; (b) Propulsive force coefficient of the rotating system; (c) Vertical force coefficient of single blade; (d) Propulsive force coefficient of single blade.

The detailed flow structures at  $\psi=46^\circ$  at three  $\lambda$  are displayed in figure 3.60 and 3.61, to describe the lift difference of the cycloidal rotor. At low  $\lambda$ , the flow separation on the left side of blade A and wakes are more violent because of the large rotating speed. The wake A has a strong interaction with blade B, which is more obvious at low  $\lambda$ . On the left side of blade A, there is a vortex B and LEV at low  $\lambda$ , but only a small vortex structure is observed and the size becomes smaller with the increase of  $\lambda$ , which is mainly caused by the stagnation point location leading to the different development of the boundary layer flows. Although the flow field over blade A is complex, the blade loadings at various  $\lambda$  are relatively small, leading to nearly the same vertical force, as is shown in figure 3.59c. Then, the flows over blade B are quite simple and the flow separation only occurs near the trailing edge of the suction side. With the increase of  $\lambda$ , the stagnation point shifts from the pressure side to the suction side gradually, resulting in the different pressure distributions for three cases. Due to the large blade loading at low  $\lambda$ , the resultant upward lift generates the positive vertical force with large value. Thus, the difference of lift coefficient is caused by the pressure distribution of blade B, due to the stagnation point shift induced by the change of pitching rate.

Under low  $\lambda$  condition, due to the complex vortical flows on the left side of blade A, the pressure there is lower than that on the right side. Thus, the pressure is upward

towards the left side, leading to the generation of positive propulsive force. However, for other two cases, the flow is relatively smooth on the pressure side and the resultant lift is downward towards the right side. Consequently, it creates the negative propulsive force, but the magnitude is larger when  $\lambda$  is 0.72. For all three cases, the lift of blade B is upward, which makes the contribution to the production of large positive propulsive force. Because of the large blade loading at low  $\lambda$  in figure 3.61b, the positive propulsive force has the largest value. Generally, the propulsive force at low  $\lambda$  is much larger, because of the positive propulsive force produced from two blades.

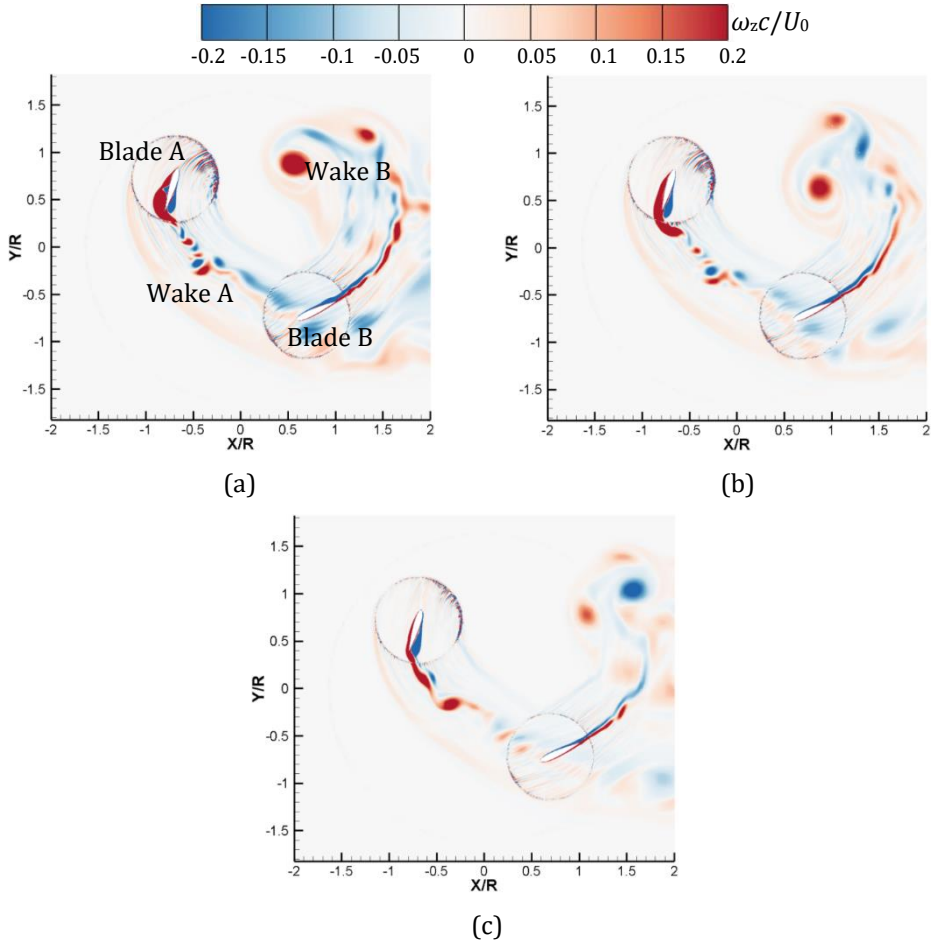


**Fig.3.60** Global flow structures at  $\psi=46^\circ$ . (a)  $\lambda=0.43$ ; (b)  $\lambda=0.52$ ; (c)  $\lambda=0.72$ .

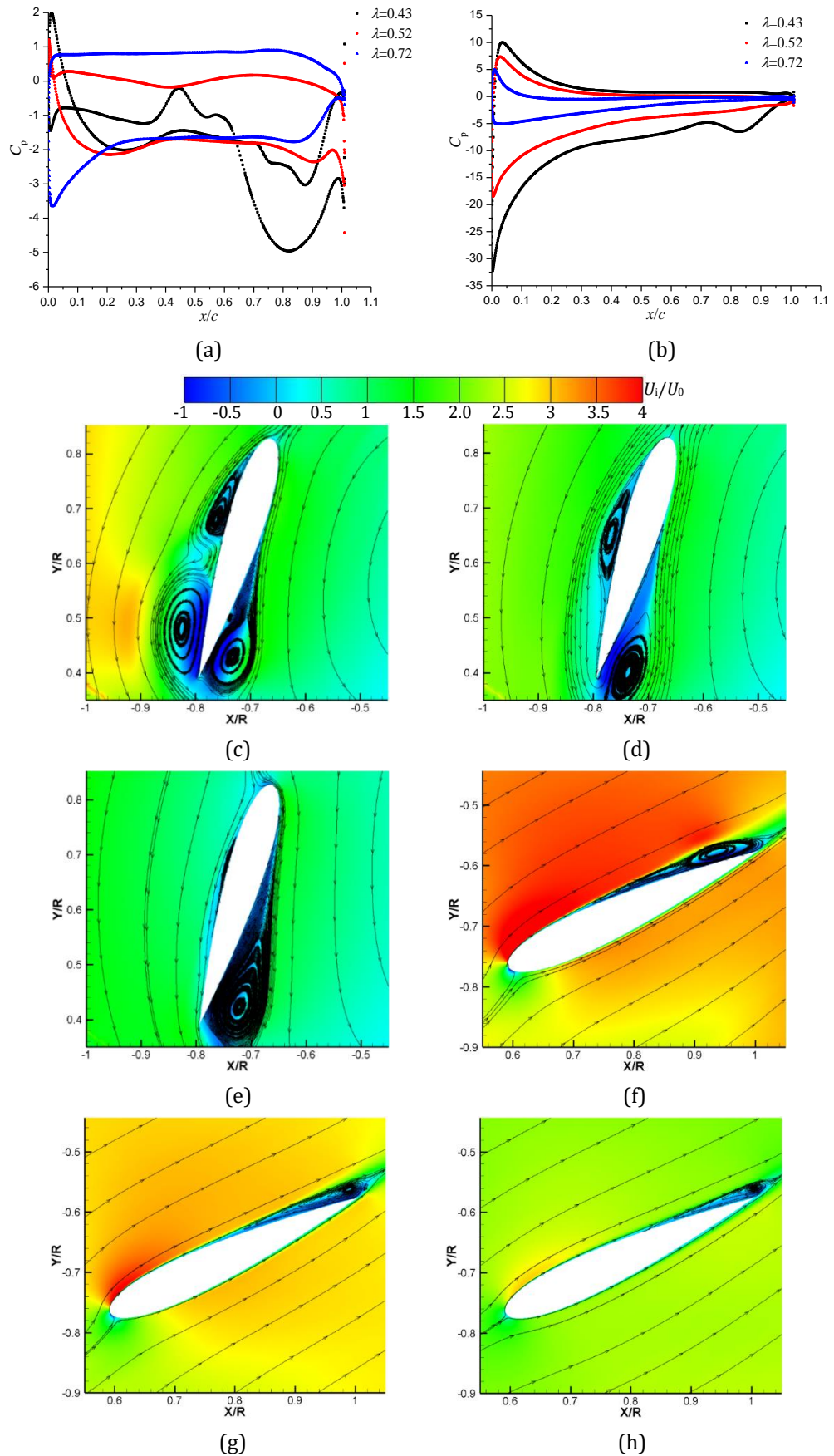


**Fig.3.61** Flow structures at  $\psi=46^\circ$ . (a) Pressure distribution of blade A; (b) Pressure distribution of blade B; (c) and (f)  $\lambda=0.43$ ; (d) and (g)  $\lambda=0.52$ ; (e) and (h)  $\lambda=0.72$ .

As  $\psi$  increase to  $145^\circ$ , the lift coefficient approaches to a peak with a negative value. At this moment, at high  $\lambda$  with small rotating speed, blade A has a high risk in interacting with its wakes, as a consequence of the low pitching rate. Besides, it seems that the flow separation on the lower side of blade B is different for three tested cases. The figures in 3.63a and 3.63b show that the pressure difference of blade B is much larger than that of blade A. On the surface of blade A, there are many small scales on the pressure side, inducing the pressure fluctuations. But on the suction side, the pressure has large difference at various  $\lambda$  due to the pitching rate changing the boundary layer flows. The vertical force has almost the same value for three cases as a result of the small blade loading. On the suction side of blade B, the flow is extremely complicated, characterized by the developed three-vortex-structure formed near the leading edge and many small-size vortices when  $\lambda$  is relatively low. However, a large-size LEV is generated as  $\lambda$  increases to 0.72. Due to the low pressure on the suction side, the downward lift is produced. Then, this lift results in the negative vertical force with large value at low  $\lambda$  because of the large blade loading shown in figure 3.63b. It concludes that the change of pitching rate totally modifies the pressure on the leading edge of suction side for blade B, which is the main reason for the difference of lift coefficient.

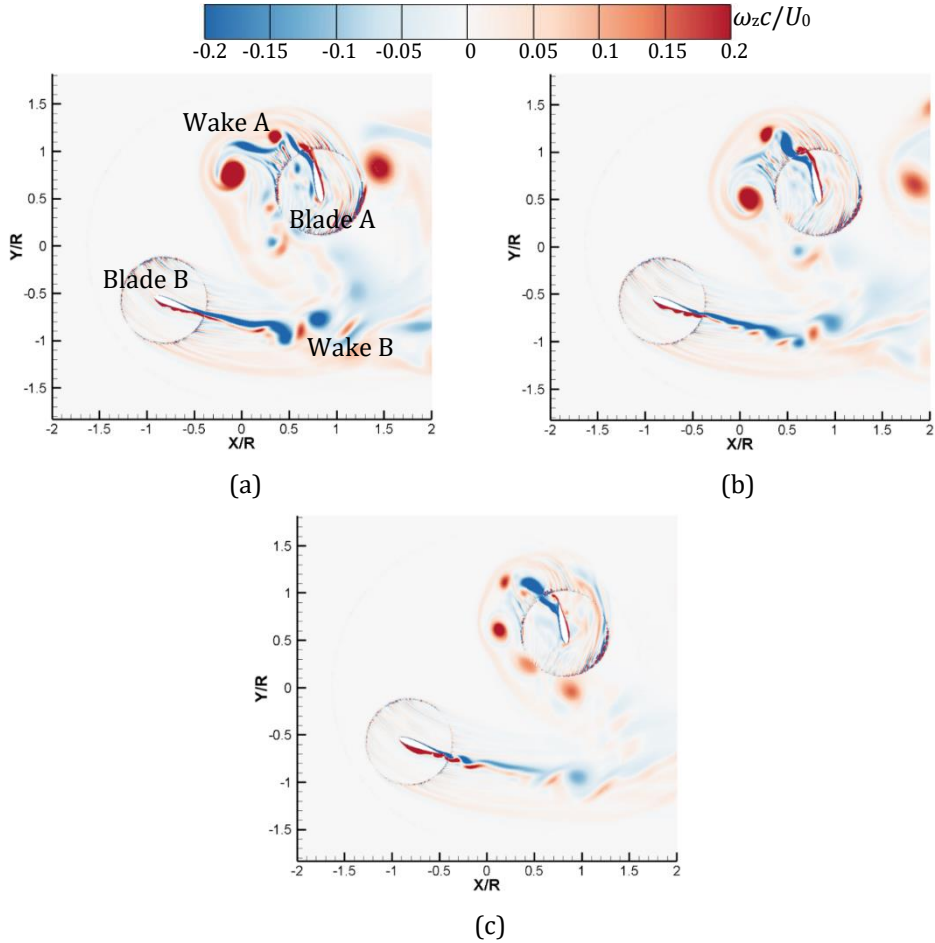


**Fig.3.62** Global flow structures at  $\psi=145^\circ$ . (a)  $\lambda=0.43$ ; (b)  $\lambda=0.52$ ; (c)  $\lambda=0.72$ .

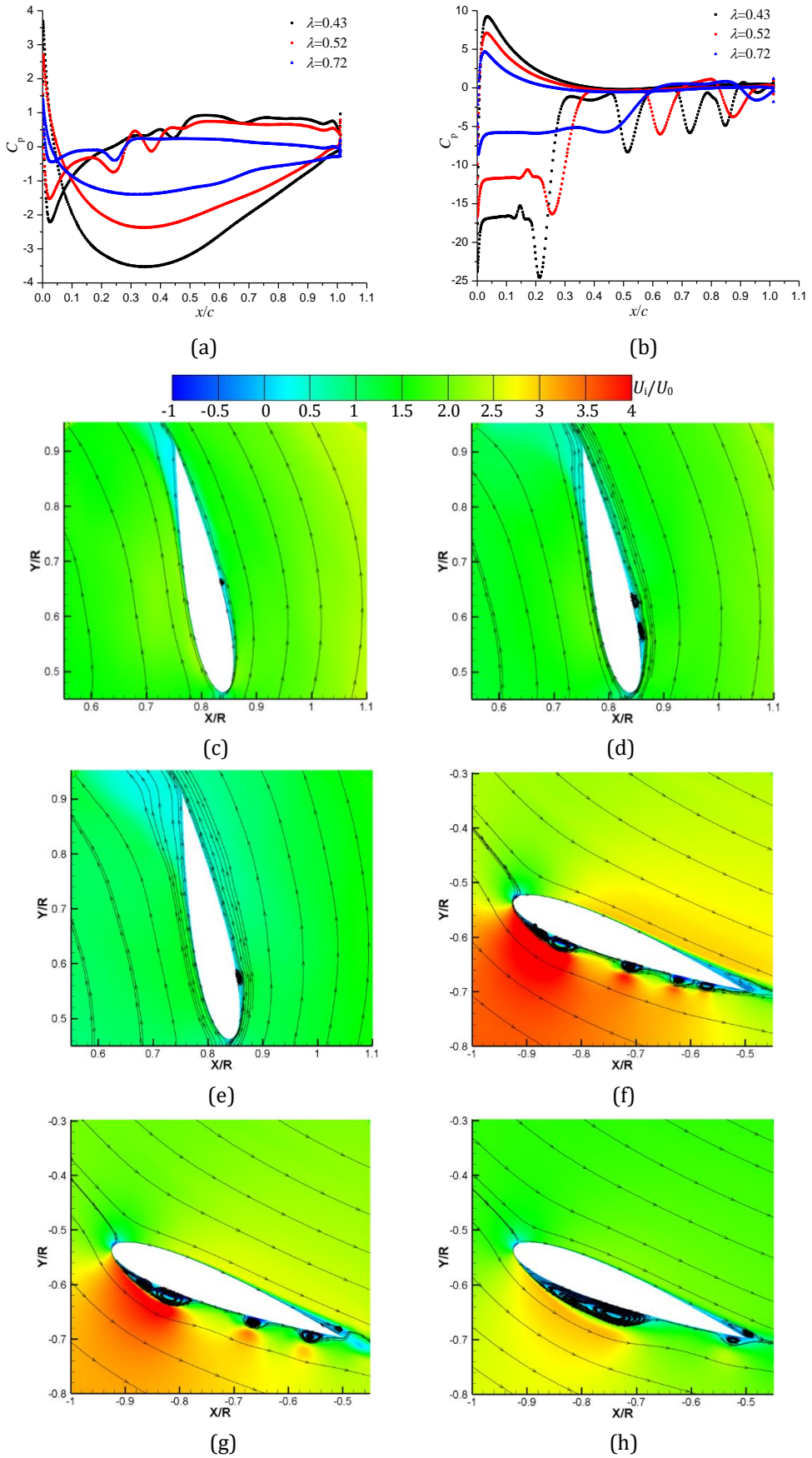


**Fig.3.63** Flow structures at  $\psi=145^\circ$ . (a) Pressure distribution of blade A; (b) Pressure distribution of blade B; (c) and (f)  $\lambda=0.43$ ; (d) and (g)  $\lambda=0.52$ ; (e) and (h)  $\lambda=0.72$ .

Further increasing  $\psi$  to  $160^\circ$ , the global flow field is similar with that at  $145^\circ$ . However, it can be seen that the leading edge of blade A would contact with the wake A at high  $\lambda$ , due to the slow dissipation of wakes. Conversely, at low  $\lambda$  with large rotating speed, the blade A would come across the wake A quickly, which is shown in figure 3.64a. The flow structures on both two sides of blade A are really simple, especially under low  $\lambda$  condition. However, the change of pitching rate leads to the pressure modification on the leading edge of the suction side. As a result, the upward lift generates the positive propulsive force and its value depends on the blade loading in figure 3.65a. Then, on the suction side of blade B, the LEV develops gradually and it occupies a large part of surface at high  $\lambda$ . Similar with that at  $145^\circ$ , although the attached LEV has great impact on the pressure, changing the pitching rate by increasing/decreasing the rotating speed is still the main contributor to the pressure modification, especially on the leading edge of the suction side. Finally, by the combination of positive propulsive force produced by two blades, the total propulsive force, especially from blade B, has the largest magnitude under low  $\lambda$  condition.

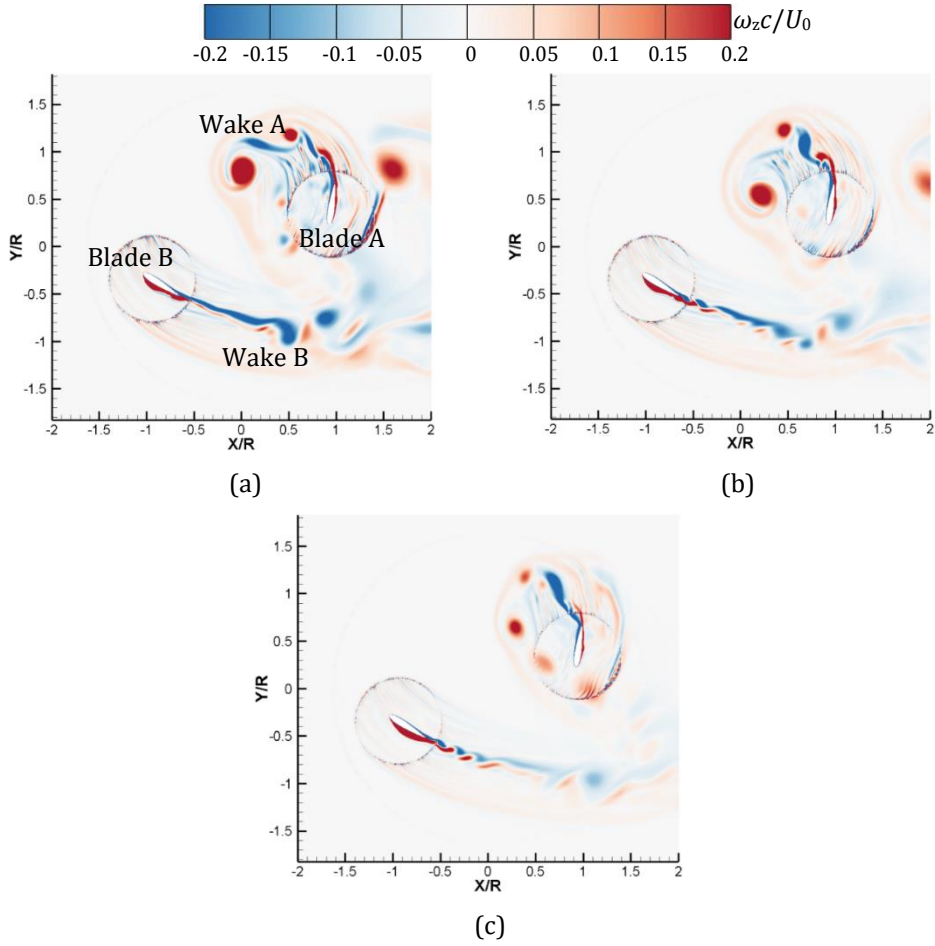


**Fig.3.64** Global flow structures at  $\psi=160^\circ$ . (a)  $\lambda=0.43$ ; (b)  $\lambda=0.52$ ; (c)  $\lambda=0.72$ .

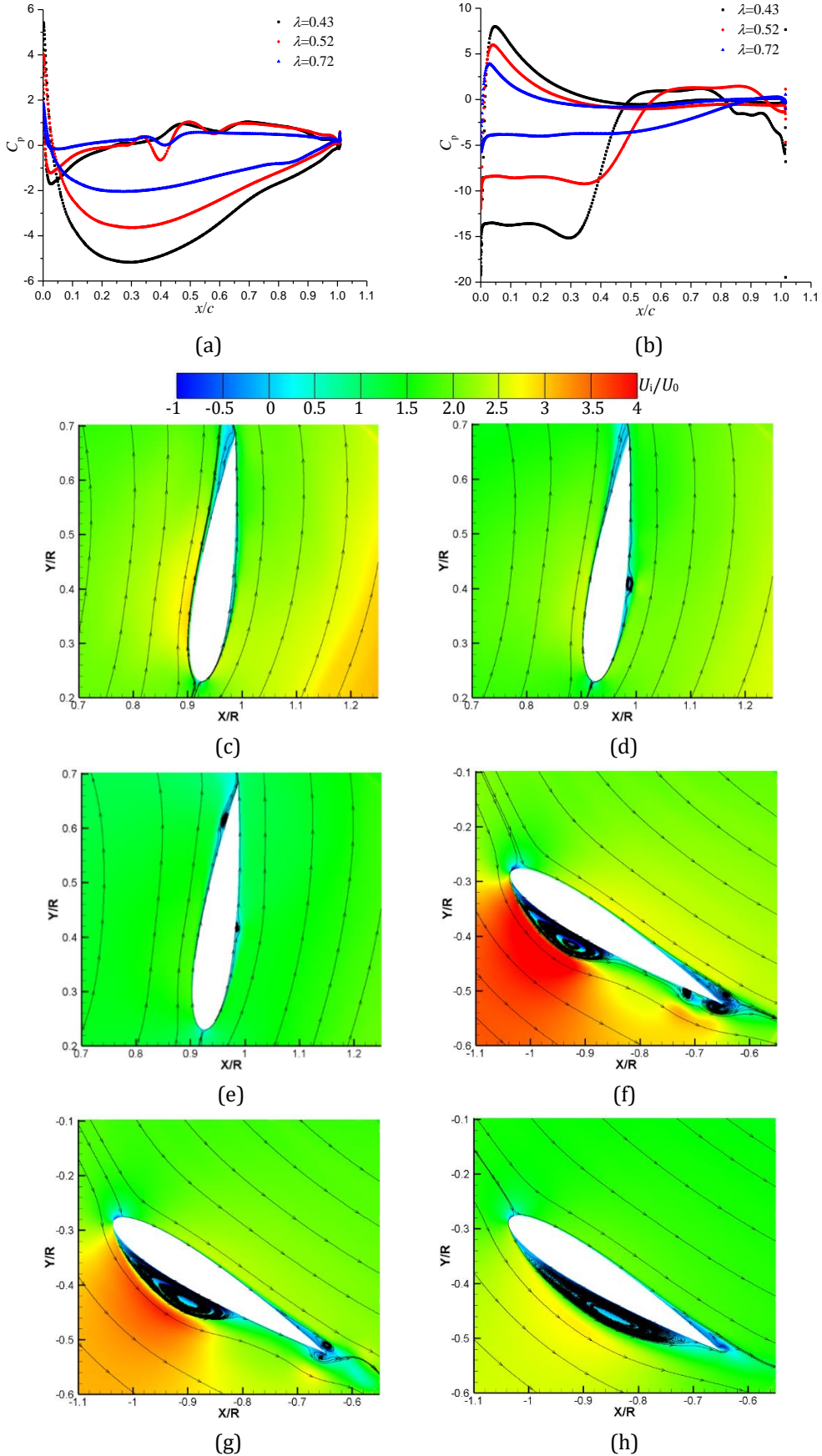


**Fig.3.65** Flow structures at  $\psi=160^\circ$ . (a) Pressure distribution of blade A; (b) Pressure distribution of blade B; (c) and (f)  $\lambda=0.43$ ; (d) and (g)  $\lambda=0.52$ ; (e) and (h)  $\lambda=0.72$ .

### 3.3.5 Conclusions

- (1) For given  $\lambda$  and  $Re$ , the case with  $x/c=0.25$  obtains the best performance. Then, when the pitch-pivot-point moves towards the blade middle chord, though the propulsive force coefficient increases, the efficiency of the cycloidal rotor becomes worse because of the higher power consumption. Simultaneously, the lift coefficient has the largest magnitude as the pitching pivot is closer to the leading edge.
- (2) For the case with a constant  $x/c$ , the efficiency of the rotating system increases with  $Re$ . At low  $Re$ , its effect can't be ignored, because the vortical flows around the blade surface appear earlier. Additionally, increasing  $Re$  leads to the change of pitching rate, further changing the position of stagnation point and the prediction of the pressure gradient, which has great impact on the boundary layer flows.
- (3) The advance coefficient  $\lambda$  has greater impact on the performance, compared with  $Re$ . The forces and power coefficients decrease with the increase of  $\lambda$ . Similarly, as the pitch-pivot-point is located near the leading edge, the system would get the higher lift coefficient at high  $\lambda$ . In addition, the best efficiency based on the propulsive force coefficient is obtained at  $\lambda=0.48$  when the pitch-pivot-point is at  $x/c=0.25$ . Also, compared with the effect of  $Re$ , the change of  $\lambda$  by modifying the rotating speed only, has more evident influence on the location of stagnation point and prediction of pressure gradient, resulting in the totally different development of the boundary layer flows. Furthermore, increasing  $\lambda$  by decreasing the rotating speed would make the vortex flows develop fully.

## 3.4 INFLUENCE OF THE BLADE PROFILE

### 3.4.1 Introduction

In this section, the effect of blade profile on the performance of the cycloidal rotor is discussed thoroughly. According to the previous investigations, in most cases, the symmetrical profiles are often employed. Although the symmetrical profile shows the better performance than the asymmetrical profile with the same thickness [98] and the optimized airfoil profile is close to the symmetrical shape [99], the detailed explanation is necessary for a better understanding of the blade profile effect when the asymmetrical blade profile is submitted to the cycloidal propeller. Besides, the placement of asymmetrical blade is seldom investigated and it is believed that this has great influence on the global performance and flow structures. Several symmetrical and asymmetrical blade profiles are adopted in the present work. Also, for a specific blade profile, the influence of  $Re$  and  $\lambda$  is still deserved to be discussed.

### 3.4.2 Symmetrical/asymmetrical profiles

Eight blade profiles, involving NACA0009, 0012, 0015, 0018, 0022, 2415, 4415 and 6415, are adopted as the objectives. The first five have the symmetrical geometry while NACA2415, 4415 and 6415 are asymmetrical profiles modified based on NACA0015. In addition, the influence of inverse NACA2415, 4415 and 6415 profiles are also studied by changing the initial geometry placement. The global performance of the cycloidal rotor with various blade profiles under different  $Re$  conditions are plotted in figure 3.66. The pitching kinematic is asymmetrical pitching with the mean incidence of  $5^\circ$  and pitching amplitude of  $35^\circ$ . Simultaneously,  $c/R=0.45$ , which has a best performance, is chosen, while the pitching pivot is located at  $x/c=0.25$ . It is observed that the asymmetrical profile can achieve the higher lift coefficient, which increases with  $Re$ . For the symmetrical profile, such as NACA0009, 0012 and 0015, the obtained lift coefficient remains unchanged nearly with  $Re$ . However, the lift coefficients obtained by NACA0018 and 0022 have a significant increase as  $Re$  increases, which is more obvious for NACA0022. When it comes to the inverse asymmetrical profile, it can be seen that the lift coefficient of inverse NACA6415 decreases remarkably with  $Re$ . The distribution of propulsive force coefficient shows a similar trend for various profiles, except for inverse NACA4415 and 6415. For a fixed  $Re$ , NACA6415 shows the best performance, followed by the other two asymmetrical and four symmetrical profiles. Although the asymmetrical profile generates the higher propulsive force coefficient, the power coefficient of the rotating system is also higher, which directly leads to the lower efficiency, as is shown in figure 3.66d. Additionally, the efficiency achieved by symmetrical profile is much higher, because of the relatively high propulsive force and low power. A very interesting phenomenon is that the inverse NACA2415 has the highest efficiency under high  $Re$  condition, due to the significant decrease of the power coefficient.

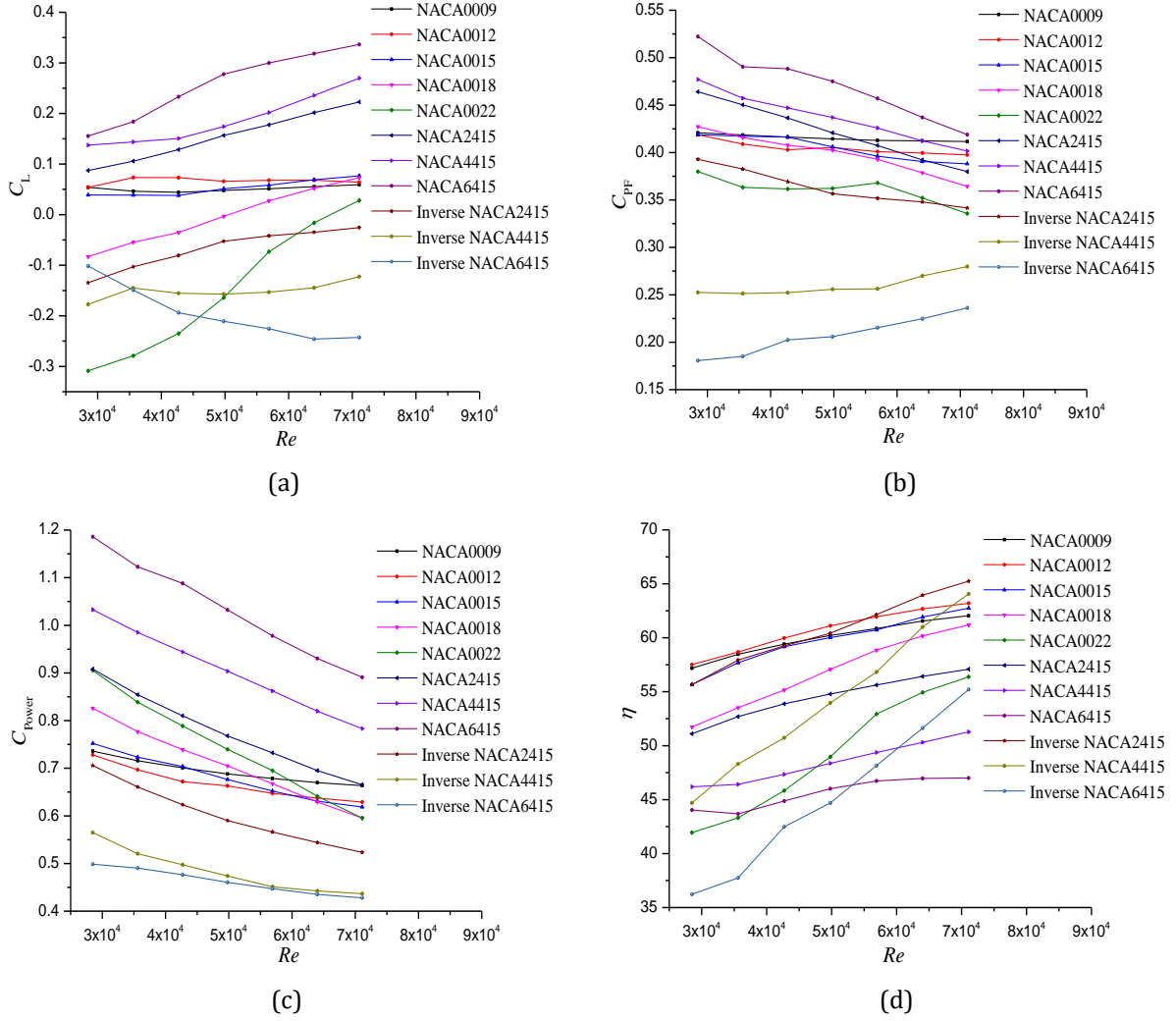


**Fig.3.66** Global performance of cycloidal rotor. (a) Lift coefficient; (b) Propulsive force coefficient; (c) Power coefficient; (d) Efficiency.

Then, the flow structures of the two-bladed cycloidal propeller with different blade profiles, involving the symmetrical and asymmetrical geometry, are displayed in figure 3.67 and 3.68 at  $\psi=0^\circ$ . As the thickness of symmetrical profile increases, the vortical flows have different patterns. There is almost no much difference in flow filed for NACA0009, 0012 and 0015. However, for NACA0018 and 0022, the wakes are more unsteady and the flow separation is more obvious on the left side of blade A. Obviously, the wake B is closer to blade B for NACA0022, which indicates that flow separation occurs earlier. Moreover, the wakes shedding from the asymmetrical profile is more disordered and there exists the massive flow separation on the left side of blade A and right side of blade B, especially for NACA6415, which should be responsible for the high consumption of power. When the asymmetrical profile is in inverse mode, it seems that the vortical flows are suppressed and the power is obviously reduced. Though the flow separation on left side of blade A is still visible, it almost disappears on blade B, as well as the wake B for inverse NACA6415.

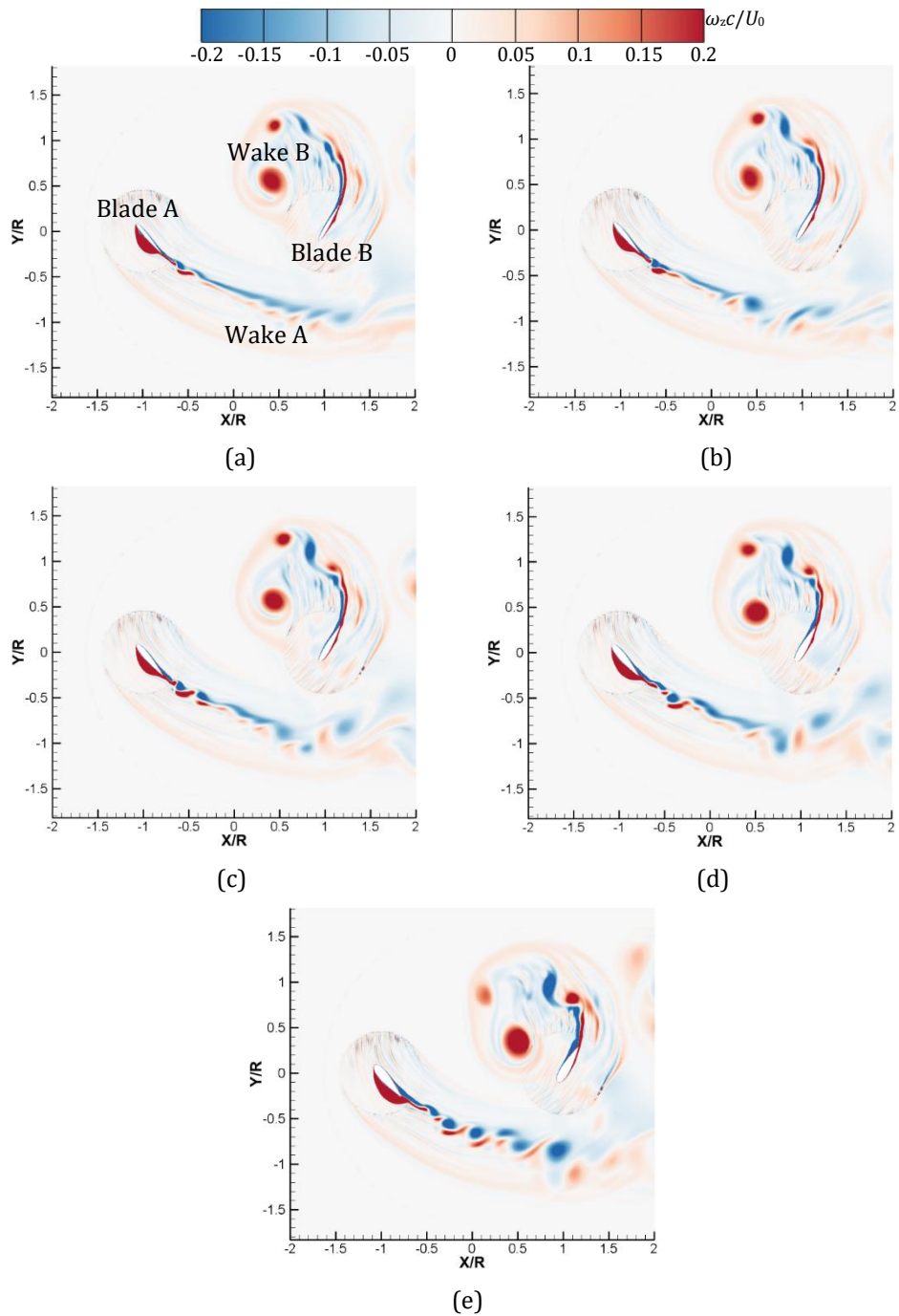


**Fig.3.67** Flow structures over symmetrical profiles at  $\psi=0^\circ$ . (a) NACA0009; (b) NACA0012; (c) NACA0015; (d) NACA0018; (e) NACA0022.

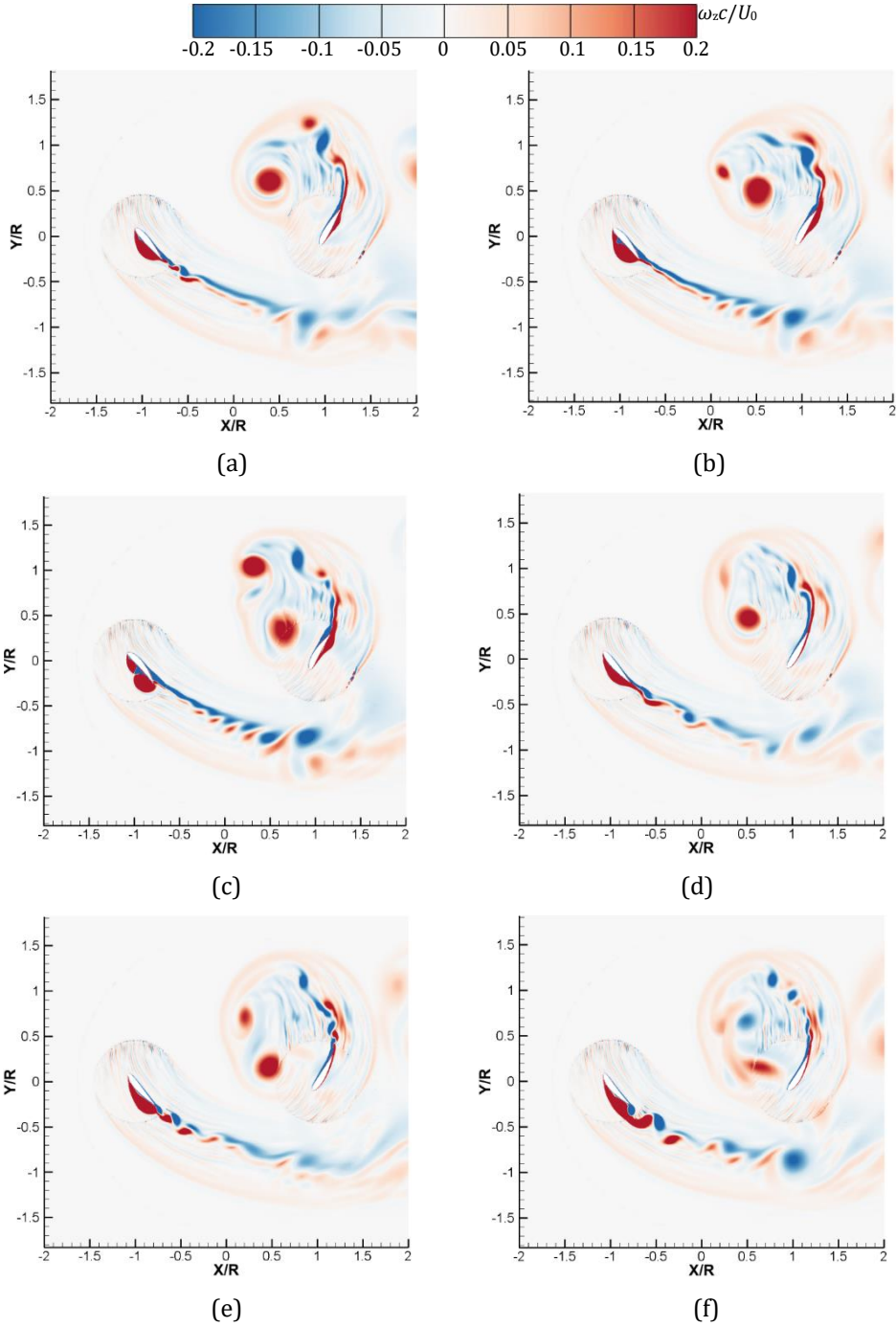


**Fig.3.68** Flow structures over asymmetrical profiles at  $\psi=0^\circ$ . (a) NACA2415; (b) NACA4415; (c) NACA6415; (d) Inverse NACA2415; (e) Inverse NACA4415; (f) Inverse NACA6415.

Then, four profiles, including NACA0015, 0022, 6415 and inverse NACA6415, are selected to study the influence of blade profile on distributions of force coefficients. The performance of the cycloidal rotor and single blade for various profiles are plotted in figure 3.69. It is evident that NACA6415 produces the highest lift and propulsive force coefficients, which nearly occurs at every position in a rotating cycle. For the distribution of lift coefficient, the main difference occurs from the azimuthal angle of  $0^\circ$  to  $145^\circ$ , while it ranges from  $\psi=0^\circ$  to  $100^\circ$  for the propulsive force coefficient. However, the change of forces for NACA6415 is more evident than other profiles. According to the force distribution of the single blade, it concludes that blade B is the main contributor to the lift

production because of the high lift coefficient generated at  $\psi=180^\circ$ - $360^\circ$ , while both blade A and B take the responsibility to the generation of propulsive force. To clarify the mechanism of flow-induced performance change, two azimuthal angles of  $46^\circ$  and  $120^\circ$  are employed to explain the lift coefficient difference, and the difference of propulsive force coefficient are analyzed by the flow structures at  $\psi=46^\circ$  and  $180^\circ$ .

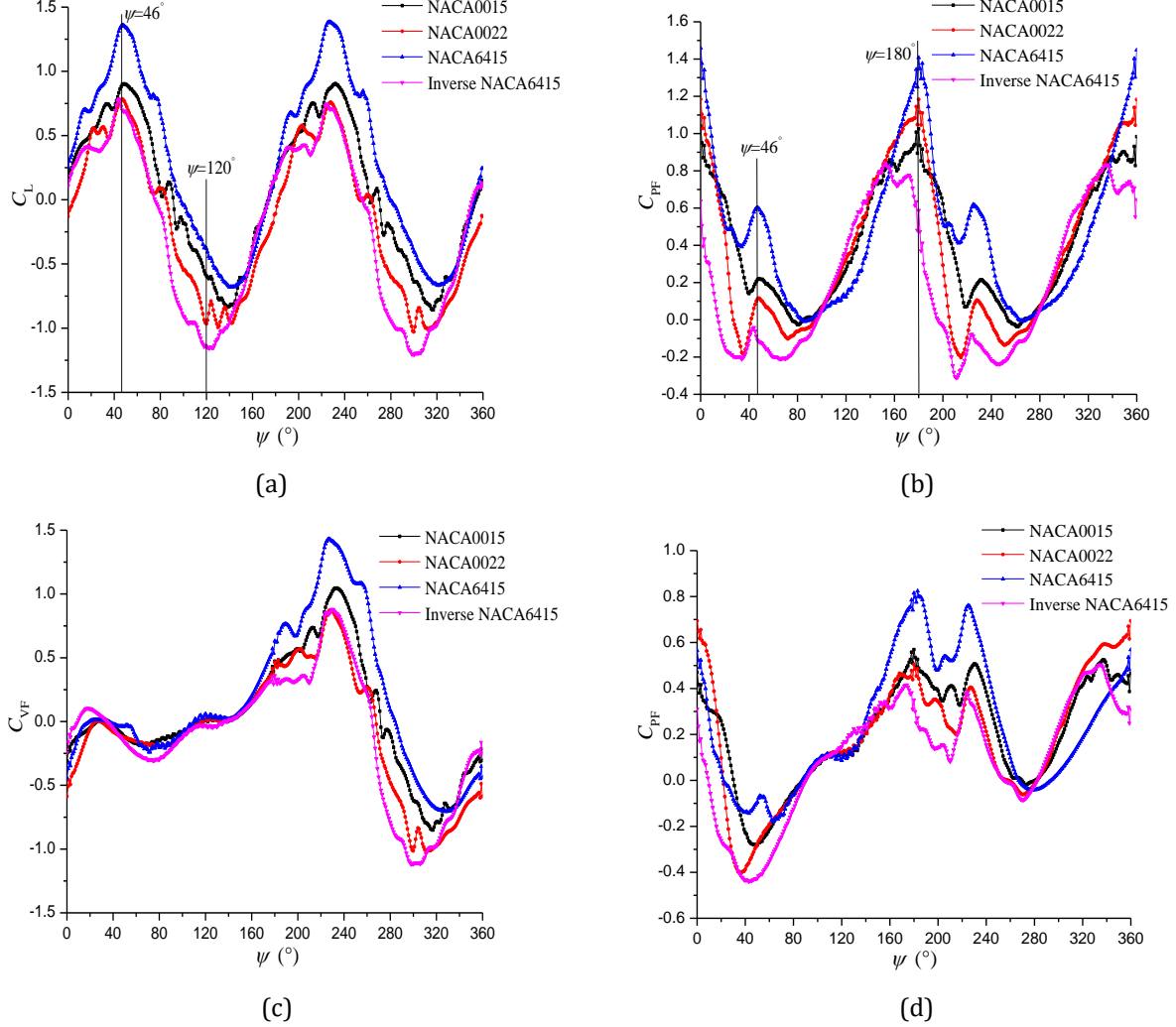


**Fig.3.69** Performance curves in a revolution. (a) Lift coefficient of cycloidal rotor; (b) Propulsive force coefficient of cycloidal rotor; (c) Vertical force coefficient of single blade; (d) Propulsive force coefficient of single blade.

The global flow structures, pressure coefficients and near-wall flows of two blades at  $\psi=46^\circ$ , are displayed in figure 3.70 and 3.71. At this position, the main flow separation occurs on blade A and it leads to the intensive vortex shedding, which interacts with the leading edge of blade B directly. With the increase of blade thickness for the symmetrical profile, the vortical flow is more evident, which consumes more power of the rotating system. In addition, the flow separation on both sides of blade A in figure 3.70c is violent and the wakes shedding from blade B is approaching to itself. However, when the asymmetrical blade is inverse, flow separation on blade A and wakes of blade B become mild, which reduces the power consumption significantly. By the comparison of near-wall flows, it seems that it is more complicated on blade A surfaces. For examples, as the symmetrical blade thickness increases, the attached vortex occupies the large part of pressure side and the flow separation vortex near the trailing edge of suction side has

already shed into wakes. Then, massive flow separation emerges on both sides of NACA6415, leading to the large fluctuation of pressure, especially on pressure side. However, as the blade is in inverse mode, the flow is quite smooth, which is shown in figure 3.71f. In figure 3.69c, it is observed that the vertical force produced by different profiles at  $\psi=46^\circ$  has almost no difference, because of the relatively small blade loading in figure 3.71a and the component of lift balanced by the drag component in vertical direction. When it comes to the blade B, it is found that the pressure difference is much larger, although the near-wall flows for NACA0015, 0022 and 6415 are quite similar. It shows that the flow separation only appears near the trailing edge of suction side, which is more obvious for NACA6415. It is very interesting that a separation bubble occurs on the leading edge of suction side for inverse NACA 6415. The pressure difference of inverse NACA6415 before the location of  $x/c=0.3$  is extremely large, but it decreases quickly. The resultant upward lift of NACA6415 creates the large vertical force due to the large blade loading in figure 3.71b, providing the large lift to the cycloidal rotor. Thus, it concludes that blade B is dominate for the lift production of the rotating system.

The global propulsive force coefficients for various profiles are also different at this azimuthal angle. The propulsive force distribution of single blade in figure 3.69d indicates that both two blades are responsible for that, but blade B is the main contributor. For a specific instance, for NACA6415, the upward lift towards the right side of blade A produces the negative propulsive force, but the magnitude is small due to the relatively small pressure difference. The large pressure difference of blade B can result in the generation of large positive propulsive force. As a result, the sum of the propulsive force from two blades makes the positive propulsive force with large magnitude, as is shown in figure 3.69b.

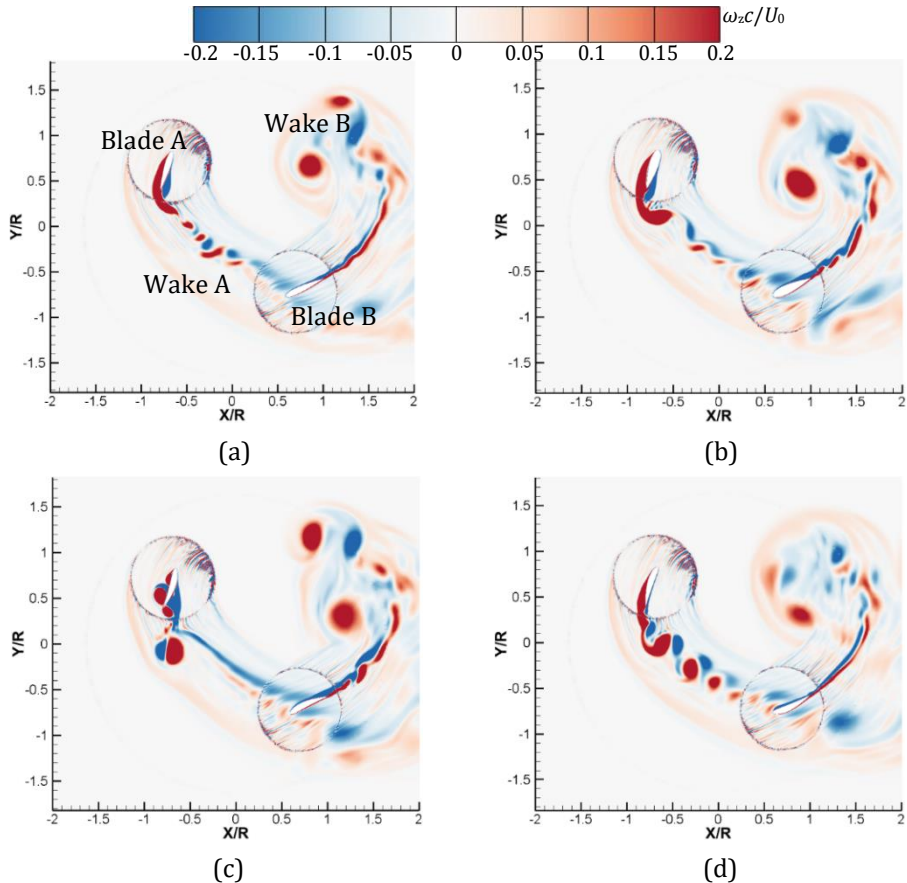
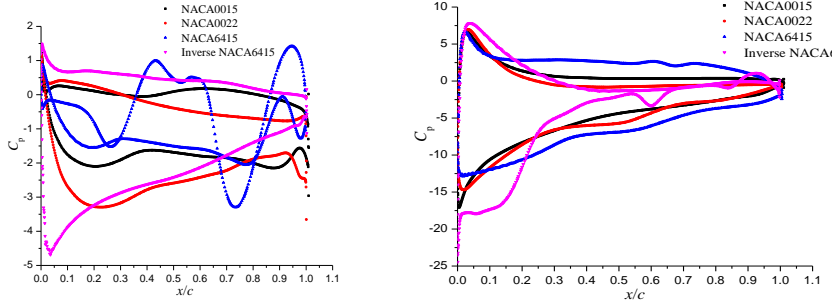


**Fig.3.70** Global flow structures at  $\psi=46^\circ$ . (a) NACA0015; (b) NACA0022; (c) NACA6415; (d) NACA6415.



(a)

(b)

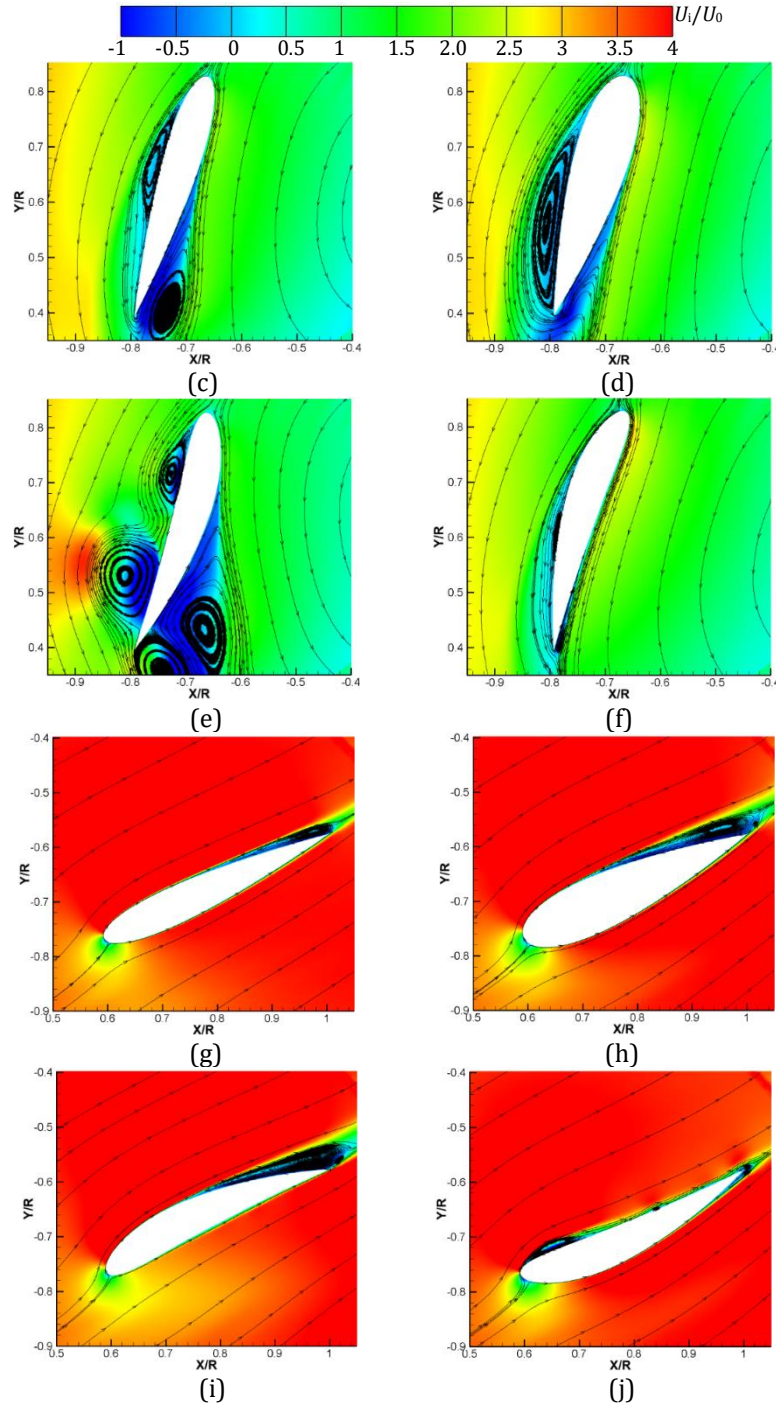


**Fig.3.71** Flow structures at  $\psi=46^\circ$ . (a) Pressure coefficient of blade A; (b) Pressure coefficient of blade B; (c) and (g) NACA0015; (d) and (h) NACA0022; (e) and (i) NACA6415; (f) and (j) Inverse NACA6415.

When blade A is experiencing the retreating side at  $\psi=120^\circ$ , it seems that the lift coefficient of the rotating system has also much difference for four different profiles. To explain this event, the flow structures, pressure distributions and near-wall flows of two blades are presented in figure 3.72 and 3.73. For NACA0022, the wakes shedding from two blades are more unsteady, compared with that from NACA0015. Besides, it is observed that the flow separation on NACA6415 is more violent, and many large scales are shedding from blade A. However, as the blade is inversed, the flow separation on the airfoil surfaces is reduced considerably. Regarding the pressure distribution and flow structure of single blade, it seems that the loading of blade A is relatively small. The flow is quite smooth on symmetrical profile while the vortical flow concentrates on one side of the asymmetrical blade. For example, for NACA6415, the flow separation is mainly on the right side while it is on the left side for inverse NACA6415, which is associated with the position of stagnation point. Consequently, the lift is downward towards the suction side, leading to the negative vertical force and positive propulsive force. However, due to the relatively large pressure difference of inverse NACA6415, the negative vertical force generated by blade A has the largest magnitude, as well as the positive propulsive force. When considering blade B, it can be found that the flow is more complex for the thick symmetrical airfoil, for an example, many small scales on suction side of NACA0022. Except for the flow separation on the trailing edge of pressure side, there is a separation bubble on the leading edge of suction side for NACA6415. However, for inverse NACA6415, the large-scale separation vortex only exists on the trailing edge of suction side. Due to the low pressure on the lower surface, the lift of blade B is downward, causing the negative vertical force in figure 3.69c. However, the vertical force created by NACA6415 is small because of the small blade loading in figure 3.73a, while it is very large for inverse NACA6415. Generally, it concludes that blade B is dominate for the lift difference of the rotating system with various blade profiles.

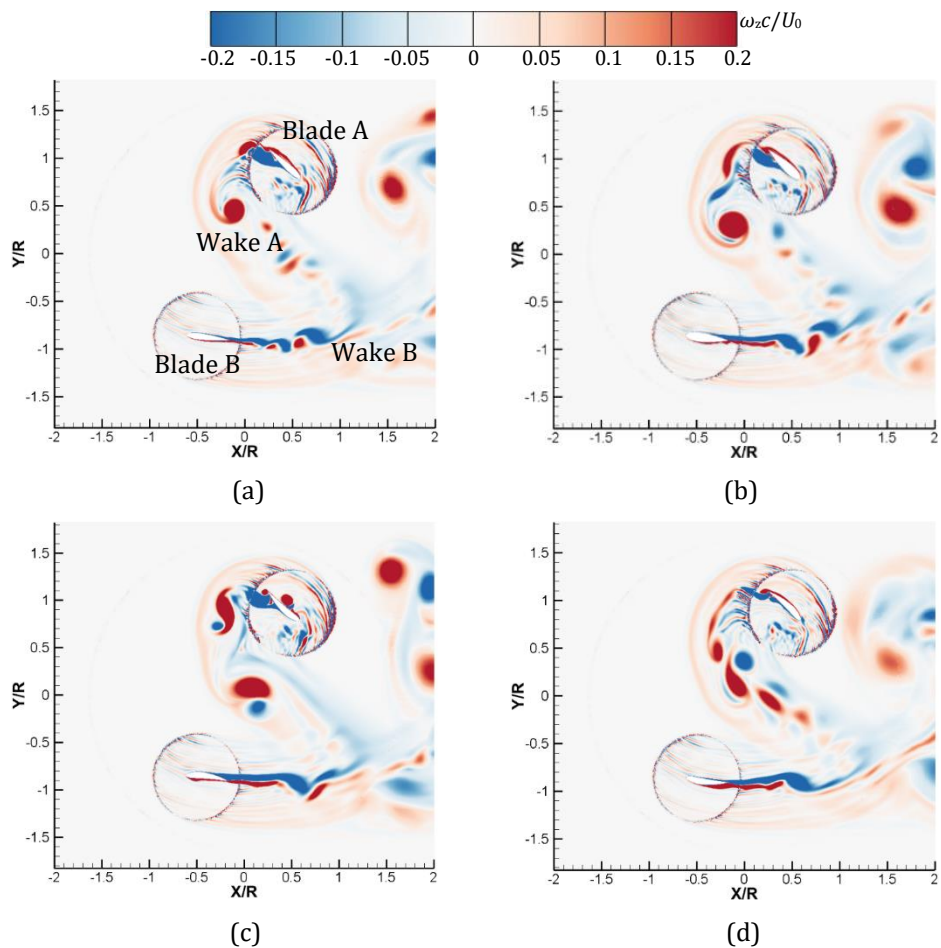


**Fig.3.72** Global flow structures at  $\psi=120^\circ$ . (a) NACA0015; (b) NACA0022; (c) NACA6415; (d) NACA6415.

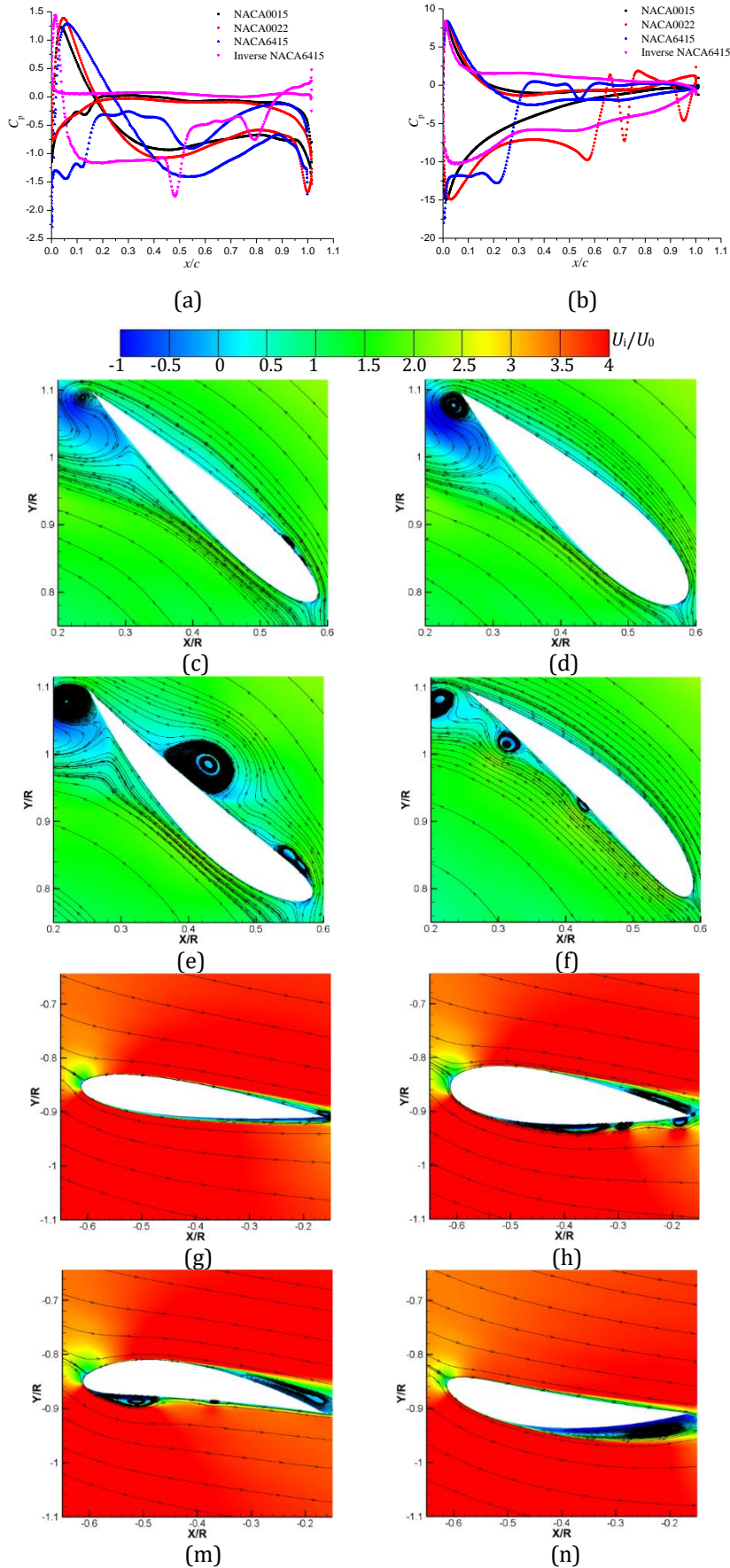


**Fig.3.73** Flow structures at  $\psi=120^\circ$ . (a) Pressure coefficient of blade A; (b) Pressure coefficient of blade B; (c) and (g) NACA0015; (d) and (h) NACA0022; (e) and (i) NACA6415; (f) and (j) Inverse NACA6415.

Then, the difference of propulsive force coefficient for various profiles is analyzed at  $\psi=180^\circ$  in figure 3.74 and 3.75. The general flow structures show that the wakes from blade A are going to interact with blade A, especially for NACA6415 and inverse NACA6415. In addition, it can be seen that the flow separation on both two blades is more evident for NACA6415. For the symmetrical profiles, as the thickness increases, the vortical flow is more intensive. As is shown in figure 3.75a and 3.75b, the pressure difference of blade A is comparable with that of blade B. On the suction side, the flow separation is mainly near the trailing edge. Simultaneously, a small-scale vortex attaches on the pressure sides of two symmetrical profiles and NACA6415. However, the near-wall flow is extremely smooth for inverse NACA6415. Due to the high pressure on the right side of blade A, the lift is upward towards the left side, bringing about the positive vertical force and propulsive force. The vertical force of blade A has the smallest value for inverse NACA6415, as a result of the small blade loading. Similarly, NACA6415 can produce the largest positive propulsive force. Afterwards, according to the flow structures on blade B, it is evident that the large-scale vortex nearly occupies the whole suction side of NACA0022, leading to the highest lift. Influenced by the vortex B and LEV on the suction side, the pressure of NACA6415 has large fluctuation, but its value is still larger than that of inverse NACA6415, where the vortex has already shed into the wake. Finally, by the sum of the propulsive force produced by two blades, it concludes that NACA6415 can create the positive propulsive force with the largest value, mainly resulting from blade A. At the same time, for NACA0022, blade B is responsible for the second largest propulsive force of the cycloidal rotor.

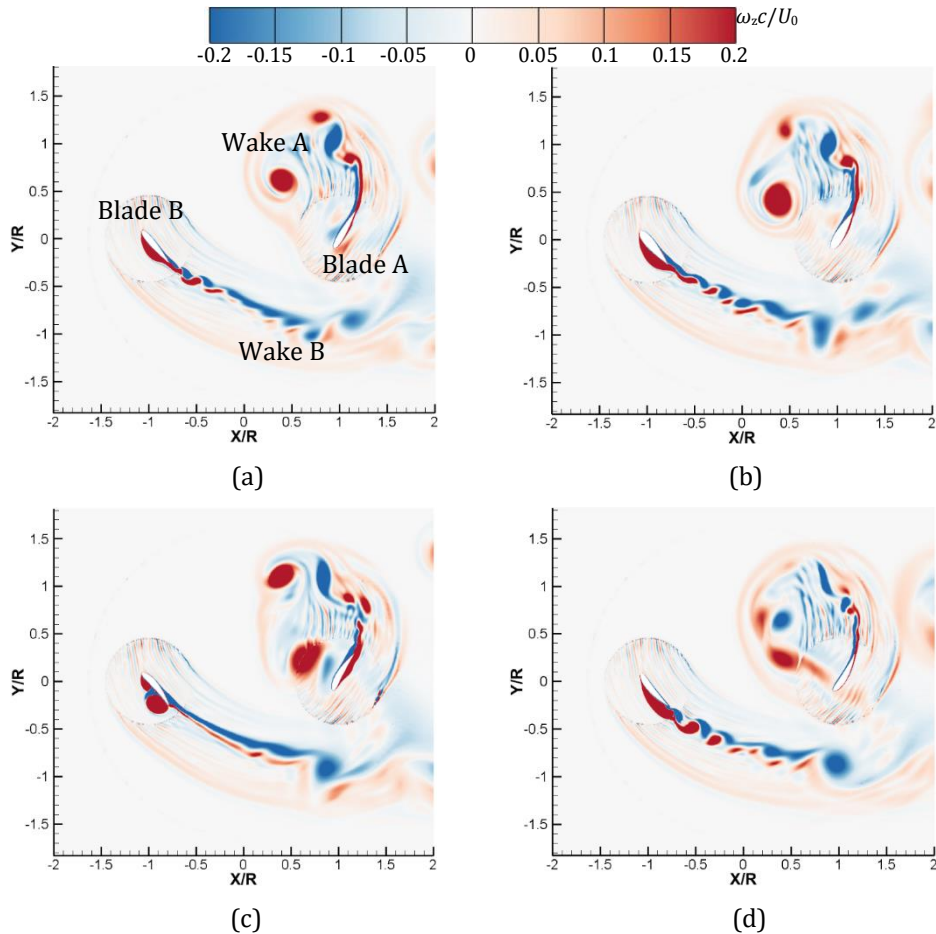


**Fig.3.74** Global flow structures at  $\psi=180^\circ$ . (a) NACA0015; (b) NACA0022; (c) NACA6415; (d) NACA6415.

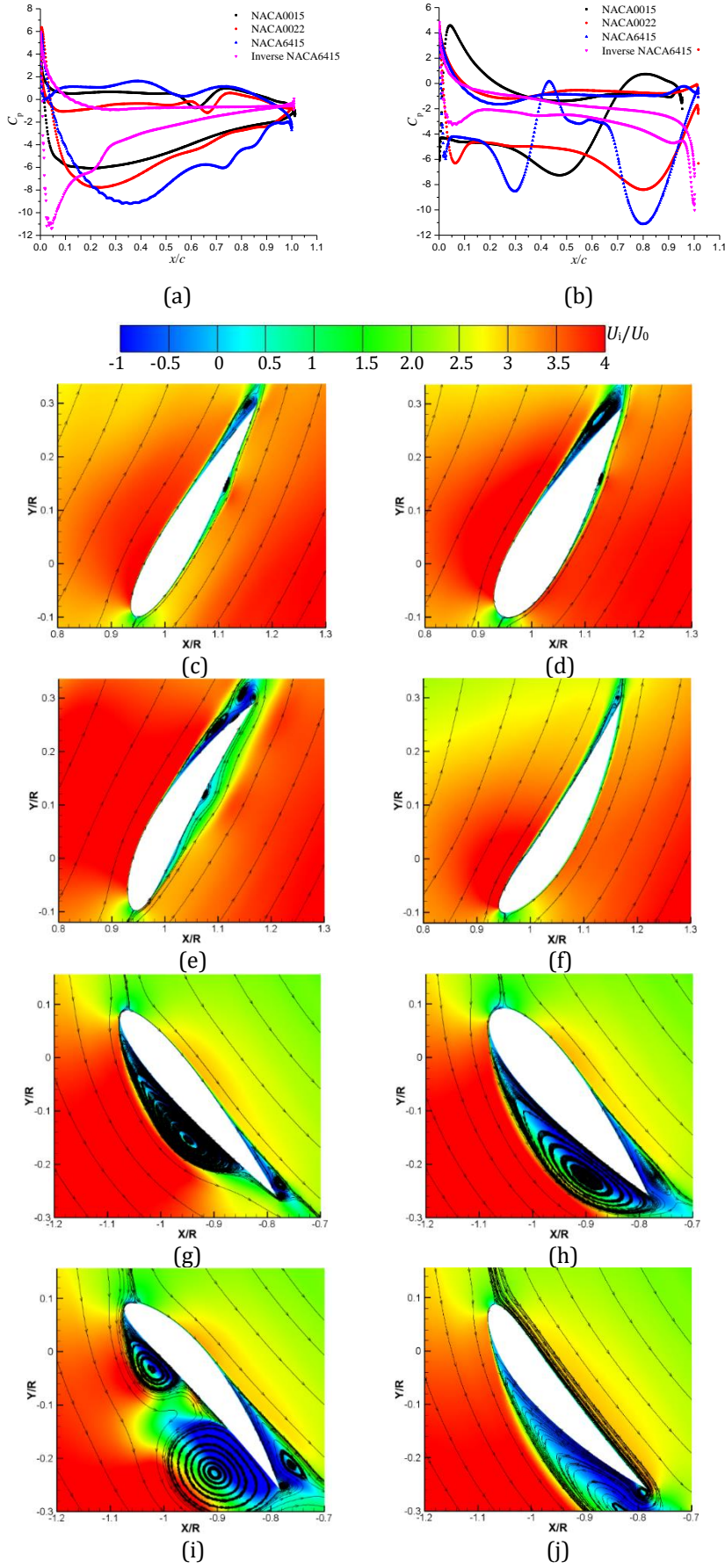


**Fig.3.75** Flow structures at  $\psi=180^\circ$ . (a) Pressure coefficient of blade A; (b) Pressure coefficient of blade B; (c) and (g) NACA0015; (d) and (h) NACA0022; (e) and (i) NACA6415; (f) and (j) Inverse NACA6415.

### 3.4.3 Effect of $Re$

As is shown in figure 3.66, with the increase of  $Re$ , the lift and propulsive force coefficients of the rotating system change remarkably. Therefore, the NACA6415 profile is selected as the objective to study the influence of  $Re$  on the performance and flow structures. Two values, representing the low and high  $Re$  conditions, are adopted in the present work. In figure 3.76, the variation of lift and propulsive force coefficients in a rotating cycle is plotted. It can be seen that the main difference of global lift coefficient at two  $Re$  is located at  $\psi=70^\circ\text{-}180^\circ$  and the maximal value is achieved at  $\psi=140^\circ$ . Moreover, the propulsive force coefficient has relatively large difference in quarter cycle from  $\psi=90^\circ$  to  $180^\circ$ . According to the distributions of these two force coefficients for the single blade, it seems that the propulsive force coefficient changes more evidently compared with the vertical force coefficient. Thus, an azimuthal angle of  $140^\circ$  is employed to investigate the difference of the lift coefficient, while the flow structures at  $\psi=50^\circ$  and  $180^\circ$  are used to clarify the difference of the propulsive force coefficient.

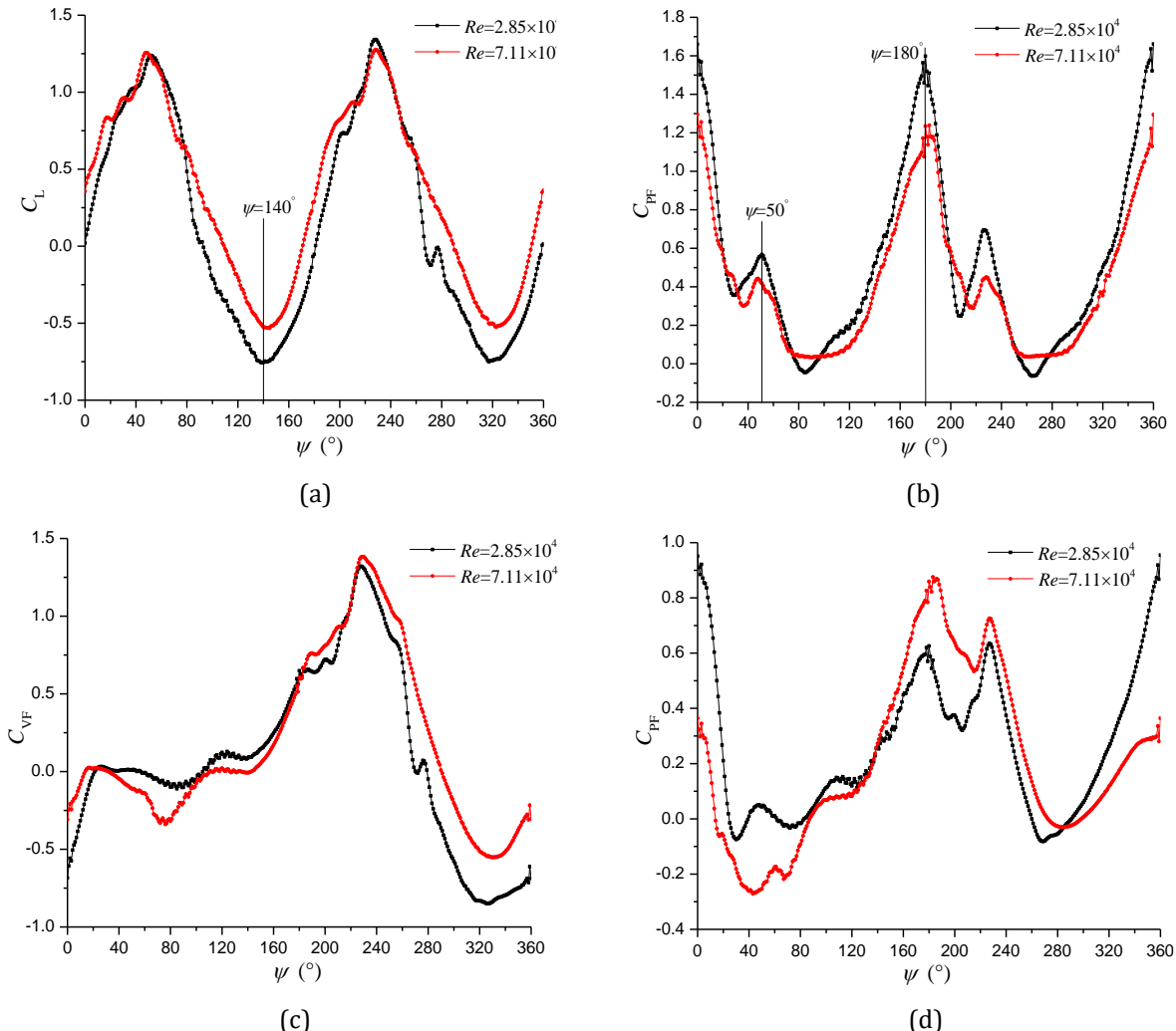


**Fig.3.76** Performance in a revolution at two  $Re$ . (a) Lift coefficient of cycloidal rotor; (b) Propulsive force coefficient of cycloidal rotor; (c) Vertical force coefficient of single blade; (d) Propulsive force coefficient of single blade.

In figure 3.77 and 3.78, the detailed flow structures and blade loadings of NACA6415 at  $\psi=140^\circ$  are presented. Obviously, when  $Re$  increases, the vortical flows are more disordered. The large-scale wakes shedding from two blades have the high risk in contacting each other. However, the flow separation on both two blades is more severe under low  $Re$  condition. Then, the blade loading distributions show that blade B has large pressure difference compared with that of blade A. On the pressure side of blade A, there is a three-vortex-structure near the leading edge, but vortex B is still at the inception stage. However, the LEV develops earlier at low  $Re$  and extends to the middle chord, while it is still in the initial time of development at high  $Re$ , which indicates that increasing the Reynolds number can delay the vortex development. This situation is also similar with that for blade B, where the vortex attached on the suction side is also delayed under high  $Re$  condition. Near the leading edge of pressure side for blade A, the existence of the attached vortex leads to the pressure drop and then it recovers quickly at high  $Re$ , producing the relatively high lift. Therefore, the negative vertical force with large value is generated at high  $Re$ . Moreover, on the suction side of blade B, the influence of the attached vortex on the pressure distribution is more apparent at low  $Re$ , resulting in the creation of the higher lift. As a result, the downward lift produces the negative vertical force with larger magnitude, which is shown in figure 3.76c. Consequently, the negative lift of the rotating system is much larger at low  $Re$ , mainly induced by the earlier development of the large-scale three-vortex-structure on the suction side of blade B.

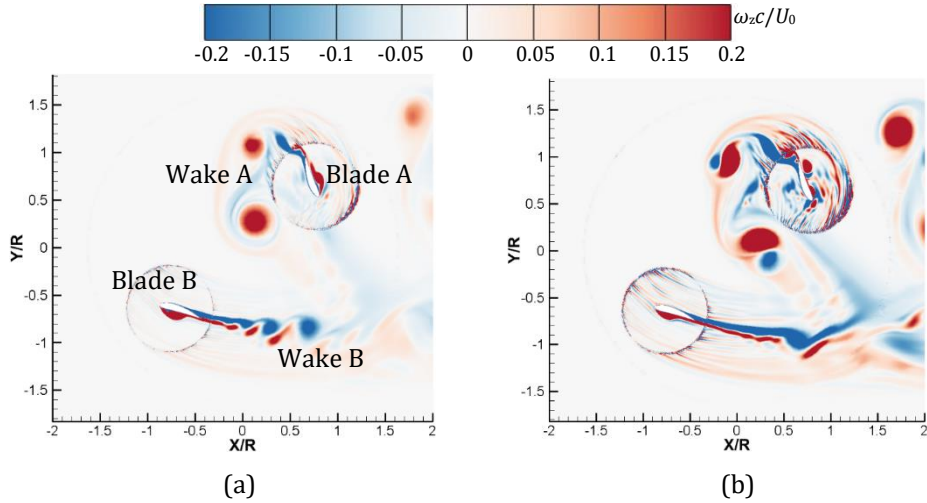


**Fig.3.77** Global flow structures at  $\psi=140^\circ$ . (a)  $Re=2.85\times 10^4$ ; (b)  $Re=7.11\times 10^4$ .

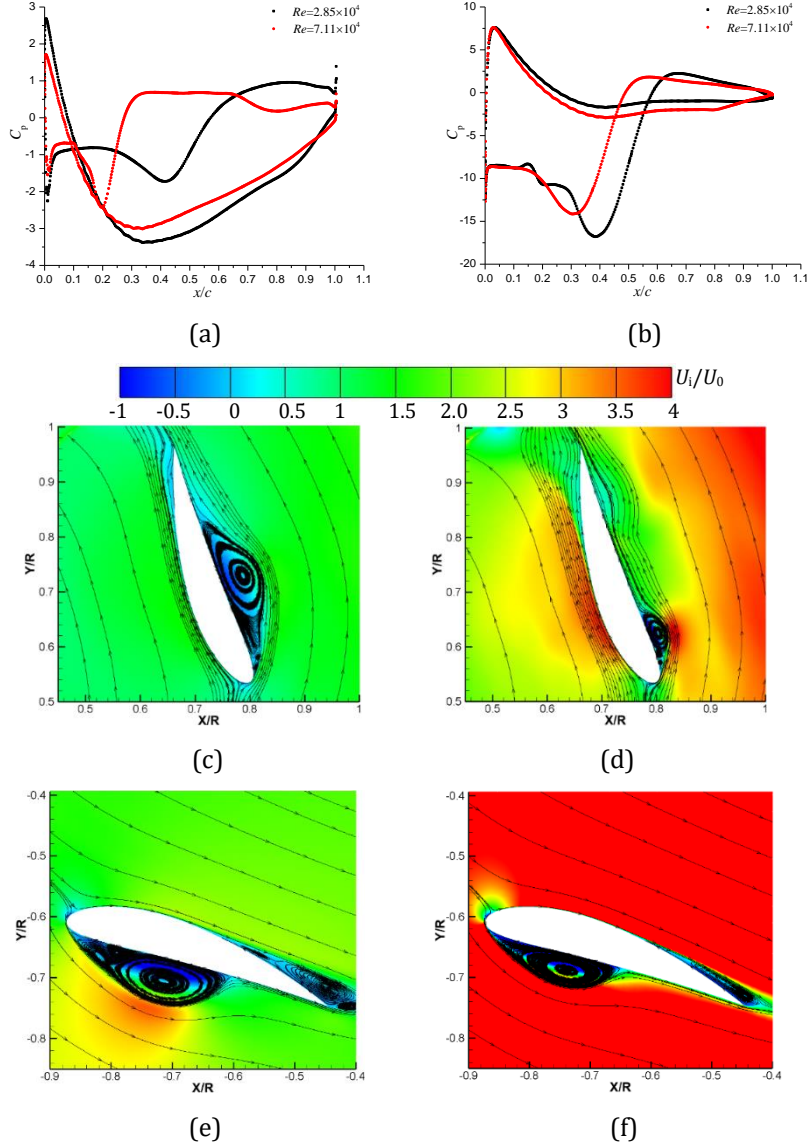


**Fig.3.78** Flow structures at  $\psi=140^\circ$ . (a) Pressure coefficients of blade A; (b) Pressure coefficients of blade B; (c) and (e)  $Re=2.85\times 10^4$ ; (d) and (f)  $Re=7.11\times 10^4$ .

Afterwards, given the difference of propulsive force coefficients at two  $Re$ , the flow structures and blade loadings at  $\psi=50^\circ$  are clarified in figure 3.79 and 3.80. It seems that the wake A has a strong interaction with blade B and wake B is approaching to itself, which is more obvious under high  $Re$  condition. Furthermore, the flow structures over blade A are quite different for two cases, where the vortex shedding is more violent at high  $Re$ . Considering the near-wall flows over blade A, the main feature of pressure side is that the LEV is located at the trailing edge and the vortex B develops near the leading edge. At high  $Re$ , although the vortex on the pressure side can drop the pressure, the large size of vortex pair near the trailing edge of suction side has great impact on the pressure, leading to the lower pressure of the whole suction surface. This situation is not the same with that at low  $Re$ , because the vortical flows on the trailing edge of the suction side are not intensive. As a consequence, the downward lift towards the right side creates the large negative propulsive force at high  $Re$ . However, at low  $Re$ , due to the low pressure difference of blade A, the propulsive force is almost equal to zero. Moreover, the flow around blade B is relatively simple and there is only flow separation near the trailing edge of suction side.

The main difference is the pressure distribution of two surfaces due to the different boundary layer flows induced by the different pitching rates. Therefore, as is shown in figure 3.80b, the positive propulsive force at high  $Re$  is a little bit larger because of the large blade loading. In general, the difference of the propulsive force coefficient of the cycloidal rotor at this position is determined by two blades, but blade A is the primary contributor because of the complex vortical flows at high  $Re$ .

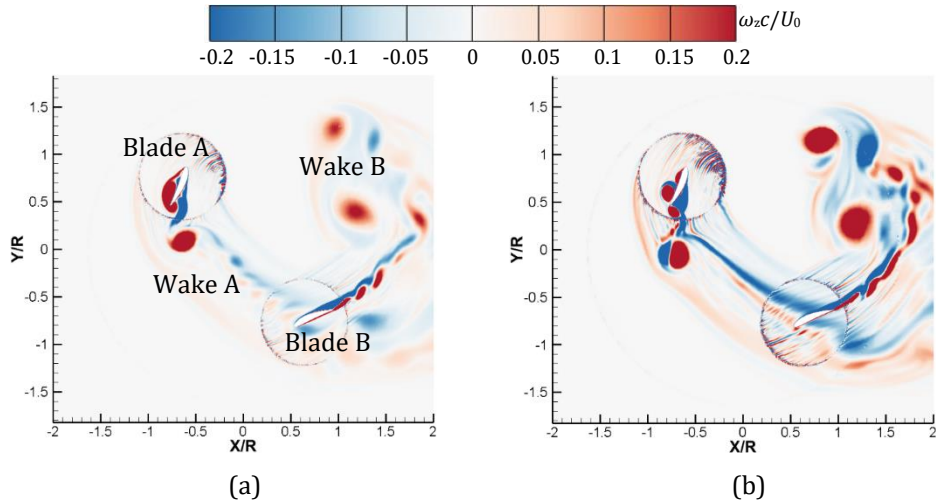


**Fig.3.79** Global flow structures at  $\psi=50^\circ$ . (a)  $Re=2.85\times 10^4$ ; (b)  $Re=7.11\times 10^4$ .

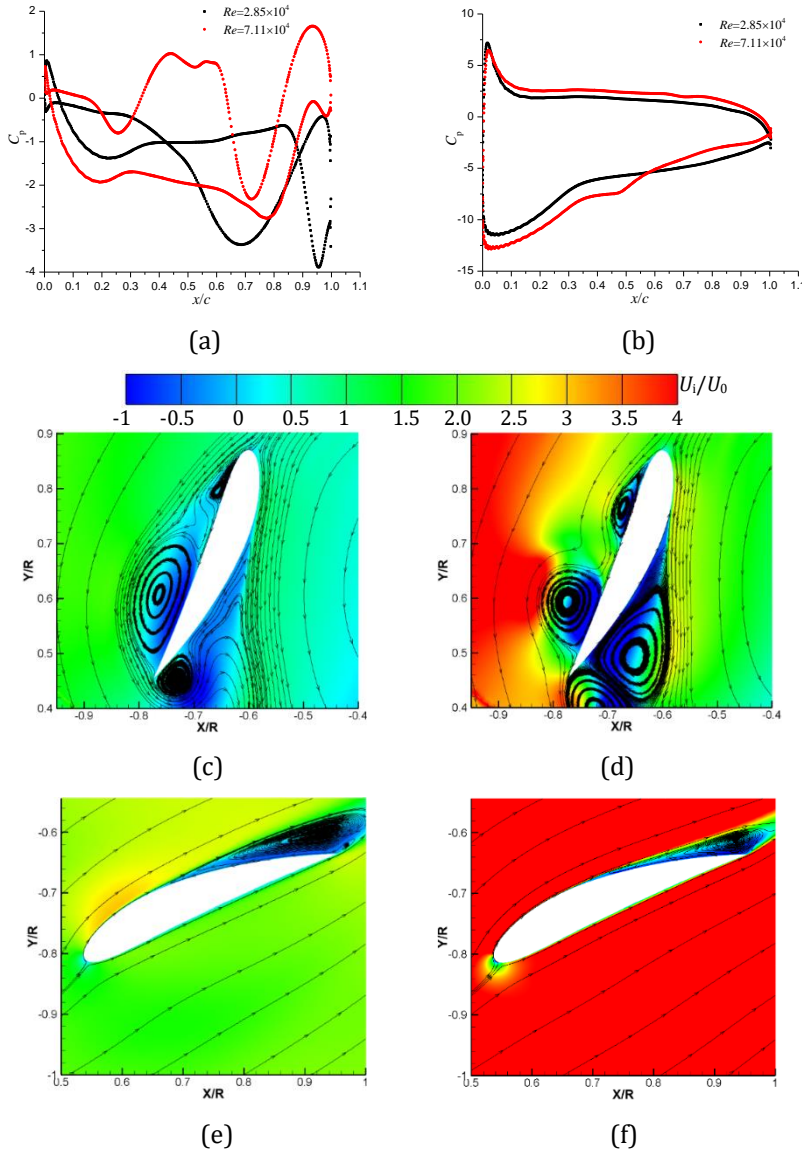


**Fig.3.80** Flow structures at  $\psi=50^\circ$ . (a) Pressure coefficients of blade A; (b) Pressure coefficients of blade B; (c) and (e)  $Re=2.85\times 10^4$ ; (d) and (f)  $Re=7.11\times 10^4$ .

When blade A moves to the initial position of blade B, the global propulsive force has much difference at two  $Re$ . Therefore, with the aid of the flow structures and pressure distributions in figure 3.81 and 3.82, this event is analyzed in detail. As is shown in figure 3.81, it can be seen that wake A has large possibility to contact with blade A at high  $Re$ . Additionally, the flow morphology on suction side of blade B is quite different. For blade A, the flow separation is located at the trailing edge of suction side and a small vortex structure is detected on the pressure side at high  $Re$ . Figure 3.82c shows that the pressure difference at two  $Re$  is due to the pressure distribution of two surfaces induced by the different boundary layer flows because of the increase of the pitching rate, which is quite similar with that in figure 3.80b. Finally, the resultant upward lift towards the left side generates the positive propulsive force, but the magnitude is larger at high  $Re$ . Then, on blade B, the flow structures are also different at two  $Re$ . For example, at low  $Re$ , the three-vortex-structure has the fully development, while only the LEV and vortex B are visible at high  $Re$ . As a result, the pressure on the suction side is much lower at low  $Re$ , leading to the larger propulsive force. Thus, it concludes that the larger propulsive force of the

cycloidal rotor at low  $Re$  mainly benefits from blade B, although blade A can also provide the large positive propulsive force at high  $Re$ .

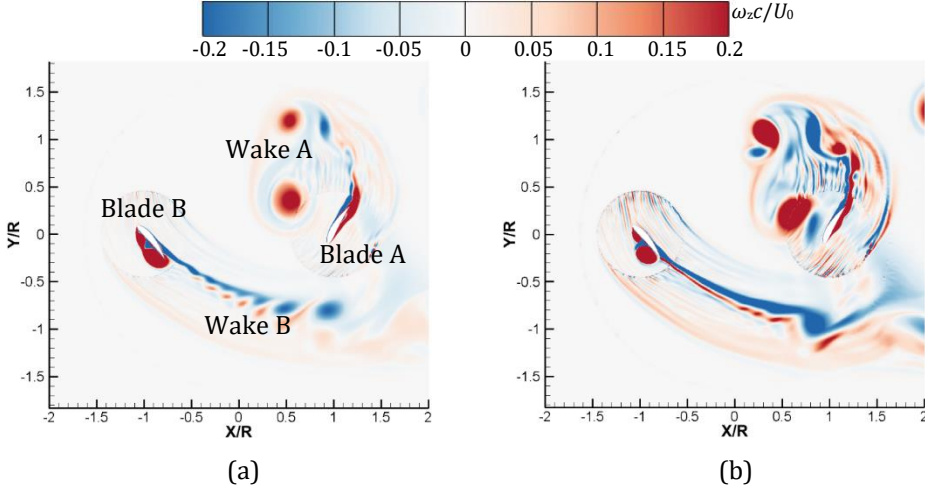


**Fig.3.81** Global flow structures at  $\psi=180^\circ$ . (a)  $Re=2.85\times 10^4$ ; (b)  $Re=7.11\times 10^4$ .

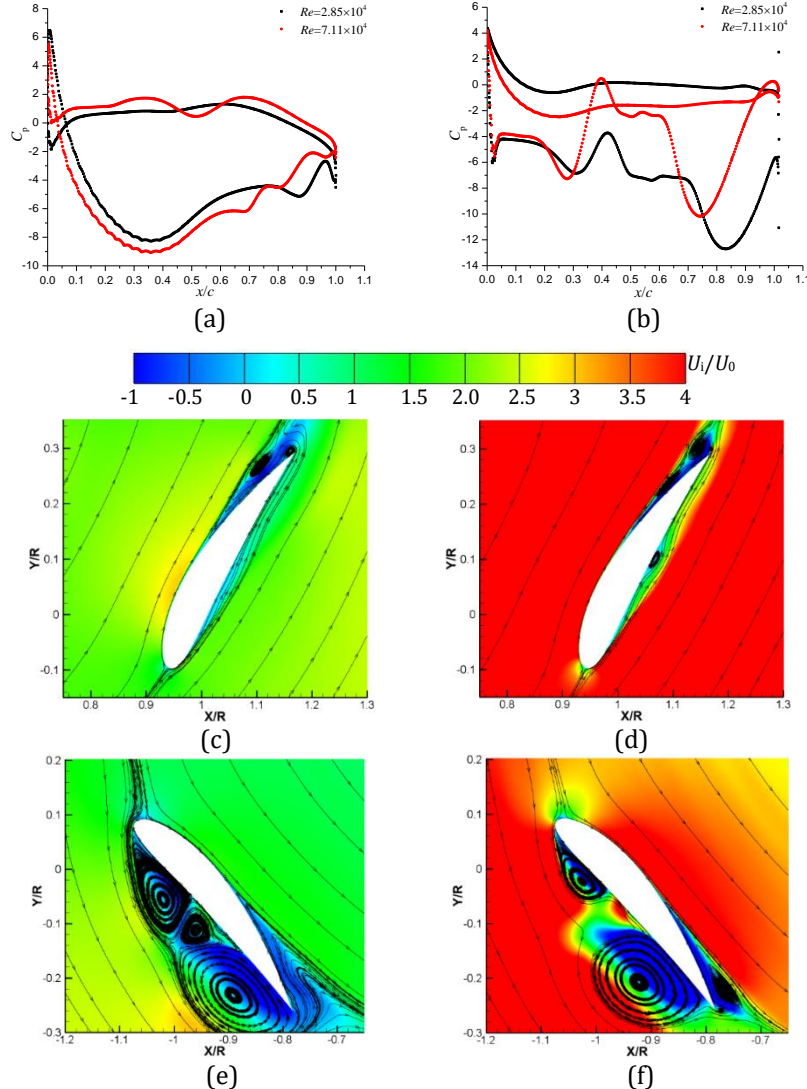


**Fig.3.82** Flow structures at  $\psi=180^\circ$ . (a) Pressure coefficients of blade A; (b) Pressure coefficients of blade B; (c) and (e)  $Re=2.85\times 10^4$ ; (d) and (f)  $Re=7.11\times 10^4$ .

### 3.4.4 Effect of $\lambda$

As an important parameter,  $\lambda$  has great impact on the global performance and flow fields of the cycloidal propeller. With a constant value of  $\lambda$ , the profile of NACA6415 produces the largest lift, propulsive force and power coefficients. With the increase of  $\lambda$  by decreasing the rotating speed, the lift coefficient decreases for a specific profile, but it decreases firstly and then increases for NACA0022, inverse NACA4415 and 6415. The propulsive force coefficient decreases significantly with the increase of  $\lambda$  for all profiles, as well as the power coefficient. Then, regarding to the calculated efficiency, it is observed that the symmetrical profiles operate in a wide range of high efficiency, but it becomes worse with the increase of the blade thickness. In addition, when  $\lambda$  is smaller than 0.5, the inverse NACA2415 shows the best performance, but it decreases dramatically at high  $\lambda$  because of the relatively low propulsive force and high power. Moreover, although NACA6415 can generate the high propulsive force coefficient at various  $\lambda$ , but the efficiency is relatively low due to the high level of power consumption. Furthermore, the efficiency of NACA0022, inverse NACA4415 and 6415 is negative as  $\lambda$  is larger than 0.625. Considering the stability of working condition with high efficiency, the symmetrical profiles, including NACA0012 and 0015, are recommended for a better design of cycloidal propeller.

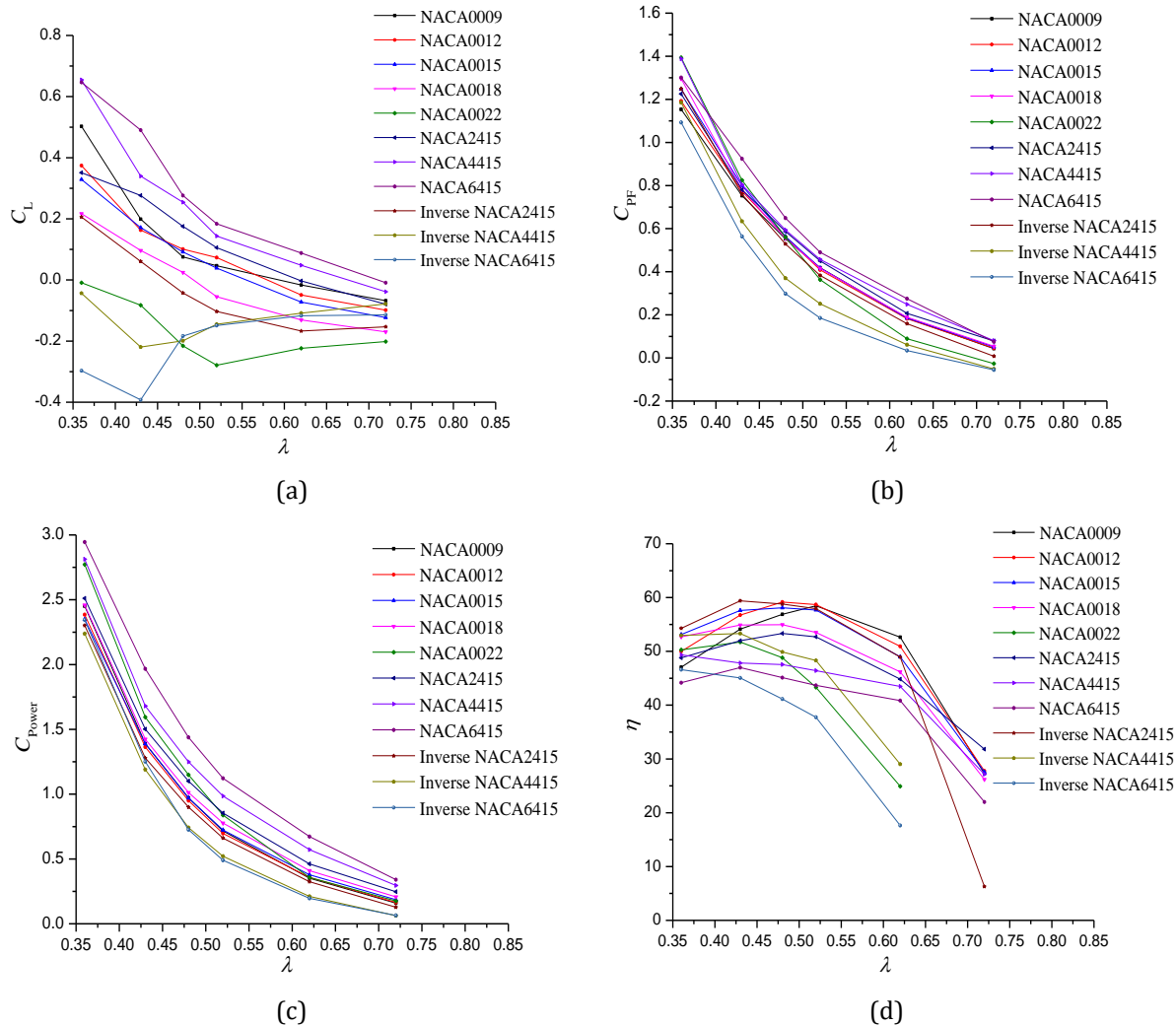


**Fig.3.83** Global performance of cycloidal rotor. (a) Lift coefficient; (b) Propulsive force coefficient; (c) Power coefficient; (d) Efficiency.

By increasing the rotating speed, the advance coefficient  $\lambda$  decreases, which results in the significant change of performance and flow structures. In figure 3.83, the lift, propulsive force and power coefficients decrease with the increase of  $\lambda$ . Therefore, two values of 0.43 and 0.72, representing the low and high  $\lambda$ , are employed in this work. The objective is NACA6415 profile because the highest force and power coefficients are achieved. The performance of the cycloidal rotor and single blade in a revolution are plotted in figure 3.84 to illustrate the force difference at two  $\lambda$ . In figure 3.51a, except the region from  $\psi=110^\circ$  to  $180^\circ$ , the lift coefficient is always much larger at low  $\lambda$ . Simultaneously, the propulsive force coefficient is also much larger at low  $\lambda$  at every position of a rotating cycle. Then, for a single blade, at two positions of  $\psi=0^\circ$ - $30^\circ$  and  $290^\circ$ - $360^\circ$ , the lift coefficient at high  $\lambda$  is larger, but the propulsive force coefficient is always larger at low  $\lambda$  in a revolution. As a consequence, two azimuthal angles of  $50^\circ$  and  $145^\circ$  and one position at  $\psi=10^\circ$  are selected to show the detailed internal flows, respectively.

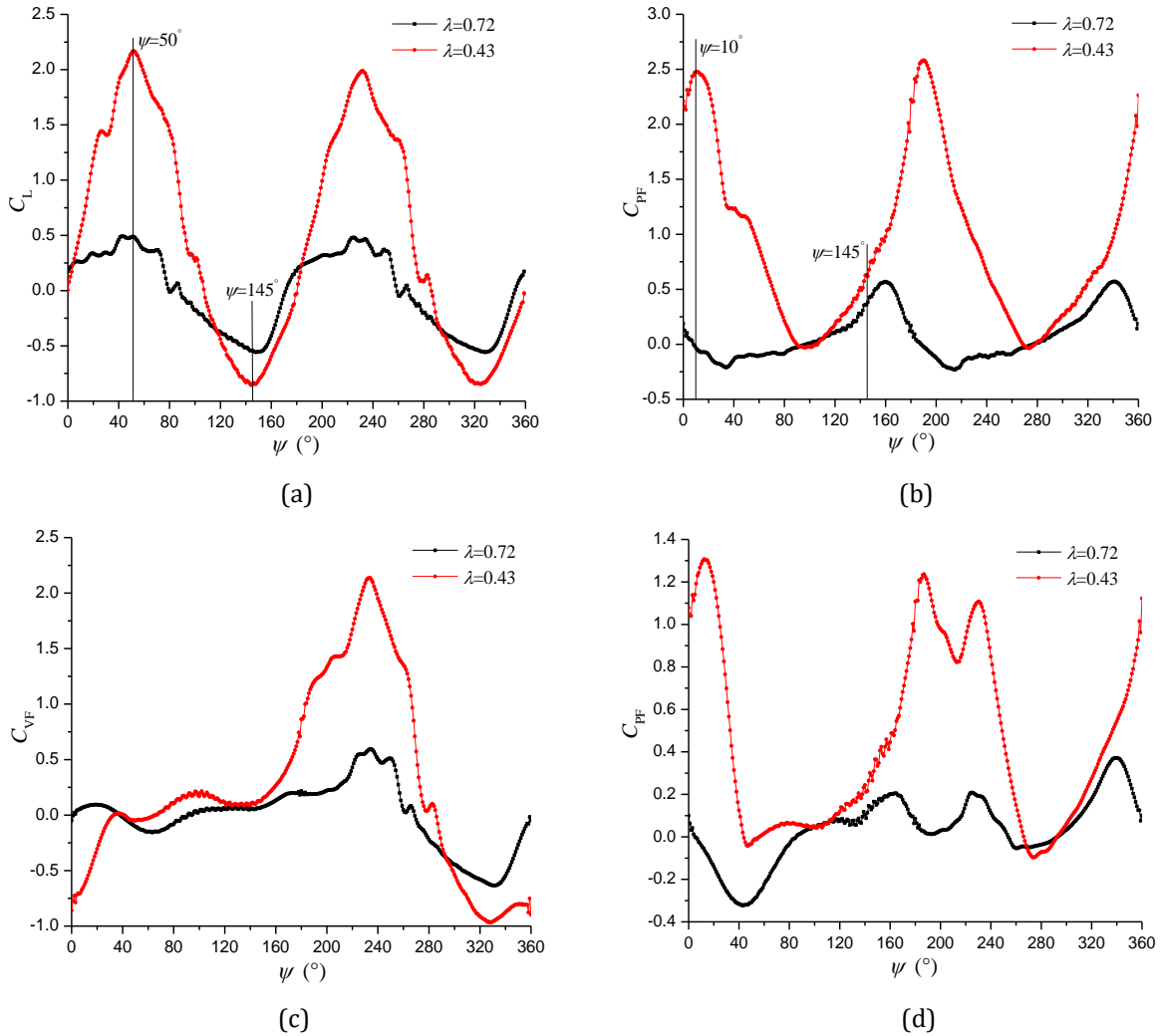


**Fig.3.84** Performance in a revolution at different  $\lambda$ . (a) Lift coefficient of cycloidal rotor; (b) Propulsive force coefficient of cycloidal rotor; (c) Vertical force coefficient of single blade; (d) Propulsive force coefficient of single blade.

In figure 3.85 and 3.86, to clarify the force coefficient difference, the flow structures and pressure distributions of two blades are displayed at  $\psi=50^\circ$ . Evidently, at two  $\lambda$ , the wakes shedding from two blades are totally different. The wake A at low  $\lambda$  has

already interacted with blade B, which is not clear at high  $\lambda$ . Additionally, the flow separation on both two sides of blade A is more intensive at low  $\lambda$ , which is responsible for the large value of power coefficient. As  $\lambda$  decreases, it is observed that the stagnation point of blade A moves from left side of leading edge to the right side, leading to the completely different boundary layer flows. For example, at high  $\lambda$ , the size of vortex on the pressure side is relatively small and the trailing edge separation vortex on the suction side has large size, which is opposite at low  $\lambda$ . As a consequence, the pressure distributions at two  $\lambda$  are totally different, which is shown in figure 3.86a. At  $\lambda=0.72$ , the lift is upward towards the right side, causing the production of negative propulsive force, but the magnitude is larger due to the components of lift and drag in the same direction. However, the propulsive force is nearly equal to zero at low  $\lambda$ , for the reason that the component of lift is balanced by the drag component in the horizontal direction. Simultaneously, although the vertical force is the sum of components of lift and drag, it still has the small value due to the small blade loading at  $\lambda=0.43$ . Furthermore, on blade B, the flow separation only appears on the trailing edge of suction side, which is stronger at low  $\lambda$ . It believes that the location of stagnation point makes the contribution to the size of trailing edge separation vortex. At low  $\lambda$ , the pressure difference is much larger than that at high  $\lambda$ , which is responsible for the generation of large positive vertical force and propulsive force. Therefore, the lift and propulsive force of the cycloidal rotor have the large values at low  $\lambda$ . Although blade B is the main contributor to the difference of lift and propulsive force, blade A more or less makes the contribution to the propulsive force difference at two  $\lambda$ .

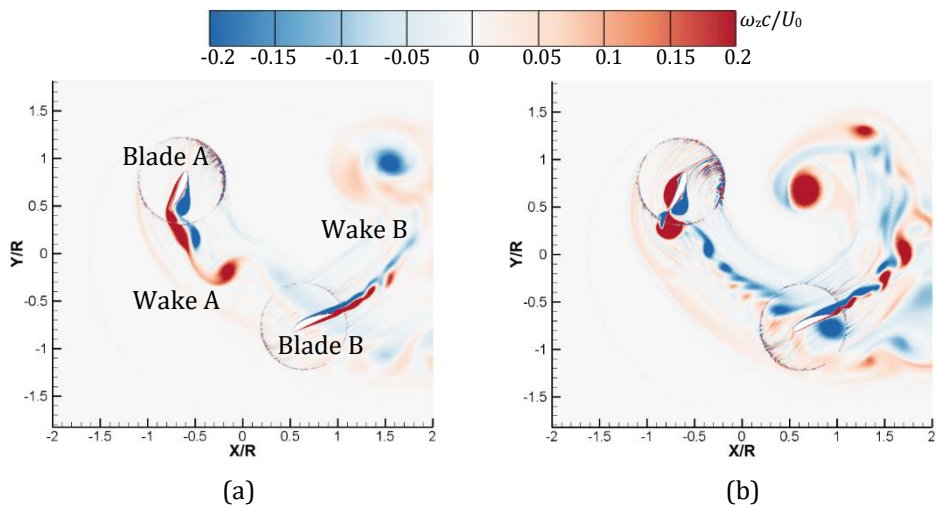


**Fig.3.85** Global flow structures at  $\psi=50^\circ$ . (a)  $\lambda=0.72$ ; (b)  $\lambda=0.43$ .

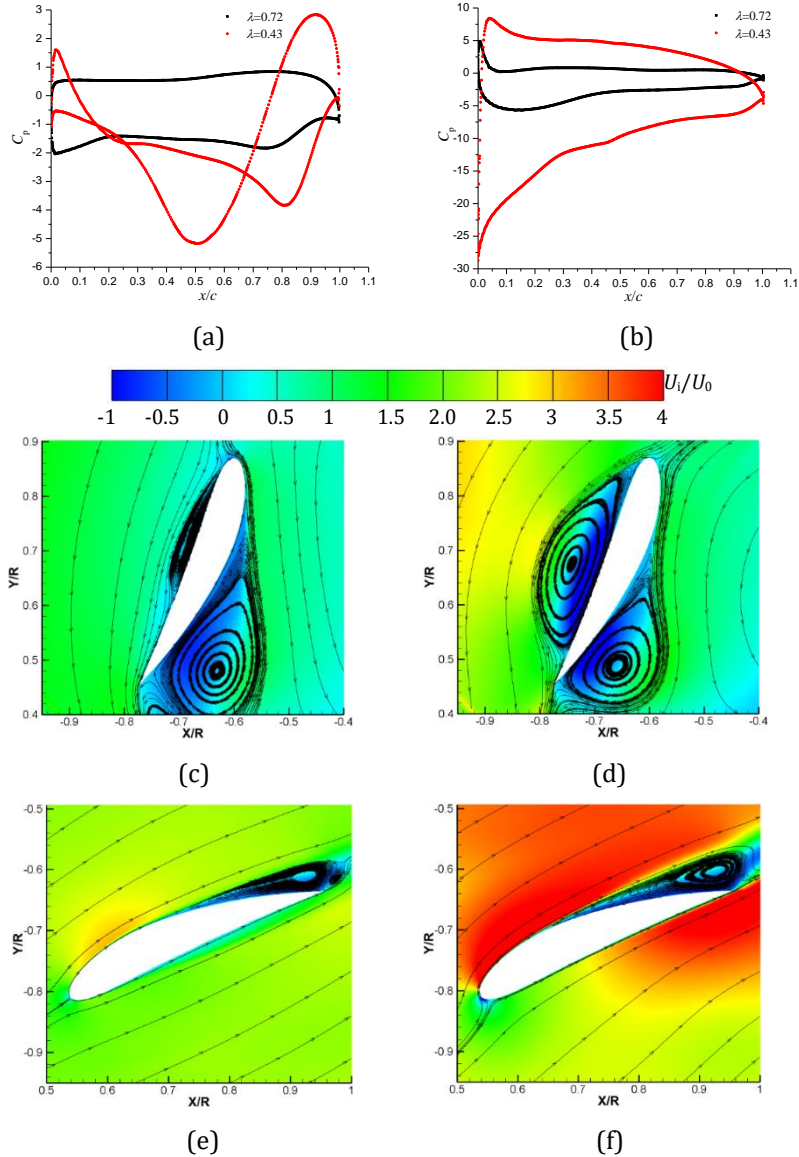


**Fig.3.86** Flow structures at  $\psi=50^\circ$ . (a) Pressure coefficients of blade A; (b) Pressure coefficients of blade B; (c) and (e)  $\lambda=0.72$ ; (d) and (f)  $\lambda=0.43$ .

At  $\psi=145^\circ$ , the gross feature of the global flow structures is that the wakes from two blades are totally different, which is more violent at low  $\lambda$ . Besides, the flow separation on the right side of blade A and lower surface of blade B also varies considerably at two  $\lambda$ . Given the flow structure and pressure distribution of blade A, it seems that the three-vortex-structure is more evident at low  $\lambda$  while it still at the initial development stage at high  $\lambda$ . Obviously, the structure has much influence on the pressure distribution at low  $\lambda$ , resulting in the relatively large propulsive force caused by the downward lift towards the left side. The vertical force of blade A has almost no difference at two  $\lambda$ , because the component of lift is nearly equal to the drag component. What is more, on the suction side of blade B, there exists a large size of attached vortex, especially at high  $\lambda$ . Based on the pressure distribution in figure 3.88b, it is observed that the attached vortex at low  $\lambda$  has a smaller size and it only influences a limited portion of airfoil surface, because of the delayed effect by increasing the pitching rate. According to the resultant downward lift towards the lower surface and large blade loading, the vertical force of blade B is negative with large magnitude at low  $\lambda$ . At the same time, though the

blade loading at low  $\lambda$  is extremely large, the positive propulsive force induced by the lift component is almost balanced by the negative propulsive force produced by the drag component. As a consequence, the total propulsive force of the cycloidal rotor has not too much difference at two  $\lambda$ . Thus, it concludes that the lift difference of the rotating system is mainly induced by blade B, while the difference of propulsive force at two  $\lambda$  should consider the contributions made by two blades.

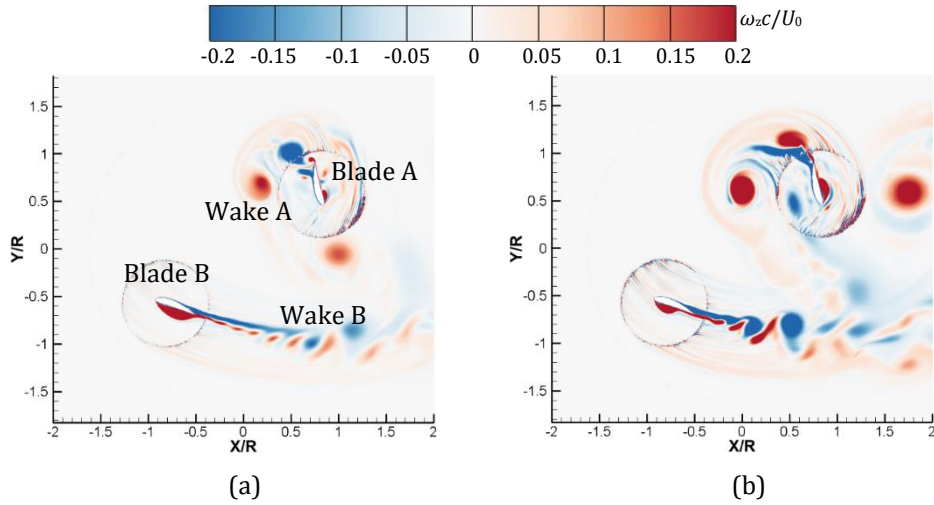


**Fig.3.87** Global flow structures at  $\psi=145^\circ$ . (a)  $\lambda=0.72$ ; (b)  $\lambda=0.43$ .

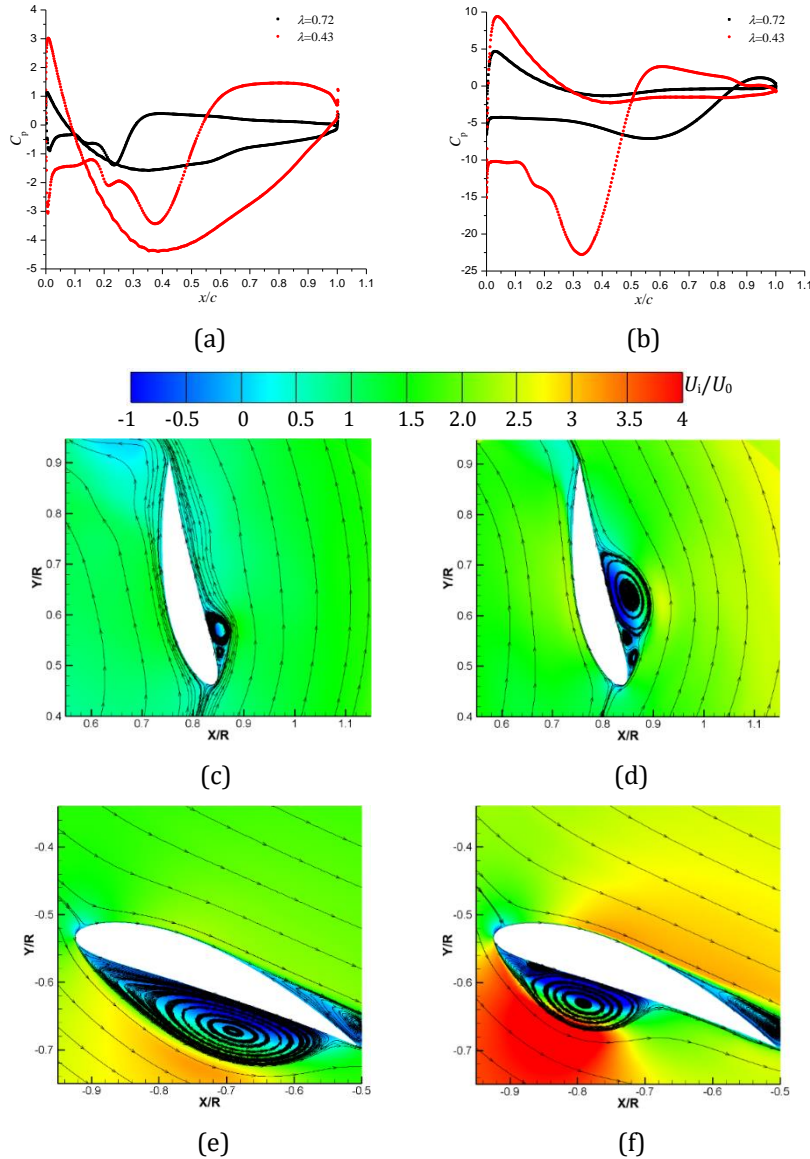


**Fig.3.88** Flow structures at  $\psi=145^\circ$ . (a) Pressure coefficients of blade A; (b) Pressure coefficients of blade B; (c) and (e)  $\lambda=0.72$ ; (d) and (f)  $\lambda=0.43$ .

At  $\psi=10^\circ$ , there is no obvious wake-blade interaction, but the wake pattern of blade B shows much difference at two  $\lambda$ . It is also evident that the flow separation on the left side of blade A and right side of blade B are extremely different. The pressure difference of blade A is comparable with that of blade B. On suction side of blade A, a slender vortex is attached at high  $\lambda$  while the fully developed three-vortex-structure occupying the whole blade surface is observed at low  $\lambda$ , which can be explained by the location of stagnation point. Due to the large blade loading at low  $\lambda$ , the downward lift towards the lower surface generates the negative vertical force with large magnitude. At the same time, it can produce the large positive propulsive force. Moreover, at high  $\lambda$ , the three-vortex-structure is detected on the pressure side of blade B, but it is absent at low  $\lambda$ . This occurrence is also caused by the stagnation point position. Because of the large blade loading at low  $\lambda$ , the blade B produces the upward lift towards the left side, as a source of the positive vertical force and propulsive force. Generally, it concludes that both blade A and B make the contributions to the difference of lift and propulsive force for the cycloidal rotor at two  $\lambda$ , due to the nearly equivalent pressure difference of two blades.

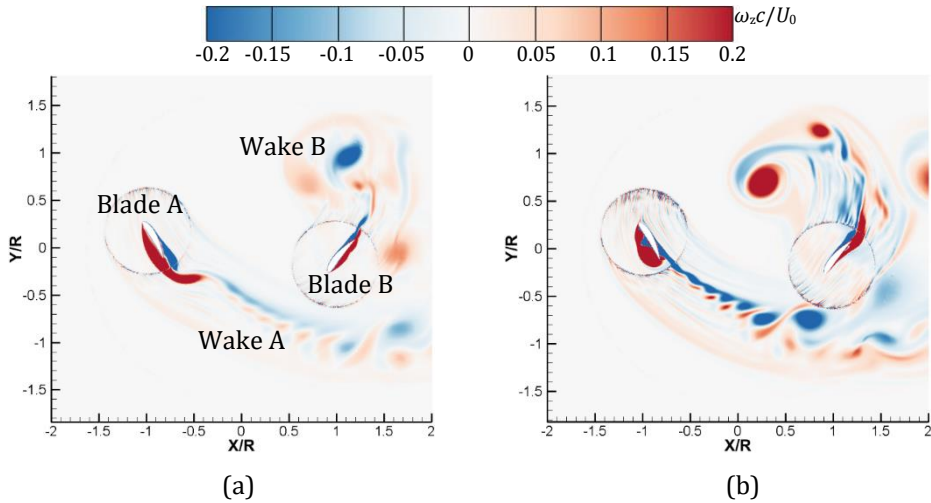


**Fig.3.89** Global flow structures at  $\psi=10^\circ$ . (a)  $\lambda=0.72$ ; (b)  $\lambda=0.43$ .

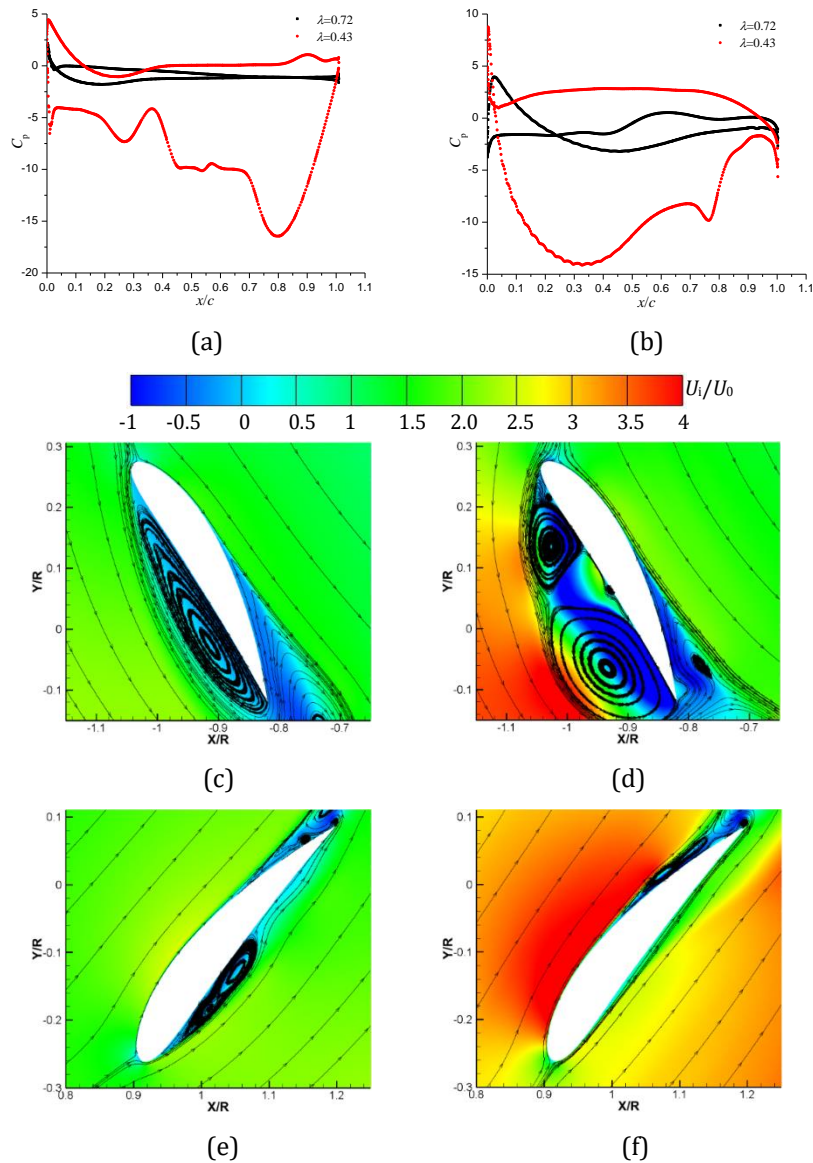


**Fig.3.90** Flow structures at  $\psi=10^\circ$ . (a) Pressure coefficients of blade A; (b) Pressure coefficients of blade B; (c) and (e)  $\lambda=0.72$ ; (d) and (f)  $\lambda=0.43$ .

### 3.4.5 Conclusions

(1) The symmetrical blade profiles, including NACA0012 and NACA0015, show a best performance in achieving the efficiency, due to the relatively moderate propulsive force and power. In contrary, the asymmetrical profile, such as NACA6415, has a worst performance, which is due to the high propulsive force and power. In addition, the inverse NACA2415 has a high potential to be optimized because it has a high efficiency at high  $Re$ .

(2) The flow field inside the cycloidal rotor presents that the vortical flows around NACA6415 are more complex, which is responsible for the large power consumption. Conversely, the flow structures over inverse NACA6415 are quite smooth, consuming the relatively low level of power.

(3) The Reynolds number also has great impact on the performance and flow structures. The cycloidal rotor obtains a low lift coefficient, but a high propulsive force coefficient at low  $Re$ . In most cases, only blade B is the main contributor to the production of large negative vertical force at low  $Re$ , due to the earlier flow separation. However, the propulsive force of the rotating system should refer to the components produced from two blades, because of the large variation of the performance for the single blade.

(4) The influence of  $\lambda$  is more obvious than that of  $Re$  because only the rotating speed is changed. Changing the rotating speed can significantly modify the stagnation point, leading to the totally different boundary layer flows at different  $\lambda$ . Normally, the difference of lift coefficient depends on blade B, while both two blades should take the responsibility to the difference of the propulsive force of the cycloidal rotor.

## 4 OVERALL SUMMARY AND PERSPECTIVES

This thesis focuses on the numerical analysis of the performance and unsteady vortical flows of a two-bladed cycloidal rotor and its optimization using the SST  $\gamma - \widetilde{Re}_{\theta t}$  transition model. This work mainly includes two parts: the first one is the validation of the transition model conducted on a single airfoil and the cycloidal rotor at two different  $\lambda$ , and the second one is the parametrical study on the cycloidal rotor, where the pitching kinematic, the chord-to-radius ratio, the pitch-pivot-point and the blade profile were varied for optimization purpose. The analysis of these important parameters is performed under different  $Re$  and  $\lambda$  conditions. The main conclusions of the thesis are listed as follows:

### 4.1 CALIBRATION AND VALIDATION OF THE SST $\gamma - \widetilde{Re}_{\theta t}$ MODEL

(1) For the single stationary airfoil, the results show primarily that the mesh resolution in the streamwise direction has a great impact on the transition. Increasing the turbulence intensity or the eddy viscosity ratio leads to the reduction of the laminar separation bubble (LSB) size, but the impact of the turbulence intensity is larger. The pressure gradient effect sometimes is not essential due to the numerical decay of the turbulence intensity imposed on the inlet section. Simultaneously, the correlations of  $F_{\text{length}}$  (controlling the transition length) and  $Re_{\theta c}$  (critical momentum thickness Reynolds number) have more or less impact on the transition. The influence of the parameter which controls the LSB size should be considered when using the transition model, which shows that the size of LSB decreases with the increase of this parameter. Comparisons between the SST  $k-\omega$  model, the Reynold Stress model (RSM), and the SST  $\gamma - \widetilde{Re}_{\theta t}$  transition model show that the latter has the capability to predict the boundary-layer flows. Then, the pressure distributions and mean velocity profiles at different incidences obtained by the computations agree well with the experiments before the reattachment, but it exhibits the large discrepancies in the fully turbulent boundary layer. What's more, with the increase of the Reynolds number, the size of LSB is reduced significantly, since the reattachment is very close to the transition point. Under very low  $Re$  condition, there exists a large-scale vortex structure attached to the surface and the transition is quite unclear.

(2) The unsteady vortical flows and laminar-turbulence transition of a two-bladed cycloidal rotor are investigated at two  $\lambda$ . The numerical results are compared with the existing numerical and experimental results, in terms of the global performance and detailed internal flow structures. Increasing  $\lambda$  can't change the transition location of the forces and power of the single blade, but the magnitudes of these variables have some changes. The transition of the vertical force is mainly at  $\psi=32^\circ$  and  $144^\circ$ , where the blade profile is almost perpendicular to the horizontal axis, while the propulsive force transition occurs at  $\psi=90^\circ$  and  $270^\circ$  when the blade geometry is parallel to the horizontal axis. Near the airfoil surface, the low-pressure and high-pressure zones near the blade leading edge due to the stagnation point deviation, the existence of the attached vortex, the massive flow separation and laminar-turbulence transition induced by the separation bubble, have great impact on the performance of the cycloidal rotor system and single blade. In addition, the blade-wake and wake-wake interactions has a strong effect on the external flow filed. The main difference of the lift coefficient is at  $\psi=30^\circ$  and  $90^\circ$  while it exists at  $\psi=30^\circ$  for the propulsive force coefficient, due to the force direction and blade loading of

the single blade. When analyzing the performance difference of the cycloidal rotor, the forces (lift and drag) acting on two blades and the blade loading of each blade are necessary. The transition induced by the separation bubble at two  $\lambda$  when the blade undergoes the advancing side are revealed. It concludes that SST TM is highly sensitive to the disturbances and has the capability to capture the evolution of transition, from the growing wave of the laminar boundary layer to the fully development of the separation bubble. However, the SST  $k-\omega$  model only resolves the turbulent flows after the formation of the separation bubble.

## 4.2 PARAMETRICAL STUDY AND OPTIMIZATION OF A CYCLOIDAL ROTOR

(1) The asymmetrical pitching kinematic with a small positive mean pitch angle results in the best performance regarding the efficiency of the cycloidal rotor, which results from the moderate propulsive force and low power. Conversely, although the symmetrical pitching with large amplitude and the asymmetrical pitching with large mean pitch angle generate a high propulsive force, the efficiency is quite low as a result of the complicated vortical flows leading to the higher power. Moreover, the asymmetrical pitching with a negative mean pitch angle produces the high lift coefficient with  $\lambda$ , but a decrease of the propulsive force coefficient. Generally, the performance of the single blade shows that the difference of the lift coefficient is mainly caused by blade B at advancing side, while it is induced by the two blades for the difference of the propulsive force coefficient. Near the airfoil surface, the flow structures are rich, including three vortex structures, roll-up vortices, flow separation vortex at the trailing edge, LSB, LEV and TEV, and the pattern of these vortices depends on the incidence importantly. When analyzing the forces on the single blade, it is interesting that when the blade undergoes the left side of the advancing side, the lift direction is opposite for the asymmetrical pitching with negative mean pitch angles compared with that in other cases, as a consequence of the stagnation point location caused by the different relative incidences.

(2) For given  $\lambda$  and  $Re$ , the cases with  $c/R=0.45$  for different blade chord lengths achieve the best efficiency. Then, at large  $c/R$ , the global flow structure is more complicated and the performance is strongly impacted, due to the small distance between two adjacent blades. When it comes to the influence of  $Re$  and  $\lambda$ , it seems that the effect of  $Re$  on the performance is very small. However, at low  $Re$ , the propulsive force is significantly different from the one obtained at relatively high  $Re$ . The advance coefficient  $\lambda$  has a large impact on the flow structures and the global performance, especially at low  $\lambda$ , which is due to the large variation of the relative velocity induced by the change of the rotating speed. It seems that at high  $\lambda$ , the wake at right side of the retreating side has a high risk in contacting with the blade, due to the low rotating speed. It is found that the cases with  $c/R=0.45$  at various  $Re$  or  $\lambda$  obtain the best efficiency. The flow structures inside a cycloidal rotor are extremely complex, including three vortex structures, roll-up vortices inside the boundary layer, LSB, flow separation vortex, wake-wake and blade-wake interactions, which depend on the operating conditions. In addition, except for the near-wall flow, the stagnation point location associated with the boundary layer development is very critical to the pressure difference of each blade. Both changing  $Re$  and  $\lambda$  can modify the direction of the relative velocity, but it is less influential for  $Re$ , because of the change of the inlet velocity and rotation speed at the same time.

(3) The case with  $x/c=0.25$  obtains the best performance. When the pitch-pivot-point moves towards the blade middle chord, though the propulsive force coefficient increases, the efficiency of the cycloidal rotor becomes worse because of the higher power that is consumed. Simultaneously, the lift coefficient has the largest magnitude as the pitching pivot is closer to the leading edge. For the case with a constant  $x/c$ , the efficiency of the rotating system increases with  $Re$ . At low  $Re$ , its effect can't be ignored, because the vortical flows around the blade surface appear earlier. Additionally, increasing  $Re$  leads to the change of pitching rate, further changing the position of stagnation point and the prediction of the pressure gradient, which has great impact on the boundary layer flows. The advance coefficient  $\lambda$  has greater impact on the performance, compared with  $Re$ . The forces and power coefficients decrease with the increase of  $\lambda$ . Similarly, as the pitch-pivot-point is located near the leading edge, the system would get a higher lift coefficient at high  $\lambda$ . In addition, the best efficiency based on the propulsive force coefficient is obtained at  $\lambda=0.48$  when the pitch-pivot-point is at  $x/c=0.25$ . Furthermore, increasing  $\lambda$  by decreasing the rotating speed would make the vortex flows develop fully.

(4) The symmetrical blade profiles, including NACA0012 and NACA0015, show a best performance in achieving the efficiency, due to the relatively moderate propulsive force and power. In contrary, the asymmetrical profile, such as NACA6415, has a worst performance, which is due to the high propulsive force and power. In addition, the inverse NACA2415 has a high potential to be optimized because it has a high efficiency at high  $Re$ . The flow field inside the cycloidal rotor presents that the vortical flows around NACA6415 are more complex, which is responsible for the large power consumption. Conversely, the flow structures over inverse NACA6415 are quite smooth, leading to the relatively low power.  $Re$  also has great impact on the performance and flow structures. The cycloidal rotor obtains a low lift coefficient, but a high propulsive force coefficient at low  $Re$ . In most cases, only blade B is the main contributor to the production of large negative vertical force at low  $Re$ , due to the earlier flow separation. However, the propulsive force of the rotating system should refer to the components of the lift and drag produced from two blades, because of the large variation of the performance for the single blade. The influence of  $\lambda$  is more obvious than that of  $Re$  because only the rotating speed is changed. Changing the rotating speed can significantly modify the stagnation point, leading to the totally different boundary layer flows at different  $\lambda$ . Normally, the difference of the lift coefficient depends on blade B, while both two blades should take the responsibility to the difference of the propulsive force of the cycloidal rotor.

### 4.3 PERSPECTIVES

In order to get a further better understanding of the flow physics inside such complex rotating configuration, some future works can still be carried out, which are proposed as follows:

(1) It shows that the blade would experience the retreating and advancing sides in a revolution, which results in the different vortical flows and blade loadings at these two positions. When the blade is located at retreating side, the sharp trailing edge becomes the leading edge, and the flow separation occurs more earlier, which is deserved to be investigated due to the more unsteady near-wall flows. Definitely, the laminar-turbulence transition also differs from that on the forward airfoil (blunt leading edge and sharp trailing edge).

(2) The 3D flows are also necessary to be performed, because the flows along the spanwise must be non-uniform. Of course, it believes that the 2D and 3D flows resolved by the transition model based on the original RANS method is quite similar. Consequently, the more advance turbulence models, such as improved delayed detached eddy simulation (IDDES) coupled with the transition model or large eddy simulation (LES) are considered.

(3) In the present work, the turbulent wakes are out of scope. The turbulent characteristics of the wakes and the wake momentum recovery under different working conditions are considered, which can help us understand the overall flow field of the cycloidal rotor comprehensively.

(4) If the cycloidal rotor is submitted to the underwater propulsive system, the occurrence of cavitation is inevitable because of the large variation of the incidence. Understanding the cavitation evolution and its influence on the overall performance under different conditions are also meaningful.

## REFERENCES

- [1] Wu, X., Zhang, X., Tian, X., Li, X., & Lu, W. (2020). A review on fluid dynamics of flapping foils. *Ocean Engineering*, 195, 106712 (1-30).
- [2] Roesler, B. T., Kawamura, M. L., Miller, E., Wilson, M., Brink-Roby, J., Clemmenson, E., Keller, M., & Epps, B. P. (2016). Experimental performance of a novel trochoidal propeller. *Journal of Ship Research*, 60(1), 48-60.
- [3] Lind, A. H., Jarugumilli, T., Benedict, M., Lakshminarayan, V. K., Jones, A. R., & Chopra, I. (2014). Flow field studies on a micro-air-vehicle-scale cycloidal rotor in forward flight. *Experiments in Fluids*, 55(12), 1826 (1-17).
- [4] Wauters, J., & Degroote, J. (2018). On the study of transitional low-Reynolds number flows over airfoils operating at high angles of attack and their prediction using transitional turbulence models. *Progress in Aerospace Sciences*, 103, 52-68.
- [5] Wang, S., Ingham, D. B., Ma, L., Pourkashanian, M., & Tao, Z. (2012). Turbulence modeling of deep dynamic stall at relatively low Reynolds number. *Journal of Fluids and Structures*, 33, 191-209.
- [6] Corke, T. C., & Thomas, F. O. (2015). Dynamic stall in pitching airfoils: aerodynamic damping and compressibility effects. *Annual Review of Fluid Mechanics*, 47, 479-505.
- [7] Carta, F. O. (1971). Effect of unsteady pressure gradient reduction on dynamic stall delay. *Journal of Aircraft*, 8(10), 839-841.
- [8] McLaren, K., Tullis, S., & Ziada, S. (2012). Measurement of high solidity vertical axis wind turbine aerodynamic loads under high vibration response conditions. *Journal of Fluids and Structures*, 32, 12-26.
- [9] Somers, D. M. (1997). Design and experimental results for the S809 airfoil. *National Renewable Energy Lab, Golden, CO (United States)*.
- [10] Yarusevych, S., Sullivan, P. E., & Kawall, J. G. (2009). On vortex shedding from an airfoil in low-Reynolds-number flows. *Journal of Fluid Mechanics*, 632, 245-271.
- [11] Burgmann, S., Dannemann, J., & Schröder, W. (2008). Time-resolved and volumetric PIV measurements of a transitional separation bubble on an SD7003 airfoil. *Experiments in Fluids*, 44(4), 609-622.
- [12] Boutilier, M. S., & Yarusevych, S. (2012). Separated shear layer transition over an airfoil at a low Reynolds number. *Physics of Fluids*, 24(8), 084105 (1-23).
- [13] Kirk, T. M., & Yarusevych, S. (2017). Vortex shedding within laminar separation bubbles forming over an airfoil. *Experiments in Fluids*, 58(5), 43 (1-17).
- [14] Koca, K., Genç, M. S., Açıkel, H. H., Çağdaş, M., & Bodur, T. M. (2018). Identification of flow phenomena over NACA 4412 wind turbine airfoil at low Reynolds numbers and role of laminar separation bubble on flow evolution. *Energy*, 144, 750-764.
- [15] Istvan, M. S., Kurelek, J. W., & Yarusevych, S. (2018). Turbulence intensity effects on laminar separation bubbles formed over an airfoil. *AIAA Journal*, 56(4), 1335-1347.
- [16] Istvan, M. S., & Yarusevych, S. (2018). Effects of free-stream turbulence intensity on transition in a laminar separation bubble formed over an airfoil. *Experiments in Fluids*, 59(3), 52 (1-21).
- [17] Roberts, S. K., & Yaras, M. I. (2006). Effects of surface-roughness geometry on separation-bubble transition. *Journal of Turbomachinery*, 128, 349-356.
- [18] Yarusevych, S., Kawall, J. G., & Sullivan, P. E. (2008). Separated-shear-layer development on an airfoil at low Reynolds numbers. *AIAA Journal*, 46(12), 3060-3069.
- [19] Ducoin, A., Astolfi, J. A., & Goert, M. L. (2012). An experimental study of boundary-layer transition induced vibrations on a hydrofoil. *Journal of Fluids and Structures*, 32, 37-51.

- [20] Delafin, P. L., Deniset, F., & Astolfi, J. A. (2014). Effect of the laminar separation bubble induced transition on the hydrodynamic performance of a hydrofoil. *European Journal of Mechanics-B/Fluids*, 46, 190-200.
- [21] Visbal, M. R., & Garman, D. J. (2018). Analysis of dynamic stall on a pitching airfoil using high-fidelity large-eddy simulations. *AIAA Journal*, 46-63.
- [22] Guillaud, N., Balarac, G., & Goncalvès, E. (2018). Large Eddy Simulations on a pitching airfoil: Analysis of the reduced frequency influence. *Computers & Fluids*, 161, 1-13.
- [23] Benton, S. I., & Visbal, M. R. (2019). The onset of dynamic stall at a high, transitional Reynolds number. *Journal of Fluid Mechanics*, 861, 860-885.
- [24] Wilcox, D. C. (1994). Simulation of transition with a two-equation turbulence model. *AIAA Journal*, 32(2), 247-255.
- [25] Walters, D. K., & Leylek, J. H. (2004). A new model for boundary layer transition using a single-point RANS approach. *Journal of Turbomachinery*, 126(1), 193-202.
- [26] Menter, F. R., Langtry, R., & Völker, S. (2006). Transition modelling for general purpose CFD codes. *Flow, Turbulence and Combustion*, 77(1-4), 277-303.
- [27] Menter, F. R., Langtry, R. B., Likki, S. R., Suzen, Y. B., Huang, P. G., & Völker, S. (2006). A correlation-based transition model using local variables—part I: model formulation. *Journal of Turbomachinery*, 128, 413-422.
- [28] Langtry, R. B., Menter, F. R., Likki, S. R., Suzen, Y. B., Huang, P. G., & Völker, S. (2006). A correlation-based transition model using local variables—part II: test cases and industrial applications. *Journal of Turbomachinery*, 128, 423-434.
- [29] Menter, F. R., Smirnov, P. E., Liu, T., & Avancha, R. (2015). A one-equation local correlation-based transition model. *Flow, Turbulence and Combustion*, 95(4), 583-619.
- [30] Schmidt, R. C., & Patankar, S. V. (1991). Simulating boundary layer transition with low-Reynolds-number  $k-\epsilon$  turbulence models: part 1—an evaluation of prediction characteristics. *Journal of Turbomachinery*, 113(1), 10-17.
- [31] Schmidt, R. C., & Patankar, S. V. (1991). Simulating boundary layer transition with low-Reynolds-number  $k-\epsilon$  turbulence models: Part 2—an approach to improving the predictions. *Journal of Turbomachinery*, 113(1), 18-26.
- [32] Biswas, D., & Fukuyama, Y. (1994). Calculation of transitional boundary layers with an improved low-Reynolds-number version of the  $k-\epsilon$  turbulence model. *Journal of Turbomachinery*, 116(4), 765-773.
- [33] Tseng, C. C., & Cheng, Y. E. (2015). Numerical investigations of the vortex interactions for a flow over a pitching foil at different stages. *Journal of Fluids and Structures*, 58, 291-318.
- [34] Tseng, C. C., & Hu, H. A. (2016). Flow dynamics of a pitching foil by Eulerian and Lagrangian viewpoints. *AIAA Journal*, 54(2), 712-727.
- [35] Lanzafame, R., Mauro, S., & Messina, M. (2013). Wind turbine CFD modeling using a correlation-based transitional model. *Renewable Energy*, 52, 31-39.
- [36] Baltazar, J., Rijpkema, D., & de Campos, J. F. (2018). On the use of the  $\gamma - \widetilde{Re}_\theta$  transition model for the prediction of the propeller performance at model-scale. *Ocean Engineering*, 170, 6-19.
- [37] Moran-Guerrero, A., Gonzalez-Gutierrez, L. M., Oliva-Remola, A., & Diaz-Ojeda, H. R. (2018). On the influence of transition modeling and crossflow effects on open water propeller simulations. *Ocean Engineering*, 156, 101-119.
- [38] Dong, H., Xia, T., Chen, L., Liu, S., Cui, Y. D., Khoo, B. C., & Zhao, A. (2019). Study on flow separation and transition of the airfoil in low Reynolds number. *Physics of Fluids*, 31(10), 103601 (1-9).

- [39] Wang, R., & Xiao, Z. (2020). Transition effects on flow characteristics around a static two-dimensional airfoil. *Physics of Fluids*, 32(3), 035113 (1-14).
- [40] Bartl, J., Sagmo, K. F., Bracchi, T., & Sætran, L. (2019). Performance of the NREL S826 airfoil at low to moderate Reynolds numbers—A reference experiment for CFD models. *European Journal of Mechanics-B/Fluids*, 75, 180-192.
- [41] Ducoin, A., Astolfi, J. A., Deniset, F., & Sigrist, J. F. (2009). Computational and experimental investigation of flow over a transient pitching hydrofoil. *European Journal of Mechanics-B/Fluids*, 28(6), 728-743.
- [42] Karbasian, H. R., & Kim, K. C. (2016). Numerical investigations on flow structure and behavior of vortices in the dynamic stall of an oscillating pitching hydrofoil. *Ocean Engineering*, 127, 200-211.
- [43] Zhang, M., Wu, Q., Wang, G., Huang, B., Fu, X., & Chen, J. (2020). The flow regime and hydrodynamic performance for a pitching hydrofoil. *Renewable Energy*, 150, 412-427.
- [44] Huang, B., Ducoin, A., & Young, Y. L. (2013). Physical and numerical investigation of cavitating flows around a pitching hydrofoil. *Physics of Fluids*, 25(10), 102109 (1-27).
- [45] Martinat, G., Braza, M., Hoarau, Y., & Harran, G. (2008). Turbulence modelling of the flow past a pitching NACA0012 airfoil at  $10^5$  and  $10^6$  Reynolds numbers. *Journal of Fluids and Structures*, 24(8), 1294-1303.
- [46] Singh, K., & Páscoa, J. C. (2019). Numerical modeling of stall and poststall events of a single pitching blade of a cycloidal rotor. *Journal of Fluids Engineering*, 141(1), 011103 (1-16).
- [47] Malan, P., Suluksna, K., & Juntasaro, E. (2009). Calibrating the  $\gamma - \widetilde{Re}_\theta$  transition model for commercial CFD. In *47th AIAA aerospace sciences meeting including the new horizons forum and aerospace exposition, Orlando, Florida*, 1142, 1-20.
- [48] Wang, Y., Zhang, Y., Li, S., & Meng, D. (2015). Calibration of a  $\gamma - \widetilde{Re}_\theta$  transition model and its validation in low-speed flows with high-order numerical method. *Chinese Journal of Aeronautics*, 28(3), 704-711.
- [49] Jing, F., Sheng, Q., & Zhang, L. (2014). Experimental research on tidal current vertical axis turbine with variable-pitch blades. *Ocean Engineering*, 88, 228-241.
- [50] Mueller, H. F. (1955). Recent developments in the design and application of the vertical axis propeller. *Transactions of the society of naval architects and marine engineers*, 63, 4-30.
- [51] Nakonechny, B. (2010). Experimental performance of a six-bladed vertical axis propeller. *Technical report 1446, Bethesda, MD: Department of the Navy, David Taylor Model Basin*.
- [52] Benedict, M., Ramasamy, M., & Chopra, I. (2010). Improving the aerodynamic performance of micro-air-vehicle-scale cycloidal rotor: an experimental approach. *Journal of Aircraft*, 47(4), 1117-1125.
- [53] Benedict, M., Ramasamy, M., Chopra, I., & Leishman, J. G. (2010). Performance of a cycloidal rotor concept for micro air vehicle applications. *Journal of the American Helicopter Society*, 55(2), 22002 (1-14).
- [54] Chen, B., Su, S., Viola, I. M., & Greated, C. A. (2018). Numerical investigation of vertical-axis tidal turbines with sinusoidal pitching blades. *Ocean Engineering*, 155, 75-87.
- [55] Chen, B., Cheng, S., Su, T. C., & Zhang, H. (2018). Numerical investigation of channel effects on a vertical-axis tidal turbine rotating at variable speed. *Ocean Engineering*, 163, 358-368.
- [56] Paillard, B., Astolfi, J. A., & Hauville, F. (2015). URANSE simulation of an active variable-pitch cross-flow Darrieus tidal turbine: Sinusoidal pitch function investigation. *International Journal of Marine Energy*, 11, 9-26.

- [57] McNaughton, J., Billard, F., & Revell, A. (2014). Turbulence modelling of low Reynolds number flow effects around a vertical axis turbine at a range of tip-speed ratios. *Journal of Fluids and Structures*, 47, 124-138.
- [58] Almohammadi, K. M., Ingham, D. B., Ma, L., & Pourkashanian, M. (2015). Modeling dynamic stall of a straight blade vertical axis wind turbine. *Journal of Fluids and Structures*, 57, 144-158.
- [59] Maeda, T., Kamada, Y., Hiromori, Y., Nakai, A., & Kasuya, T. (2017). Study on stall behavior of a straight-bladed vertical axis wind turbine with numerical and experimental investigations. *Journal of Wind Engineering and Industrial Aerodynamics*, 164, 1-12.
- [60] Rezaeiha, A., Montazeri, H., & Blocken, B. (2019). On the accuracy of turbulence models for CFD simulations of vertical axis wind turbines. *Energy*, 180, 838-857.
- [61] Marsh, P., Ranmuthugala, D., Penesis, I., & Thomas, G. (2017). The influence of turbulence model and two and three-dimensional domain selection on the simulated performance characteristics of vertical axis tidal turbines. *Renewable Energy*, 105, 106-116.
- [62] Yu, H., Lang, Z. H., & Qi, W. G. (2018). Two-dimensional and three-dimensional numerical simulations of cycloidal propellers in hover. *Proceedings of the Institution of Mechanical Engineers, Part G: Journal of Aerospace Engineering*, 232(7), 1223-1234.
- [63] Tang, J., Hu, Y., Song, B., & Yang, H. (2018). An unsteady free wake model for aerodynamic performance of cycloidal propellers. *Proceedings of the Institution of Mechanical Engineers, Part G: Journal of Aerospace Engineering*, 232(2), 290-307.
- [64] Wang, Y., Shen, S., Li, G., Huang, D., & Zheng, Z. (2018). Investigation on aerodynamic performance of vertical axis wind turbine with different series airfoil shapes. *Renewable Energy*, 126, 801-818.
- [65] Subramanian, A., Yogesh, S. A., Sivanandan, H., Giri, A., Vasudevan, M., Mugundhan, V., & Velamati, R. K. (2017). Effect of airfoil and solidity on performance of small scale vertical axis wind turbine using three dimensional CFD model. *Energy*, 133, 179-190.
- [66] Baghdadi, M., Elkoush, S., Akle, B., & Elkhoury, M. (2020). Dynamic shape optimization of a vertical-axis wind turbine via blade morphing technique. *Renewable Energy*, 154, 239-251.
- [67] Ismail, M. F., & Vijayaraghavan, K. (2015). The effects of aerofoil profile modification on a vertical axis wind turbine performance. *Energy*, 80, 20-31.
- [68] Tang, J., Hu, Y., Song, B., & Yang, H. (2017). Unsteady aerodynamic optimization of airfoil for cycloidal propellers based on surrogate model. *Journal of Aircraft*, 54(4), 1241-1256.
- [69] Tirandaz, M. R., & Rezaeiha, A. (2021). Effect of airfoil shape on power performance of vertical axis wind turbines in dynamic stall: symmetric airfoils. *Renewable Energy*, 173, 422-441.
- [70] Eboibi, O., Danao, L. A. M., & Howell, R. J. (2016). Experimental investigation of the influence of solidity on the performance and flow field aerodynamics of vertical axis wind turbines at low Reynolds numbers. *Renewable Energy*, 92, 474-483.
- [71] Rezaeiha, A., Montazeri, H., & Blocken, B. (2018). Towards optimal aerodynamic design of vertical axis wind turbines: Impact of solidity and number of blades. *Energy*, 165, 1129-1148.
- [72] Sagharichi, A., Zamani, M., & Ghasemi, A. (2018). Effect of solidity on the performance of variable-pitch vertical axis wind turbine. *Energy*, 161, 753-775.
- [73] Chen, B., Nagata, S., Murakami, T., & Ning, D. (2019). Improvement of sinusoidal pitch for vertical-axis hydrokinetic turbines and influence of rotational inertia. *Ocean Engineering*, 179, 273-284.

- [74] Benedict, M., Jarugumilli, T., & Chopra, I. (2016). Effects of Asymmetric Blade-Pitching Kinematics on Forward-Flight Performance of a Micro-Air-Vehicle-Scale Cycloidal-Rotor. *Journal of Aircraft*, 53(5), 1568-1573.
- [75] Walther, C. M., Saemi, F., Benedict, M., & Lakshminarayan, V. (2019). Symmetric Versus Asymmetric Pitching of a Cycloidal Rotor Blade at Ultra-Low Reynolds Numbers. *Journal of Aircraft*, 56(3), 1179-1199.
- [76] Benedict, M., Jarugumilli, T., Lakshminarayan, V., & Chopra, I. (2014). Effect of flow curvature on forward flight performance of a micro-air-vehicle-scale cycloidal-rotor. *AIAA Journal*, 52(6), 1159-1169.
- [77] Benedict, M., Jarugumilli, T., & Chopra, I. (2013). Effect of rotor geometry and blade kinematics on cycloidal rotor hover performance. *Journal of Aircraft*, 50(5), 1340-1352.
- [78] Xisto, C. M., Páscoa, J. C., & Trancossi, M. (2016). Geometrical parameters influencing the aerodynamic efficiency of a small-scale self-pitch high-solidity VAWT. *Journal of Solar Energy Engineering*, 138(3), 031006 (1-8).
- [79] Jarugumilli, T., Benedict, M., & Chopra, I. (2011). Experimental optimization and performance analysis of a MAV scale cycloidal rotor. In *49th AIAA Aerospace Sciences Meeting including the New Horizons Forum and Aerospace Exposition, Orlando, Florida*, 821, 1-11.
- [80] Menter, F. R., Kuntz, M., & Langtry, R. (2003). Ten years of industrial experience with the SST turbulence model. *Turbulence, Heat and Mass Transfer*, 4(1), 625-632.
- [81] Breuer, M. (2018). Effect of inflow turbulence on an airfoil flow with laminar separation bubble: An LES study. *Flow, Turbulence and Combustion*, 101(2), 433-456.
- [82] Abu-Ghannam, B. J., & Shaw, R. (1980). Natural transition of boundary layers—the effects of turbulence, pressure gradient, and flow history. *Journal of Mechanical Engineering Science*, 22(5), 213-228.
- [83] Langtry, R. B. (2006). A correlation-based transition model using local variables for unstructured parallelized CFD codes. *PhD Thesis*, <http://dx.doi.org/10.18419/opus-1705>
- [84] Suluksna, K., Dechaumphai, P., & Juntasaro, E. (2009). Correlations for modeling transitional boundary layers under influences of freestream turbulence and pressure gradient. *International Journal of Heat and Fluid Flow*, 30(1), 66-75.
- [85] Winslow, J., Otsuka, H., Govindarajan, B., & Chopra, I. (2018). Basic understanding of airfoil characteristics at low Reynolds numbers ( $10^4$ - $10^5$ ). *Journal of Aircraft*, 55(3), 1050-1061.
- [86] Jarugumilli, T. (2013). An experimental investigation of a micro air vehicle-scale cycloidal rotor in forward flight. *Master of science*, URI: <http://hdl.handle.net/1903/14822>.
- [87] Langtry, R. B., Menter, F. R., Likki, S. R., Suzen, Y. B., Huang, P. G., & Vo'lker, S. (2004). A correlation-based transition model using local variables: Part II—test cases and industrial applications. *ASME-GT2004-53454, ASME TURBO EXPO 2004, Vienna, Austria*.
- [88] Gauthier, E., Kinsey, T., & Dumas, G. (2016). Impact of blockage on the hydrodynamic performance of oscillating-foils hydrokinetic turbines. *Journal of Fluids Engineering*, 138(9), 091103 (1-13).
- [89] Kinsey, T., & Dumas, G. (2012). Computational fluid dynamics analysis of a hydrokinetic turbine based on oscillating hydrofoils. *Journal of Fluids Engineering*, 134(2), 021104 (1-16).
- [90] Negi, P. S., Vinuesa, R., Hanifi, A., Schlatter, P., & Henningson, D. S. (2018). Unsteady aerodynamic effects in small-amplitude pitch oscillations of an airfoil. *International Journal of Heat and Fluid Flow*, 71, 378-391.

- [91] Pascazio, M., Autric, J., Favier, D., & Maresca, C. (1996). Unsteady boundary-layer measurement on oscillating airfoils-Transition and separation phenomena in pitching motion. In *34th Aerospace Sciences Meeting and Exhibit* (p.35).
- [92] Choudhuri, P. G., & Knight, D. D. (1996). Effects of compressibility, pitch rate, and Reynolds number on unsteady incipient leading-edge boundary layer separation over a pitching airfoil. *Journal of Fluid Mechanics*, 308, 195-217.
- [93] Kim, D. H., Chang, J. W., & Sohn, M. H. (2017). Unsteady aerodynamic characteristics depending on reduced frequency for a pitching NACA0012 airfoil at  $Re_c=2.3\times 10^4$ . *International Journal of Aeronautical and Space Sciences*, 18(1), 8-16.
- [94] Yilmaz, T., Ol, M., & Rockwell, D. (2010). Scaling of flow separation on a pitching low aspect ratio plate. *Journal of Fluids and Structures*, 26(6), 1034-1041.
- [95] Visbal, M. R., & Shang, J. S. (1989). Investigation of the flow structure around a rapidly pitching airfoil. *AIAA Journal*, 27(8), 1044-1051.
- [96] Tian, W., Bodling, A., Liu, H., Wu, J. C., He, G., & Hu, H. (2016). An experimental study of the effects of pitch-pivot-point location on the propulsion performance of a pitching airfoil. *Journal of Fluids and Structures*, 60, 130-142.
- [97] Li, X., Feng, L. H., & Li, Z. Y. (2019). Flow mechanism for the effect of pivot point on the aerodynamic characteristics of a pitching airfoil and its manipulation. *Physics of Fluids*, 31(8), 087108 (1-9).
- [98] Zhang, T., Wang, Z., Huang, W., Ingham, D., Ma, L., & Pourkashanian, M. (2020). A numerical study on choosing the best configuration of the blade for vertical axis wind turbines. *Journal of Wind Engineering and Industrial Aerodynamics*, 201, 104162 (1-12).
- [99] Jafaryar, M., Kamrani, R., Gorji-Bandpy, M., Hatami, M., & Ganji, D. D. (2016). Numerical optimization of the asymmetric blades mounted on a vertical axis cross-flow wind turbine. *International Communications in Heat and Mass Transfer*, 70, 93-104.

## FRENCH EXTENDED SUMMARY

Les ailes oscillantes à cinématique complexe sont largement utilisées dans de nombreuses applications techniques, telles que les éoliennes à axe vertical (VAWT), les systèmes de propulsion sous-marine, les équipements d'extraction d'énergie marine et les micro-véhicules aériens (MAV). Comme le montre la figure 1.1, le mode de mouvement des ailes oscillantes peut être classé en trois catégories : plongée (ou soulèvement), tangage et battement (combinaison des mouvements de soulèvement et de tangage). Le mouvement de tangage est une cinématique relativement simple selon laquelle les profils tournent autour d'un pivot le long de la corde dans une plage d'incidence limitée. Dans le processus d'oscillation, l'incidence du profil varie continuellement, ce qui modifie considérablement la charge de la pale et les organisations de l'écoulement sur les surfaces. À faible incidence, l'écoulement est fixé sur la surface du film et la transition laminaire-turbulence est le principal facteur de modification des variables près de la paroi. Avec l'augmentation de l'angle d'attaque, l'écoulement commence à se séparer de la surface et à générer des lâchers de tourbillons dans les sillages, ce qui entraîne l'apparition du décrochage.

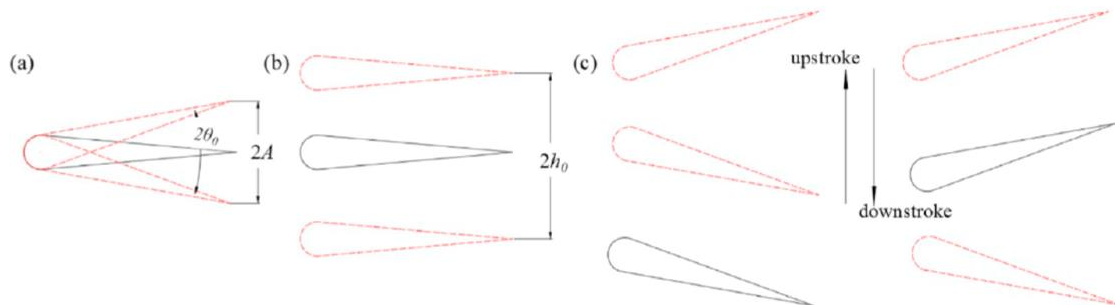


**Fig.1.1** Croquis de (a) mouvement de tangage, (b) mouvement de soulèvement et (c) mouvement de battement [1].

En tant que nouveau système de propulsion de type nouveau, le rotor cycloïdal, qui se compose de plusieurs pales verticales ou horizontales, a suscité beaucoup d'attention récemment. La figure 1.2 présente les applications de l'hélice cycloïdale aux navires de grande taille et aux systèmes d'aéronefs sans pilote. Le principe principal de l'oscillation est que la pale ne tourne pas seulement autour du centre du rotor, mais a également un mouvement de tangage basé sur le point de pivot de tangage. Ce type d'hélice peut produire une large gamme de poussée et de forces latérales par les variations de la portance et de la traînée des pales.



**Fig.1.2** Application de l'hélice cycloïdale. (a) Navire de grande taille ; (b) Avion sans pilote.

Lorsque le coefficient d'avance absolu  $\lambda$ , donné par le rapport  $\lambda = V_s / \omega R$  (où  $V_s$  est la vitesse de l'écoulement principal,  $\omega$  est la vitesse de rotation et  $R$  est le rayon de rotation) est plus petit que 1, l'hélice est appelée hélice cycloïdale (dispositif à pas faible), tandis que dans les autres cas, il s'agit d'une hélice trochoïdale (dispositif à pas élevé). La figure 1.3a montre le schéma représentant l'angle de pale pour une nouvelle hélice trochoïdale conçue avec un mouvement de tangage sinusoïdal [2]. Les fonctions de commande de pas sinusoïdal pour les dispositifs à pas faible et à pas élevé sont données par les équations 1.1 et 1.2 (où  $\beta$  est l'angle de pas relatif,  $\beta_{abs}$  est l'angle de pas absolu,  $\alpha$  est l'amplitude de tangage,  $\Phi$  est l'angle azimutal et  $\Phi_p$  est l'angle de phase). Le mouvement des pales et la définition du système de coordonnées sont représentés sur la figure 1.3b pour un rotor cycloïdal appliqué au MAV [3]. Le rotor cycloïdal à deux pales avec un pas sinusoïdal des pales peut produire une force propulsive en continu en vol avant, en modifiant l'incidence, c'est-à-dire l'angle entre la ligne de corde des pales et la direction tangentielle de la trajectoire de rotation. L'angle relatif de la pale  $\theta_A$  est fonction de l'angle azimutal  $\psi$  et peut être exprimé par la fonction sinusoïdale donnée par l'équation 1.3 (où  $\theta_{amp}$  est l'amplitude du tangage et  $\phi$  est l'angle de phase).

$$\beta = -\alpha \sin(\Phi + \Phi_p) \quad \lambda < 1 \quad (1.1)$$

$$\beta_{abs} = -\alpha \sin(\Phi + \Phi_p) \quad \lambda > 1 \quad (1.2)$$

$$\theta_A = \theta_{amp} \sin(\psi + \phi) \quad (1.3)$$

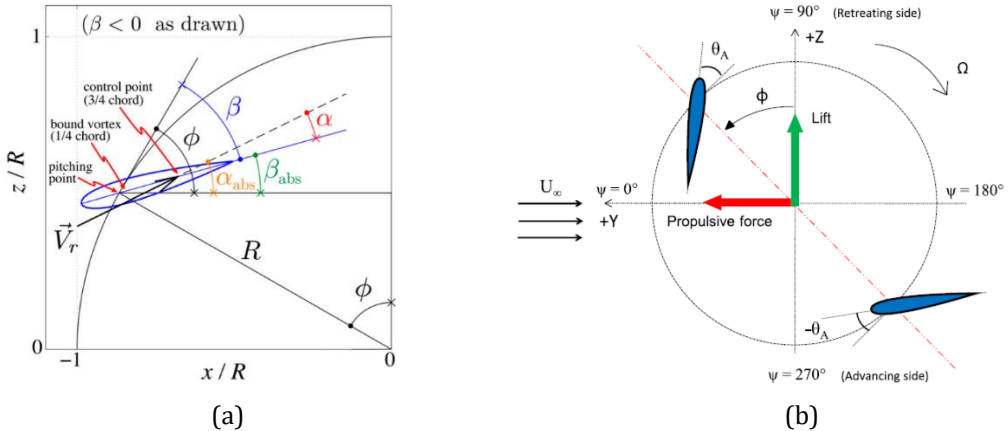


**Fig.1.3** Esquisse du mouvement de l'aile. (a) Définition de l'angle de la pale ; (b) Système de coordonnées.

Le début et l'étendue de la transition laminaire-turbulence sont d'une importance majeure dans de nombreux dispositifs d'ingénierie, allant du simple profil d'aile en air ou en eau aux turbomachines aux configurations complexes. Aujourd'hui, deux principaux types de transition ont été particulièrement étudiés. Le premier est la transition de contournement, largement répandue dans les compresseurs et les turbines avec un niveau de turbulence élevé dans le flux libre (généralement environ 5% à 10%), dans laquelle les ondes de Tollmien-Schlichting (TS) sont complètement contournées et les tâches turbulentées sont directement produites dans la couche limite induite par la turbulence du flux libre. L'autre mécanisme de transition est la transition induite par la séparation, où la couche limite laminaire sur les pales se sépare, en raison du gradient de pression défavorable, et la transition se développe au sein de la couche de cisaillement séparée. Si la couche de cisaillement séparée se rattache au côté aspiration, une région de

recirculation appelée bulle de séparation laminaire (LSB) est créée. Dans le cas contraire, si la couche de cisaillement séparée ne se rattache pas, une région de recirculation ouverte comprenant des tourbillons de différentes tailles se forme. Le mécanisme de génération de la LSB est décrit dans la figure 1.4a [4].

Le décrochage dynamique désigne le phénomène impliquant une grande quantité de séparations et de rattachements de l'écoulement qui se produisent sur un profil, ou toute autre surface portante, lorsqu'il est soumis à un mouvement rapide et instable tel que des mouvements de tangage, de plongée, de battement et de translation verticale dans l'écoulement du fluide, avec une incidence maximale supérieure à l'angle de décrochage statique normal [5]. Le décrochage dynamique typique peut être divisé en quatre étapes clés successives pendant les processus de montée et de descente : l'écoulement attaché à faible incidence, le développement d'un tourbillon de bord d'attaque (LEV), le délestage du LEV causant le décrochage complet et le rattachement des écoulements. La figure 1.4b montre la naissance et le développement du LEV, du tourbillon de bord d'attaque (TEV) et d'autres tourbillons sur le côté aspiration d'un profil de tangage. Lorsque le profil a un mouvement oscillant, on observe que la portance augmente jusqu'au décrochage dynamique profond, qui se produit lorsque l'incidence maximale dépasse l'angle d'attaque de décrochage du profil stable. Ce phénomène peut être attribué à deux mécanismes : (a) un retard dans la séparation de l'écoulement de la couche limite ; (b) la génération d'une bulle de séparation fermée près du bord d'attaque de la feuille. Deux raisons expliquent le retard dans la séparation de la couche limite : (a) une augmentation de la cambrure effective qui est prédite par la théorie des profils minces ; (b) l'accélération de la couche limite due à l'effet Magnus produit par le mouvement du bord d'attaque, comme le montre la référence [6]. Carta [7] a rapporté analytiquement que le gradient de pression négative sur le côté aspiration d'un profil en tangage est plus faible que dans le cas d'un profil stationnaire, et qu'il est encore plus réduit lorsque le taux de tangage augmente. Le décrochage dynamique a un impact important sur les performances de nombreux dispositifs de conversion d'énergie, tels que les éoliennes à axe horizontal (HAWT) et les VAWT. En outre, en plus de ces effets néfastes sur les performances, le décrochage dynamique est également une source importante de vibrations structurelles pertinentes pour la fatigue de l'éolienne [8].

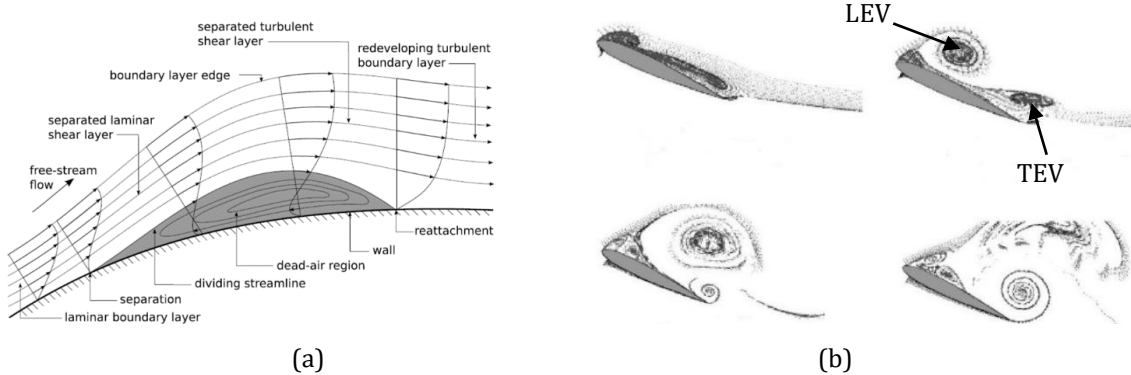


**Fig.1.4** Esquisse de la transition et du décrochage dynamique. (a) Mécanisme de génération de LSB ; (b) Tourbillons typiques du décrochage dynamique.

Les études de la transition laminaire-turbulence et du décrochage dynamique pour les profils aérodynamiques ou hydrodynamiques simples sont largement réalisées en utilisant des approches expérimentales et numériques. À une incidence relativement faible, l'apparition de la transition basée sur la séparation, la transition et le rattachement de la couche de cisaillement est le principal mécanisme. Ensuite, avec l'augmentation de

l'angle d'attaque, le LSB se déplace progressivement vers le bord d'attaque. En augmentant encore l'incidence, près de la condition de décrochage, le LSB est presque situé près du bord d'attaque et une région de recirculation ouverte est générée après le point de séparation de l'écoulement. Il est nécessaire de comprendre les mécanismes de transition et de décrochage dynamique afin de fournir des directives pour contrôler ces événements nuisibles.

La mesure expérimentale est un moyen direct et efficace d'obtenir des informations riches sur le LSB et le délestage tourbillonnaire sur la surface portante. Les techniques de vélocimétrie par images de particules (PIV) et de fil de fumée sont utilisées pour visualiser et caractériser les structures de l'écoulement, tandis que les prises de pression directement sur la surface de l'aile fournissent des mesures de la pression statique moyenne. En outre, les profils de vitesse à l'intérieur de la couche limite peuvent être mesurés à l'aide de sondes à fil chaud. Plus spécifiquement, plusieurs travaux expérimentaux ont contribué à l'étude du processus de transition au cours des 20 dernières années : Somers [9] a effectué des mesures des coefficients de portance et de traînée ainsi que des distributions de pression sur un nouveau profil aérodynamique, afin de concevoir un profil à portance élevée et à faible traînée pour les applications des éoliennes, et les résultats montrent un bon résultat. En outre, Yarusevych et al. [10] ont étudié l'effet de la couche de cisaillement séparée sur les caractéristiques des structures cohérentes pour les écoulements à faible nombre de Reynolds, et deux régimes d'écoulement communs ont été identifiés : l'un est la formation de bulles de séparation et l'autre est la séparation de la couche limite sans rattachement. On observe également que la fréquence fondamentale des tourbillons de la couche de cisaillement présente une dépendance de type loi de puissance par rapport au nombre de Reynolds pour les deux régimes d'écoulement, tandis que la fréquence du délestage des tourbillons de sillage est corrélée linéairement avec le nombre de Reynolds. De plus, à l'aide d'une PIV à résolution temporelle et d'un dispositif de PIV à balayage stéréo, Burgmann et al. [11] ont découvert que la dynamique temporelle et spatiale de l'enroulement des tourbillons est induite par l'instabilité de Kelvin-Helmholtz (K-H). Récemment, Boutilier et Yarusevych [12] ont combiné la visualisation de l'écoulement, la mesure par fil chaud, le test de pression de surface et l'analyse de stabilité pour clarifier le mécanisme de développement des perturbations dans la couche de cisaillement par la prévision du taux de croissance des perturbations, les spectres du nombre d'ondes des perturbations et la vitesse de convection. En outre, Kirk et Yarusevych [13] ont donné un nouvel aperçu du développement des structures cohérentes dans les bulles de séparation et de leurs relations avec la dynamique globale des bulles et la topologie moyenne des bulles. Il est bien connu que certains paramètres ont un grand impact sur le processus de transition, qui doit être analysé en détail afin de caractériser les conséquences négatives pour de tels flux. Koca et al. [14] ont montré que la longueur des LSB s'allonge lorsque l'incidence augmente, ce qui entraîne une fréquence plus faible du délestage tourbillonnaire. De même, avec l'augmentation du nombre de Reynolds, le LSB devient plus court et son emplacement est beaucoup plus proche du bord d'attaque. En ce qui concerne l'influence de la turbulence du flux d'entrée, Istvan et al. [15] et Istvan et Yarusevych [16] ont démontré que la longueur des bulles est réduite en raison de la séparation retardée et du rattachement avancé lorsque l'intensité de la turbulence du flux d'entrée augmente. Simultanément, il est également observé qu'un niveau de turbulence plus élevé peut conduire à l'augmentation de la portance et retarder le décrochage dans des conditions de pré-décrochage. En ce qui concerne l'effet de la rugosité de surface sur la transition de la bulle de séparation, Roberts et Yaras [17] ont observé que l'augmentation de la hauteur

de la rugosité, l'espacement des éléments de rugosité et une forme de rugosité avec une asymétrie négative peuvent favoriser le début plus précoce de la transition, et la hauteur de la rugosité est le paramètre le plus influent. Bien que les mesures expérimentales aient déjà permis d'obtenir des informations détaillées sur les structures d'écoulement près de la paroi, elles comportent encore des incertitudes importantes, en raison de la perturbation due aux éléments extérieurs. Yarusevych et al. [18] ont constaté que les sondes conventionnelles à fil chaud ne peuvent pas capturer l'écoulement inverse dans la région séparée et surestiment également les vitesses en raison des pertes thermiques supplémentaires. Par conséquent, Ducoin et al. [19] ont appliqué le système de velocimétrie Doppler laser (LDV) pour obtenir les profils de vitesse moyenne autour de l'hydroptère à une incidence de 2°, ce qui est validé par les simulations numériques [20], même pour la prédiction de la vitesse négative dans le sens du courant dans la région de séparation de l'écoulement.

En complément de ces travaux expérimentaux, la dynamique des fluides numérique (CFD), basée principalement sur la méthodologie RANS (Reynolds Averaged Navier-Stokes), mais aussi sur la simulation des grands tourbillons (LES), peut permettre de mieux comprendre les écoulements transitoires et les caractéristiques dynamiques de décrochage pour les profils aérodynamiques/hydrodynamiques statiques ou oscillants. Lorsqu'un profil a un mouvement d'oscillation, l'apparition du phénomène de décrochage est beaucoup plus tardive que dans un cas stationnaire, en raison de l'existence du vortex de bord d'attaque (LEV), qui peut maintenir la haute performance pendant une période plus longue. Visbal et Garman [21] ont accordé une grande attention à la génération et au développement du tourbillon de décrochage dynamique avec le changement d'incidence. Ensuite, Guillaud et al. [22] ont constaté que la séparation de la couche limite et la fréquence d'éjection du LEV sont retardées à haute incidence lorsque la fréquence réduite augmente, ce qui indique que la durée de vie du LEV du côté de l'aspiration diminue de manière significative. De plus, Benton et Visbal [23] ont étudié le processus de décrochage dynamique en utilisant la méthodologie LES pour les écoulements à nombre de Reynolds élevé, en mettant l'accent sur la sensibilité au nombre de Reynolds.

Les modèles de turbulence basés sur la méthode RANS sont toujours le premier choix pour la plupart des écoulements techniques en raison de leurs faibles exigences en matière de ressources de calcul et de leur précision acceptable. Cependant, ils ne résolvent que les écoulements entièrement turbulents et doivent être modifiés lorsque l'effet de transition est pris en compte. Comme l'ont signalé Wauters et Degroote [4], il existe principalement quatre modèles de transition basés sur la RANS, à savoir le transport de contrainte de cisaillement (SST)  $k-\omega$  avec correction de faible Re [24],  $k-k_l-\omega$  [25], SST  $k-\omega \gamma - \tilde{R}e_{\theta t}$  [26-28] et SST  $k-\omega \gamma$  [29]. Les avantages et inconvénients de chaque modèle sont discutés dans les références associées. Les modèles de turbulence à faible nombre de Reynolds, qui sont souvent utilisés pour prédire la transition technique, sont basés sur les fonctions d'amortissement de paroi des modèles de turbulence sous-jacents, pour déclencher le début de la transition. Un progrès significatif qui a également été fait par ce type de concept attrayant. Schmidt et Patankar [30-31] ont d'abord proposé un modèle de turbulence  $k-\varepsilon$  à faible nombre de Reynolds pour prédire la transition dans les écoulements de la couche limite externe soumis à la turbulence du flux libre, puis ils ont modifié ce modèle en limitant le terme de production dans l'équation de l'énergie cinétique de la turbulence, en utilisant un critère de stabilité simple et la corrélation avec le niveau de turbulence du flux libre. Ensuite, Biswas et Fukutama [32] ont apporté quelques modifications aux modèles  $k-\varepsilon$  à faible nombre de Reynolds en considérant le comportement du limiteur de paroi, le niveau de turbulence du flux libre et l'équilibre

entre la production et la destruction de la turbulence. En outre, Tseng et Cheng [33] et Tseng et Hu [34] ont appliqué un modèle  $k-\omega$  modifié à faible nombre de Reynolds pour clarifier le mécanisme du retard de décrochage induit par le tourbillon de bord d'attaque (LEV) à deux stades, avant et après la formation du LEV, et suivre la trajectoire des différentes structures tourbillonnaires en utilisant les structures cohérentes lagrangiennes (LCS). Cependant, l'expérience montre que cette approche n'est pas capable de capturer l'influence de nombreux facteurs, y compris les gradients de pression et la séparation de l'écoulement, le nombre de Mach, l'échelle de longueur de la turbulence, la rugosité de la paroi et la courbure de la ligne de courant.

Par la suite, le modèle de transition SST  $\gamma - \widetilde{Re}_{\theta t}$  a été développé par Menter et al. [26-27], puis il a été largement appliqué à de nombreux écoulements techniques avec des effets de transition [35-37]. En plus des deux équations originales du modèle de turbulence SST  $k-\omega$ , deux autres équations, pour l'intermittence  $\gamma$  et le nombre de Reynolds d'épaisseur de momentum de transition  $\widetilde{Re}_{\theta t}$ , sont obtenues en introduisant l'intermittence effective dans les termes de production et de destruction dans l'équation d'énergie cinétique de la turbulence. Plusieurs modifications supplémentaires ont été obtenues jusqu'à présent : Dong et al [38] ont testé l'effet du nombre de Reynolds sur les structures de l'écoulement à l'intérieur de la couche limite et ont conclu que des structures non classiques, y compris le tourbillon majeur et les petites échelles, émergent lorsque le nombre de Reynolds augmente de  $3 \times 10^5$  à  $5 \times 10^5$ .

Wang et Xiao [39] ont utilisé le modèle SST  $\gamma$  pour prédire la transition avec l'augmentation de l'incidence de  $0^\circ$  à  $18^\circ$ , le régime d'écoulement subit différents processus, à savoir la transition de l'écoulement, la séparation de l'écoulement et l'interaction entre la LSB et la bulle de séparation du bord de fuite, ce qui correspond au stade de soulèvement linéaire, au stade de décrochage léger et au stade de décrochage profond. Pour les écoulements de transition 3D, Bartl et al. [40] ont trouvé que la prédiction de l'emplacement et de la longueur moyenne de la LSB ainsi que la distribution de la pression montrent un bon accord avec les expériences dans des conditions de pré-décrochage. Ensuite, pour les profils oscillants, Ducoin et al. [41] ont étudié l'effet de la vitesse de tangage sur les événements de la couche limite et sur la charge hydrodynamique, et les résultats montrent que la transition est retardée avec l'augmentation de la vitesse de tangage et peut même être supprimée à la vitesse de tangage la plus élevée pendant la phase de montée. Dans les travaux de Karbasian et Kim [42], l'importance de la durée de vie des tourbillons spéciaux, tels que le LEV primaire, le TEV et le LEV secondaire, due à l'interaction entre différents tourbillons, est soulignée, ainsi que le retard entre la circulation maximale des tourbillons principaux et le pic correspondant du coefficient de portance. Récemment, Zhang et al. [43] ont également vérifié l'influence du taux de tangage sur les performances hydrodynamiques et les structures tourbillonnaires instationnaires. Les résultats montrent principalement que le taux de tangage élevé peut retarder le décrochage dynamique, tandis que le taux de tangage faible réduit les boucles d'hystérésis et intensifie les fluctuations de force. Pour les écoulements cavitants diphasiques plus compliqués, Huang et al. [44] ont observé que le volume de cavitation augmente avec la vitesse de tangage, ce qui modifie la fréquence d'éjection de la cavité et, par conséquent, les charges hydrodynamiques. Pendant le mouvement de tangage, les performances générales obtenues par le modèle de transition basé sur la méthode RANS sont assez bonnes en raison des caractéristiques bidimensionnelles, alors qu'il y a un écart relativement important lorsque l'aile subit le processus de descente sous l'effet d'un fort effet tridimensionnel le long de l'envergure [45]. Par conséquent, Wang et al. [5] et Singh et Páscoit [46] ont appliqué le modèle de

transition SST  $\gamma - \widetilde{Re}_{\theta t}$  couplé à la simulation des tourbillons détachés (DES) et à la simulation adaptative à l'échelle (SAS), respectivement, et ont pu améliorer considérablement les résultats pendant le mouvement de descente. Cependant, dans le modèle de transition, certains coefficients et certaines corrélations empiriques doivent être calibrés. Par exemple, Malan et al. [47] se sont concentrés sur le calibrage du modèle de transition SST  $\gamma - \widetilde{Re}_{\theta t}$  dans la CFD commerciale, en accordant une grande attention à la corrélation de  $F_{length}$  (qui contrôle la longueur de la région de transition) et du nombre de Reynolds de l'épaisseur critique de l'impulsion  $Re_{\theta c}$  avec  $\widetilde{Re}_{\theta t}$ . De plus, la corrélation de  $Re_{\theta c}$  avec  $\widetilde{Re}_{\theta t}$  a été modifiée par Wang et al. [48], et les résultats de la longueur de transition et de la distribution du frottement pariétal sont en bon accord avec les expériences. En général, le modèle de transition couplé à des modèles de turbulence basés sur RANS a la capacité de prédire la dynamique de la transition et la performance globale, mais il doit être utilisé avec précaution en raison de sa sensibilité à de nombreux paramètres.

Il existe de nombreux types de turbines à axe vertical (VAT) appliquées aux dispositifs de conversion d'énergie. Sur la base des différentes techniques utilisées pour contrôler la cinématique de tangage, les turbines à axe vertical peuvent être généralement divisées en trois types : les turbines à pas variable de type cycloïdal, les turbines à pas variable contrôlé par ressort et les turbines à pas variable passif. Les schémas de ces différentes turbines sont présentés dans la figure 1.5 [49]. En tant que type particulier de système de propulsion, la VAT à pas variable de type cycloïdal produit une force de poussée qui est perpendiculaire à l'axe de rotation. Comme l'amplitude et la direction de la force de poussée varient continuellement avec l'angle de tangage des pales, une grande maniabilité du système de propulsion peut être obtenue. Pour les systèmes de propulsion marine, tels que l'hélice Voith Schneider (VSP), chaque pale de l'hélice cycloïdale peut être contrôlée à l'aide d'un système cinématique complexe, ce qui entraîne la présence de l'excentricité  $e=OP/R$  ( $R$  étant le rayon) entre le centre du boîtier du rotor et le centre du système cinématique, où la corrélation de l'angle azimutal  $\varphi$  avec l'angle de tangage  $\Phi$  est donnée par

$$\Phi = -\alpha \tan^{-1} \left( \frac{e \sin \varphi}{1 + e \cos \varphi} \right) \quad (1.4)$$

où  $\alpha$  est l'amplitude du tangage.

En général, lorsque  $e$  est inférieur à 1, l'hélice cycloïdale est connue comme une hélice à pas faible, tandis qu'elle est considérée comme une hélice à pas élevé avec  $e > 1$ .

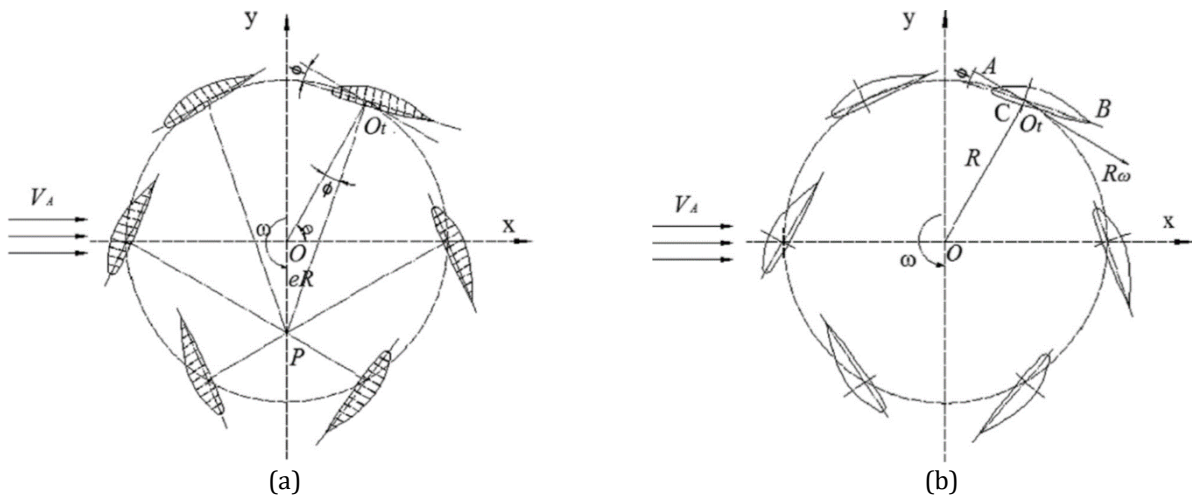


**Fig.1.5** Schémas de principe de différents VAT. (a) VAT cycloidal à pas variable ; (b) VAT à pas variable.

La turbine à axe vertical à pas variable commandée par ressort est un nouveau type et son mécanisme de tangage est assez similaire à celui du type passif à pas variable. Les turbines tournent autour du centre de la circularité et la pale tourne autour du centre de rotation de la pale. Cependant, dans le cas des turbines passives à pas variable, la pale n'oscille que dans une plage d'incidence limitée et la variation du pas de la pale est contrôlée par l'équilibre entre le moment hydrodynamique et le moment d'inertie de manière continue. L'avantage de cette turbine est sa structure simple et fiable, ainsi que ses meilleures capacités d'auto-démarrage.

Bien que l'hélice à pas variable à pas sinusoïdal soit moins efficace que l'hélice cycloïdale à pas variable, les données expérimentales précédentes montrent que l'hélice cycloïdale à pas variable présente une quantité de données bruitées et de mauvais résultats en raison de la friction élevée des dispositifs de contrôle du pas [2]. Simultanément, le mouvement cycloïdal peut être remplacé par le mouvement sinusoïdal pour la raison qu'il a un mécanisme plus simple, moins de pièces, moins de pertes par friction et une construction plus robuste [50]. Nakonechny [51] a mené des expériences sur l'hélice à pas variable avec un mouvement sinusoïdal modifié, et a montré que le rendement est plus élevé que celui de l'hélice cycloïdale à pas variable avec le même angle de pas maximal. En outre, les mouvements sinusoïdaux du pas des pales ont été utilisés avec succès dans de nombreux macro-véhicules aériens [52-53].

Par rapport à la VAT à pales fixes, les turbines à pas sinusoïdal peuvent améliorer la performance globale. Avec une amplitude de tangage appropriée, non seulement le rendement énergétique augmente, mais les fluctuations de la puissance, de la vitesse de rotation et du couple sont également réduites de manière significative [54]. Chen et al. [55] ont étudié l'effet du canal de type ponton sur les couples hydrodynamiques de la pale et du rotor, et ils ont constaté que lorsque la turbine est placée dans un canal, les fluctuations des couples hydrodynamiques et de la vitesse de rotation sont considérablement réduites, tandis que la puissance de sortie est supérieure de plus de 30% à celle de la turbine isolée. Avec le mouvement de tangage sinusoïdal, Paillard et al. [56] ont utilisé le modèle de transition SST  $\gamma - \widetilde{Re}_{\theta t}$  pour étudier l'effet de l'angle de tangage sur le coefficient de couple et le rendement de l'hydrolienne à flux transversal, et les résultats montrent que la fonction de tangage de deuxième harmonique, définie comme  $\theta=2(\cos(2\omega t)-1)$ , peut fournir une grande amélioration des performances. Le choix du modèle de turbulence est critique pour la précision de la simulation dans les calculs RANS. Par exemple, le modèle standard SST  $k-\omega$  sur-prévoit le coefficient de puissance maximal

lorsque les turbines fonctionnent dans des conditions de faible nombre de Reynolds, ce qui est attribué à la sous-prédition de la séparation de l'écoulement après le décrochage rapportée par McNaughton et al [57]. Par conséquent, la version à faible nombre de Reynolds et certaines modifications sont nécessaires pour prédire la séparation laminaire correcte et reproduire les structures d'écoulement liées au décrochage dynamique. De plus, l'effet de transition est vital pour prédire l'apparition du décrochage en raison de l'existence de la bulle de séparation laminaire qui peut conduire à une grande divergence de la prédition de puissance [58]. Li et al. [59] ont observé que le coefficient de portance est plus faible que dans les expériences lorsque le modèle SST  $k-\omega$  est employé pour résoudre les écoulements entièrement turbulents. Rezaeih et al. [60] ont comparé le coefficient de puissance obtenu par plusieurs modèles de turbulence et ont constaté que les variantes du modèle SST (SST  $k-\omega$ , SST  $\gamma$  et SST  $\gamma - \widetilde{Re}_{\theta t}$ ) peuvent fournir un accord raisonnable avec les expériences. La tridimensionnalité a également un grand impact sur le coefficient de puissance car l'écoulement 2D ne tient pas compte des effets de l'extrémité de la pale et de l'entretoise. Par conséquent, Marsh et al. [61] suggèrent que le domaine 3D avec un maillage de la couche limite entièrement résolu devrait être utilisé pour prédire la puissance de sortie de la turbine. En outre, les propriétés instantanées de la performance et de l'évolution des tourbillons sont assez différentes entre les écoulements 2D et 3D, bien qu'il n'y ait qu'une petite erreur dans la force moyenne dans le temps. Hu et al. [62] ont constaté que la fluctuation de la force aérodynamique est considérablement réduite pour les écoulements 3D en raison de l'affaiblissement des interactions tourbillonnaires des pales parallèles induites par les tourbillons de décrochage dynamiques. L'interaction pale-vortex est un problème qui doit être analysé clairement car elle peut produire des forces supplémentaires pour le système rotatif. Lind et al [3] ont découvert que les interactions pale-vortex sont fortement associées aux pics des forces instantanées, ce qui montre leur importance dans la génération de la portance et de la force propulsive du rotor cycloïdal. En outre, la façon de modéliser le sillage complexe est discutable en raison de sa complexité. Par conséquent, Tang et al. [63] ont combiné la théorie de la quantité de mouvement, la méthode de la ligne de levage, le modèle de sillage libre et le modèle de décrochage dynamique semi-empirique de Leishman-Beddoes, pour modéliser les sillages instables des hélices cycloïdales. En général, la plupart des travaux précédents se concentrent sur la prédition de la performance globale et de l'évolution tourbillonnaire instationnaire des turbines et des hélices à pas variable, mais la façon dont les structures d'écoulement internes influencent la performance du système rotatif et de la pale unique est moins bien comprise à faible nombre de Reynolds, lorsque l'effet de transition ne peut pas être négligé.

L'objectif final de l'étude des structures d'écoulement à l'intérieur de ces turbines ou hélices en fonctionnement est de les optimiser en vérifiant l'effet d'un seul paramètre indépendamment, ou en combinant plusieurs facteurs à l'aide de certaines approches d'optimisation. Dans les machines rotatives complexes, il existe de nombreux paramètres importants qui affectent plus ou moins la force de propulsion et l'efficacité de ces dispositifs. Par conséquent, une brève revue de la littérature est effectuée ci-après.

La modification des paramètres géométriques est le premier choix pour l'optimisation de la performance basée sur les structures d'écoulement interne. Dans le cas des éoliennes à axe vertical, de nombreux exemples d'optimisation peuvent être trouvés dans la littérature. Par exemple, Wang et al. [64] ont comparé les coefficients de puissance de profils symétriques et asymétriques en considérant l'influence de l'épaisseur, de la position maximale de l'épaisseur, de la cambrure et de la position maximale de la cambrure, et les résultats montrent une tendance différente du coefficient

de puissance. Subramanian et al. [65] ont trouvé qu'un profil épais est plus performant pour un faible rapport de vitesse de pointe  $\lambda$  (TSR) alors que le profil mince a une meilleure performance pour  $\lambda > 1,8$ . Baghdadi et al. [66] ont testé quelques pales de rotor avec un bord de fuite déformé et ont observé que le profil modifié peut améliorer la puissance de sortie de l'éolienne. En utilisant une optimisation entièrement automatisée basée sur l'approximation de la surface de réponse, Ismail et Vijayaraghavan [67] ont mené des recherches sur un profil avec une fossette en demi-cercle vers l'intérieur et un volet de Gurney sur la surface inférieure et les résultats montrent que l'aérodynamique de l'éolienne est grandement améliorée. De plus, Tang et al. [68] ont établi une méthode de conception et d'optimisation aérodynamique pour obtenir un nouveau profil avec une épaisseur maximale et une petite partie de cambrure positive, qui peut produire une poussée plus élevée et un couple plus faible par rapport à la géométrie de base. Récemment, Tirandaz et Rezaeiha [69] ont testé une série de profils symétriques pour l'optimisation des VAWT en modifiant l'épaisseur maximale de la pale, la position de l'épaisseur maximale et le rayon du bord d'attaque. Les résultats montrent que ces trois paramètres ont un impact couplé sur les coefficients de puissance et de poussée de la turbine, ainsi que sur les caractéristiques de décrochage dynamique. Ensuite, la solidité, définie comme  $\sigma = Nc/r$  (où  $N$  est le nombre de pales,  $c$  est la corde de la pale et  $r$  est le rayon du rotor), s'avère également influencer les performances aérodynamiques. Eboibi et al. [70] ont réalisé des expériences pour étudier la variation du coefficient de puissance causée par le changement de la corde des pales et ont découvert que la turbine ayant la solidité la plus grande atteignait un meilleur coefficient de puissance en raison du retardement du décrochage dynamique. En mettant l'accent sur la solidité et le nombre de pales, Rezaeiha et al. [71] ont démontré qu'en ce qui concerne l'uniformité de la puissance de sortie et les charges structurelles, un grand nombre de pales produisant des charges et une puissance instantanée plus uniformes est recommandé, car il réduit les fluctuations de la charge à grande échelle en raison de la plus petite corde des pales pour une solidité donnée. En utilisant le modèle de turbulence SST  $k-\omega$ , Sagharichi et al. [72] ont observé que le VAWT à pas variable à haute solidité est intéressant car il génère moins de structures tourbillonnaires et plus de poussée.

Le mouvement sinusoïdal est la cinématique de tangage la plus courante pour les turbines et les hélices à pas variable. Mais si le mouvement sinusoïdal original est transformé en un mouvement asymétrique ou en une cinématique différente pour différents angles azimutaux, les performances globales peuvent être améliorées. Chen et al. [73] ont adopté un mouvement sinusoïdal asymétrique pour des angles azimutaux compris entre  $0^\circ$  et  $180^\circ$ , et un petit angle de tangage fixe de  $180^\circ$  à  $360^\circ$ , ce qui a permis d'augmenter le rendement énergétique de 20%. Lorsqu'elle est appliquée à des micro-véhicules aériens, la cinématique de tangage asymétrique, impliquant l'incidence moyenne, l'amplitude de tangage et l'angle de phase, a un impact important sur les performances du rotor cycloïdal et les interactions entre le sillage et la pale, comme l'ont rapporté Benedict et al [74]. En considérant la cambrure virtuelle dynamique induite par la courbure de l'écoulement, Walther et al. [75] ont constaté que la portance de la pale diminue dans la moitié supérieure de la trajectoire circulaire en raison de la cambrure négative, tandis qu'elle augmente dans la moitié inférieure, grâce à la cambrure positive. Ils ont donc introduit une cinématique de tangage asymétrique avec un tangage plus élevé dans la moitié supérieure et un tangage plus faible dans la moitié inférieure. En outre, en raison de l'effet de courbure de l'écoulement, les performances du rotor cycloïdal dépendent fortement du rapport corde/rayon et de l'emplacement du pivot de tangage des pales. Benedict et al. [76-77] ont souligné que l'augmentation de la solidité en

augmentant la corde des pales et en déplaçant l'emplacement du pivot d'environ 25-35% par rapport au bord d'attaque entraîne une amélioration importante de la charge de puissance (poussée/puissance). Ils ont également observé qu'à de faibles amplitudes de tangage, le rotor cycloïdal à courte portée a une charge de puissance plus élevée. Pour une éolienne à axe vertical autopilotée à haute solidité, Xisto et al. [78] ont étudié l'effet de différents paramètres sur l'efficacité aérodynamique et ont constaté que le couple le plus élevé est obtenu à un rapport de vitesse de pointe très faible avec de grandes pales. Ils ont également constaté que l'emplacement optimal de l'axe de tangage des pales se situe entre 35% et 50% de la corde. Après avoir considéré presque tous les paramètres, Jarugumilli et al. [79] ont conclu que le rotor cycloïdal à 4 pales utilisant une section de pale NACA0015 de 1,3 pouce avec un tangage asymétrique de 45° en haut et de 25° en bas et un pivot de tangage de 25 % de la corde atteint une charge de puissance plus élevée par rapport au rotor conventionnel.

D'après les travaux mentionnés ci-dessus, il semble que l'accent soit mis sur l'optimisation de la performance globale en augmentant l'efficacité et en diminuant la consommation d'énergie, mais l'influence des structures d'écoulement sur le changement de performance dans diverses conditions de fonctionnement n'a pas été étudiée de manière approfondie.

Le but de mon travail de recherche est d'étudier les structures d'écoulement détaillées à l'intérieur d'un rotor cycloïdal à deux pales avec un tangage sinusoïdal en utilisant le modèle de transition RANS SST  $\gamma - \widetilde{Re}_{\theta t}$ , en mettant l'accent sur le changement de performance induit par l'écoulement du système rotatif et d'une seule pale dans diverses conditions de fonctionnement. Le travail se compose principalement des deux parties suivantes :

(1) Tout d'abord, le modèle de transition SST  $\gamma - \widetilde{Re}_{\theta t}$  est calibré sur un profil aérodynamique à différentes incidences, en vérifiant les effets du maillage dans la direction de l'écoulement et perpendiculairement à celui-ci, les conditions de turbulence du flux entrant, les corrélations et les paramètres dans le modèle de transition, et le modèle de turbulence. Les calculs sont comparés aux expériences disponibles, en termes de pression moyenne dans le temps, de profils de vitesse près de la paroi et d'emplacements de séparation, de transition et de rattachement. Ensuite, le modèle de transition optimisé est appliqué directement à un rotor cycloïdal à deux pales, afin d'étudier les structures détaillées de l'écoulement interne et la façon dont elles influencent les performances du système rotatif et de la pale unique. Les résultats obtenus par le modèle de transition sont comparés aux expériences existantes et à certains résultats obtenus avec d'autres modèles de turbulence.

(2) La deuxième partie se concentre sur l'impact de quatre paramètres importants : la cinématique de tangage (tangage symétrique/asymétrique), le rapport corde/rayon, l'emplacement du pivot de tangage et le profil de la pale, dans le but d'optimiser l'hélice cycloïdale et d'expliquer comment les écoulements près de la paroi affectent les performances. L'attention est portée sur les variations de performance induites par l'écoulement à différentes conditions de nombre de Reynolds et de coefficient d'avance.

## **PREMIERE PARTIE : CALIBRATION ET VALIDATION DU MODELE SST $\gamma - \widetilde{Re}_{\theta t}$**

### **ÉCOULEMENTS TRANSITOIRES AUTOUR D'UN PROFIL AÉRODYNAMIQUE NACA0018**

Dans cette section, le modèle de transition SST  $\gamma - \widetilde{Re}_{\theta t}$  a été tout d'abord calibré, en termes de résolution de maillage, de conditions de turbulence d'entrée, de corrélations et de paramètre dans le modèle de transition, puis il est appliqué aux écoulements de transition sur un profil d'avion NACA0018, pour vérifier l'influence du modèle de turbulence, de l'angle d'attaque et du nombre de Reynolds. Les principales conclusions sont énumérées ci-dessous:

(1) Les maillages structurés et non structurés peuvent tous deux capturer le même emplacement de transition, mais la faible différence de pression prédictive dans la région d'écoulement laminaire est le principal facteur contribuant à la différence de performance. Pour obtenir une meilleure prédition de la transition, le maillage doit être raffiné non seulement dans la direction normale, mais aussi dans la direction de l'écoulement.

(2) L'augmentation de l'intensité de la turbulence du flux entrant fait que le point de séparation se déplace vers l'aval, et que les points de transition et de rattachement se déplacent vers l'amont, ce qui indique que la longueur de la LSB diminue. Par rapport aux points de séparation et de transition le lieu de rattachement est plus facilement affecté par les conditions turbulentées du flux entrant. Simultanément, l'effet de l'intensité de la turbulence sur la transition est plus évident que le rapport de viscosité tourbillonnaire.

(3) Les résultats sont influencés par la modification de la corrélation  $Re_{\theta t}$  avec NZPG, mais cet effet peut être omis en raison de la compensation par la décroissance de l'intensité de la turbulence d'entrée. En outre, les points de séparation, de transition et de rattachement se déplacent vers l'aval si les corrélations de  $F_{length}$  et  $Re_{\theta c}$  sont modifiées en même temps. Ensuite, avec l'augmentation du paramètre  $S1$  dans le modèle de transition, la longueur de LSB est réduite, à cause du mouvement des points de séparation, de transition et de rattachement.

(4) Le modèle de transition SST  $\gamma - \widetilde{Re}_{\theta t}$  démontre sa supériorité dans la prédition de la transition couche limite, suivi par le modèle RSM, qui peut également détecter l'existence de la LSB. À l'inverse, le modèle SST  $k-\omega$  ne résout que l'écoulement entièrement turbulent.

(5) En comparant les profils de vitesse moyenne et les emplacements de transition, on observe que le modèle de transition SST  $\gamma - \widetilde{Re}_{\theta t}$  a une bonne performance avant le rattachement lorsque l'incidence est inférieure à  $10^\circ$ . Une grande divergence est systématiquement obtenue dans la couche limite entièrement turbulente. En outre, à  $15^\circ$ , en raison à la fois de la courte région de transition et du délestage tourbillonnaire après la transition, la capture de ces caractéristiques de l'écoulement devient plus difficile pour le modèle de transition basé sur la RANS.

(6) Lorsque le nombre de Reynolds augmente, la longueur du LSB se raccourcit considérablement et le point de transition est très proche du rattachement dans des

conditions de nombre de Reynolds relativement élevé. De plus, lorsque le nombre de Reynolds est inférieur à  $5,0 \times 10^4$ , un tourbillon à grande échelle est attaché à la surface de la feuille et la transition devient moins évidente avec la réduction supplémentaire du nombre de Reynolds.

### **APPLICATION DU MODÈLE SST $\gamma - \widetilde{Re}_{\theta t}$ À UN ROTOR CYCLOÏDAL**

Les écoulements tourbillonnaires instationnaires et la transition laminaire-turbulence d'un rotor cycloïdal à deux pales sont étudiés en utilisant le modèle original SST  $k-\omega$  et le modèle SST TM optimisé. Les résultats obtenus sont comparés aux données numériques et expérimentales disponibles. Les principales conclusions sont les suivantes:

- (1) Parmi les différents modèles de turbulence, le SST TM a la supériorité pour prédire la performance globale du rotor cycloïdal, et les résultats obtenus par RSM ont de grandes fluctuations importantes dues au maillage très raffiné et au petit pas de temps.
- (2) La transition des forces et de la puissance pour une pale est analysée en utilisant les distributions de force, ce qui montre que l'augmentation/diminution de  $\lambda$  n'a pas d'impact sur cela. La transition de la force verticale est principalement à  $\psi=32^\circ$  et  $144^\circ$ , où le profil de la pale est presque perpendiculaire à l'axe horizontal, tandis que la transition de la force de propulsion se produit à  $\psi=90^\circ$  et  $270^\circ$ , lorsque la géométrie de la pale est parallèle à l'axe horizontal.
- (3) Près de la surface de l'aile, les zones de basse pression et de haute pression près du bord d'attaque des pales en raison de la déviation du point de stagnation, l'existence du tourbillon attaché, la séparation massive de l'écoulement et la transition laminaire-turbulence induite par la bulle de séparation, ont un impact important sur les performances du rotor cycloïdal et de la pale unique. En outre, les interactions entre les pales et le sillage ont un effet important sur le champ d'écoulement externe.
- (4) La principale différence de portance se situe à  $\psi=30^\circ$  et  $90^\circ$ , tandis qu'elle existe à  $\psi=30^\circ$  pour la force de propulsion, en raison de la direction de la force et du chargement d'une seule pale. Lors de l'analyse de la différence de force du rotor cycloïdal, la distribution de la force (force verticale et force de propulsion) de la pale unique, les forces (portance et traînée) agissant sur la pale et la différence de pression de chaque pale sont nécessaires.
- (5) La transition induite par la bulle de séparation à deux  $\lambda$  lorsque la pale subit le côté d'avancement sont révélés. On en conclut que le modèle SST TM est très sensible aux perturbations et à la capacité de capturer l'évolution de la transition, de l'onde croissante de la couche limite laminaire au développement complet de la bulle de séparation. Cependant, le modèle SST  $k-\omega$  ne résout que les écoulements turbulents après la formation de la bulle de séparation.

## **DEUXIÈME PARTIE : ÉTUDE PARAMÉTRIQUE ET OPTIMISATION D'UN ROTOR CYCLOÏDAL**

Dans cette deuxième partie, l'influence de différents paramètres a été étudiée : l'influence de la cinématique de tangage, l'influence du rapport corde/rayon, l'influence du point de pivotement et l'influence de la forme du profil.

### **INFLUENCE DE LA CINÉMATIQUE DE TANGAGE**

Les principales conclusions sont les suivantes:

(1) La cinématique de tangage asymétrique avec un petit angle de tangage moyen positif donne les meilleures performances en ce qui concerne l'efficacité du rotor cycloïdal, qui résulte de la force propulsive modérée et de la faible puissance. Inversement, bien que le tangage symétrique avec une grande amplitude et le tangage asymétrique avec un grand angle de tangage moyen génèrent une force de propulsion élevée, l'efficacité est assez faible en raison des flux tourbillonnaires compliqués qui entraînent une puissance plus élevée. De plus, le tangage asymétrique avec un angle de tangage moyen négatif produit le coefficient de portance élevé avec  $\lambda$ , mais une diminution du coefficient de la force propulsive.

(2) En général, les performances de la pale unique montrent que la différence du coefficient de portance est principalement causée par la pale B du côté de l'avance, tandis qu'elle est induite par les deux pales pour la différence du coefficient de force propulsive. Près de la surface du profil, les structures d'écoulement sont riches, y compris trois structures tourbillonnaires, les tourbillons d'enroulement, le tourbillon de séparation d'écoulement au bord de fuite, LSB, LEV et TEV, et le modèle de ces tourbillons dépend de l'incidence importante. Lors de l'analyse des forces sur la pale unique, il est intéressant de noter que lorsque la pale subit le côté gauche du côté de l'avance, la direction de la portance est opposée pour le tangage asymétrique avec des angles de tangage moyens négatifs par rapport aux autres cas, en raison de l'emplacement du point de stagnation causé par les différentes incidences relatives.

### **INFLUENCE DU RAPPORT CORDE/RAYON**

Les principales conclusions sont les suivantes :

(1) Pour des valeurs de  $\lambda$  et de  $Re$  données, les cas avec  $c/R=0,45$  pour différentes longueurs de corde de pale atteignent le meilleur rendement. Ensuite, à grand  $c/R$ , la structure globale de l'écoulement est plus compliquée et les performances sont fortement impactées, en raison de la faible distance entre deux pales adjacentes.

(2) En ce qui concerne l'influence des nombres  $Re$  et  $\lambda$ , il semble que l'effet de  $Re$  sur les performances soit très faible. Cependant, à faible  $Re$ , la force propulsive est significativement différente de celle obtenue à  $Re$  relativement élevé. Le coefficient d'avance  $\lambda$  a un grand impact sur les structures d'écoulement et sur la performance globale, surtout à faible  $\lambda$ , ce qui est dû à la grande variation de la vitesse relative induite par le changement de la vitesse de rotation. Il semble que pour un  $\lambda$  élevé, le sillage à droite a un risque élevé de contact avec la pale, en raison

de la faible vitesse de rotation. Il s'avère que les cas avec  $c/R=0.45$  à différents  $Re$  ou  $\lambda$  obtiennent le meilleur rendement.

(3) Les structures d'écoulement à l'intérieur d'un rotor cycloïdal sont extrêmement complexes, y compris les structures à trois tourbillons, les tourbillons d'enroulement à l'intérieur de la couche limite, le LSB, le tourbillon de séparation de l'écoulement, les interactions sillage-sommet et pale-sommet, et dépendent des conditions de fonctionnement. En outre, à l'exception de l'écoulement près de la paroi, l'emplacement du point de stagnation associé au développement de la couche limite est très critique pour chaque changement de pale. Le changement de  $Re$  et de  $\lambda$  peut modifier la direction de la vitesse relative, mais il est moins influent pour  $Re$ , en raison du changement de la vitesse d'entrée et de la vitesse de rotation en même temps.

## L'INFLUENCE DU POINT DE PIVOTEMENT

Les principales conclusions sont les suivantes :

(1) Pour  $\lambda$  et  $Re$  donnés, le cas avec  $x/c=0.25$  (distance adimensionnelle entre le bord d'attaque et le point de pivotement) obtient la meilleure performance. Ensuite, lorsque le point de pivot de tangage se déplace vers la corde médiane de la pale, bien que le coefficient de force propulsive augmente, l'efficacité du rotor cycloïdal se dégrade en raison de la consommation d'énergie plus élevée. Simultanément, le coefficient de portance a la plus grande amplitude lorsque le point de pivot de tangage est plus proche du bord d'attaque.

(2) Pour le cas avec un  $x/c$  constant, l'efficacité du système rotatif augmente avec  $Re$ . À faible  $Re$ , son effet ne peut être ignoré, car les écoulements tourbillonnaires autour de la surface de la pale apparaissent plus tôt. De plus, l'augmentation de  $Re$  entraîne un changement du taux de tangage, ce qui modifie la position du point de stagnation et la prédiction du gradient de pression, ce qui a un impact important sur les écoulements de la couche limite.

(3) Le coefficient d'avance  $\lambda$  a un impact plus important sur les performances, par rapport à  $Re$ . Les coefficients de forces et de puissance diminuent avec l'augmentation de  $\lambda$ . De même, comme le point de pivot de tangage est situé près du bord d'attaque, le système obtiendrait le coefficient de portance le plus élevé à  $\lambda$  élevé. En outre, la meilleure efficacité basée sur le coefficient de force propulsive est obtenue à  $\lambda=0,48$  lorsque le point de pivot de tangage est à  $x/c=0,25$ . En outre, par rapport à l'effet de  $Re$ , le changement de  $\lambda$  en modifiant uniquement la vitesse de rotation, a une influence plus évidente sur l'emplacement du point de stagnation et la prédiction du gradient de pression, ce qui entraîne le développement totalement différent des flux de la couche limite. En outre, l'augmentation de  $\lambda$  en diminuant la vitesse de rotation ferait se développer pleinement les flux tourbillonnaires.

## **INFLUENCE DU PROFIL D'AILE**

Les principales conclusions sont les suivantes :

(1) Les profils de pales symétriques, notamment NACA0012 et NACA0015, présentent les meilleures performances en termes d'efficacité, en raison de la force et de la puissance propulsives relativement modérées. En revanche, le profil asymétrique, tel que le NACA6415, présente les pires performances, en raison d'une force et d'une puissance de propulsion élevées. En outre, le NACA2415 inverse a un fort potentiel d'optimisation car il présente une efficacité élevée à  $Re$  élevé.

(2) Le champ d'écoulement à l'intérieur du rotor cycloïdal présente que les flux tourbillonnaires autour du NACA6415 sont plus complexes, ce qui est responsable de la grande consommation d'énergie. À l'inverse, les structures d'écoulement au-dessus du NACA6415 inverse sont assez lisses, consommant un niveau d'énergie relativement faible.

(3) Le nombre de Reynolds a également un impact important sur les performances et les structures d'écoulement. Le rotor cycloïdal obtient un faible coefficient de portance, mais un coefficient de force propulsive élevé à faible  $Re$ . Dans la plupart des cas, seule la pale B est le principal contributeur à la production d'une grande force verticale négative à faible  $Re$ , en raison de la séparation antérieure de l'écoulement. Cependant, la force de propulsion du système rotatif devrait se référer aux composants produits par deux pales, en raison de la grande variation des performances d'une seule pale.

(4) L'influence de  $\lambda$  est plus évidente que celle de  $Re$  car seule la vitesse de rotation est modifiée. Le changement de la vitesse de rotation peut modifier de manière significative le point de stagnation, conduisant à des écoulements de couche limite totalement différents à différents  $\lambda$ . Normalement, la différence de coefficient de portance dépend de la pale B, alors que les deux pales devraient prendre la responsabilité de la différence de la force de propulsion du rotor cycloïdal.

## **RÉSUMÉ GÉNÉRAL**

Pour conclure, cette thèse porte sur l'analyse numérique des performances et des écoulements tourbillonnaires instationnaires d'un rotor cycloïdal à deux pales et sur son optimisation à l'aide du modèle de transition SST  $\gamma - \widetilde{Re}_{\theta t}$ . Ce travail comprend principalement deux parties : la première est la validation du modèle de transition menée sur un seul profil et le rotor cycloïdal à deux  $\lambda$  différents, et la seconde est l'étude paramétrique sur le rotor cycloïdal, où l'influence de la cinématique de tangage, le rapport corde/rayon, le point de pivot de tangage et le profil de la pale a été étudiée dans un but d'optimisation. L'analyse de ces paramètres importants est effectuée dans différentes conditions  $Re$  et  $\lambda$ . Les principales conclusions de la thèse sont les suivantes :

### **CALIBRATION ET VALIDATION DU MODÈLE SST $\gamma - \widetilde{Re}_{\theta t}$**

(1) Pour le profil stationnaire simple, les résultats montrent principalement que la résolution du maillage dans le sens de l'écoulement a un impact important sur la transition. L'augmentation de l'intensité de la turbulence ou du rapport de

viscosité tourbillonnaire conduit à la réduction de la taille de la bulle de séparation laminaire (LSB), mais l'impact de l'intensité de la turbulence est plus important. L'effet du gradient de pression n'est parfois pas essentiel en raison de la décroissance numérique de l'intensité de la turbulence imposée à la section d'entrée. Simultanément, les corrélations de  $F_{\text{length}}$  (contrôlant la longueur de transition) et  $Re_{\theta c}$  (nombre de Reynolds de l'épaisseur critique du momentum) ont plus ou moins d'impact sur la transition. L'influence du paramètre qui contrôle la taille du LSB doit être prise en compte lors de l'utilisation du modèle de transition, qui montre que la taille du LSB diminue avec l'augmentation de ce paramètre. Les comparaisons entre le modèle SST  $k-\omega$ , le modèle de contrainte de Reynolds (RSM) et le modèle de transition SST  $\gamma - \widetilde{Re}_{\theta t}$  montrent que ce dernier a la capacité de prédire les écoulements en couche limite. Ensuite, les distributions de pression et les profils de vitesse moyenne à différentes incidences obtenues par les calculs concordent bien avec les expériences avant le rattachement, mais il présente les grandes divergences dans la couche limite entièrement turbulente. De plus, avec l'augmentation du nombre de Reynolds, la taille de la LSB est réduite de manière significative, puisque le rattachement est très proche du point de transition. Dans des conditions de très faible Re, il existe une structure tourbillonnaire à grande échelle attachée à la surface et la transition est assez peu claire.

(2) Les écoulements tourbillonnaires instationnaires et la transition laminaire-turbulence d'un rotor cycloïdal à deux pales sont étudiés à deux valeurs de  $\lambda$ . Les résultats numériques sont comparés aux résultats numériques et expérimentaux existants, en termes de performance globale et de structures d'écoulement internes détaillées. L'augmentation de  $\lambda$  ne peut pas changer le lieu de transition des forces et de la puissance de la pale unique, mais les amplitudes de ces variables ont quelques changements. La transition de la force verticale se situe principalement à  $\psi=32^\circ$  et  $144^\circ$ , où le profil de la pale est presque perpendiculaire à l'axe horizontal, tandis que la transition de la force propulsive se produit à  $\psi=90^\circ$  et  $270^\circ$  lorsque la géométrie de la pale est parallèle à l'axe horizontal. Près de la surface du profil, les zones de basse pression et de haute pression près du bord d'attaque de la pale en raison de la déviation du point de stagnation, l'existence du tourbillon attaché, la séparation massive de l'écoulement et la transition laminaire-turbulence induite par la bulle de séparation, ont un grand impact sur les performances du système de rotor cycloïdal et de la pale unique. En outre, les interactions entre la pale et le sillage et entre le sillage et la pale ont un effet important sur l'écoulement externe. La principale différence du coefficient de portance se situe à  $\psi=30^\circ$  et  $90^\circ$  alors qu'elle existe à  $\psi=30^\circ$  pour le coefficient de force propulsive, en raison de la direction de la force et de la charge de la pale unique. Lors de l'analyse de la différence de performance du rotor cycloïdal, les forces (portance et traînée) agissant sur deux pales et la charge de chaque pale sont nécessaires. La transition induite par la bulle de séparation à deux  $\lambda$  lorsque la pale subit le côté avançant sont révélés. On conclut que le SST TM est très sensible aux perturbations et a la capacité de capturer l'évolution de la transition, depuis l'onde croissante de la couche limite laminaire jusqu'au développement complet de la bulle de séparation. Cependant, le modèle SST  $k-\omega$  ne résout que les écoulements turbulents après la formation de la bulle de séparation.

## ÉTUDE PARAMÉTRIQUE ET OPTIMISATION D'UN ROTOR CYCLOÏDAL

(1) La cinématique de tangage asymétrique avec un petit angle de tangage moyen positif donne les meilleures performances en ce qui concerne l'efficacité du rotor cycloïdal, qui résulte de la force propulsive modérée et de la faible puissance. Inversement, bien que le tangage symétrique avec une grande amplitude et le tangage asymétrique avec un grand angle de tangage moyen génèrent une force de propulsion élevée, l'efficacité est assez faible en raison des flux tourbillonnaires compliqués qui entraînent une puissance plus élevée. De plus, le tangage asymétrique avec un angle de pas moyen négatif produit le coefficient de portance élevé avec  $\lambda$ , mais une diminution du coefficient de la force propulsive. En général, les performances de la pale unique montrent que la différence du coefficient de portance est principalement causée par la pale B du côté de l'avancement, alors qu'elle est induite par les deux pales pour la différence du coefficient de force propulsive. Près de la surface du profil, les structures d'écoulement sont riches, y compris trois structures tourbillonnaires, les tourbillons d'enroulement, le tourbillon de séparation d'écoulement au bord de fuite, LSB, LEV et TEV, et le modèle de ces tourbillons dépend de l'incidence importante. En analysant les forces sur la lame unique, il est intéressant de constater que lorsque la lame subit le côté gauche de l'avancée, la direction de la portance est opposée pour le tangage asymétrique avec des angles de tangage moyens négatifs par rapport aux autres cas, en raison de l'emplacement du point de stagnation causé par les différentes incidences relatives.

(2) Pour des  $\lambda$  et  $Re$  donnés, les cas avec  $c/R=0,45$  pour différentes longueurs de corde de pale atteignent le meilleur rendement. Ensuite, à grand  $c/R$ , la structure globale de l'écoulement est plus compliquée et les performances sont fortement impactées, en raison de la faible distance entre deux pales adjacentes. En ce qui concerne l'influence de  $Re$  et  $\lambda$ , il semble que l'effet de  $Re$  sur les performances soit très faible. Cependant, à faible  $Re$ , la force propulsive est significativement différente de celle obtenue à  $Re$  relativement élevé. Le coefficient d'avance  $\lambda$  a un grand impact sur les structures d'écoulement et la performance globale, surtout à faible  $\lambda$ , ce qui est dû à la grande variation de la vitesse relative induite par le changement de la vitesse de rotation. Il semble que pour un  $\lambda$  élevé, le sillage à droite du côté du retrait a un risque élevé de contact avec la pale, en raison de la faible vitesse de rotation. Il est constaté que les cas avec  $c/R=0.45$  à différents  $Re$  ou  $\lambda$  obtiennent la meilleure efficacité. Les structures d'écoulement à l'intérieur d'un rotor cycloïdal sont extrêmement complexes, y compris les structures à trois tourbillons, les tourbillons d'enroulement à l'intérieur de la couche limite, le LSB, le tourbillon de séparation d'écoulement, les interactions sillage-sommet et pale-sommet, qui dépendent des conditions de fonctionnement. En outre, à l'exception de l'écoulement près de la paroi, l'emplacement du point de stagnation associé au développement de la couche limite est très critique pour la différence de pression de chaque pale. Le changement de  $Re$  et de  $\lambda$  peut modifier la direction de la vitesse relative, mais il est moins influent pour  $Re$ , en raison du changement de la vitesse d'entrée et de la vitesse de rotation en même temps.

(3) Le cas avec  $x/c=0.25$  obtient la meilleure performance. Lorsque le point de pivot de tangage se déplace vers la corde médiane de la pale, bien que le coefficient de force de propulsion augmente, l'efficacité du rotor cycloïdal se dégrade en raison

de la puissance plus élevée qui est consommée. Simultanément, le coefficient de portance a la plus grande magnitude lorsque le pivot de tangage est plus proche du bord d'attaque. Dans le cas d'un  $x/c$  constant, l'efficacité du système de rotation augmente avec  $Re$ . À faible  $Re$ , son effet ne peut être ignoré, car les écoulements tourbillonnaires autour de la surface de la pale apparaissent plus tôt. De plus, l'augmentation de  $Re$  entraîne un changement du taux de tangage, modifiant encore la position du point de stagnation et la prédiction du gradient de pression, ce qui a un grand impact sur les flux de la couche limite. Le coefficient d'avance  $\lambda$  a un impact plus important sur les performances, comparé à  $Re$ . Les coefficients de forces et de puissance diminuent avec l'augmentation de  $\lambda$ . De même, comme le point de pivot de tangage est situé près du bord d'attaque, le système obtiendrait un coefficient de portance plus élevé à  $\lambda$  élevé. En outre, la meilleure efficacité basée sur le coefficient de force propulsive est obtenue à  $\lambda=0,48$  lorsque le point de pivot de tangage est à  $x/c=0,25$ . De plus, l'augmentation de  $\lambda$  en diminuant la vitesse de rotation permettrait aux flux tourbillonnaires de se développer pleinement.

(4) Les profils de pales symétriques, notamment NACA0012 et NACA0015, présentent les meilleures performances en termes d'efficacité, en raison de la force et de la puissance propulsives relativement modérées. En revanche, le profil asymétrique, tel que le NACA6415, présente les pires performances, en raison d'une force et d'une puissance de propulsion élevées. De plus, le profil inverse NACA2415 a un fort potentiel d'optimisation car il a un rendement élevé à  $Re$  élevé. Le champ d'écoulement à l'intérieur du rotor cycloïdal présente que les flux tourbillonnaires autour du NACA6415 sont plus complexes, ce qui est responsable de la grande consommation d'énergie. Inversement, les structures d'écoulement au-dessus du NACA6415 inverse sont assez lisses, ce qui conduit à une puissance relativement faible.  $Re$  a également un impact important sur les performances et les structures d'écoulement. Le rotor cycloïdal obtient un faible coefficient de portance, mais un coefficient de force propulsive élevé à faible  $Re$ . Dans la plupart des cas, seule la pale B est le principal contributeur à la production d'une grande force verticale négative à faible  $Re$ , en raison de la séparation antérieure de l'écoulement. Cependant, la force de propulsion du système rotatif doit se référer aux composantes de la portance et de la traînée produites par deux pales, en raison de la grande variation des performances pour la pale unique. L'influence de  $\lambda$  est plus évidente que celle de  $Re$  car seule la vitesse de rotation est modifiée. Le changement de la vitesse de rotation peut modifier de manière significative le point de stagnation, conduisant à des écoulements de couche limite totalement différents à différents  $\lambda$ . Normalement, la différence du coefficient de portance dépend de la pale B, tandis que les deux pales devraient assumer la responsabilité de la différence de la force de propulsion du rotor cycloïdal.

## PERSPECTIVES

Afin d'obtenir une meilleure compréhension de la physique de l'écoulement à l'intérieur d'une telle configuration rotative complexe, certains travaux futurs peuvent encore être menés, qui sont proposés comme suit :

(1) Il montre que la pale subit un retrait et une avance au cours d'une révolution, ce qui entraîne des écoulements tourbillonnaires et des charges de pale

différents dans ces deux positions. Lorsque la pale est située du côté du recul, le bord de fuite aigu devient le bord d'attaque, et la séparation de l'écoulement se produit plus tôt, ce qui mérite d'être étudié en raison des écoulements plus instationnaires près de la paroi. Définitivement, la transition laminaire-turbulence diffère également de celle du profil avant (bord d'attaque émoussé et bord de fuite aigu).

(2) Il est également nécessaire de réaliser les écoulements 3D, car les écoulements dans le sens de l'envergure doivent être non uniformes. Bien entendu, on estime que les écoulements 2D et 3D résolus par le modèle de transition basé sur la méthode RANS originale sont assez similaires. Par conséquent, les modèles de turbulence plus avancés, tels que la simulation améliorée de tourbillons détachés retardés (IDDES) couplée au modèle de transition ou la simulation de grands tourbillons (LES) sont envisagés.

(3) Dans le présent travail, les sillages turbulents ne sont pas pris en compte. Les caractéristiques turbulentes des sillages et la récupération de la quantité de mouvement du sillage dans différentes conditions de travail doivent être considérées, ce qui peut nous aider à comprendre le champ d'écoulement global du rotor cycloïdal de manière exhaustive.

(4) Si le rotor cycloïdal est soumis au système de propulsion sous-marin, l'apparition de la cavitation est inévitable en raison de la grande variation de l'incidence. Il est également important de comprendre l'évolution de la cavitation et son influence sur les performances globales dans différentes conditions.

# Etude numérique d'hélices cycloïdales : Analyse des écoulements tourbillonnaires instationnaires et optimisation

## Résumé

En tant que nouveau système de propulsion, l'hélice cycloïdale a récemment attiré plus d'attention. Pour une meilleure conception d'un tel dispositif, il est d'une grande importance de comprendre la physique de l'écoulement autour du propulseur cycloïdal et de déterminer comment elle affecte les performances du propulseur, dans différentes conditions de travail. Dans cette thèse, les écoulements tourbillonnaires instationnaires sur un rotor cycloïdal bipale sont modélisés en utilisant le modèle de turbulence de transition SST  $k - \widetilde{Re}_{\theta t}$ . Les principales contributions du présent travail peuvent être résumées comme suit : (1) étalonnage du modèle de transition SST  $k - \widetilde{Re}_{\theta t}$  sur un profil aérodynamique fixe isolé par étude d'influence des paramètres de distribution du maillage, des conditions limites de turbulence à l'entrée, des corrélations et des paramètres du modèle de transition et par comparaison aux résultats expérimentaux à différentes incidences et différents nombres de Reynolds ; (2) application du modèle de transition optimisé à un rotor cycloïdal pour deux coefficients d'avance, pour étudier en détail les structures d'écoulement internes, notamment l'interaction pale-sillage, l'interaction sillage-sillage, les écoulements vortex près de la paroi et la transition laminaire-turbulence ; (3) optimisation des paramètres du rotor cycloïdal : de la cinématique de tangage, du rapport corde/rayon, de la position du point de pivot, du pas et du profil de pale. Analyse des performances globales pour différents nombres de Reynolds et coefficients d'avance, sur la base de l'analyse des performances de la pale unique, forces (portance et traînée), coefficients de pression et écoulements près de la paroi sur deux pales.

**Mots clés :** Hélice cycloïdale, Modèle de transition, Écoulements tourbillonnaires, Optimisation

## Résumé en anglais

As a new type of propulsion system, the cycloidal propeller has been attracting more attention recently. For a better design of such device, it is of great importance to understand the flow physics of the cycloidal propeller and how it affects the performance under different working conditions. In this thesis, the unsteady vortical flows over a two-bladed cycloidal rotor are simulated using the SST  $k - \widetilde{Re}_{\theta t}$  transition model. The main contributions of the present work can be summarized as follows: (1) calibration of the SST  $k - \widetilde{Re}_{\theta t}$  transition model over a single airfoil, in terms of the mesh distribution, inlet turbulence condition, correlations and parameters in the transition model, and then comparing the results with the experiments at different incidences and Reynolds numbers; (2) applying the optimized transition model to a cycloidal rotor at two advance coefficients, to investigate the internal flow structures in detail, mainly including the blade-wake interaction, wake-wake interaction, near-wall vortex flows and laminar-turbulence transition; (3) optimizing the cycloidal propeller, including the pitching kinematic, chord-to-radius ratio, pitch-pivot-point and blade profile, and explaining how the global performance changes at different Reynolds numbers and advance coefficients, based on the analysis of the performance of the single blade, forces (lift and drag), pressure coefficients and near-wall flows on two blades.

**Key words:** Cycloidal propeller, Transition model, Vortical flows, Optimization